

NIU-18478

DDC Document No.

08400 1-T

NASA-CR-107 956

# HARMONIC GENERATION IN NONLINEAR BEAM-PLASMA SYSTEMS

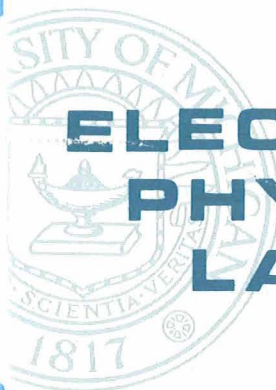
TECHNICAL REPORT NO. 112

## CASE FILE COPY

By

G. T. KONRAD

January, 1969



### ELECTRON PHYSICS LABORATORY

DEPARTMENT OF ELECTRICAL ENGINEERING  
THE UNIVERSITY OF MICHIGAN, ANN ARBOR

CONTRACT WITH:

OFFICE OF SPACE SCIENCE AND APPLICATIONS, NATIONAL  
AERONAUTICS AND SPACE ADMINISTRATION, WASHINGTON, D. C.  
RESEARCH GRANT NO. NGL 23-005-183.

THE UNIVERSITY OF MICHIGAN  
ANN ARBOR, MICHIGAN

HARMONIC GENERATION IN NONLINEAR BEAM-PLASMA SYSTEMS

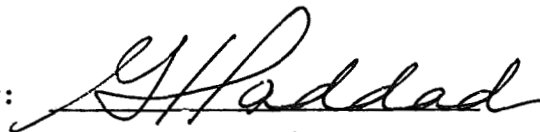
Technical Report No. 112

Electron Physics Laboratory  
Department of Electrical Engineering

By

G. T. Konrad

Approved by:



G. I. Haddad, Director  
Electron Physics Laboratory

Project 08400

RESEARCH GRANT NO. NGL 23-005-183  
OFFICE OF SPACE SCIENCE AND APPLICATIONS  
NATIONAL AERONAUTICS AND SPACE ADMINISTRATION  
WASHINGTON, D. C. 20546

January, 1969



## ABSTRACT

The purpose of this study is to investigate both theoretically and experimentally the saturation characteristics of beam-plasma devices. The gain, power output, efficiency and the magnitude of the higher harmonic components that pertain to such devices are of particular interest.

The geometry treated in this study consists of a cylindrical plasma column which serves as a slow-wave circuit along which electromagnetic energy can propagate. A cylindrical electron stream is assumed to be concentric with the plasma column. Amplification of an RF signal takes place when a fraction of the kinetic energy of the stream electrons is converted into RF wave energy.

The plasma is assumed to remain linear during the interaction process so that it is possible to derive an equivalent circuit for which the various elements are given in terms of the plasma parameters. Beam and plasma collisions are included in the analysis and give rise to lossy elements in the equivalent circuit. The electron stream is shown to become nonlinear much more easily than the plasma so that it is justifiable to treat only the stream in a nonlinear fashion. A Lagrangian (ballistic) analysis is used to calculate the trajectories of the various charge groups into which the electron stream is subdivided. One- as well as two-dimensional stream models are used. A digital computer is employed to calculate both the charge group trajectories and the RF currents and circuit voltages of the fundamental signal and its harmonics generated by the nonlinear operation. Intermodulation and cross-modulation effects in multisignal operation are also studied.

An experimental test vehicle is described which permits correlation of the theoretically calculated results with those obtainable from an actual beam-plasma interaction. A xenon plasma column 10.5 cm long is generated by either a hot cathode Penning discharge or by ionization due to the beam electrons passing through the xenon gas. Values of electronic gain as high as 35 dB in the vicinity of 2.0 GHz are obtained experimentally by the latter scheme. Harmonic components through the fifth are observed with the second harmonic being only 5 dB below the fundamental under certain conditions. When collision effects are taken into account in the theoretical calculations, it is shown that the agreement with the experimentally observed values is quite good for the cases that can be compared.

Coupling of RF energy into and out of the beam-plasma device is considered in detail theoretically and experimentally. Short sections of a slow-wave structure outside of the plasma region are used in the device under test for much of the experimental work. Another coupling scheme making use of quasi-optical techniques is a set of elliptic cavity couplers.



These are found to yield a coupling loss of only 10 to 15 dB per coupler over a frequency range of slightly greater than 20 percent in the low S-band frequency region. This coupling approach is much less lossy than most other methods employed previously. Efforts to use these couplers for RF amplification measurements are shown to be unsuccessful due to cathode poisoning at the higher gas pressures required.

## ACKNOWLEDGMENTS

The author wishes to express his gratitude to his doctoral committee. In particular, the guidance and encouragement of his doctoral committee chairman, Professor Joseph E. Rowe, were deeply appreciated throughout the course of this work. Special thanks are due to Mr. O. H. Wagner for his conscientious efforts in constructing the experimental device. Finally the author is grateful to Mr. Leslie Shive, draftsman, Mrs. June Corkin, editor, and Mrs. Wanita Remali, typist, for their excellent work in the preparation of this manuscript.

A portion of the theoretical work described in this report was supported by NSF Grant GK-1708. The initial phases of the experimental work were supported under Contract DA-28-043 AMC-01315(E) sponsored by the United States Army Electronics Command, Fort Monmouth, New Jersey.

## TABLE OF CONTENTS

	<u>Page</u>
ABSTRACT	iii
ACKNOWLEDGMENTS	v
LIST OF ILLUSTRATIONS	ix
LIST OF TABLES	xviii
CHAPTER I. INTRODUCTION	1
1.1 Historical Survey and Critique	1
1.1.1 General Description of Plasmas and Beam- Plasma Interactions	1
1.1.2 Wave Propagation Through Plasmas	4
1.1.3 Harmonic Generation in Plasmas	7
1.1.4 Description of Electron Beam-Plasma Systems	8
1.2 Theory of Beam-Plasma Interactions	12
1.2.1 Linear Beam-Plasma Theories	12
1.2.2 Large-Signal Theories	14
1.3 Coupling to Beam-Plasma Systems	16
1.4 Objectives and Outline of the Present Study	19
CHAPTER II. DEVELOPMENT OF THE ONE-DIMENSIONAL CIRCUIT EQUATION FOR PLASMA WAVE PROPAGATION	22
2.1 Introduction	22
2.2 The Dispersion Equation for a Plasma Column	23
2.3 Derivation of the Equivalent Circuit Elements	34
2.4 Derivation of the Circuit Equation	43
CHAPTER III. LAGRANGIAN FORMULATION OF THE ONE-DIMENSIONAL BEAM-PLASMA INTERACTION EQUATIONS	55
3.1 Lagrangian Coordinates	55
3.2 The Circuit Equations in Lagrangian Coordinates for $v = 0$	62
3.3 The Lorentz Force Equation in Lagrangian Coordinates	70
3.4 Inclusion of Loss Due to Plasma Particle Collisions in the Large-Signal Equations	74
3.5 Initial Conditions and Input Data	81

	<u>Page</u>
CHAPTER IV. TWO-DIMENSIONAL LARGE-SIGNAL BEAM-PLASMA ANALYSIS	85
4.1 Introduction	85
4.2 Variation of the Electric Field Across the Plasma Column	88
4.3 Derivation of the Circuit Equations	93
4.4 Derivation of the Force Equations	102
4.5 Initial Conditions and Input Data	109
4.6 Discussion on the Quasi-Two-Dimensional Model Used	111
CHAPTER V. SOLUTION OF THE LARGE-SIGNAL EQUATIONS ON A DIGITAL COMPUTER	112
5.1 Introduction	112
5.2 Solution of the One-Dimensional Equations	113
5.3 One-Dimensional Results	117
5.3.1 No Collisions	117
5.3.2 Effect of Beam Collisions	127
5.3.3 Effect of Plasma Collisions	127
5.3.4 Two-Signal Operation	132
5.4 Solution of the Two-Dimensional Equations	137
5.5 Two-Dimensional Results	138
CHAPTER VI. EXPERIMENTAL STUDY OF BEAM-PLASMA INTERACTIONS	155
6.1 Description of the Experimental Apparatus	155
6.1.1 Vacuum System	155
6.1.2 Test Vehicle	157
6.1.3 RF Couplers	162
6.1.4 Axial Magnetic Field	164
6.2 Characteristics of the Xenon Plasma Column	169
6.2.1 Measurement of Plasma Density in the Plasma Tester	169
6.2.2 Plasma Generation in the Beam-Plasma Device	176
6.3 RF Test Results	181
6.3.1 Gain and Harmonic Generation Tests	187
6.3.2 Intermodulation and Cross-Modulation Tests Using Two RF Signals	202

	<u>Page</u>
CHAPTER VII. COUPLING TO BEAM-PLASMA SYSTEMS	214
7.1 Introduction	214
7.2 Analysis of Elliptic Cavity Couplers	214
7.3 Test Results Using Elliptic Cavity Couplers	225
CHAPTER VIII. CONCLUSIONS AND RECOMMENDATIONS FOR FURTHER STUDY	228
8.1 Summary and Conclusions	228
8.2 Recommendations for Further Study	230
APPENDIX A. DISPERSION RELATION FOR A GENERAL BEAM-PLASMA SYSTEM	233
APPENDIX B. DERIVATION OF THE DIELECTRIC TENSOR FOR A PLASMA	241
APPENDIX C. DERIVATION OF THE SPACE-CHARGE FIELD EXPRESSIONS	246
BIBLIOGRAPHY	258
LIST OF SYMBOLS	265

## LIST OF ILLUSTRATIONS

<u>Figure</u>	<u>Page</u>
1.1 Schematic Diagram of an Electron Beam Interaction System.	9
1.2 Typical Beam-Plasma Interaction System.	18
2.1 Geometry of a Plasma Column Slow-Wave Circuit.	24
2.2 Forward Wave Passband Characteristics for the Lowest Order Axially Symmetric Mode in a Dielectric-Lined Metallic Cylinder Filled with Plasma. ( $a/b = 1.2$ , $\kappa_e = 6.0$ , $\omega_p = 2.52 \cdot 10^{10}$ rad/s, $b = 0.152$ cm)	31
2.3 Phase Characteristics for the Lowest Order Axially Symmetric Mode in a Dielectric-Lined Metallic Cylinder. ( $a/b = 2.0$ , $\omega_p/\omega_c = 2.0$ , $\omega_p = 2.52 \cdot 10^{10}$ rad/s, $b = 0.152$ cm)	32
2.4 Equivalent Transmission Line with Distributed Elements for a Plasma Column.	40
2.5 Equivalent Circuit Components for a Plasma Column. ( $\omega_p/\omega = 2.49$ , $\omega_c/\omega = 0.428$ , $\omega_p = 2.65 \cdot 10^{10}$ rad/s, $a/b = 6.26$ , $b = 0.152$ cm, $v/\omega = 0$ )	42
2.6 Equivalent Transmission Line for a Collisionless Plasma Column Showing the Various Resonances.	44
2.7 Electron Beam Interacting with a Plasma Column.	45
2.8 Real Part of the Characteristic Impedance of a Plasma Column. ( $\omega_p/\omega = 2.49$ , $\omega_c/\omega = 0.428$ , $\omega_p = 2.65 \cdot 10^{10}$ rad/s, $a/b = 6.26$ , $b = 0.152$ cm)	48
2.9 Real Part of the Characteristic Impedance of a Plasma Column. ( $\omega_p = 2.65 \cdot 10^{10}$ rad/s, $a/b = 6.26$ , $b = 0.152$ cm, $\kappa_e = 2.0$ )	49
2.10 Real Part of the Characteristic Impedance of a Plasma Column. ( $\omega_c/\omega = 0.428$ , $\omega = 1.068 \cdot 10^{10}$ rad/s, $a/b = 6.26$ , $b = 0.152$ cm, $\kappa_e = 2.0$ )	50

<u>Figure</u>	<u>Page</u>
2.11 Real Part of the Characteristic Impedance of a Plasma Column. ( $\omega_p/\omega = 2.49$ , $\omega_p = 2.65 \cdot 10^{10}$ rad/s, $a/b = 6.26$ , $b = 0.152$ cm, $\kappa_e = 2.0$ )	51
2.12 Real Part of the Characteristic Impedance of a Plasma Column. ( $\omega_p = 4.4 \cdot 10^{10}$ rad/s, $a/b = 1.2$ , $b = 0.792$ cm, $\kappa_e = 6.0$ , $\omega_p/\omega_c = 5.0$ )	52
2.13 Characteristic Impedance of a Plasma Column. ( $\omega_p/\omega = 2.49$ , $\omega_c/\omega = 0.428$ , $\omega_p = 2.65 \cdot 10^{10}$ rad/s, $a/b = 6.26$ , $b = 0.152$ cm, $\kappa_e = 2.0$ )	54
3.1 Electron Motion in a One-Dimensional System.	56
3.2 Large-Signal Flight-Line Diagram.	61
4.1 Model for an Electron Stream Passing Through a Plasma Column.	87
4.2 Dispersion Curves for a Plasma Column.	90
4.3 Axial Electric Field Variation as a Function of Radius for the Case of $\omega_c < \omega_p$ .	91
5.1 Operating Parameters for the Beam-Confined Mode of a Beam-Generated Plasma Column Interacting with the Electron Beam. ( $f_p = 4.24$ GHz, $f_c = 728$ MHz, $a/b = 6.26$ , $b/b' = 1.217$ )	118
5.2 Voltage Amplitude and Power Level of the Fundamental as a Function of Distance Along a Beam-Plasma Amplifier. ( $C_1 = 0.111$ , $b_1 = 0.8$ , $Z_{o1} = 324 \Omega$ , $v_c/\omega = 0$ , $f_p = 4.24$ GHz, $f_c = 728$ MHz, $f_s = 1.79$ GHz)	119
5.3 Voltage Amplitude and Power Level of the Fundamental and the Second Harmonic as a Function of Distance Along a Beam-Plasma Amplifier. ( $C_1 = 0.111$ , $b_1 = 0.8$ , $Z_{o1} = 324 \Omega$ , $v_c/\omega = 0$ , $f_p = 4.24$ GHz, $f_c = 728$ MHz, $f_s = 1.79$ GHz)	121
5.4 Voltage Amplitude and Power Level of the Fundamental and the First Two Harmonics as a Function of Distance Along a Beam-Plasma Amplifier. ( $C_1 = 0.111$ , $b_1 = 0.8$ , $Z_{o1} = 324 \Omega$ , $v_c/\omega = 0$ , $f_p = 4.24$ GHz, $f_c = 728$ MHz, $f_s = 1.79$ GHz)	122

<u>Figure</u>		<u>Page</u>
5.5	Voltage Amplitude and Signal Level of the Fundamental and the First Three Harmonics as a Function of Distance Along a Beam-Plasma Amplifier. ( $C_1 = 0.111$ , $b_1 = 0.8$ , $Z_{o1} = 324 \Omega$ , $v_c/\omega = 0$ , $f_p = 4.24$ GHz, $f_c = 728$ MHz, $f_s = 1.79$ GHz)	123
5.6	Saturation Characteristics for a Beam-Plasma Interaction as a Function of the Velocity Parameter. ( $C_1 = 0.113$ , $Z_{o1} = 324 \Omega$ , $v_c/\omega = 0$ )	125
5.7	Saturation Characteristics for a Beam-Plasma Interaction as a Function of the Gain Parameter. ( $b_1 = 1.0$ , $Z_{o1} = 324 \Omega$ , $v_c/\omega = 0$ )	126
5.8	Voltage Amplitude and Signal Level of the Fundamental as a Function of Distance Along a Beam-Plasma Amplifier, with Beam-Plasma Collisions Included. ( $C_1 = 0.113$ , $b_1 = 0$ , $Z_{o1} = 340 \Omega$ , $f_p = 4.24$ GHz, $f_c = 728$ MHz, $f_s = 1.70$ GHz)	128
5.9	Voltage Amplitude and Signal Level of the Fundamental as a Function of Distance Along a Beam-Plasma Amplifier, with Beam-Plasma Collisions Included. ( $C_1 = 0.110$ , $b_1 = 1.4$ , $Z_{o1} = 312 \Omega$ , $f_p = 4.24$ GHz, $f_c = 728$ MHz, $f_s = 1.85$ GHz)	129
5.10	Voltage Amplitude and Signal Level of the Fundamental and First Three Harmonics as a Function of Distance Along a Beam-Plasma Amplifier. ( $C_1 = 0.111$ , $b_1 = 0.8$ , $Z_{o1} = 324 \Omega$ , $v_c/\omega = 0.001$ , $f_p = 4.24$ GHz, $f_c = 728$ MHz, $f_s = 1.79$ GHz)	130
5.11	Voltage Amplitude and Signal Level of the Fundamental as a Function of Distance Along a Beam-Plasma Amplifier Showing the Effect of Plasma Collisions. ( $C_1 = 0.111$ , $b_1 = 0.8$ , $Z_{o1r} = 324 \Omega$ , $v_c/\omega = 0$ , $f_p = 4.24$ GHz, $f_c = 728$ MHz, $f_s = 1.79$ GHz)	131
5.12	Voltage Amplitude and Signal Level of the Fundamental and the First Three Harmonics as a Function of Distance Along a Beam-Plasma Amplifier with Plasma Collisions Included. ( $C_1 = 0.111$ , $b_1 = 0.8$ , $Z_{o1r} = 324 \Omega$ , $Z_{oi}/ Z_{o1}  = -0.0303$ , $v_c/\omega = 0$ , $f_p = 4.24$ GHz, $f_c = 728$ MHz, $f_s = 1.79$ GHz)	133



<u>Figure</u>		<u>Page</u>
5.13	Two-Signal Operation of a Beam-Plasma Amplifier Showing Two Intermodulation Components. ( $C_a = 0.111$ , $b_a = 0.8$ , $Z_{oa} = 338 \Omega$ , $f_p = 4.24$ GHz, $f_c = 728$ MHz, $f_a = 1.7$ GHz, $f_b = 1.8$ GHz)	135
5.14	Two-Signal Operation of a Beam-Plasma Amplifier Showing Two Intermodulation Components. ( $C_a = 0.111$ , $b_a = 0.8$ , $Z_{oa} = 338 \Omega$ , $f_p = 4.24$ GHz, $f_c = 728$ MHz, $f_a = 1.7$ GHz, $f_b = 1.8$ GHz)	136
5.15	Comparison of One-Dimensional and Two-Dimensional Analyses of a Beam-Plasma System. ( $C_1 = 0.111$ , $b_1 = 0.8$ , $Z_{o1} = 324 \Omega$ , $v_c/\omega = 0$ , $f_p = 4.24$ GHz, $f_b = 259$ MHz, $f_c = 728$ MHz, $f_s = 1.79$ GHz)	139
5.16	Electron Trajectories in a Beam-Plasma Amplifier when Beam Space-Charge Effects Are Neglected. ( $C_1 = 0.110$ , $b_1 = 1.4$ , $Z_{o1} = 312 \Omega$ , $v_c/\omega = 0$ , $f_p = 4.24$ GHz, $f_b = 259$ MHz, $f_c = 728$ MHz, $f_s = 1.85$ GHz)	140
5.17	Electron Trajectories in a Beam-Plasma Amplifier when Beam Space-Charge Effects Are Included. ( $C_1 = 0.110$ , $b_1 = 1.4$ , $Z_{o1} = 312 \Omega$ , $v_c/\omega = 0$ , $f_p = 4.24$ GHz, $f_b = 259$ MHz, $f_c = 728$ MHz, $f_s = 1.85$ GHz)	141
5.18	RF Velocity of the Beam Electrons as a Function of Normalized Phase at Four Positions Along a Beam-Plasma Amplifier. ( $C_1 = 0.110$ , $b_1 = 1.4$ , $Z_{o1} = 312 \Omega$ , $v_c/\omega = 0$ , $f_p = 4.24$ GHz, $f_b = 259$ MHz, $f_c = 728$ MHz, $f_s = 1.85$ GHz)	143
5.19	RF Harmonic Currents as a Function of Distance Along a Beam-Plasma Amplifier with Beam Space-Charge Effects Included. ( $C_1 = 0.111$ , $b_1 = 0.8$ , $Z_{o1} = 324 \Omega$ , $v_c/\omega = 0$ , $f_p = 4.24$ GHz, $f_b = 259$ MHz, $f_c = 728$ MHz, $f_s = 1.79$ GHz)	144
5.20	Fundamental RF Currents in the Three Beam Layers as a Function of Distance Along a Beam-Plasma Amplifier with Beam Space-Charge Effects Included. ( $C_1 = 0.111$ , $b_1 = 0.8$ , $Z_{o1} = 324 \Omega$ , $v_c/\omega = 0$ , $f_p = 4.24$ GHz, $f_b = 259$ MHz, $f_c = 728$ MHz, $f_s = 1.79$ GHz)	145

<u>Figure</u>		<u>Page</u>
5.21	Second Harmonic Currents in the Three Beam Layers as a Function of Distance Along a Beam-Plasma Amplifier with Beam Space-Charge Effects Included. ( $C_1 = 0.111$ , $b_1 = 0.8$ , $Z_{O1} = 324 \Omega$ , $v_c/\omega = 0$ , $f_p = 4.24$ GHz, $f_b = 259$ MHz, $f_c = 728$ MHz, $f_s = 1.79$ GHz)	146
5.22	Saturation Gain and Efficiency as a Function of Frequency in a Beam-Plasma Amplifier. ( $v_c/\omega = 0$ , $f_p = 4.24$ GHz, $f_b = 259$ MHz, $f_c = 728$ MHz)	148
5.23	Saturation Gain and Efficiency as a Function of Frequency in a Beam-Plasma Amplifier. ( $v_c/\omega = 0$ , $f_p = 4.17$ GHz, $f_b = 247$ MHz, $f_c = 1.357$ GHz)	149
5.24	Position of First Maxima in the Voltage Amplitude, $A(y)$ , and the Harmonic Currents as a Function of $b_1$ . ( $C_1 = 0.113$ , $Z_{O1} = 340 \Omega$ , $v_c/\omega = 0$ , $f_p = 4.24$ GHz, $f_b = 259$ MHz, $f_c = 728$ MHz, $f_s = 1.7$ GHz)	151
5.25	Maximum Values of the RF Currents as a Function of $b_1$ . ( $C_1 = 0.113$ , $Z_{O1} = 340 \Omega$ , $v_c/\omega = 0$ , $f_p = 4.24$ GHz, $f_b = 259$ MHz, $f_c = 728$ MHz, $f_s = 1.7$ GHz)	152
5.26	Maximum Values of the Voltage Amplitude, Saturation Gain and Efficiency as a Function of $b_1$ . ( $C_1 = 0.113$ , $Z_{O1} = 340 \Omega$ , $v_c/\omega = 0$ , $f_p = 4.24$ GHz, $f_b = 259$ MHz, $f_c = 728$ MHz, $f_s = 1.7$ GHz)	153
6.1	Vacuum System.	156
6.2	Diagram of the Beam-Plasma Device.	158
6.3	Photograph of the Completed Beam-Plasma Device.	159
6.4	Photograph of the Various Subunits Before Final Assembly.	160
6.5	Coupled-Helix Couplers.	163
6.6	Diagram of an Elliptic Cavity Coupler.	165
6.7	Photograph of an Elliptic Cavity Coupler.	166

<u>Figure</u>		<u>Page</u>
6.8	Placement of RF Couplers on the Beam-Plasma Device.	167
6.9	Magnetic Field Coils for Focusing the Electron Beam.	168
6.10	Photograph of the Plasma Tester.	170
6.11	Diagram of the Plasma Tester.	171
6.12	Plasma Frequency vs. Discharge Current Measured in a Xenon Plasma Column with Zero Magnetic Field. ( $P = 2 \cdot 10^{-2}$ Torr)	172
6.13	Plasma Frequency and Electron Temperature at the Center of the Xenon Plasma Column as Measured with the Double Probe. ( $P = 2 \cdot 10^{-2}$ Torr, Discharge Current = 400 mA/Cathode)	175
6.14	Discharge Voltage Drop vs. Pressure for Various Values of Discharge Current. ( $B_0 = 485$ G)	178
6.15	Experimental Test Facility.	182
6.16	Cold Loss of the Beam-Plasma Device Through the Coupled-Helix Couplers with Neither Beam nor Plasma Present.	183
6.17	Beam Transmission Through the Beam-Plasma Device at Pressures Less than Approximately $2 \cdot 10^{-4}$ Torr for Focusing Field Values of 260 and 485 G.	185
6.18	Variation of Various Electrode Currents in the Millitorr Pressure Range. ( $B_0 = 485$ G, $V_0 = 600$ V)	186
6.19	Small-Signal Gain vs. Beam Voltage for a Beam-Plasma Device Using Coupled-Helix Couplers. ( $B_0 = 260$ G, $f_c = 728$ MHz, $f_s = 2.0$ GHz, $f_p \cong 4.3$ GHz, $P = 2 \cdot 10^{-4}$ Torr)	188
6.20	Typical Spectrum Analyzer Patterns of the Output from a Beam-Plasma Device. ( $f_s = 2.0$ GHz, Drive Power = 250 mW, $P = 2 \cdot 10^{-4}$ Torr, $f_c = 728$ MHz, $f_p \cong 4.3$ GHz, $I_0 = 10$ mA, $V_0 = 585$ V)	189
6.21	Small-Signal Electronic Gain in a Beam-Plasma System Using Coupled-Helix Couplers. ( $B_0 = 260$ G, $f_c = 728$ MHz, $f_p \cong 4.3$ GHz, $P = 2 \cdot 10^{-4}$ Torr)	191

<u>Figure</u>		<u>Page</u>
6.22	Saturation Data for a Beam-Plasma Device Using Coupled-Helix Couplers. ( $f_s = 1.045$ GHz, $V_o = 770$ V, $I_o = 7.1$ mA, $B_o = 260$ G, $f_c = 728$ MHz, $f_p \cong 4.3$ GHz, $P = 2 \cdot 10^{-4}$ Torr, Small-Signal Gain = 6 dB)	192
6.23	Saturation Data for a Beam-Plasma Device Using Coupled-Helix Couplers. ( $f_s = 1.7$ GHz, $V_o = 600$ V, $I_o = 10.2$ mA, $B_o = 260$ G, $f_c = 728$ MHz, $f_p \cong 4.3$ GHz, $P = 2 \cdot 10^{-4}$ Torr, Small-Signal Gain = 24 dB)	193
6.24	Harmonic Level Below the Fundamental at Saturation in a Beam-Plasma Amplifier. ( $V_o \cong 600$ V, $I_o \cong 10.2$ mA, $B_o = 260$ G, $f_p \cong 4.3$ GHz, $P = 2 \cdot 10^{-4}$ Torr)	194
6.25	Small-Signal Electronic Gain in a Beam-Plasma System Using Coupled-Helix Couplers. ( $B_o = 485$ G, $f_c = 1.357$ GHz, $f_p \cong 4.2$ GHz, $P = 2 \cdot 10^{-4}$ Torr)	195
6.26	Harmonic Level Below the Fundamental at Saturation in a Beam-Plasma Amplifier. ( $V_o \cong 570$ V, $I_o = 8.4$ mA, $B_o = 260$ G, $f_p \cong 4.3$ GHz, $P = 2 \cdot 10^{-4}$ Torr)	196
6.27	Comparison of Beam Confined and Total Glow Modes. ( $f_s = 2.013$ GHz, $f_c = 1.357$ GHz)	200
6.28	Output Characteristics of a Beam-Plasma Device Operating in the Total Glow Mode with the Input Signal Close to the Cyclotron Frequency. ( $V_o = 580$ V, $I_o = 7.2$ mA, $f_c = 1260$ MHz, $f_s = 1150$ MHz, $f_p \cong 9.56$ GHz)	201
6.29	Output as a Function of the Input Drive Level for the Beam-Plasma Device Operating in the Total Glow Mode at a Frequency of 745 MHz. ( $V_o = 580$ V, $I_o = 7.8$ mA, $B_o = 280$ G, $f_c = 780$ MHz, $P = 3 \cdot 10^{-3}$ Torr, $f_p \cong 9.5$ GHz)	203
6.30	Spectrum Analyzer Display of the Fundamental and Its First Two Harmonics in the Output from a Beam-Plasma Device Operating in the Total Glow Mode. ( $V_o = 580$ V, $I_o = 7.8$ mA, $f_c = 780$ MHz, $f_s = 745$ MHz)	204

<u>Figure</u>		<u>Page</u>
6.31	Output as a Function of the Input Drive Level for the Beam-Plasma Device Operating in the Total Glow Mode at a Frequency of 924 MHz. ( $V_o = 580$ V, $I_o = 7.2$ mA, $B_o = 450$ G, $f_c = 1260$ MHz, $P = 3 \cdot 10^{-3}$ , $f_p \cong 9.5$ GHz)	205
6.32	Spectrum Analyzer Display of the Fundamental and the Second Harmonic at the Output of a Beam-Plasma Device Operating in the Total Glow Mode. ( $V_o = 580$ V, $I_o = 7.2$ mA, $f_c = 1260$ MHz, $f_s = 924$ MHz)	206
6.33	Intermodulation Components and Higher Frequency Output as the Lower Frequency Input Level Is Varied. [ $f_a = 1.994$ GHz, $f_b = 2.000$ GHz (140 mW Drive Power), Small-Signal Gain = 33 dB, $V_o = 573$ V, $I_o = 8.9$ mA, $B_o = 485$ G, $f_p \cong 4.2$ GHz, $P = 2 \cdot 10^{-4}$ Torr]	208
6.34	Intermodulation Components and Lower Frequency Output as the Higher Frequency Input Level Is Varied. [ $f_a = 1.994$ GHz (140 mW Drive Power), $f_b = 2.000$ GHz, Small-Signal Gain = 33 dB, $V_o = 573$ V, $I_o = 8.9$ mA, $B_o = 485$ G, $f_p \cong 4.2$ GHz, $P = 2 \cdot 10^{-4}$ Torr]	209
6.35	Spectrum Analyzer Display of the Output of a Beam-Plasma Device with Two Input Signals. ( $f_a = 1.994$ GHz, $f_b = 2.000$ GHz, $V_o = 573$ V, $I_o = 8.9$ mA, $B_o = 485$ G)	210
6.36	Intermodulation Components and Higher Frequency Output as the Lower Frequency Input Level Is Varied. [ $f_a = 2.009$ GHz, $f_b = 2.010$ GHz (150 mW Drive Power), Small-Signal Gain = 33 dB, $V_o = 573$ V, $I_o = 8.9$ mA, $B_o = 485$ G, $f_p \cong 4.2$ GHz, $P = 2 \cdot 10^{-4}$ Torr]	212
6.37	Spectrum Analyzer Display of the First Two Sets of Intermodulation Components at the Output of a Beam-Plasma Device. ( $f_a = 2.009$ GHz, $f_b = 2.010$ GHz, $V_o = 573$ V, $I_o = 8.9$ mA, $B_o = 485$ G)	213
7.1	Development of an Elliptic Cavity Coupler.	215

<u>Figure</u>		<u>Page</u>
7.2	Input Impedance of a Radial Transmission Line Terminated in $50 \Omega$ . ( $k_{oi} = 0.416$ )	219
7.3	Concept of an Elliptic Cavity Coupler.	220
7.4	Cross Section Through an Elliptic Cavity Coupler.	223
7.5	Photograph Showing the Inside of an Elliptic Cavity Coupler.	224
7.6	Insertion Loss Through Two Elliptic Cavity Couplers and a 2.36 cm Long Plasma Column Created by a Dual Hot-Cathode Discharge for Various Values of Discharge Current. ( $P = 3 \cdot 10^{-2}$ Torr, $B_o = 332$ G, $f_c = 934$ MHz)	226
A.1	General Beam-Plasma Geometry.	234
A.2	Solution of the Dispersion Equation for a Beam-Plasma System. ( $\omega_c/\omega_p = 0.316$ , $\rho_p/\rho_b = 10^3$ , Beam Microperveance = 1.0) (Simpson <sup>39</sup> )	240
C.1	Model for the Derivation of the Space-Charge Fields.	248
C.2	Rings of Charge in an Electron Stream Flowing Through a Drift Tube.	253

LIST OF TABLES

<u>Table</u>		<u>Page</u>
5.1	Plasma Device Parameters.	116
5.2	Equivalent Circuit Impedance Values.	117
6.1	RF Helix Parameters.	161
6.2	Characteristics of a Beam-Generated Plasma in Xenon.	181
6.3	Comparison of Experimental and Theoretical Results.	198
7.1	Cavity Dimensions.	221

## CHAPTER I. INTRODUCTION

### 1.1 Historical Survey and Critique

#### 1.1.1 General Description of Plasmas and Beam-Plasma Interactions.

If the temperature of a gas is raised to a sufficiently high value, the thermal agitation of the gas particles may be so large that electrons are stripped off by the collisions among the particles. The dynamical behavior of the gas may then become dominated by the long-range electromagnetic forces acting on the free ions and electrons. The behavior of such a fluid differs sufficiently from that of an ordinary gas to warrant the introduction of a new name, the "plasma." A plasma is thus an assembly of charged particles with additional characteristics to be described more fully in the following paragraphs.

The electric and magnetic fields of such an assembly of charged particles may add together in a coherent way, provided the density of the charged particles is sufficiently great so that space-charge effects dominate. This is a very general proviso and does not necessarily depend upon the degree of ionization of the assembly of charged particles or its neutrality. As an example, it is well known that an unneutralized electron beam behaves in many respects like a plasma. Ordinarily, when one speaks of a plasma, however, gross charge neutrality is assumed to exist. The tendency toward quasi-neutrality is very strong because the forces on the individual particles are always in a direction to reduce the space-charge density. Thus a more limited definition of a plasma includes quasi-neutrality.



Statistically speaking, a shielding cloud forms around each ionized particle in the plasma so as to cancel out the electric potential of that particle at a sufficiently large distance from it. This distance is known as the Debye length, a concept developed in the study of electrolytes by P. Debye, and is given by

$$\lambda_D^2 = \frac{kT\epsilon_0}{nq^2} , \quad (1.1)$$

where T is the temperature in °K characterizing the motion of the particles, n is the particle density in particles/m<sup>3</sup>, q is the charge of the particles, k is Boltzmann's constant, 1.380·10<sup>-23</sup> J/°K, and ε<sub>0</sub> is the permittivity of free space, 8.854·10<sup>-12</sup> F/m. Thus the Debye length is a fundamental parameter in plasma physics because any collection of charged particles can be called a plasma only if its dimensions are much larger than a Debye length.

The discussion above is sensible only if there are many charged particles in a Debye sphere. This implies that

$$N_D = \frac{4}{3} \pi \lambda_D^3 n \gg 1 , \quad (1.2)$$

where N<sub>D</sub> is the number of particles in a Debye sphere. In highly ionized gases, which are of interest in this discussion, Eq. 1.2 is always satisfied. Taking the spacing between the ionized particles to be L ≅ n<sup>-1/3</sup>, then the average potential energy is given by

$$\langle PE \rangle \cong \frac{q^2}{4\pi\epsilon_0 L} = \frac{q^2 n^{1/3}}{4\pi\epsilon_0} , \quad (1.3)$$

while the mean kinetic energy is  $kT$ . From Eqs. 1.1 through 1.3 one obtains

$$\frac{\langle KE \rangle}{\langle PE \rangle} \cong \frac{kT}{q^2 n^{1/3} / 4\pi\epsilon_0} = 4\pi n^{2/3} \lambda_D^2 \quad (1.4)$$

and so for a plasma,

$$\frac{\langle KE \rangle}{\langle PE \rangle} \cong (36\pi)^{1/3} N_D^{2/3} \gg 1 \quad (1.5)$$

It appears reasonable that if an ionized gas is not to recombine, the kinetic energy should be greater than the potential energy.

Plasma physics became a recognizable field of study with the work of Tonks and Langmuir,<sup>1</sup> who observed oscillations in a plasma of electrons and positive ions. These authors neglected the thermal velocities of the electrons and described the oscillations observed as displacements of groups of electrons with respect to a background of positive ions. They established the well known relationship for these characteristic oscillations or "plasma oscillations" as

$$\omega_p^2 = \frac{ne^2}{m\epsilon_0} \quad (1.6)$$

where  $\omega_p$  is the frequency of oscillation in rad/s,  $n$  is the electron density in electrons/m<sup>3</sup>,  $e$  and  $m$  are the charge and mass, respectively, of the electron, and  $\epsilon_0$  is the permittivity of free space.

The modern theory of plasma oscillations had its real beginning around 1950 with the work of Bohm and Gross,<sup>2-4</sup> who discussed electron oscillations associated with the presence of electrostatic potential waves in a plasma. These authors considered the effects of random thermal motion, collisions, boundaries of their plasma model, and the presence of

electron beams. A prediction of the Bohm and Gross theory was that an electron beam sent through a homogeneous plasma should excite plasma oscillations. The experimental results of Merrill and Webb<sup>5</sup> described in 1939 and also those of Looney and Brown,<sup>6</sup> the latter appearing to be in disagreement with the Bohm and Gross theory, in fact substantiate the theory of Bohm and Gross. The apparent paradox between the Looney and Brown results and the Bohm and Gross theory was resolved by Sturrock,<sup>7</sup> who was among the first to work out a systematic procedure of interpreting dispersion laws for plasma models such as those analyzed by Bohm and Gross.

1.1.2 Wave Propagation Through Plasmas. In an elementary plasma model the small disturbances, which always oscillate at the plasma frequency, do not propagate away from their point of origin. Since the convection current of the electrons is exactly cancelled by the displacement current, there is no magnetic field associated with the oscillatory motion; hence the disturbances remain localized. If the plasma electrons have a finite temperature, however, these disturbances do propagate away from their point of origin with a velocity comparable to their thermal speed.

If the disturbance has a fixed wavelength initially, then the energy associated with this disturbance can diffuse into other wavelengths by a process of collisionless damping, generally known as Landau damping.<sup>8</sup> Physically this damping process is due to the fact that there is a decreasing number of particles in higher velocity classes. Hence there are slightly more particles traveling more slowly compared with the original disturbance than there are particles traveling faster, resulting in a decrease of the amplitude of the original disturbance.

The electromagnetic waves that can propagate in an ionized medium are frequently studied by choosing a simple zero-temperature plasma model. The response to an oscillating RF field is accounted for in terms of an equivalent charge-free frequency-dependent permittivity,  $\epsilon$ , given by

$$\epsilon = \epsilon_0 (1 - \omega_p^2 / \omega^2) \quad (1.7)$$

for a homogeneous, isotropic plasma; where  $\omega$  is the radian RF frequency. This equivalent permittivity is employed in the usual way in the solution of the Maxwell field equations. When the plasma is immersed in a magnetic field, the permittivity becomes both anisotropic and frequency-dependent, so that it is then a tensor quantity. Solving Maxwell's equations, a dispersion equation may be found which shows that electromagnetic waves do not propagate in an ionized gas below the plasma frequency and that the plasma has little effect on the waves at frequencies much higher than the plasma frequency.

Many models of analysis assume that the collision frequency is negligible compared with the RF wave frequency so that an electron can oscillate many cycles before it makes a collision. In those models where this assumption is not valid, the effects of collisions on the damping of the waves can be taken into account by assuming the frequency to be complex and replacing  $\omega^2$  by  $\omega(\omega - j\nu)$ , where  $\nu$  is the radian collision frequency.

The propagation characteristics have been worked out in considerable detail for many such models. Regarding the plasma as a dielectric and solving the resulting field equations, Trivelpiece and Gould<sup>9</sup> found that slow waves propagating on a plasma of finite transverse dimensions can exist even in the absence of a drift motion or thermal

velocities. Their use of the quasistatic assumption was justified because their model did not include fast waves. Bevc and Everhart<sup>10</sup> and Bevc<sup>11</sup> considered wave propagation in plasma-filled waveguides without this restriction and also considered transverse magnetic waves. Cyclotron waves, which are due to the cyclotron frequency resonance (or gyroresonance), were also included in their analyses. It is at the cyclotron radian frequency,  $\omega_c$ , that the electrons spiral about the magnetic field lines. For electrons

$$\omega_c = \frac{e}{m} B, \quad (1.8)$$

where  $e/m$  is the charge-to-mass ratio of the electron and  $B$  is the magnetic field strength in  $\text{Wb/m}^2$ . It should be noted that the gyroresonance for ions is much lower in frequency than for electrons, due to the much higher mass of the ions. Consequently, the ion cyclotron waves will be of little interest in the present study.

In a plasma column not bounded by a good conductor, surface waves of an incompressible nature can propagate in addition to the space-charge or body waves discussed so far. These surface waves<sup>9,12-14</sup> have a finite electric field along the axis of a cylindrical model. The electric field increases radially to the plasma edge and then discontinuously falls to zero at the conducting wall. In these respects the surface wave is similar to the wave propagating along a slow-wave structure in a traveling-wave amplifier. Surface waves on a plasma column in free space and in the absence of a magnetic field propagate at velocities less than the velocity of light and have a passband<sup>14</sup> extending from  $\omega = 0$  to  $\omega = \omega_p/\sqrt{2}$ . The resonance frequency is at  $\omega = \omega_p/\sqrt{2}$ . When the medium outside the plasma column is a homogeneous isotropic dielectric with dielectric constant  $\epsilon$ , the resonance frequency is at

$$\omega = \frac{\omega_p}{\sqrt{1 + \epsilon/\epsilon_0}} . \quad (1.9)$$

If a magnetic field is present, two surface wave resonances occur. For the case of the plasma column in free space with  $\omega_p \gg \omega_{ce}$  one resonance is at  $\omega_1 = \omega_p/\sqrt{2}$ , as before. The second one occurs at

$$\omega_2 = \sqrt{\omega_{ce}\omega_{ci}} , \quad (1.10)$$

which is the electron-ion hybrid resonance, where  $\omega_{ce}$  and  $\omega_{ci}$  are the electron and ion cyclotron frequencies in rad/s, respectively.

1.1.3 Harmonic Generation in Plasmas. One of the early applications of a plasma discharge was in the generation of harmonics. Margenau and Hartman<sup>15</sup> considered this aspect theoretically for electrons in a gas with a sinusoidal electric field applied. One of the first experimental investigations of this problem was carried out by Inada et al.,<sup>16</sup> who applied microwave power in the order of 25 watts at a frequency near 3.0 GHz to a low-Q cavity containing the plasma. The power levels generated were 24, 29 and 34 dB below the input power at the second, third and fourth harmonics, respectively.

If an electromagnetic wave is impressed on a uniform plasma in the absence of any dc electric field and a constant (independent of particle velocity) electron collision frequency is assumed, then there is no harmonic generation. It was found, however, that if the effects of the electromagnetic wave modulation of the collision frequency, resulting in a velocity dependent collision frequency, are included, then harmonic generation may be realized.<sup>17,18</sup> Krenz<sup>17</sup> showed that the third harmonic current, for example, resulting from a velocity dependent

collision frequency depends upon the various moments of the static, isotropic part of the electron velocity distribution function. This effect may be expected to be small compared to nonlinear phenomena, of which a particular type will be considered below, because of the resistive nature of the collisions present.

1.1.4 Description of Electron Beam-Plasma Systems. In a conventional microwave interaction device making use of an electron beam it is necessary to pass the beam close to some form of a metallic slow-wave circuit or a resonant structure in order to convert a fraction of the energy in the electron beam into RF energy. A schematic diagram of a particular form of such a system is shown in Fig. 1.1. The physical dimensions of the interaction structure must be comparable to a free-space wavelength, if the interaction is to be efficient. Thus the size of the electron beam, and hence the current that can be carried, is limited. In a beam-plasma system the RF interaction structure is replaced by a plasma, through which the beam is allowed to pass. Consequently, the beam and the plasma are intimately mixed and the RF fields do not vary appreciably over the cross-sectional area of the beam. This relieves the restriction on the beam diameter, and at the same time the size restrictions on a metallic structure in the vicinity of the electron beam may be greatly alleviated. These characteristics make the beam-plasma interaction attractive at high power levels and at very high frequencies, such as millimeter wavelengths.

Except perhaps for some very idealized and simple systems it is impossible to predict by intuition what type of interactions can take place in a beam-plasma system. On the other hand, a detailed solution

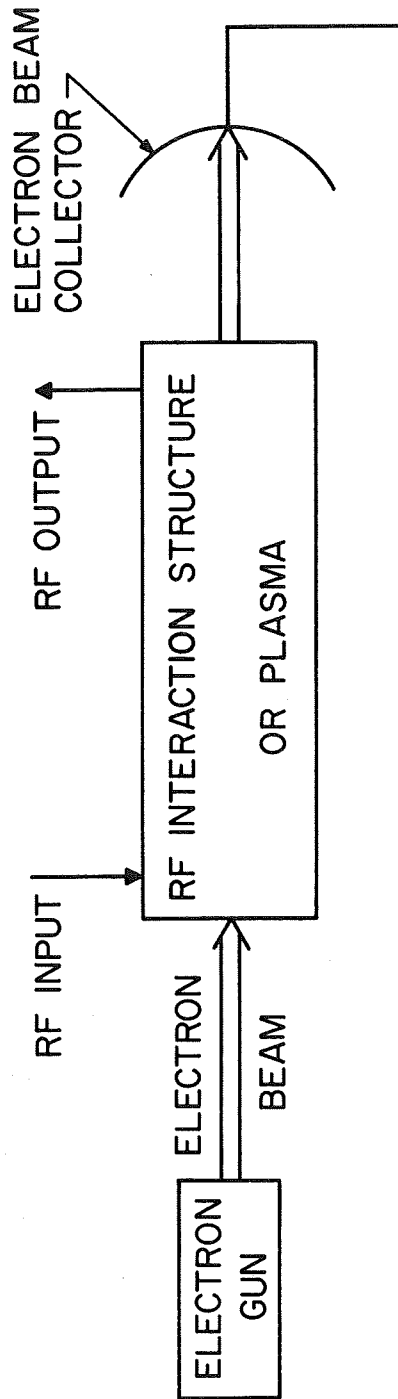


FIG. 1.1.1 SCHEMATIC DIAGRAM OF AN ELECTRON BEAM INTERACTION SYSTEM.



of the boundary value problem describing the system frequently becomes complicated and tedious. In some cases the only information required is whether or not an RF signal applied to a plasma device will grow or decrease in amplitude or whether inherent instabilities may be expected. For that purpose some methods have been developed which reveal this information through an examination of the dispersion equation, which is an algebraic equation in the radian frequency,  $\omega$ , and the propagation constant,  $k$ . Both  $\omega$  and  $k$  are complex quantities in general and it is common practice to assume that the system wave function has a time and spatial dependence of the form  $e^{j(\omega t - kz)}$ . Sturrock's<sup>19</sup> approach differentiates between evanescent and propagating waves on the one hand and growing waves or instabilities on the other. Instabilities, again, may be divided into two classes: convective or amplifying and nonconvective or absolute. Buneman,<sup>20</sup> too, was able to separate amplifying from evanescent modes for certain physical systems with specified boundary conditions at the ends.

The procedures described by Briggs<sup>21</sup> and Sudan<sup>22</sup> are slightly different, although equivalent, methods of analyzing a dispersion relation in order to determine the type of instability in a plasma. In both cases, if the dispersion equation yields real values of  $\omega$  for real values of  $k$  and real values of  $k$  for real values of  $\omega$ , one concludes that the waves are purely propagating and no instability exists. In Briggs's method, a double root of  $k$  separating to different halves of the complex  $k$ -plane, as the imaginary part of  $\omega$  approaches  $-\infty$ , indicates an absolute instability. If a real value of  $\omega$  yields a complex value of  $k$  and the imaginary part of  $k$  changes its sign as the imaginary part of  $\omega$  approaches  $-\infty$ , then the

instability is convective. If the change in sign does not occur, the wave is evanescent.

In Sudan's method it is necessary to examine the causality or noncausality of the roots of the dispersion equation. Causality of the roots is necessary for instabilities or evanescent waves to exist. If distinct branch points of  $k$  exist, at least one of which must be in the lower half of the  $\omega$ -plane, then there is a nonconvective instability. If there are no branch points, but the real part of  $-jk$  is greater than zero with the imaginary part of  $\omega$  equal to zero, then a convective instability exists.

The plasma necessary in a beam-plasma device may be produced by any one of a large variety of discharges, by contact ionization, or by the electron beam itself. Getty and Smullin<sup>23</sup> have looked at the beam-generated plasma in detail. The electron beam, when turned on, ionized the background gas and after a few microseconds the excited plasma electrons became the dominant ionization source. In their experiment a nonconvective instability initiated RF oscillations, which first appeared at the electron cyclotron frequency. Then a convective instability at the plasma frequency generated the oscillations that sustained the discharge. Targ and Levine,<sup>24</sup> as well as Hedvall,<sup>25</sup> also studied beam-generated plasmas and reported on their characteristics, such as plasma density, pressure ranges and the frequency regions of the observed oscillations. In fact, electron beam excitation is employed exclusively in many beam-plasma systems and partially in many others in order to generate the plasma.

It is usually impossible to design an experiment on a beam-plasma system in which the plasma is everywhere homogeneous. In a cylindrical geometry, for example, there are usually density variations in the radial as well as the axial directions.<sup>12,26,27</sup> Chorney and Madore<sup>28</sup> derived a typical plasma density profile for a cylindrical geometry and noted the agreement with experimental devices to be quite good. They found that in the axial direction there was a sinusoidal variation of density, with the density dropping to zero at the metal end walls. In the radial direction the plasma extended by ambipolar diffusion into those regions where there was no ionization, with the density again dropping to zero at the conducting cylinder walls. Nonuniformities in the plasma density make theoretical analyses of realistic laboratory devices considerably more difficult, but, as will be seen below, these inhomogeneities may have beneficial effects on the coupling of RF energy to the beam-plasma system.

## 1.2 Theory of Beam-Plasma Interactions

1.2.1 Linear Beam-Plasma Theories. If an electron beam is introduced into a plasma, an interaction may take place between the beam and the plasma, as has already been mentioned. Combining the terminology of plasma physics with that of the microwave tube field, the beam-plasma device is an amplifier if a convective instability exists, while it is an oscillator if a nonconvective instability exists. Boyd et al.<sup>29</sup> conducted the first conclusive experiments demonstrating microwave amplification when an electron beam is passed through an arc discharge plasma. They showed that amplification occurred at frequencies below the plasma frequency,  $f_p$ , reached a peak at  $f_p$  and extended to slightly higher frequencies depending upon collisions and velocity distributions of the

electrons in the beam and the plasma. Shortly thereafter Bogdanov et al.<sup>30</sup> reported on similar work in which amplifications of 20-40 dB in the 1-10 GHz range were observed. Berezin et al.<sup>31,32</sup> measured the energy loss of the electron beam as it gave up part of its kinetic energy to the high frequency wave, yielding the efficiency of the energy exchange process. The strength of the high frequency fields was also measured.

A great many researchers in this country and abroad have considered the beam-plasma interaction both theoretically and experimentally. The work to be reviewed in the following few paragraphs thus can be only a representative sample of what has been done. In a series of papers Vlaardingerbroek et al.<sup>33-35</sup> derived the dispersion equations for cylindrically symmetric geometries for one or more beams of charged particles in both infinite and finite magnetic fields. The same group of investigators<sup>36</sup> has reported on an experiment in which 60-70 dB electronic gain was observed over a length of 20 cm of mercury plasma.

When the beam and plasma are infinite in extent, an infinite growth rate of oscillations occurs at the plasma frequency. In order to provide for a physically realistic finite growth rate, some authors have incorporated the effects of particle collisions or thermal velocity distributions in their models of infinite cross section.

Crawford<sup>37</sup> considered both infinite and finite beams in an infinite, uniform, warm plasma. At the beam-plasma interface the Hahn<sup>38</sup> rippled surface charge model was used when the beam and plasma were both cold. For a warm plasma, where the electronic Debye length may be comparable to or greater than the RF excursions of the beam electrons, this model was not considered to be appropriate because the surface charge effects on the

plasma side of the beam-plasma interface became negligible. Therefore, the Hahn model was replaced by a continuity condition of pressure and plasma current across the beam-plasma boundary.

It has been shown by Kislov and Bogdanov,<sup>12</sup> by Bogdanov et al.<sup>30</sup> and by Vlaardingerbroek et al.<sup>33</sup> that growing waves with finite growth rates occur in cold, collisionless beam-plasma systems of bounded cross section. In plasmas with parameters of the usual values attainable in the laboratory, the finite geometry has a considerably greater damping effect than do thermal velocities and collisions, as was shown by Simpson.<sup>39</sup> He, as well as Karplyuk and Levitskii,<sup>40</sup> Golant et al.<sup>41</sup> and Stover,<sup>42</sup> considered the effects of dielectrics, such as a glass or ceramic tube containing the plasma, on the dispersion equation. Such realistic additions add extra boundary conditions to be satisfied in the solution of the field equations before the final dispersion equation is obtained. It is found that for such models the dispersion equation quickly becomes intractable for solution, even on a modern, high-speed digital computer.

1.2.2 Large-Signal Theories. Many investigators have solved the dispersion equation for beam-plasma systems under various simplifying assumptions. The complex propagation constants appearing in the dispersion equation yield the small-signal gain of the system as a function of frequency.<sup>26,27,33-35,39,43,44</sup> The general result of these theories is that maximum values of gain in the order of 3-15 dB/cm may be expected for low level operation of a beam-plasma system. As the signal level increases, however, nonlinearities begin to set in, limiting the power output of the device. Thus, for efficiency computations and harmonic generation analyses, it is necessary to employ a large-signal analysis.

Rowe<sup>45, 46</sup> used a Lagrangian (ballistic) theory to calculate particle trajectories and the extent of energy conversion between the beam, the plasma and the RF wave. Microscopic collisions within each charge group were not included in the calculations, but Rowe pointed out<sup>47</sup> that collision effects may be introduced simply by adding an additional electric field term appropriate to the collision model in the Lorentz force equation. Finite temperature effects were accounted for by assigning appropriate particle distribution functions in velocity-phase space. Gould and Allen<sup>48</sup> subdivided the electron beam into disks and determined the forces on them from potentials found by appropriate Fourier transformations, which is a permissible approach since the plasma was assumed to remain linear and superposition is valid in that case. The plasma was also assumed to be warm, thus including the electron thermal speeds and the dissipative effects of short-range collisions. Geidne<sup>49</sup> also used the disk model for the electron beam as well as the plasma electrons. He expanded the force equation to third order for the beam electrons and to first order for the plasma electrons (the plasma was assumed to respond linearly to the electric field in this treatment also).

All three of the nonlinear theories described above yield information on harmonic generation in a beam-plasma system. It is known from the small-amplitude zero-space charge ballistic theory for klystrons<sup>46</sup> that

$$\frac{i_1}{I_0} = 2J_1 \Big|_{\max} = 2(0.58) = 1.16, \quad (1.11)$$

where  $i_1$  and  $I_0$  are the fundamental RF and the dc beam currents, respectively.  $J_1$  is the Bessel function of the first kind and first order.

Similarly, for the maximum second harmonic current,  $i_2/I_0 = 0.98$ . There is a relatively slow diminution of the harmonic amplitude as the harmonic order increases, arising from the very sharp peaks in the current density in a tightly bunched electron stream. Large-signal calculations, including space-charge effects, yield values of  $i_1/I_0$  in the vicinity of 1.6 under optimum conditions in traveling-wave amplifiers and klystrons. Similar results have been found for beam-plasma interactions, with harmonic to dc current magnitudes being on the order of unity.<sup>45</sup> Some experimental results to support these theories have been reported by Berezin et al.<sup>50</sup> and by Allison and Kino.<sup>51</sup>

### 1.3 Coupling to Beam-Plasma Systems

Since space-charge waves do not possess a time-varying magnetic field, they do not radiate into space. To couple to them it is necessary to use probes, slow-wave structures or waveguides, for example. These structures have external fields which may couple to the fringing fields of the space-charge wave. Another possibility is mode coupling, which is ordinarily a weak effect, however. Coupling to a plasma column without the presence of material walls, probes or beams can occur at steep density gradients or in certain directions in anisotropic media. An example of the former are the Tonks-Dattner resonances,<sup>52</sup> which are resonances due to space-charge oscillations. These were analyzed and explained theoretically by Nickel et al.<sup>53</sup> as follows.

When the frequency of an applied RF wave exceeds the electron plasma frequency at the plasma column edge, a wave of the type discussed by Bohm and Gross<sup>2</sup> can propagate in toward the column axis. As it does so, it propagates up an electron density gradient until a point is reached

at which the applied frequency equals the local plasma frequency. Beyond this point the wave is evanescent. At a discrete number of applied frequencies, standing waves can occur between the column edge and the high-density core of the plasma. Waves at these particular frequencies thus give rise to the Tonks-Dattner resonances because the standing waves transverse to the column also represent the cutoffs of a series of modes propagating along the column.

In beam-plasma amplifiers it is highly desirable to couple as much of the input signal as possible into the space-charge waves of the device. Unfortunately this is not a simple procedure. In most practical cases the net power output and the actual gain of the device are quite severely limited by the coupling methods so far employed,<sup>26,54</sup> even though a considerable amount of work has been expended in improving the coupling<sup>26,55</sup> and even though many different schemes have been used. Among them are cavities, reduced height waveguides, coupling helices and slow-wave structures immersed in the plasma. A typical beam-plasma system having helices as coupling structures is depicted in Fig. 1.2.

One very attractive coupling scheme has been investigated fairly extensively theoretically. Feinstein<sup>56</sup> has examined the conversion of longitudinal wave energy of bunched charges into transverse electromagnetic form in electron tubes and multistream plasmas. Neufeld and Doyle<sup>57</sup> showed that the longitudinal oscillations in a homogeneous plasma due to an electron beam may be converted into transverse oscillations when the longitudinal waves interact with the density fluctuations of the plasma electrons. Allen et al.<sup>58</sup> pointed out that in certain frequency regions the anisotropic dielectric "constant" of a homogeneous plasma is such that the radial dielectric constant,  $\epsilon_{rr}$ , is negative



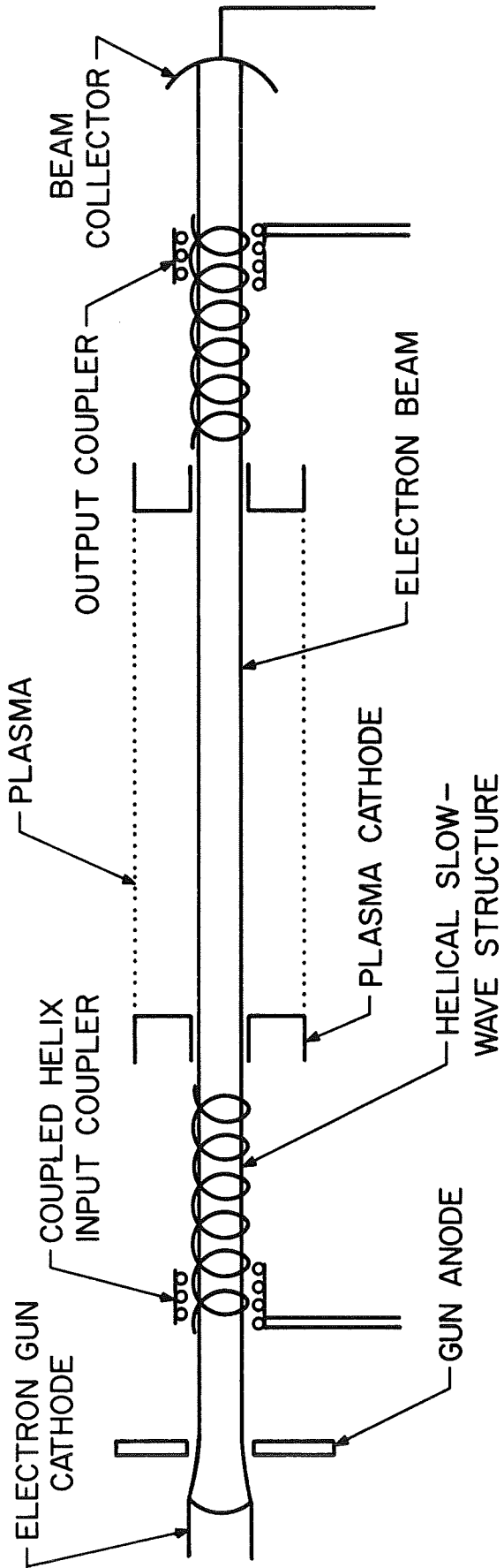


FIG. 1.2 TYPICAL BEAM-PLASMA INTERACTION SYSTEM.

while the longitudinal dielectric constant  $\epsilon_{zz}$  is positive, a situation which results in real propagation constants in both the radial and the longitudinal directions. Thus the fields in the plasma do not fall off radially, as they do on conventional slow-wave circuits.

When radial density variations exist, as is usually the case in practice, Stover and Kino<sup>59</sup> showed that it is not necessarily possible to obtain radial propagation through the plasma column. This is so because the sign of  $\epsilon_{rr}/\epsilon_{zz}$  may change across the plasma, the density of which was assumed to vary parabolically across the column. This type of variation does not necessarily exist in practice due to sheath formations. Allen et al.<sup>60</sup> reported on an experiment in which the presence of a plasma increased the coupling in a system consisting of two waveguide couplers by approximately 20 dB. They cautioned, however, that the optimum plasma density for coupling is not ordinarily the same as for maximum gain. A number of Russian investigators also reported on radial propagation as a means of coupling to a beam-plasma system.<sup>61-63</sup>

When designing a coupling circuit, it is important to know the impedance of the coupler and that of the beam-plasma system. Gould and Trivelpiece<sup>64</sup> have analyzed the latter by use of equivalent circuits, for which the impedance can be determined quite readily. Guest<sup>65</sup> obtained a closed-form expression for the impedance of a pair of idealized plane grids immersed in a one-dimensional beam-plasma medium, while Christy<sup>66</sup> made measurements of the plasma impedance in a gridded gap.

#### 1.4 Objectives and Outline of the Present Study

In the present study the large-signal characteristics of nonlinear beam-plasma interactions will be considered. In particular, saturation

effects and harmonic generation under high-drive conditions will be studied theoretically and experimentally. The coupling problem in beam-plasma systems will be considered also. The impedance of an elliptic cavity coupler will be computed and matched to the impedance of a beam-plasma system.

In Chapter II a linear plasma model is chosen and transmission-line elements are derived for the equivalent circuit representing such a plasma. The characteristic impedance of the equivalent transmission line is completely determined by the plasma parameters and the geometry. Plasma collisions, which represent a loss mechanism, contribute resistive components to the equivalent circuit. These resistive elements appear as the imaginary part of the complex characteristic impedance.

The one-dimensional nonlinear equations for a beam-plasma system are developed in Chapter III. The method of Lagrangian mechanics is employed which essentially consists of following each beam particle individually through the interaction region. Electron overtaking and saturation effects are thus accounted for. A similar approach is employed in the two-dimensional analysis of Chapter VI. The electron stream is accorded a full two-dimensional treatment, while the plasma "circuit" is handled in a quasi-two-dimensional fashion. This is done by using the one-dimensional circuit field expressions corrected by a weighting function proportional to the radial variation of the longitudinal electric field.

In Chapter V the solution of the nonlinear equations on a digital computer is described and the results of typical calculations are presented. Saturation characteristics for the fundamental as well as for

the first few harmonics are shown. Effects of beam as well as plasma collisions are studied.

Chapter VI deals with the experimental work. The beam-plasma system used for these studies is described. The test vehicle contains a cylindrical plasma column into which an electron beam can be injected axially. RF energy is coupled into and out of the interaction region by means of slow-wave structures and cavity couplers. Test results consisting of saturation data, harmonic power output and multisignal characteristics are presented and correlated with the theoretical calculations of Chapter V.

Coupling methods are considered in detail in Chapter VII. The impedance of an elliptic cavity coupler, which is essentially a quasi-optical coupling structure, is calculated. The requirements of matching such a coupler to a beam-plasma system are discussed. Comparison is made between this method of coupling and other methods, such as sections of slow-wave structure in the vicinity of the electron beam.

CHAPTER II. DEVELOPMENT OF THE ONE-DIMENSIONAL CIRCUIT EQUATION  
FOR PLASMA WAVE PROPAGATION

2.1 Introduction

When an electron beam is passed through a plasma, amplification of an RF signal propagating through the plasma may take place under certain conditions. In this analysis cylindrical systems, i.e., plasma columns and drifting electron beams, will be considered. Maximum use will be made of previously developed traveling-wave tube theory, which can be readily adapted to this study.

It is possible to think of a plasma column by itself as a slow-wave "circuit" along which RF energy can propagate just as along a transmission line. For such a transmission line an equivalent circuit may be found which is made up of distributed elements given in terms of the plasma parameters. This approach restricts the plasma to linear behavior. Geidne<sup>49</sup> has calculated the electron displacements and the RF currents in the beam and the plasma of a beam-plasma system. He found that when the device approaches saturation the beam electrons are driven beyond overtaking, while the displacement of the plasma electrons is very small. Physically speaking, the charge density of a typical electron beam is much smaller than the charge density in the plasma. Since the same fields must be supported in both the beam and the plasma, the space-charge restoring forces in the plasma are then much greater than in the beam. This prevents the plasma particles from making large RF excursions. Thus it is justifiable to assume linear behavior for the plasma and introduce the nonlinearities in the electron beam.

In this chapter the plasma characteristics will be studied.

Subsequently an electron stream will be introduced and the interaction of the waves in the plasma with the space-charge waves on the electron stream will be considered.

## 2.2 The Dispersion Equation for a Plasma Column

Consider the geometry for a plasma column coaxial with a conducting cylinder, as shown in Fig. 2.1. First the following assumptions are made about the plasma column.

1. The plasma is cold, stationary, uniform and neutral.
2. A static magnetic field  $B_0 = B_z$  is assumed to exist along the z-direction.
3. Nonrelativistic mechanics applies.
4. A quasistatic analysis is appropriate.
5. A one-dimensional treatment is appropriate for the time being.

The one-dimensional treatment limits the motion of the electrons in the plasma "circuit" to the axial direction. This approach is of course a good one in the case of an infinite or very strong axial magnetic field. For a more moderate magnetic field it is reasonable to assume that in a plasma column of fairly small transverse dimensions this restriction on the motion can be satisfied regardless of the magnitude of the magnetic field by assuming that the plasma is in a region where the axial RF electric field is strong compared with the transverse electric field.

In most microwave beam-type amplifiers the RF wave is slowed sufficiently so that it travels at approximately the same velocity as the beam electrons. The velocity of the beam electrons in turn is usually substantially less than the speed of light. Thus the wavelength of the

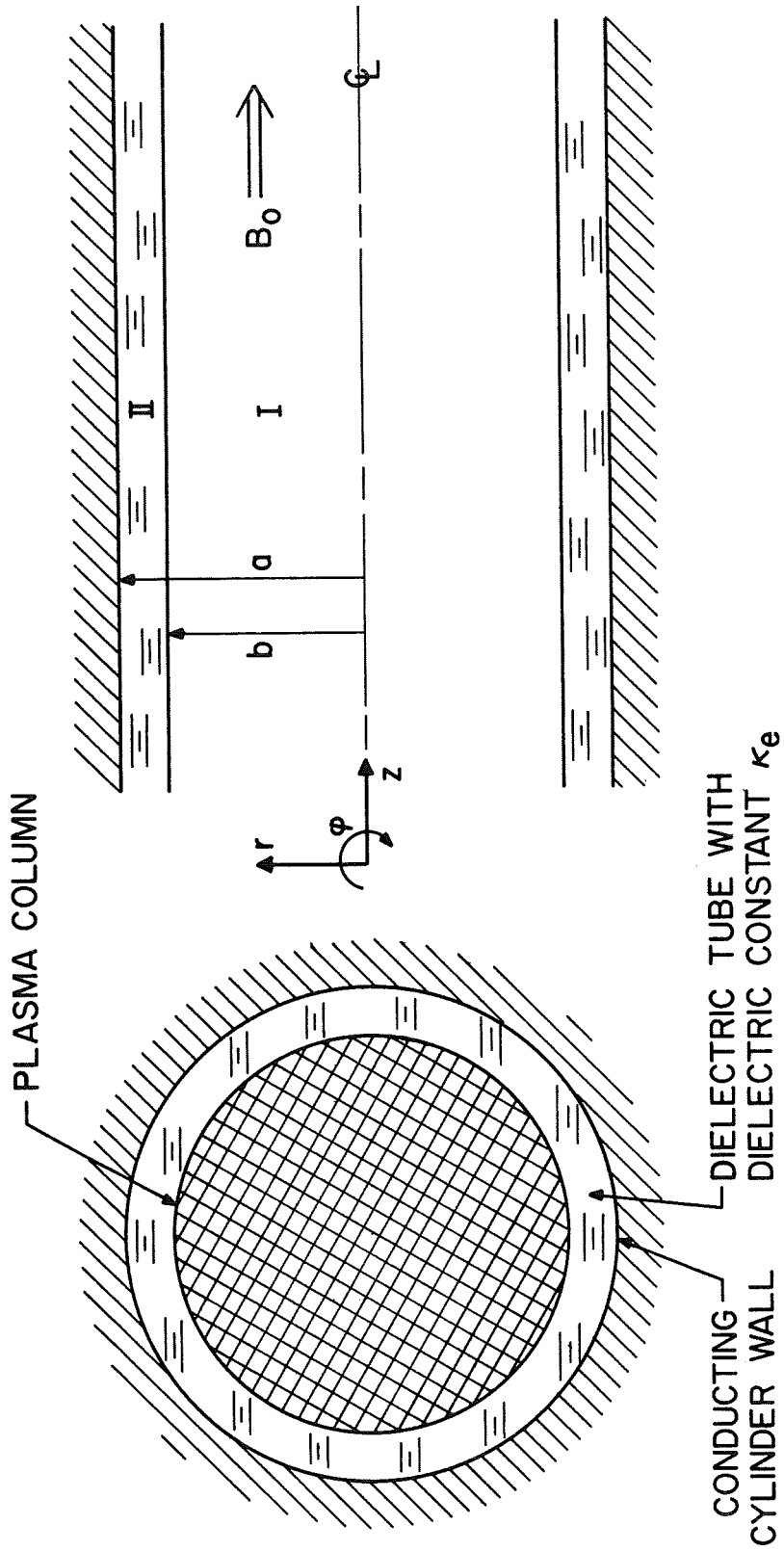


FIG. 2.1 GEOMETRY OF A PLASMA COLUMN SLOW-WAVE CIRCUIT.

disturbances in the slow-wave system is much less than a free-space wavelength. This fact permits the use of a quasistatic analysis, in which Maxwell's equations describing the model under consideration in this study are simplified considerably by replacing the full set of field equations by the equations of electrostatics.

It is possible to find a simple relation between the electric field in the z-direction and the "circuit" voltage. In terms of the magnetic vector potential,  $\vec{A}$ , given by

$$\vec{B} = \nabla \times \vec{A} , \quad (2.1)$$

where  $\vec{B}$  is the magnetic field strength, and the scalar potential,  $V'$ , the electric field may be written as

$$\vec{E} = -\nabla V' - \frac{\partial \vec{A}}{\partial t} . \quad (2.2)$$

In the quasistatic analysis  $\vec{B}$  is time independent, so that one of Maxwell's curl equations becomes

$$\nabla \times \vec{E} = - \frac{\partial \vec{B}}{\partial t} = 0 \quad (2.3)$$

and  $\vec{E}$  is directly derivable from the scalar potential. Taking the z-component of Eq. 2.2,

$$E_z = - \frac{\partial V'}{\partial z} - \frac{\partial A_z}{\partial t} . \quad (2.4)$$

Since  $\vec{A}$  and  $V'$  are arbitrary,  $\vec{A}$  may be expressed in terms of  $V'$  by the Lorentz gauge condition,

$$\nabla \cdot \vec{A} + \mu_0 \epsilon_0 \frac{\partial V'}{\partial t} = 0 . \quad (2.5)$$



Assume that the RF quantities in general vary as  $\exp[j(\omega t - n\phi - kz)]$ .  
 Note that  $k$  is a complex propagation constant, in general given by

$$jk = \alpha + j\beta$$

or

$$k = \beta - j\alpha, \quad (2.6)$$

where  $\beta$  is the phase constant and  $\alpha$  is the attenuation constant. A negative value of  $\alpha$  implies a growth in the wave amplitude. Utilizing the fact that there is no radial component of current and no azimuthal variation of  $\vec{A}$  in the present analysis, Eq. 2.5 becomes

$$\frac{\partial A_z}{\partial z} = -jkA_z = -j\omega\mu_0\epsilon_0 V' \quad (2.7)$$

Substitute  $A_z$  from Eq. 2.7 into Eq. 2.4 to obtain

$$A_z = \frac{\omega\mu_0\epsilon_0}{k} V' ,$$

$$E_z = -\frac{\partial V'}{\partial z} - \frac{\omega\mu_0\epsilon_0}{k} \frac{\partial V'}{\partial t} = -\frac{\partial V'}{\partial z} - \frac{\omega\mu_0\epsilon_0 k}{k^2} j\omega V' ,$$

$$E_z = -\frac{\partial V'}{\partial z} + \frac{\omega^2\mu_0\epsilon_0}{k^2} \frac{\partial V'}{\partial z} .$$

Let  $k_0 = \omega\sqrt{\mu_0\epsilon_0}$  be the propagation constant of free space, so that

$$E_z = -\frac{\partial V'}{\partial z} \left(1 - \frac{k_0^2}{k^2}\right) = -\frac{\partial V'}{\partial z} \left(\frac{k^2 - k_0^2}{k^2}\right) .$$

The radial propagation constant,  $\gamma$ , is defined by

$$\gamma^2 \triangleq k^2 - k_0^2 . \quad (2.8)$$

For slow waves,

$$\gamma^2 = k^2 - k_0^2 \cong k^2, \quad (2.9)$$

so that

$$E_z = -\frac{\partial V'}{\partial z} \left( \frac{\gamma^2}{k^2} \right) \cong -\frac{\partial V'}{\partial z}. \quad (2.10)$$

Thus

$$E_z \cong jkV'. \quad (2.11)$$

If  $V'$  at  $r = b$  is the "circuit voltage,"  $V$ , of the plasma column, then

$$E_{zb} = jkV. \quad (2.12)$$

From Maxwell's equations given in Appendix A, and using  $\nabla \times \vec{E} \cong 0$ , one obtains

$$E_r = -\frac{1}{jk} \frac{\partial E_z}{\partial r} \quad (2.13)$$

and

$$E_\phi = \frac{n}{kr} E_z, \quad (2.14)$$

where it is assumed again that the field quantities vary as  $\exp[j(\omega t - n\phi - kz)]$ . The wave equation for propagation in a plasma column may then be written as

$$\frac{1}{r} \frac{\partial}{\partial r} \left( r \frac{\partial E_z}{\partial r} \right) + \left( T_p^2 - \frac{n^2}{r^2} \right) E_z = 0. \quad (2.15)$$

Here the radial propagation constant in the plasma,  $T_p$ , is related to the longitudinal propagation constant,  $k$ , by

$$T_p^2 = -k^2 \frac{\kappa_{\parallel}}{\kappa_{\perp}} = -k^2 \left[ \frac{1 - \frac{(\omega_p/\omega)^2}{1 - j(\nu/\omega)}}{1 - \frac{(\omega_p/\omega)^2 [1 - j(\nu/\omega)]}{[1 - j(\nu/\omega)]^2 - (\omega_c/\omega)^2}} \right]. \quad (2.16)$$

The  $\kappa$ 's are components of the specific inductive capacity tensor derived in Appendix B,  $\omega_p$  is the radian plasma frequency given by

$$\omega_p^2 \triangleq \frac{e^2 n_e}{m \epsilon_0}, \quad (2.17)$$

$\omega_c$  is the angular electron cyclotron frequency given by

$$\omega_c \triangleq \eta B_0, \quad (2.18)$$

where  $\eta$  is the absolute value of the charge-to-mass ratio of the electron, and  $\nu$  is the radian collision frequency.

In the plasma region (Region I of Fig. 2.1) the solution to Eq. 2.15 for  $E_z$  is given in terms of Bessel functions of the first kind only due to the singularity of the functions of the second kind at  $r = 0$ . Hence

$$E_{zI}(r) = A_n J_n(T_p r), \quad (2.19)$$

where  $A_n$  is an arbitrary constant. Outside of the plasma (Region II), where the radial propagation constant is  $\gamma$ , given by  $\gamma^2 = k^2 - k_0^2$ , the modified Bessel functions may be used, because with  $T_p^2 = -k^2$  the second term in Eq. 2.15 is negative. Thus

$$E_{zII}(r) = B_n I_n(\gamma r) + C_n K_n(\gamma r). \quad (2.20)$$

For slow waves,  $\gamma^2 \cong k^2$ , and in the one-dimensional case there are no  $\phi$ -variations. Hence  $n = 0$ . Thus

$$E_{zI}(r) = AJ_o(T_p r) \quad (2.21)$$

and

$$E_{zII}(r) = BI_o(kr) + CK_o(kr) \quad (2.22)$$

Since there is a perfectly conducting metallic boundary at  $r = a$ ,

$$E_{zII}(a) = 0 = BI_o(ka) + CK_o(ka) \quad ,$$

$$B = -C \frac{K_o(ka)}{I_o(ka)} \quad (2.23)$$

Then,

$$E_{zII}(r) = CK_o(kr) - C \frac{K_o(ka)}{I_o(ka)} I_o(kr) \quad ,$$

$$E_{zII}(r) = \frac{C}{I_o(ka)} [K_o(kr)I_o(ka) - K_o(ka)I_o(kr)] \quad ,$$

$$E_{zII}(r) = C_i [K_o(kr)I_o(ka) - K_o(ka)I_o(kr)] \quad , \quad (2.24)$$

where

$$C_i = \frac{C}{I_o(ka)} \quad .$$

Differentiate Eq. 2.24 to obtain

$$\frac{\partial E_{zII}(r)}{\partial r} = -C_i k [I_o(ka)K_1(kr) + K_o(ka)I_1(kr)] \quad (2.25)$$

At  $r = b$ ,

$$E_{zI}(r) \Big|_{r=b} = E_{zII}(r) \Big|_{r=b} \quad (2.26)$$

Therefore from Eqs. 2.21 and 2.24,

$$AJ_o(T_p b) = C_i [K_o(kb)I_o(ka) - K_o(ka)I_o(kb)] \quad ,$$

$$A = \frac{C_i}{J_o(T_p b)} [K_o(kb)I_o(ka) - K_o(ka)I_o(kb)] \quad (2.27)$$

Substitute Eq. 2.27 into Eq. 2.21 to obtain

$$E_{zI}(r) = \frac{C_i}{J_0(T_p b)} [K_0(kb)I_0(ka) - K_0(ka)I_0(kb)] J_0(T_p r) \quad (2.28)$$

Differentiate Eq. 2.28 to obtain

$$\frac{\partial E_{zI}(r)}{\partial r} = - \frac{C_i T_p J_1(T_p r)}{J_0(T_p b)} [K_0(kb)I_0(ka) - K_0(ka)I_0(kb)] \quad (2.29)$$

In view of Eq. 2.13 and since  $D_r = \epsilon_o \kappa_{\perp} E_r$  inside the plasma, while  $D_r = \epsilon_o \kappa_e E_r$  outside of the plasma, in the absence of surface charges one finds that inside the plasma

$$D_r = \epsilon_o \kappa_{\perp} E_r = - \frac{\epsilon_o \kappa_{\perp}}{jk} \frac{\partial E_z}{\partial r} \quad (2.30)$$

Since the radial displacement vector,  $D_r$ , is continuous at  $r = b$ , it follows from Eqs. 2.25 and 2.29 that

$$\frac{\epsilon_o \kappa_e}{jk} C_i k [I_0(ka)K_1(kb) + K_0(ka)I_1(kb)] = \frac{\epsilon_o \kappa_{\perp}}{jk} \frac{C_i T_p J_1(T_p b)}{J_0(T_p b)} \cdot [K_0(kb)I_0(ka) - K_0(ka)I_0(kb)] \quad (2.31)$$

Therefore

$$1 = \frac{\kappa_{\perp} T_p}{\kappa_e k} \frac{J_1(T_p b)}{J_0(T_p b)} \frac{K_0(kb)I_0(ka) - K_0(ka)I_0(kb)}{I_0(ka)K_1(kb) + K_0(ka)I_1(kb)} \quad (2.31)$$

This is the dispersion relation connecting  $\omega$  with  $k$ . For the case of free space between the plasma column and the metallic wall,  $\kappa_e = 1$ .

In many cases the collision frequency,  $\nu$ , is so small compared with  $\omega$  that one may set  $\nu/\omega = 0$ . Then  $k = \beta$  and complex argument Bessel functions may be avoided in Eq. 2.31. The solution of the dispersion equation is then fairly straightforward. Figures 2.2 and 2.3 show the solution for a typical set of values encountered in a plasma column useful

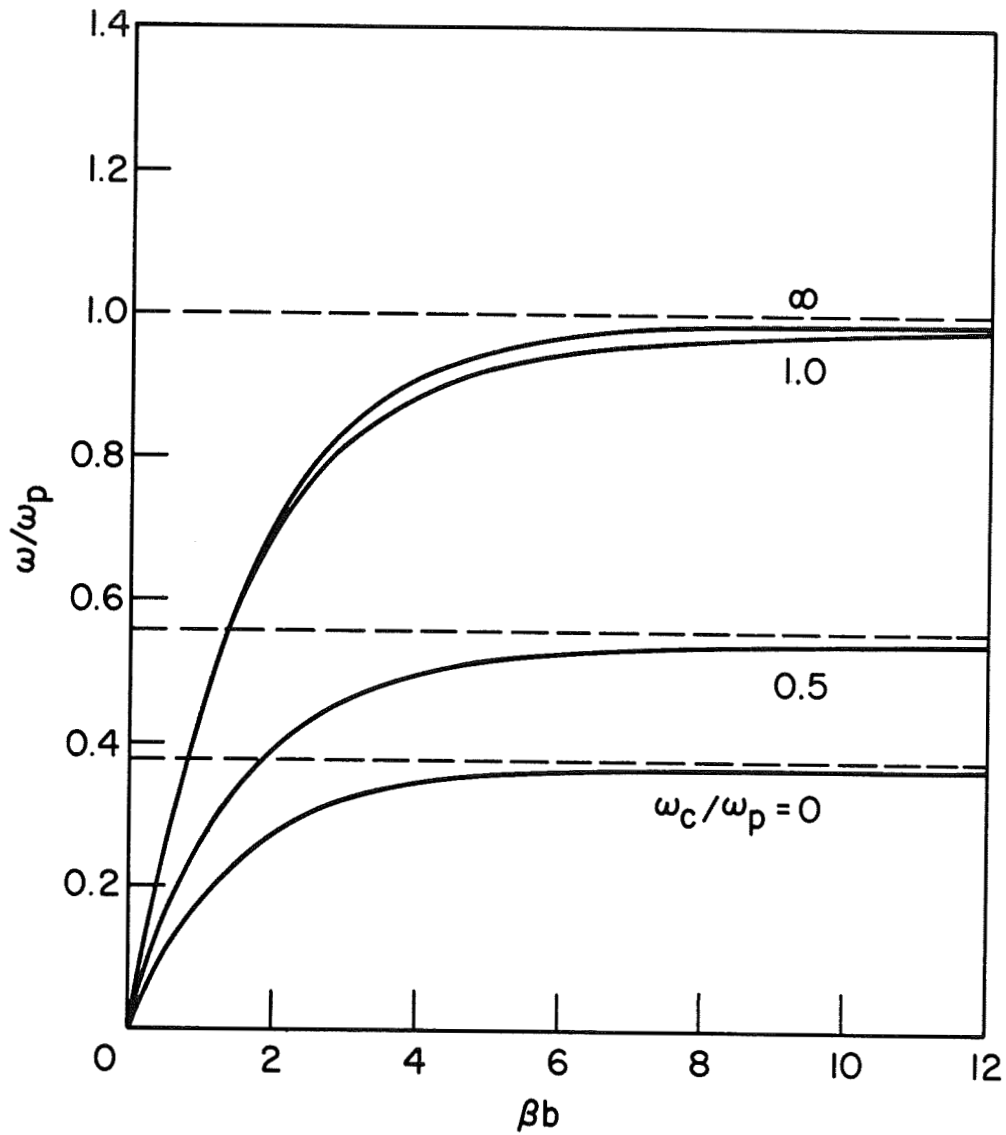


FIG. 2.2 FORWARD WAVE PASSBAND CHARACTERISTICS FOR THE LOWEST ORDER AXIALLY SYMMETRIC MODE IN A DIELECTRIC-LINED METALLIC CYLINDER FILLED WITH PLASMA. ( $a/b = 1.2$ ,  $\kappa_e = 6.0$ ,  $\omega_p = 2.52 \cdot 10^{10}$  rad/s,  $b = 0.152$  cm)

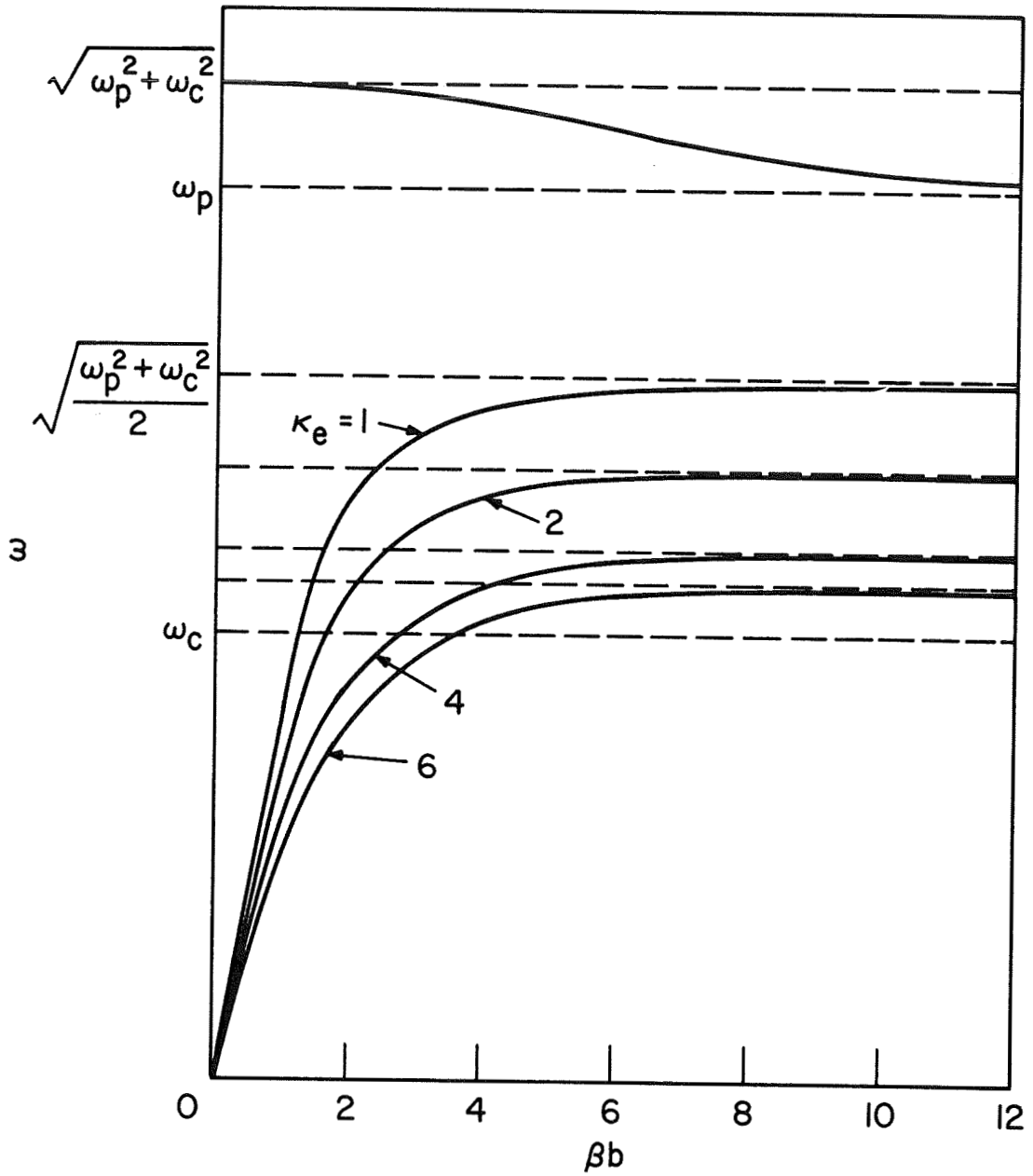


FIG. 2.3 PHASE CHARACTERISTICS FOR THE LOWEST ORDER AXIALLY SYMMETRIC MODE IN A DIELECTRIC-LINED METALLIC CYLINDER. ( $a/b = 2.0$ ,  $\omega_p/\omega_c = 2.0$ ,  $\omega_p = 2.52 \cdot 10^{10}$  rad/s,  $b = 0.152$  cm)

in the type of beam-plasma interaction to be considered in the present study. It will be shown later that the case of  $\omega_c < \omega_p$  is of particular interest. Thus Fig. 2.3 shows this case for dielectric materials of several values of  $\kappa_e$  (see Fig. 2.1). The forward-wave branch is seen to depend on  $\kappa_e$ , while the backward-wave branch does not. For the forward-wave branch, the frequency  $\omega_\infty$ , where  $\beta$  approaches infinity, can be found by noting that  $T_p$  is imaginary for  $\omega_c < \omega < \omega_p$  and  $\omega_c < \omega_p$  (provided  $\nu = 0$ ). Thus

$$\kappa_e^2 = \kappa_{\parallel} \kappa_{\perp} \quad (2.32)$$

as  $\beta \rightarrow \infty$ . Substituting from Appendix B this may be solved to yield

$$\omega_\infty^2 = -\frac{\omega_p^2}{\kappa_e^2 - 1} + \frac{\omega_c^2}{2} \pm \sqrt{\frac{[2\omega_p^2 - \omega_c^2(\kappa_e^2 - 1)]^2}{4(\kappa_e^2 - 1)^2} + \frac{\omega_p^4 + \omega_c^2\omega_p^2}{\kappa_e^2 - 1}}. \quad (2.33)$$

For the cases of  $\omega_c = 0$  or  $\kappa_e = 1$  much simpler expressions may be obtained from Eq. 2.33. Thus for  $\kappa_e = 1$  and  $\omega_c \neq 0$ ,

$$\omega_\infty = \sqrt{\frac{\omega_p^2 + \omega_c^2}{2}}, \quad (2.34)$$

and for  $\omega_c = 0$  and  $\kappa_e \neq 1$ ,

$$\omega_\infty = \frac{\omega_p}{\sqrt{1 + \kappa_e}}. \quad (2.35)$$

The asymptotes shown in Fig. 2.3 were found using the appropriate expression from above.



### 2.3 Derivation of the Equivalent Circuit Elements

The equation of motion for a plasma electron is given by the following force equation (c.f., Appendix B):

$$\frac{d\vec{v}_1}{dt} = \frac{\partial\vec{v}_1}{\partial t} + (\vec{v}_1 \cdot \nabla)\vec{v}_1 + \nu\vec{v}_1 = -\eta(\vec{E} + \vec{v}_1 \times \vec{B}) \quad , \quad (2.36)$$

where  $\vec{v}_1$  is the RF velocity, and the dc velocity is zero for a stationary plasma. In the one-dimensional case, with  $\vec{B} = B_z$  along the z-direction, and retaining first-order terms only, Eq. 2.36 reduces to

$$\frac{\partial v_1}{\partial t} + \nu v_1 = -\eta E_{zI} \quad , \quad (2.37)$$

where  $v_1$  is the axial RF velocity and  $E_{zI}$  is the total axial electric field in the plasma. Since all RF quantities are assumed to vary as  $\exp[j(\omega t - kz)]$ ,

$$(j\omega + \nu)v_1 = -\eta E_{zI} \quad ,$$

or

$$v_1 = -\frac{\eta}{j\omega + \nu} E_{zI} \quad . \quad (2.38)$$

The convection current density is given by

$$J_{zc} = (\rho_0 + \rho_1)v_1 \quad , \quad (2.39)$$

where  $\rho_0$  and  $\rho_1$  are the dc and RF charge densities, respectively, in the plasma. Neglecting the second-order term, Eq. 2.39 becomes

$$J_{zc} = \rho_0 v_1 \quad . \quad (2.40)$$

In view of Eq. 2.38 one obtains

$$J_{zc} = -\frac{\eta\rho_0}{j\omega + \nu} E_{zI} \quad .$$

Since

$$\omega_p^2 = \frac{e^2 n_e}{m \epsilon_0} = - \frac{e \rho_0}{m \epsilon_0} = - \frac{\eta \rho_0}{\epsilon_0} ,$$

this becomes

$$J_{zc} = \frac{\epsilon_0 \omega_p^2}{j\omega + \nu} E_{zI}(r) . \quad (2.41)$$

The total convection current for the plasma column may be expressed

as

$$\begin{aligned} I_{zc} &= \int_0^{2\pi} \int_0^b J_{zc} r \, dr \, d\phi , \\ I_{zc} &= \int_0^{2\pi} \int_0^b \frac{\epsilon_0 \omega_p^2}{j\omega + \nu} E_{zI}(r) r \, dr \, d\phi , \\ I_{zc} &= \frac{2\pi \epsilon_0 \omega_p^2}{j\omega + \nu} \int_0^b E_{zI}(r) r \, dr . \end{aligned} \quad (2.42)$$

From Eq. 2.28,

$$I_{zc} = \frac{2\pi \epsilon_0 \omega_p^2}{j\omega + \nu} \int_0^b \frac{C_i [K_0(kb)I_0(ka) - K_0(ka)I_0(kb)]}{J_0(T_p b)} J_0(T_p r) r \, dr$$

and

$$I_{zc} = \frac{2\pi \epsilon_0 \omega_p^2}{j\omega + \nu} C_i \frac{K_0(kb)I_0(ka) - K_0(ka)I_0(kb)}{J_0(T_p b)} \frac{b}{T_p} J_1(T_p b) .$$

Therefore, since by Eqs. 2.24 and 2.26

$$E_{zb} = E_{zI}(r) \Big|_{r=b} = C_i [K_0(kb)I_0(ka) - K_0(ka)I_0(kb)] ,$$

it follows that

$$I_{zc} = \frac{2\pi \epsilon_0 \omega_p^2 b}{(j\omega + \nu) T_p} \frac{J_1(T_p b)}{J_0(T_p b)} E_{zb} . \quad (2.43)$$

Combining Eqs. 2.10 and 2.43 one obtains

$$\frac{\partial I_{zc}}{\partial t} = \frac{2j\omega\pi\epsilon_o\omega_p^2 b}{(j\omega + \nu)T_p} \frac{J_1(T_p b)}{J_o(T_p b)} \left( -\frac{\partial V}{\partial z} \right) ,$$

or

$$\frac{\partial V}{\partial z} + \frac{(j\omega + \nu)T_p}{2j\omega\pi\epsilon_o\omega_p^2 b} \frac{J_o(T_p b)}{J_1(T_p b)} \frac{\partial I_{zc}}{\partial t} = 0 .$$

After rearranging,

$$\frac{\partial V}{\partial z} + \frac{[1 - j(\nu/\omega)]T_p}{2\pi\epsilon_o\omega_p^2 b} \frac{J_o(T_p b)}{J_1(T_p b)} \frac{\partial I_{zc}}{\partial t} = 0 . \quad (2.44)$$

From Maxwell's curl  $\vec{H}$  equation and Stokes' theorem one finds that at  $r = b$ ,

$$2\pi b H_{\phi I}(b) = I_{zc} + I_{zd} , \quad (2.45)$$

where  $I_{zd}$  is the plasma column displacement current through the cross-sectional area of the plasma.  $I_{zd}$  may be expressed by

$$\begin{aligned} I_{zd} &= \int_0^{2\pi} \int_0^b j\omega\epsilon_o E_{zI}(r) r dr d\phi , \quad (2.46) \\ I_{zd} &= 2\pi j\omega\epsilon_o \int_0^b E_{zI}(r) r dr , \\ I_{zd} &= 2\pi j\epsilon_o \omega C_i \frac{K_o(kb)I_o(ka) - K_o(ka)I_o(kb)}{J_o(T_p b)} \int_0^b J_o(T_p r) dr , \\ I_{zd} &= \frac{2\pi j\omega\epsilon_o b}{T_p} C_i \frac{K_o(kb)I_o(ka) - K_o(ka)I_o(kb)}{J_o(T_p b)} J_1(T_p b) , \\ I_{zd} &= \frac{2\pi j\omega\epsilon_o b}{T_p} \frac{J_1(T_p b)}{J_o(T_p b)} E_{zb} . \quad (2.47) \end{aligned}$$

It is apparent from Eqs. 2.43 and 2.47 that

$$\begin{aligned}
 I_{zc} + I_{zd} &= \left( \frac{2\pi\epsilon_0\omega_p^2 b}{(j\omega + \nu)T_p} - \frac{2\pi\epsilon_0\omega^2 b}{j\omega T_p} \right) \frac{J_1(T_p b)}{J_0(T_p b)} E_{zb} , \\
 I_{zc} + I_{zd} &= \left( 1 - \frac{\omega(\omega - j\nu)}{\omega_p^2} \right) \frac{2\pi\epsilon_0\omega_p^2 b}{(j\omega + \nu)T_p} \frac{J_1(T_p b)}{J_0(T_p b)} E_{zb} , \\
 I_{zc} + I_{zd} &= \left( 1 - \frac{\omega(\omega - j\nu)}{\omega_p^2} \right) I_{zc} . \tag{2.48}
 \end{aligned}$$

Substituting Eq. 2.48 into Eq. 2.45 one obtains

$$2\pi b H_{\varphi I}(b) = \left( 1 - \frac{\omega(\omega - j\nu)}{\omega_p^2} \right) I_{zc} . \tag{2.49}$$

From Appendix A,  $H_{\varphi I}$  is given by

$$-j \frac{n}{r} H_{zI} + jk H_{\varphi I} = j\epsilon_0 E_{rI} \omega \kappa_{\perp} - \epsilon_0 E_{\varphi I} \omega \kappa_x . \tag{2.50}$$

But by Eq. 2.13,

$$E_{\varphi I} = \frac{n}{kr} E_{zI} ,$$

and since there are no  $\varphi$ -variations ( $n = 0$ ), Eq. 2.50 becomes

$$jk H_{\varphi I} = j\epsilon_0 E_{rI} \omega \kappa_{\perp} . \tag{2.51}$$

But by Eq. 2.13,

$$E_{rI} = -\frac{1}{jk} \frac{\partial E_{zI}}{\partial r} .$$

Thus

$$jkH_{\phi I} = -j\omega\epsilon_0 \frac{1}{jk} \frac{\partial E_{zI}}{\partial r} \kappa_1$$

or

$$H_{\phi I} = j\epsilon_0 \frac{\omega}{k^2} \frac{\partial E_{zI}}{\partial r} \kappa_1 \quad (2.52)$$

Since the displacement vector is continuous at  $r = b$ ,

$$\kappa_1 E_{rI} \Big|_{r=b} = \kappa_e E_{rII} \Big|_{r=b} \quad .$$

Hence

$$\frac{\partial E_{zI}}{\partial r} = \frac{\kappa_e}{\kappa_1} \frac{\partial E_{zII}}{\partial r} \quad .$$

In view of Eq. 2.25 one can see that Eq. 2.52 becomes

$$H_{\phi I}(r) = -j\epsilon_0 \frac{\kappa_e \kappa_1}{\kappa_1} \frac{\omega}{k^2} C_1 k [I_0(ka)K_1(kr) + K_0(ka)I_1(kr)] \quad ,$$

or

$$H_{\phi I}(r) \Big|_{r=b} = -j\epsilon_0 \kappa_e \frac{\omega}{k} C_1 [I_0(ka)K_1(kb) + K_0(ka)I_1(kb)] \quad (2.53)$$

Making use of Eqs. 2.24 and 2.26 it is possible to write Eq. 2.53 as

$$H_{\phi}(b) = -j\epsilon_0 \frac{\omega}{k} \kappa_e B' E_{zb} \quad , \quad (2.54)$$

where

$$B' \triangleq \frac{I_0(ka)K_1(kb) + K_0(ka)I_1(kb)}{K_0(kb)I_0(ka) - K_0(ka)I_0(kb)} \quad . \quad (2.55)$$

Substituting Eq. 2.54 into Eq. 2.49 yields

$$-2\pi b j \epsilon_0 \frac{\omega}{k} \kappa_e B' E_{zb} = \left( 1 - \frac{\omega(\omega - j\nu)}{\omega_p^2} \right) I_{zc} \quad .$$

By Eq. 2.12 this becomes

$$2\pi b j \epsilon_o \kappa_e k B' j \omega V = j k I_{zc} \left( 1 - \frac{\omega(\omega - j\nu)}{\omega_p^2} \right)$$

or

$$\frac{\partial I_{zc}}{\partial z} + 2\pi b \epsilon_o \kappa_e \left( \frac{I_o(ka)K_1(kb) + K_o(ka)I_1(kb)}{K_o(kb)I_o(ka) - K_o(ka)I_o(kb)} \right) \left[ \frac{1}{1 - \frac{1 - j(\nu/\omega)}{(\omega_p/\omega)^2}} \right] \frac{\partial V}{\partial t} = 0 \quad (2.56)$$

Equations 2.44 and 2.56 describe the transmission line pictured in Fig. 2.4, if they are written as follows:

$$\frac{\partial V}{\partial z} + L_o \frac{\partial I_{zc}}{\partial t} = 0 \quad (2.57a)$$

and

$$\frac{\partial I_{zc}}{\partial z} + C_o \frac{\partial V}{\partial t} = 0 \quad (2.57b)$$

Then

$$L_o = \frac{T_p [1 - j(\nu/\omega)]}{2\pi \epsilon_o \omega_p^2 b} \frac{J_o(T_p b)}{J_1(T_p b)} \quad (2.58)$$

and

$$C_o = 2\pi b \kappa_e \epsilon_o \left[ \frac{1}{1 - \frac{1 - j(\nu/\omega)}{(\omega_p/\omega)^2}} \right] \left( \frac{I_o(ka)I_1(kb) + K_o(ka)I_1(kb)}{K_o(kb)I_o(ka) - K_o(ka)I_o(kb)} \right) \quad (2.59)$$

Inspection of the last two equations reveals that the collision terms introduce resistive components in the equivalent circuit. In Fig. 2.4 the lossy elements are not shown separately, but are included in  $L_o$  and  $C_o$ . If collisions are negligible,  $\nu/\omega \rightarrow 0$  and  $L_o$  and  $C_o$  are pure inductances and capacitances per unit length, respectively. Some typical

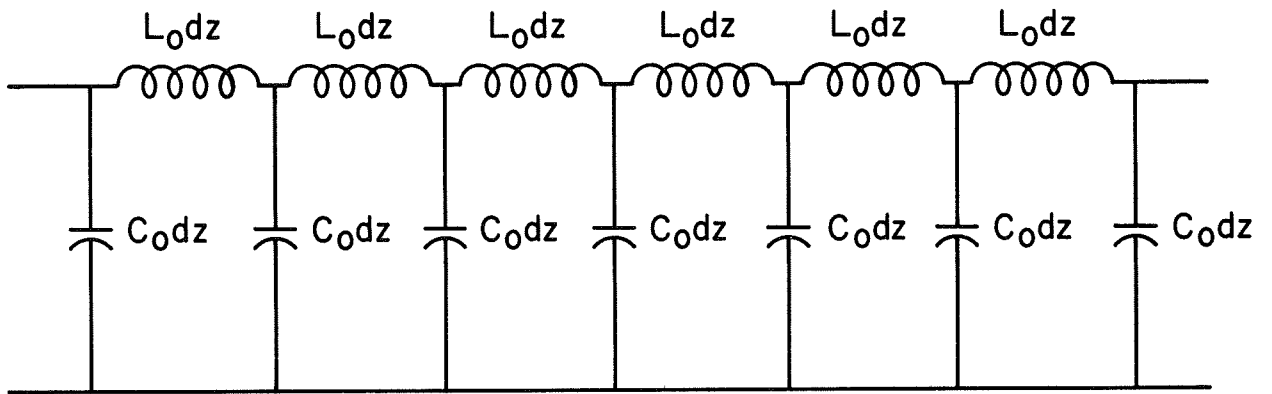


FIG. 2.4 EQUIVALENT TRANSMISSION LINE WITH DISTRIBUTED ELEMENTS FOR A PLASMA COLUMN.

values of  $L'_0$  and  $C'_0$  as a function of  $\beta b$  when  $v = 0$  are shown in Fig. 2.5. The parameters needed in calculating these values of  $L'_0$  and  $C'_0$  are chosen to be representative of a plasma column useful in the beam-plasma interaction device to be studied later.

For the transmission line of Fig. 2.4 the phase velocity,  $v_0$ , is given by

$$v_0 = \frac{\omega}{\beta} . \quad (2.60)$$

In general

$$\frac{\omega^2}{k^2} = \frac{\omega^2}{(\beta - j\alpha)^2} = \frac{1}{L'_0 C'_0} , \quad (2.61)$$

which reduces to

$$v_0^2 = \frac{\omega^2}{\beta^2} = \frac{1}{L'_0 C'_0} , \quad (2.62)$$

where  $L'_0$  and  $C'_0$  are  $L_0$  and  $C_0$ , respectively, with  $v = 0$ . From Eq. 2.61

$$k^2 = \omega^2 L_0 C_0 , \quad (2.63)$$

which should yield the dispersion equation, Eq. 2.31, derived previously. This can be shown by substituting Eqs. 2.58 and 2.59 into Eq. 2.63. Thus

$$k^2 = \omega^2 \frac{T_p [1 - j(v/\omega)]}{2\pi\epsilon_0 \omega_p^2 b} \frac{J_0(T_p b)}{J_1(T_p b)} 2\pi b \epsilon_0 \kappa_e \kappa_B' \left[ \frac{1}{1 - \frac{1 - j(v/\omega)}{(\omega_p/\omega)^2}} \right] .$$

Rearranging,

$$1 = \frac{T_p}{k} \frac{J_0(T_p b)}{J_1(T_p b)} \kappa_e \kappa_B' \left[ - \frac{1}{1 - \frac{(\omega_p/\omega)^2}{1 - j(v/\omega)}} \right] .$$



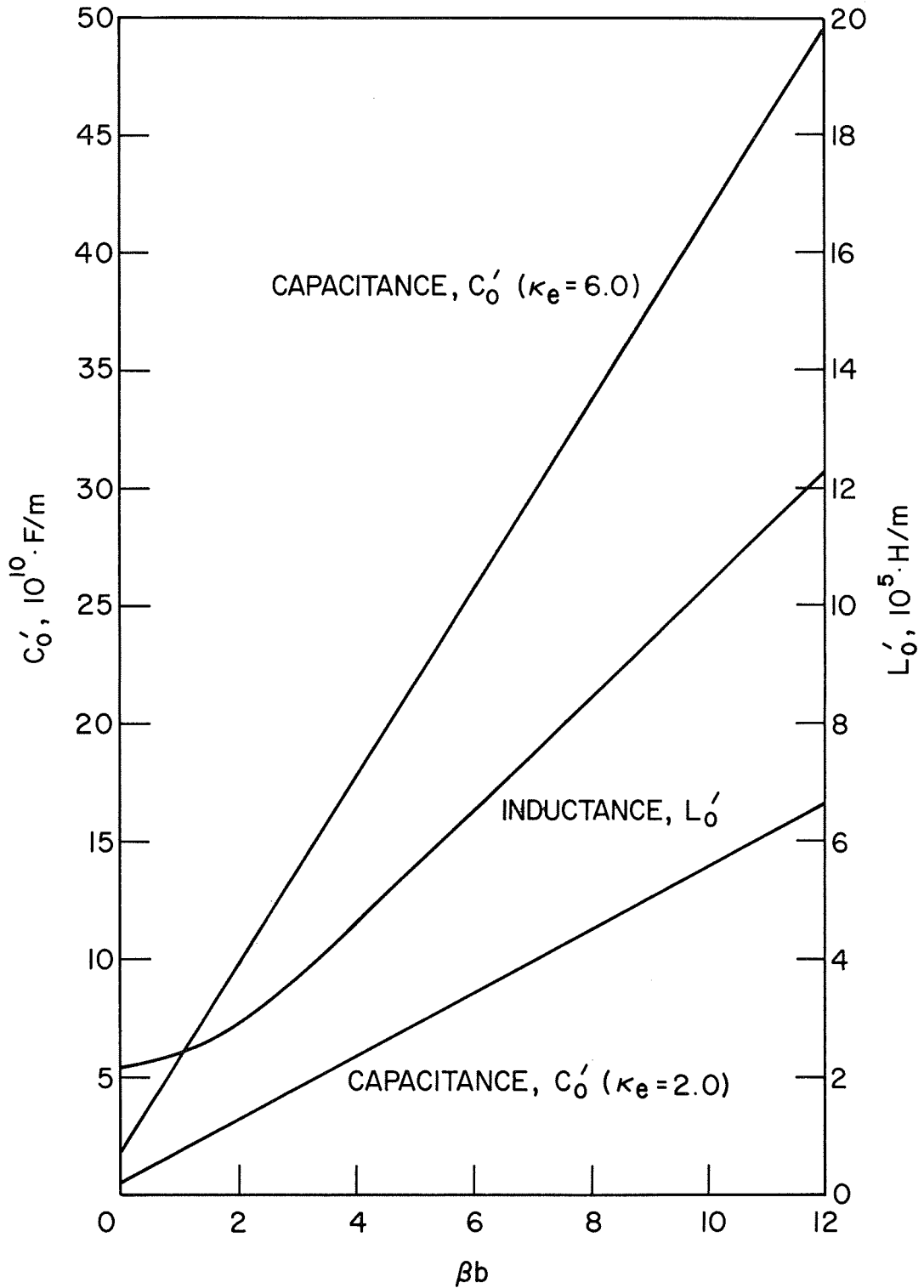


FIG. 2.5 EQUIVALENT CIRCUIT COMPONENTS FOR A PLASMA COLUMN. ( $\omega_p/\omega = 2.49$ ,  $\omega_c/\omega = 0.428$ ,  $\omega_p = 2.65 \cdot 10^{10}$  rad/s,  $a/b = 6.26$ ,  $b = 0.152$  cm,  $v/\omega = 0$ )

But from Eq. 2.16

$$1 - \frac{\kappa_1}{(\omega_p/\omega)^2} = \frac{k^2}{1 - j(\nu/\omega) T_p^2}$$

Therefore

$$1 = \frac{\kappa_1}{\kappa_e} \frac{T_p}{k} \frac{J_1(T_p b)}{J_0(T_p b)} \left[ \frac{K_0(kb)I_0(kb) - K_0(ka)I_0(kb)}{I_0(ka)K_1(kb) + K_0(ka)I_1(kb)} \right] \quad (2.64)$$

This is precisely Eq. 2.31 and agrees with the dispersion equation given by Trivelpiece and Gould,<sup>9</sup> if  $\nu = 0$  and  $k = \beta$ .

Gould and Trivelpiece<sup>6,4</sup> derived a more detailed equivalent circuit for a collisionless plasma column, as shown in Fig. 2.6. The combination of  $L_1$  and  $C_1$  is resonant at  $\omega_p$ , while the combination of  $L_2$ ,  $C_2$  and  $C_3$  gives rise to the hybrid resonance at  $(\omega_c^2 + \omega_p^2)^{1/2}$ . Capacitance  $C_4$  is due to the dielectric loading of the space between the plasma column and the conducting cylinder coaxial with it. If the plasma column fills the cylinder,  $C_4$  becomes infinite. This equivalent circuit shows more of the details of the plasma column characteristics, but the simple equivalent circuit lumping all these components together into  $L'_0$  and  $C'_0$  is entirely adequate in the treatment to follow. This is so because in the present analysis  $Z_0$ , determined by the lumped elements, is of primary importance, as will be seen in subsequent chapters.

## 2.4 Derivation of the Circuit Equation

If an electron beam with convection current  $-i_z$  is allowed to pass near or through a plasma, one has in effect a beam-loaded plasma column transmission line. This is depicted in Fig. 2.7. The impressed current

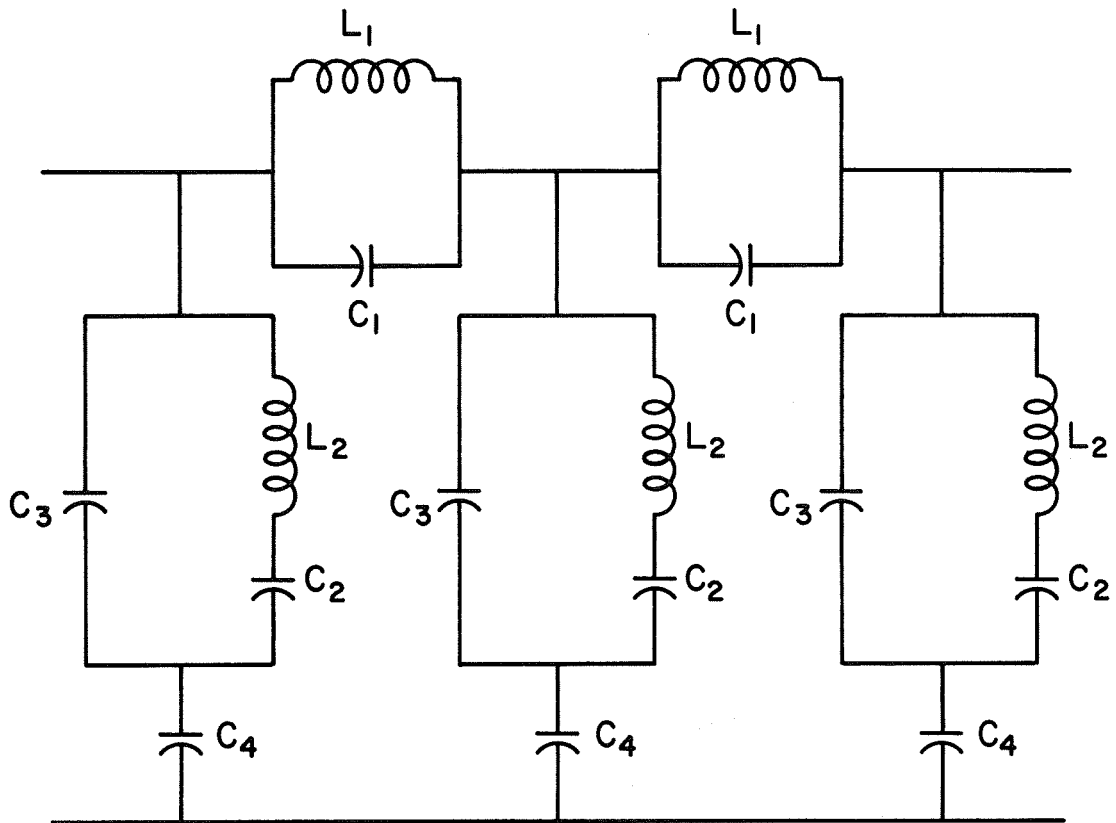


FIG. 2.6 EQUIVALENT TRANSMISSION LINE FOR A COLLISIONLESS PLASMA COLUMN SHOWING THE VARIOUS RESONANCES.

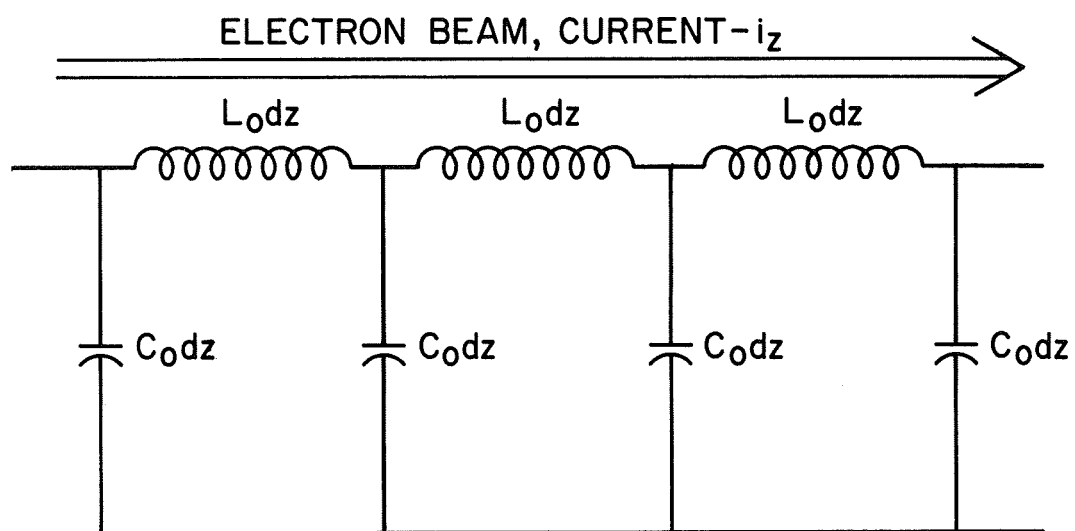


FIG. 2.7 ELECTRON BEAM INTERACTING WITH A PLASMA COLUMN.

in the plasma due to the motion of the electrons in the beam is  $\partial i_z / \partial z$ .

One thus modifies Eqs. 2.57 to include the presence of the beam as follows:

$$\frac{\partial V(z,t)}{\partial z} + L_o \frac{\partial I_{zc}(z,t)}{\partial t} = 0 \quad (2.65a)$$

and

$$\frac{\partial I_{zc}(z,t)}{\partial z} + C_o \frac{\partial V(z,t)}{\partial t} = \frac{\partial i_z(z,t)}{\partial z} . \quad (2.65b)$$

But

$$i_z = - \frac{\partial q_z(z,t)}{\partial t} \quad (2.66)$$

and

$$\frac{\partial q_z(z,t)}{\partial z} = \rho_z(z,t) , \quad (2.67)$$

where  $q_z$  is the charge giving rise to the current  $i_z$  and  $\rho_z$  is the charge density. Then Eqs. 2.65 become

$$\frac{\partial V(z,t)}{\partial z} + L_o \frac{\partial I_{zc}(z,t)}{\partial t} = 0 \quad (2.68a)$$

and

$$\frac{\partial I_{zc}(z,t)}{\partial z} + C_o \frac{\partial V(z,t)}{\partial t} = - \frac{\partial \rho_z(z,t)}{\partial t} . \quad (2.68b)$$

Differentiating the first of Eqs. 2.68 with respect to  $z$  and the second with respect to  $t$  and combining them so as to eliminate  $I_{zc}(z,t)$  (the order of differentiation with respect to  $z$  or  $t$  being immaterial), one obtains a wave equation, which will be designated the "circuit" equation. Thus

$$\frac{\partial^2 V(z,t)}{\partial z^2} - L_0 C_0 \frac{\partial^2 V(z,t)}{\partial t^2} = -L_0 \frac{\partial^2 \rho_z(z,t)}{\partial t^2} .$$

Recalling Eqs. 2.60 and 2.61 and noting that the characteristic impedance of the transmission line of Fig. 2.4 is given by

$$Z_0 = \sqrt{\frac{L_0}{C_0}} , \quad (2.69)$$

the final form of the circuit equation is

$$\frac{\partial^2 V(z,t)}{\partial z^2} - \frac{1}{v_0^2} \frac{\partial^2 V(z,t)}{\partial t^2} = -\frac{Z_0}{v_0} \frac{\partial^2 \rho(z,t)}{\partial t^2} , \quad (2.70)$$

provided  $\alpha \ll \beta$  so that  $\beta \cong k$ . In a typical laboratory plasma column useful for beam-plasma interaction this requirement is readily satisfied, as will be shown later.

Figures 2.8 through 2.12 show the real part of the characteristic impedance as a function of  $\beta b$  for  $\nu \ll \omega$ . The modulus of  $Z_0$  is chosen to correspond to the interaction impedance used in traveling-wave tube theory, while the imaginary part of  $Z_0$ , which is usually small compared to the real part by virtue of  $\nu \ll \omega$ , gives rise to the "circuit" loss. The parameters chosen for the computation of  $Z_0$  in Figs. 2.8 through 2.12 apply to a plasma column with a particle density of approximately  $1.5 \times 10^{11}$  to  $6.0 \times 10^{11} \text{ cm}^{-3}$  ( $f_p = 3.5$  to  $f_p = 7.0$  GHz) and a cyclotron frequency of 0.75 to 1.4 GHz, with  $\omega_c < \omega < \omega_p$ . Figures 2.8 through 2.11 are for  $a/b = 6.26$  and thus are appropriate for a typical beam-generated plasma. Figure 2.12 is for  $a/b = 1.2$  and would thus apply to

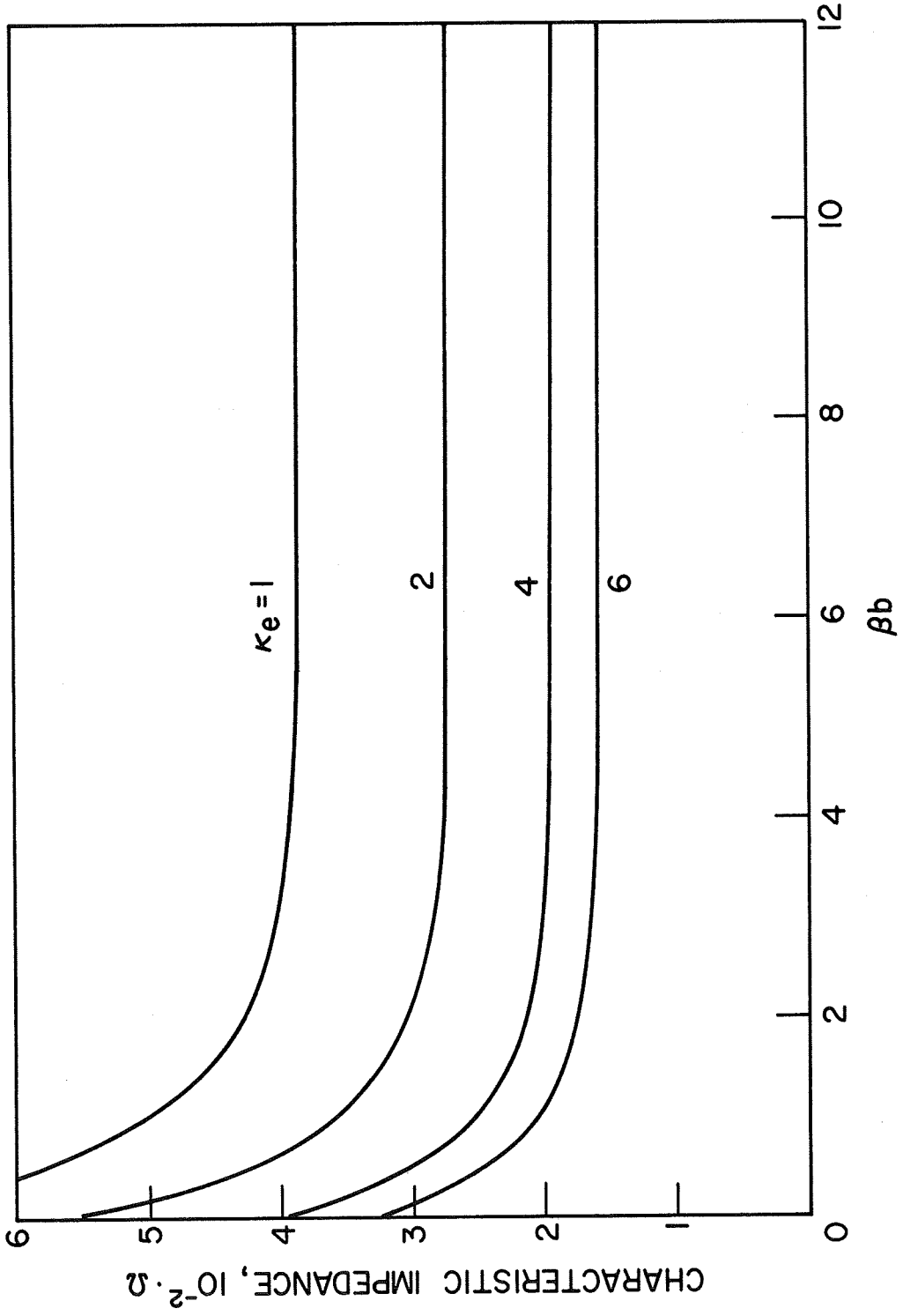


FIG. 2.8 REAL PART OF THE CHARACTERISTIC IMPEDANCE OF A PLASMA COLUMN. ( $\omega_p/\omega = 2.49$ ,  $\omega_c/\omega = 0.428$ ,

$\omega_p = 2.65 \cdot 10^{10}$  rad/s,  $a/b = 6.26$ ,  $b = 0.152$  cm)

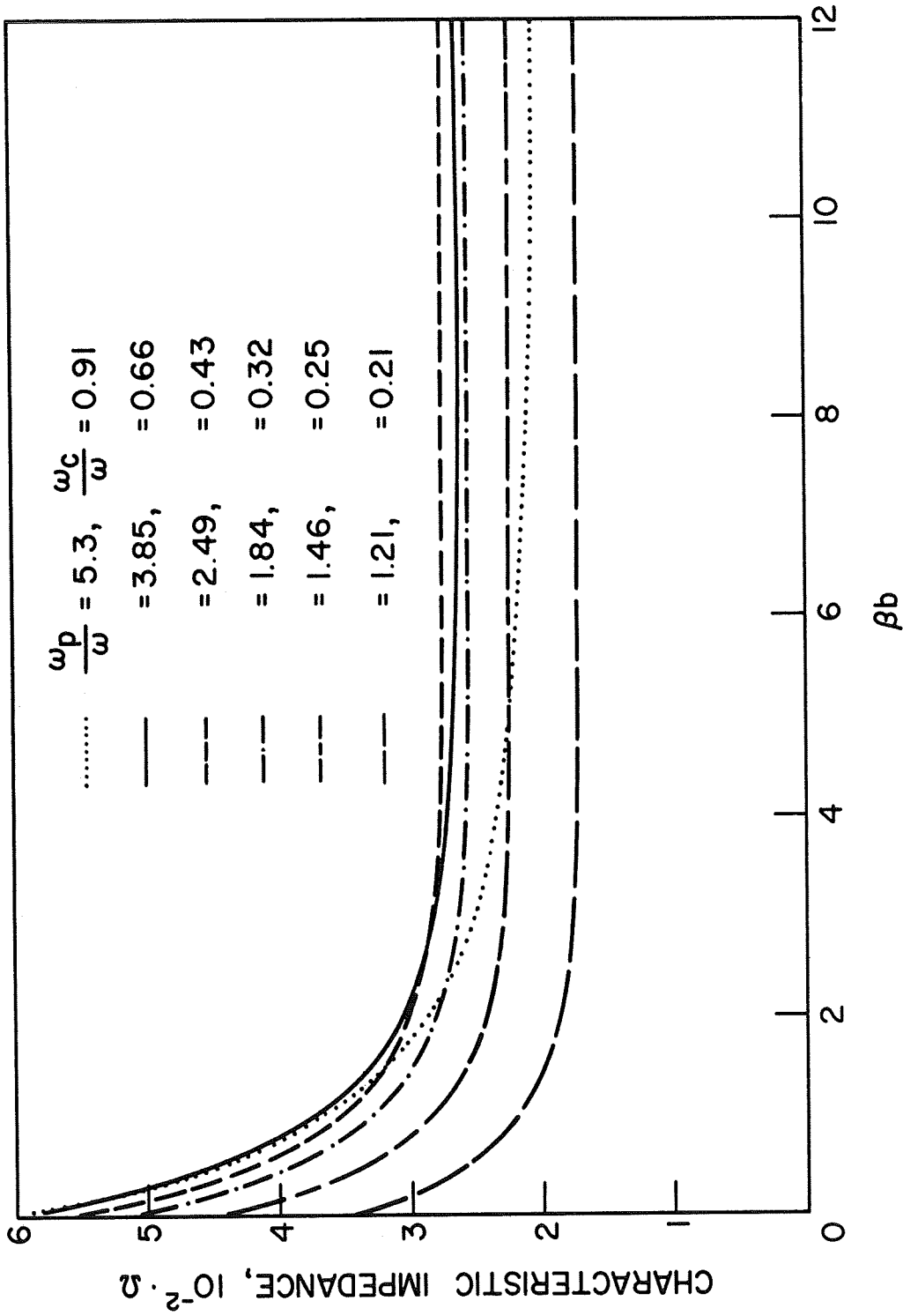


FIG. 2.9 REAL PART OF THE CHARACTERISTIC IMPEDANCE OF A PLASMA COLUMN. ( $\omega_p = 2.65 \cdot 10^{10}$  rad/s,  $a/b = 6.26$ ,  $b = 0.152$  cm,  $\kappa_e = 2.0$ )



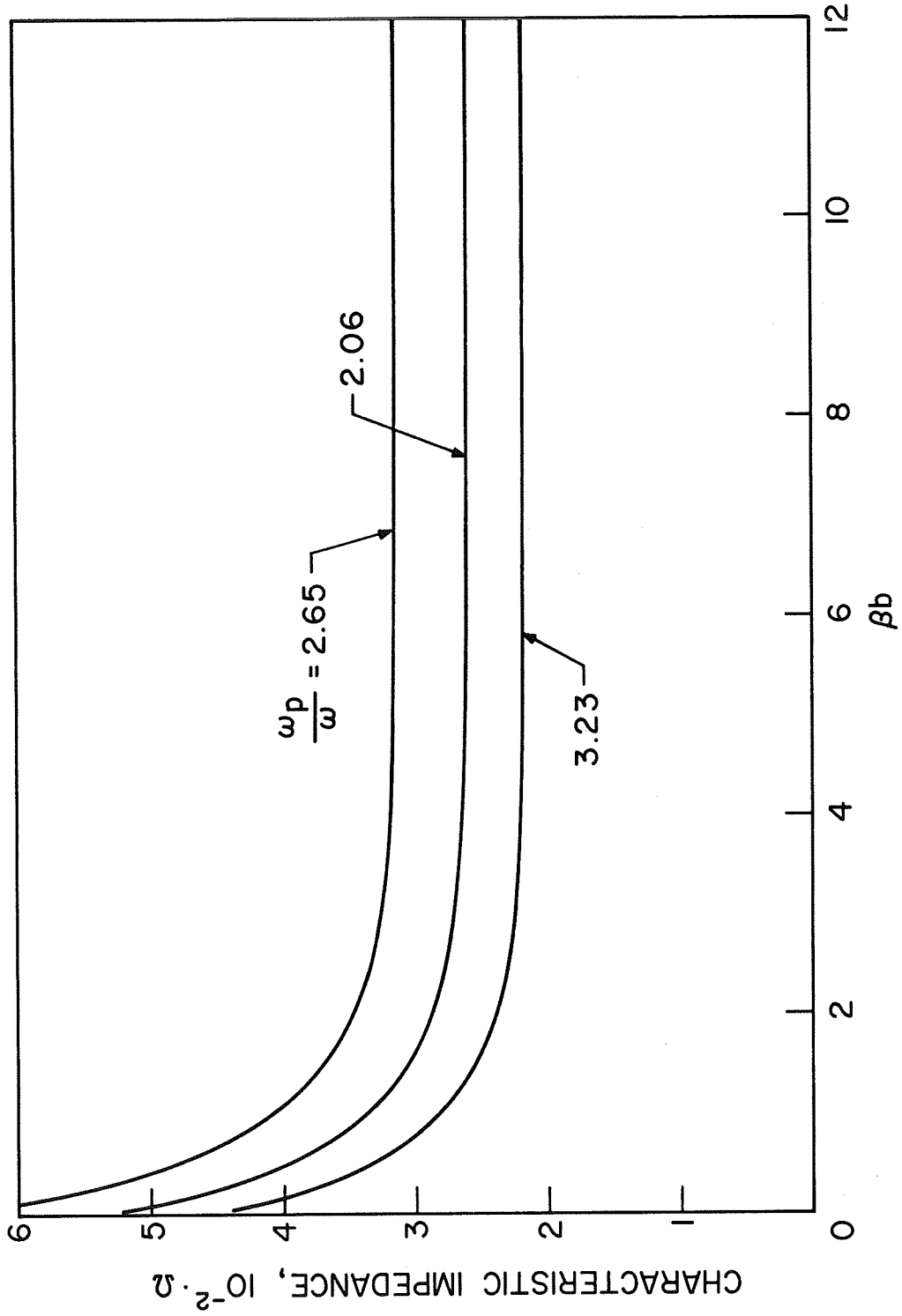


FIG. 2.10 REAL PART OF THE CHARACTERISTIC IMPEDANCE OF A PLASMA COLUMN. ( $\omega_c/\omega = 0.428$ ,  $\omega = 1.068 \cdot 10^{10}$  rad/s,  $a/b = 6.26$ ,  $b = 0.152$  cm,  $\kappa_e = 2.0$ )

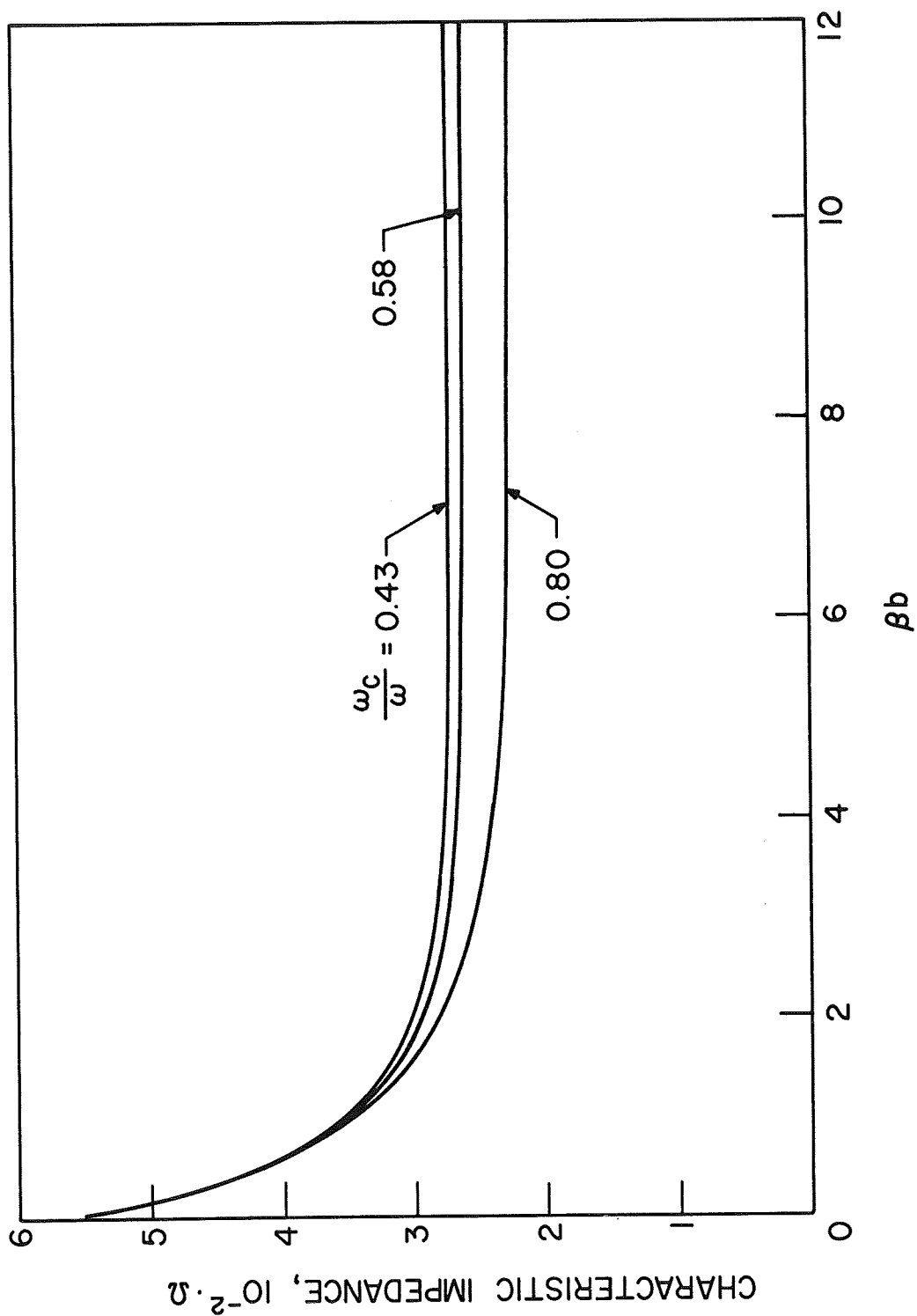


FIG. 2.11 REAL PART OF THE CHARACTERISTIC IMPEDANCE OF A PLASMA COLUMN. ( $\omega_p/\omega = 2.49$ ,  $\omega_p = 2.65 \cdot 10^{10}$  rad/s,  $a/b = 6.26$ ,  $b = 0.152$  cm,  $\kappa_e = 2.0$ )

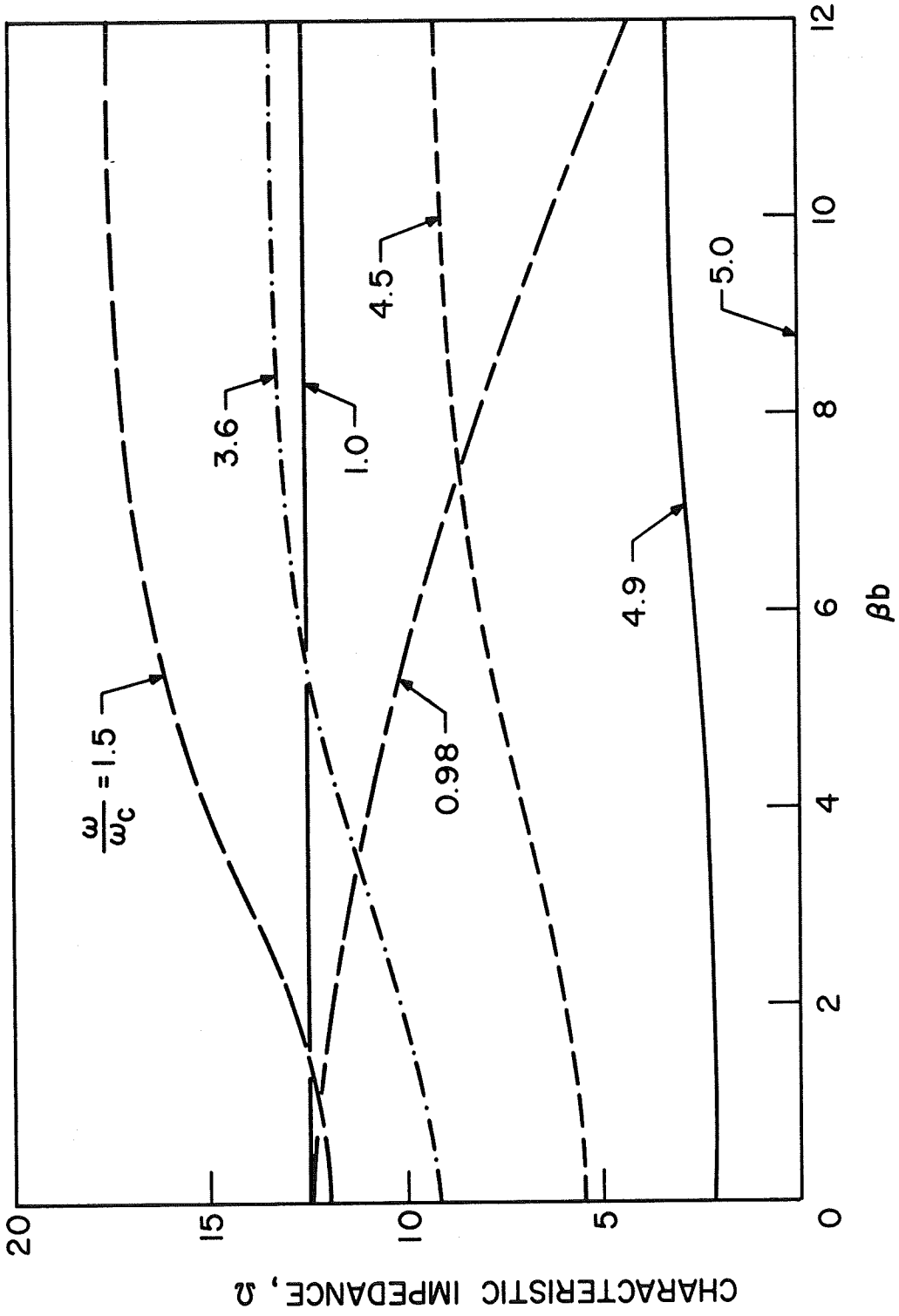


FIG. 2.12 REAL PART OF THE CHARACTERISTIC IMPEDANCE OF A PLASMA COLUMN. ( $\omega_p = 4.4 \cdot 10^{10}$  rad/s,  $a/b = 1.2$ ,  $b = 0.792$  cm,  $\kappa_e = 6.0$ ,  $\omega_p/\omega_c = 5.0$ )

a plasma filling the whole dielectric cylinder. Such a plasma could for example be generated by a Penning discharge. Comparison of the figures shows that the former type of plasma column has a substantially higher characteristic impedance and would thus result in better beam-plasma interaction. This is borne out by experiment. In Fig. 2.13 both the real and the imaginary parts of the complex characteristic impedance are shown for the  $\kappa_e = 2.0$  case of Fig. 2.8. Note that the imaginary part is quite small compared to the real part and is negative. This is so because the imaginary part of the equivalent inductance,  $L_o$ , is small but negative, while the imaginary part of the equivalent capacitance,  $C_o$ , is positive and in general has a slightly larger phase angle than the inductance. The value of  $v/\omega = 0.0012$  is typical for the beam-plasma experiments to be described later in this study.

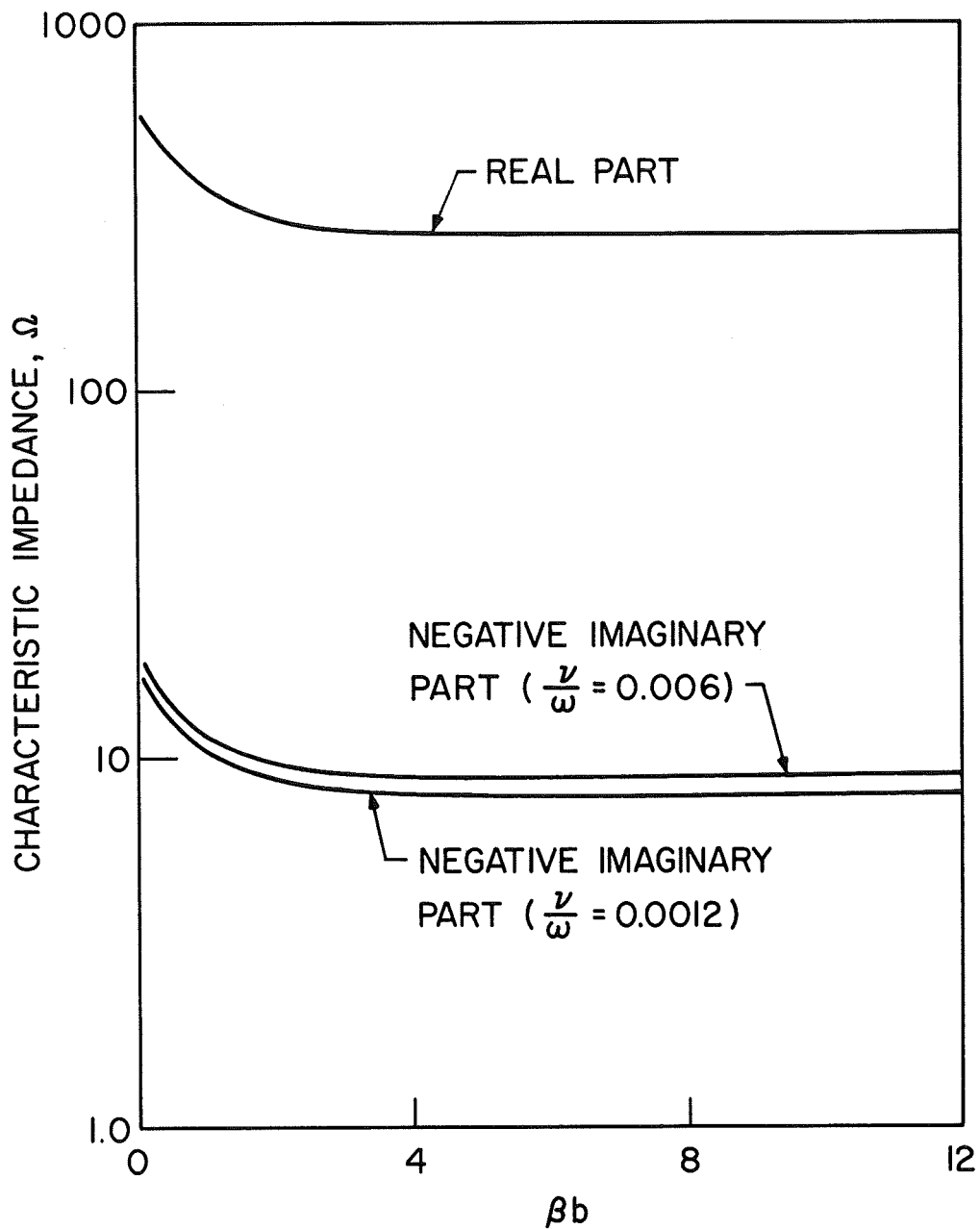


FIG. 2.13 CHARACTERISTIC IMPEDANCE OF A PLASMA COLUMN. ( $\omega_p/\omega = 2.49$ ,  
 $\omega_c/\omega = 0.428$ ,  $\omega_p = 2.65 \cdot 10^{10}$  rad/s,  $a/b = 6.26$ ,  $b = 0.152$  cm,  
 $\kappa_e = 2.0$ )

CHAPTER III. LAGRANGIAN FORMULATION OF THE ONE-DIMENSIONAL  
BEAM-PLASMA INTERACTION EQUATIONS

3.1 Lagrangian Coordinates

Consider electrons moving in the  $z$ -direction (one-dimensional analysis) as shown in Fig. 3.1. All the charge passing plane  $z_0$  at  $t = 0$  arrives at plane  $z$ , but the amount of charge passing plane  $z_0$  during a time interval  $dt_0$  may take a longer or shorter time interval  $dt$  to pass through plane  $z$ . During an infinitesimal interval of time  $dt_0$  a total charge

$$dq = -I_0 dt_0 \quad (3.1)$$

passes plane  $z_0$  at a time  $t = 0$ , where  $I_0$  is the injected current and is a positive quantity. Following the same set of electrons, at plane  $z$ ,

$$dq = -I(t)dt \quad (3.2)$$

Equating Eqs. 3.1 and 3.2, since no charges are created or destroyed in the intervening space between  $z_0$  and  $z$ ,

$$I(t) = I_0 \frac{dt_0}{dt} \quad (3.3)$$

In the two-dimensional analysis of Chapter VI provision is made in the computer calculations for beam electrons leaving the plasma column.

(This corresponds to beam interception on the circuit in a traveling-wave amplifier.) Since

$$\rho(z_0, 0) = -\frac{I_0}{u_0} \quad (3.4)$$

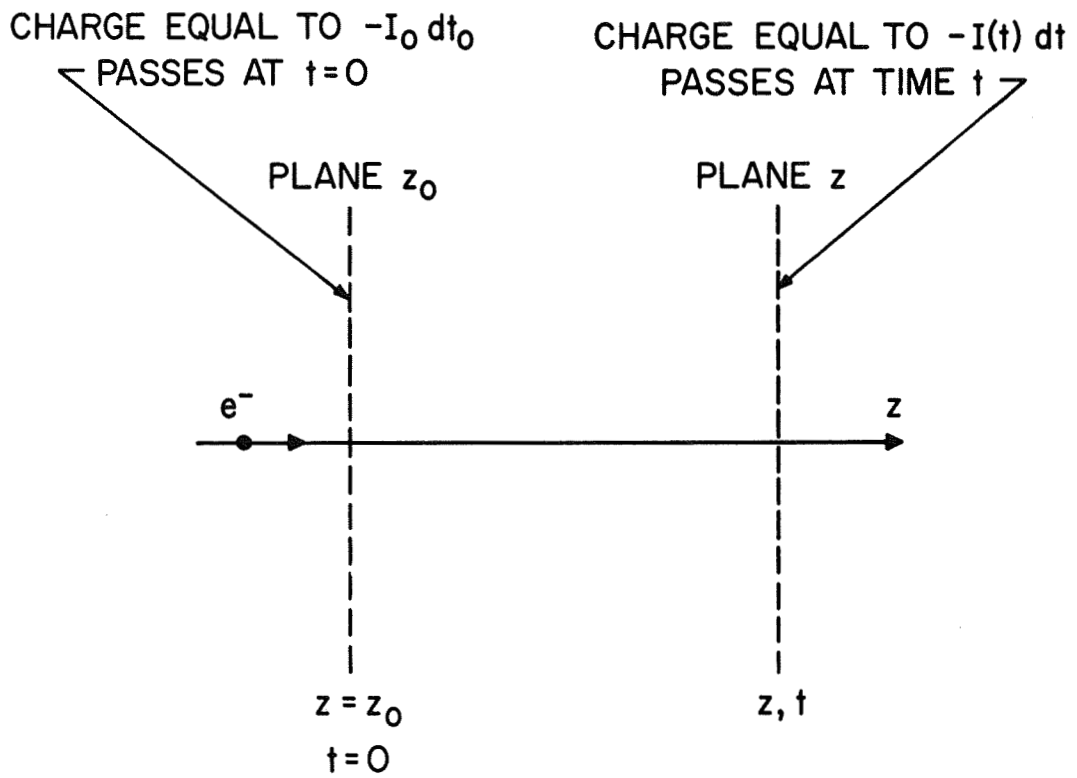


FIG. 3.1 ELECTRON MOTION IN A ONE-DIMENSIONAL SYSTEM.

where  $u_0$  is the velocity of the electrons crossing plane  $z_0$ , it is possible to write the following expression involving the charge density represented by these electrons. Thus

$$\rho(z,t) = -\frac{I_0}{u_0} \left| \frac{\partial z_0}{\partial z} \right|_t, \quad (3.5)$$

where the absolute value sign must be introduced due to the multivalued nature of the charge density. Physically, this accounts for electron crossings between planes  $z_0$  and  $z$ . Equation 3.5 is the conservation of charge equation used in a Lagrangian treatment.

While in an Eulerian analysis the independent variables are usually distance and time, it is convenient to choose the distance and the entry phase,  $\Phi_{01}$ , of the fundamental RF component as the independent variables in a Lagrangian treatment. With an appropriate normalization the distance variable is expressed in terms of the fundamental frequency as follows:

$$y_1 = \frac{C_1 \omega}{u_0} z = C_1 \beta_e z = 2\pi C_1 N_s, \quad (3.6)$$

where  $\beta_e$  is the stream phase constant and  $C_1$  is a beam-circuit coupling parameter, or gain parameter, for the fundamental frequency given by

$$C_1^3 = \frac{|Z_{01}| I_0}{4V_0}. \quad (3.7)$$

$N_s \triangleq z/\lambda_s$  is the number of stream wavelengths at the fundamental frequency. In Eq. 3.7,  $Z_{01}$  is the interaction impedance obtainable from Eq. 2.69,  $I_0$  is the dc current in the stream, and  $V_0$  is the stream voltage. Note that the modulus of  $Z_{01}$  is used in the definition



of the gain parameter. This is necessary when  $\nu \neq 0$  (and hence  $Z_{01}$  is complex) in order to keep  $C_1$  a real number, which insures that quantities such as  $y_1$  and some of the other normalizations in the following remain physically meaningful quantities.

The entrance phase for the fundamental frequency is defined by

$$\Phi_{01} \triangleq \frac{\omega z_0}{u_0} = -\omega t_0 \quad (3.8)$$

It is convenient to define dependent variables normalized with respect to the initial average electron velocity,  $u_0$ . In a nonlinear theory the average stream velocity is a function of displacement and so the dependent velocity variable is

$$u_z = \left. \frac{dz}{dt} \right|_{t, z_0} = \frac{u_0}{C_1 \omega} \frac{dy_1}{dt} \triangleq u_0 \left( 1 + 2C_1 u(y_1, \Phi_{01}) \right) \quad (3.9)$$

or

$$\frac{dy_1}{dt} = C_1 \omega \left( 1 + 2C_1 u(y_1, \Phi_{01}) \right) \quad (3.10)$$

Here  $2C_1 u_0 u(y_1, \Phi_{01})$  denotes the RF velocity of an electron at a given displacement plane.

Recall the conservation of charge equation, Eq. 3.5, which can be written as

$$\rho(z, t) = -\frac{I_0}{u_0} \left| \frac{\frac{\partial z_0}{\partial t}}{\frac{\partial z}{\partial t}} \right|_t \quad .$$

In Lagrangian variables,

$$\frac{\partial z}{\partial t} = u(y_1, \Phi_{01}) = u_0 \left( 1 + 2C_1 u(y_1, \Phi_{01}) \right)$$

and

$$\frac{\partial z_o}{\partial t} = \frac{\partial z_o}{\partial \Phi_{o1}} \frac{\partial \Phi_{o1}}{\partial \Phi_n} \frac{\partial \Phi_n}{\partial t} = u_o n \frac{\partial \Phi_{o1}}{\partial \Phi_n} ,$$

where  $n$  denotes the harmonic number of the RF wave component to be considered. Note that  $\Phi_n$  represents the phase of the  $n$ th harmonic component relative to the phase at the entrance to the interaction region.  $\Phi_n$  is based on a coordinate system which moves with the dc stream velocity,  $u_o$ . The conservation of charge equation in the new variables now becomes

$$\rho(y_1, \Phi_{o1}) = - \frac{I_o}{u_o} \left| \frac{\partial \Phi_{o1}}{\partial \Phi_n} \right|_{y_1} \cdot \left( \frac{n}{1 + 2C_1 u(y_1, \Phi_{o1})} \right) . \quad (3.11)$$

In a beam-wave interaction device the actual wave traveling along the circuit has a phase shift (a phase lag for a typical amplifier) with respect to a hypothetical wave traveling at the stream velocity  $u_o$ . This phase shift,  $\theta_n(y_1)$ , is due to the beam loading as energy is given to the wave. The phases of the  $j$ th particle at any value of  $[y_1, \Phi_n(y_1, \Phi_{o1,j})]$  denote phase positions relative to the wave at that  $y_1$ -plane. Hence at any displacement plane,

$$\Phi_{o1,j} + n \frac{y_1}{C_1} - \theta_n(y_1) = \Phi_{o1,j} + n\omega t + \Phi_n(y_1, \Phi_{o1,j}) ,$$

or, dropping the particle label,  $j$ ,

$$\theta_n(y_1) = n \frac{y_1}{C_1} - n\omega t - \Phi_n(y_1, \Phi_{o1}) . \quad (3.12)$$

This may be written as

$$y_1 = \frac{C_1}{n} \left( \Phi_n(y_1, \Phi_{o1}) + \theta_n(y_1) + n\omega t \right) . \quad (3.13)$$

Also note that

$$\left. \frac{\partial \Phi_n(y_1, \Phi_{o1})}{\partial y_1} \right|_t = \frac{n}{C_1} - \frac{d\theta_n(y_1)}{dy_1} . \quad (3.14)$$

In Fig. 3.2 representative curves are shown in order to depict some of these quantities. Curve A represents a reference trajectory of slope  $C_1/n$  for an electron starting at zero time and position which moves through the device at a uniform velocity  $u_o$ . Due to the large-signal interaction all electrons are speeded up or slowed down, so that Curve B, of slope

$$\left. \frac{dy_1}{d\Phi_n} \right|_{y_1, \Phi_{o1}} = \frac{C_1}{n} \left( 1 + 2C_1 u(y_1, \Phi_{o1}) \right) ,$$

obtained from Eq. 3.9, represents the actual electron velocity. Curve C, of slope  $(C_1/n)/(1+C_n b_n)$ , represents the circuit cold phase velocity, where  $b_n$  is known as the injection velocity parameter and is a measure of the beam-wave relative velocity. By definition

$$b_n \triangleq \frac{u_o - v_{on}}{C_n v_{on}} , \quad (3.15)$$

where  $v_{on}$  and  $C_n$  are the phase velocity and coupling parameter, respectively, for the nth harmonic RF component. Curve D, of slope  $C_1/\{n-C_1[d\theta_n(y_1)/dy_1]\}$  represents the actual wave phase velocity.

Differentiating Eq. 3.13 with respect to the time,  $t$ , and equating the result to Eq. 3.10, one obtains

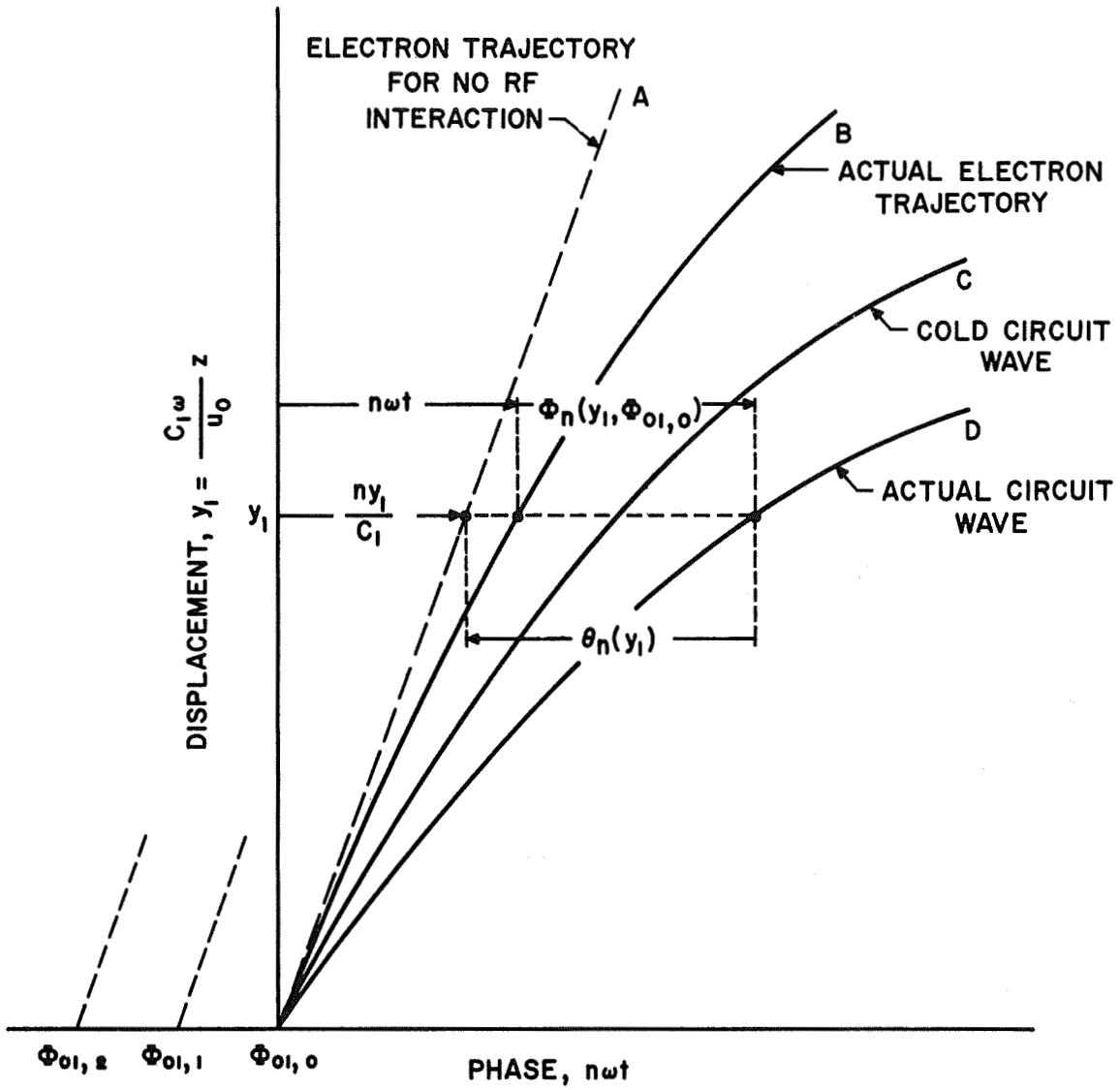


FIG. 3.2 LARGE-SIGNAL FLIGHT-LINE DIAGRAM.

$$\frac{dy_1}{dt} = \frac{c_1}{n} \left( \frac{\partial \Phi_n(y_1, \Phi_{o1})}{\partial y_1} \frac{dy_1}{dt} + \frac{d\theta_n(y_1)}{dy_1} \frac{dy_1}{dt} + n\omega \right),$$

$$\frac{dy_1}{dt} = c_1 \omega \left( 1 + 2C_1 u(y_1, \Phi_{o1}) \right)$$

and

$$\frac{\partial \Phi_n(y_1, \Phi_{o1})}{\partial y_1} \frac{dy_1}{dt} + \frac{d\theta_n(y_1)}{dy_1} \frac{dy_1}{dt} = 2C_1 n \omega u(y_1, \Phi_{o1}).$$

Thus it follows that

$$\frac{\partial \Phi_n}{\partial y_1} + \frac{d\theta_n(y_1)}{dy_1} = \frac{2C_1 n \omega u(y_1, \Phi_{o1})}{c_1 \omega [1 + 2C_1 u(y_1, \Phi_{o1})]}$$

or

$$\frac{\partial \Phi_n(y_1, \Phi_{o1})}{\partial y_1} + \frac{d\theta_n(y_1)}{dy_1} = \frac{2nu(y_1, \Phi_{o1})}{1 + 2C_1 u(y_1, \Phi_{o1})}. \quad (3.16)$$

This is the velocity-phase equation giving a relation between  $u$  and  $\Phi$ .

It represents one of the large-signal analysis working equations.

### 3.2 The Circuit Equations in Lagrangian Coordinates for $\nu = 0$

The circuit equations taking higher harmonic components of the RF wave into account may be easily deduced from the result obtained in Chapter II. Thus

$$\frac{\partial^2 V_n(z, t)}{\partial z^2} - \frac{1}{v_{on}^2} \frac{\partial^2 V_n(z, t)}{\partial t^2} = - \frac{Z_{on}}{v_{on}} \frac{\partial^2 \rho_n(z, t)}{\partial t^2}. \quad (3.17)$$

$Z_{on}$  and  $v_{on}$  are the interaction impedance and the phase velocity,

respectively, at the  $n$ th harmonic. In terms of the notation of Chapter II,

$$Z_{on} = \sqrt{\frac{L'_{on}}{C'_{on}}}, \quad (3.18)$$

$$\frac{1}{v_{on}^2} = L'_{on} C'_{on} = \frac{T_{pn} \beta_n \kappa_e}{\omega_p^2 \left(1 - \frac{1}{(\omega_p/n\omega)^2}\right)} \frac{J_0(T_{pn} b)}{J_1(T_{pn} b)}$$

$$\cdot \left[ \frac{I_0(\beta_n a) K_1(\beta_n b) + K_0(\beta_n a) I_1(\beta_n b)}{K_0(\beta_n b) I_0(\beta_n a) - K_0(\beta_n a) I_0(\beta_n b)} \right] \quad (3.19)$$

and

$$\frac{Z_{on}}{v_{on}} = \frac{1}{C'_{on}} = \frac{1}{2\pi b \epsilon_o \kappa_e \beta_n} \left(1 - \frac{1}{(\omega_p/n\omega)^2}\right)$$

$$\cdot \left[ \frac{K_0(\beta_n b) I_0(\beta_n a) - K_0(\beta_n a) I_0(\beta_n b)}{I_0(\beta_n a) K_1(\beta_n b) + K_0(\beta_n a) I_1(\beta_n b)} \right]. \quad (3.20)$$

Equation 3.17 will now be cast into a form that makes use of the Lagrangian variables. There are actually n circuit equations, one for each harmonic. The circuit voltage may be written as

$$V(z,t) = \text{Re} \left[ \sum_{n=1}^{\infty} V_n(z) e^{j(n\omega t - \beta_n z)} \right], \quad (3.21)$$

where it is assumed that the voltage components can be defined as the product of two slowly varying functions, one of distance and one of phase. In view of the discussion following Eq. 3.11 define  $\Phi_n$  such that

$$\Phi_n(y_1, \Phi_{o1}) \triangleq -n\omega t + \beta_n z, \quad (3.22)$$

where  $\beta_n$  is the circuit phase constant used previously.

Making use of the Lagrangian variables, Eq. 3.21 becomes

$$V(y_1, \Phi_{o1}) \triangleq \text{Re} \left[ \frac{Z_{o1} I_o}{C_1} \sum_{n=1}^{\infty} A_n(y_1) e^{-j\Phi_n(y_1, \Phi_{o1})} \right], \quad (3.23)$$

where  $A_n(y_1)$  is the normalized voltage amplitude for the nth harmonic along the circuit and  $C_1$  is the coupling parameter for the fundamental RF component.

The beam charge density  $\rho(z, t)$  for a tightly bunched beam may be expected to have a large number of harmonics. Thus, expanding  $\rho$  into a Fourier series in the phase variable,  $\Phi_n$ ,

$$\rho(z, t) = \sum_{n=1}^{\infty} \left( a_n \sin(-\Phi_n) + b_n \cos(-\Phi_n) \right). \quad (3.24)$$

Since the fundamental frequency and its harmonics have commensurate periods, the Fourier coefficients for the various harmonics may be obtained from

$$\rho_n(z) = \frac{2}{Tn\omega} \int_0^{Tn\omega} \rho_n(z, \Phi_n) e^{-j\Phi_n} d\Phi_n, \quad (3.25)$$

where  $T = 2\pi L/\omega$  and  $L$  is an integer. Thus

$$a_n = \frac{1}{n\pi L} \int_0^{2\pi L} \rho_n(z, \Phi_n) \sin(-\Phi_n) d\Phi_n$$

and

$$b_n = \frac{1}{n\pi L} \int_0^{2\pi L} \rho_n(z, \Phi_n) \cos(-\Phi_n) d\Phi_n .$$

Substituting these into Eq. 3.24 one obtains

$$\begin{aligned} \rho_n(z, t) = \sum_{n=1}^{\infty} \frac{1}{n\pi L} & \left[ \left( \int_0^{2\pi L} \rho_n(z, \Phi_n) \sin(-\Phi_n) d\Phi_n \right) \sin(-\Phi_n) \right. \\ & \left. + \left( \int_0^{2\pi L} \rho_n(z, \Phi_n) \cos(-\Phi_n) d\Phi_n \right) \cos(-\Phi_n) \right] . \quad (3.26) \end{aligned}$$

Since

$$\cos(-\Phi_n) + j \sin(-\Phi_n) = e^{-j\Phi_n} ,$$

Eq. 3.26 becomes

$$\begin{aligned} \rho_n(z, t) = \operatorname{Re} \left\{ \sum_{n=1}^{\infty} \frac{1}{n\pi L} \right. & \left[ - \left( \int_0^{2\pi L} \rho_n(z, \Phi_n) \sin \Phi_n d\Phi_n \right) \sin(-\Phi_n) \right. \\ & + j \left( \int_0^{2\pi L} \rho_n(z, \Phi_n) \sin \Phi_n d\Phi_n \right) \cos(-\Phi_n) + \left( \int_0^{2\pi L} \rho_n(z, \Phi_n) \cos \Phi_n d\Phi_n \right) \\ & \left. \left. \cdot \cos(-\Phi_n) + j \left( \int_0^{2\pi L} \rho_n(z, \Phi_n) \cos \Phi_n d\Phi_n \right) \sin(-\Phi_n) \right] \right\} \end{aligned}$$

or

$$\begin{aligned} \rho_n(z, t) = \operatorname{Re} \left[ \sum_{n=1}^{\infty} \frac{1}{n\pi L} e^{-j\Phi_n} \right. & \left( j \int_0^{2\pi L} \rho_n(z, \Phi_n) \sin \Phi_n d\Phi_n \right. \\ & \left. + \int_0^{2\pi L} \rho_n(z, \Phi_n) \cos \Phi_n d\Phi_n \right) \left. \right] . \end{aligned}$$



Substituting from the Lagrangian variable continuity equation, Eq. 3.11, this becomes

$$\rho(z,t) = -\operatorname{Re} \left[ \frac{I_0}{u_0 \pi L} \sum_{n=1}^{\infty} e^{-j\Phi_n} \left( \int_0^{2\pi L} \frac{\cos \Phi_n(y_1, \Phi'_{o1}) d\Phi'_{o1}}{1 + 2C_1 u(y_1, \Phi'_{o1})} + j \int_0^{2\pi L} \frac{\sin \Phi_n(y_1, \Phi'_{o1}) d\Phi'_{o1}}{1 + 2C_1 u(y_1, \Phi'_{o1})} \right) \right], \quad (3.27)$$

where the prime denotes the variable of integration.

Note that from Eq. 3.27 one may write

$$\rho_n = \rho_{nc} \cos \Phi_n + \rho_{ns} \sin \Phi_n. \quad (3.28)$$

The first and second time derivatives of the space-charge density are

$$\frac{\partial \rho_n}{\partial t} = \frac{\partial \rho_n}{\partial \Phi_n} \frac{\partial \Phi_n}{\partial t} \quad (3.29)$$

and

$$\frac{\partial^2 \rho_n}{\partial t^2} = \frac{\partial \rho_n}{\partial \Phi_n} \frac{\partial^2 \Phi_n}{\partial t^2} + \left( \frac{\partial \Phi_n}{\partial t} \right)^2 \frac{\partial^2 \rho_n}{\partial \Phi_n^2}. \quad (3.30)$$

If the normalized circuit voltage given by Eq. 3.23 is used, the circuit equation may now be written as

$$\begin{aligned}
 & \sum_{n=1}^{\infty} \left\{ \frac{Z_{o1} I_o}{C_1} \left( \frac{\omega C_1}{u_o} \right)^2 \frac{d^2 A_n(y_1)}{dy_1^2} \cos \Phi_n - \frac{Z_{o1} I_o}{C_1} \left( \frac{\omega C_1}{u_o} \right)^2 A_n(y_1) \left[ \frac{d^2 \Phi_n}{dy_1^2} \sin \Phi_n \right. \right. \\
 & \left. \left. + \left( \frac{d\Phi_n}{dy_1} \right)^2 \cos \Phi_n \right] - 2 \frac{Z_{o1} I_o}{C_1} \left( \frac{\omega C_1}{u_o} \right)^2 \frac{dA_n(y_1)}{dy_1} \frac{d\Phi_n}{dy_1} \sin \Phi_n + \frac{Z_{o1} I_o}{C_1 v_{on}^2} \right. \\
 & \left. \cdot A_n(y_1) \left[ \frac{\partial^2 \Phi_n}{\partial t^2} \sin \Phi_n + \left( \frac{\partial \Phi_n}{\partial t} \right)^2 \cos \Phi_n \right] \right\} = \sum_{n=1}^{\infty} - \frac{Z_{on}}{v_{on}} \left[ - \frac{n^2 \omega^2}{\pi L} \frac{I_o}{u_o} \right. \\
 & \left. \cdot \left( - \int_0^{2\pi L} \frac{\cos \Phi_n(y_1, \Phi'_{o1}) d\Phi'_{o1}}{1 + 2C_1 u(y_1, \Phi'_{o1})} \cos \Phi_n - \int_0^{2\pi L} \frac{\sin \Phi_n(y_1, \Phi'_{o1}) d\Phi'_{o1}}{1 + 2C_1 u(y_1, \Phi'_{o1})} \sin \Phi_n \right) \right] .
 \end{aligned} \tag{3.31}$$

From Eq. 3.12 one finds that

$$\begin{aligned}
 \frac{d\Phi_n}{dy_1} &= \frac{n}{C_1} - \frac{d\theta_n(y_1)}{dy_1} , \\
 \frac{d^2 \Phi_n}{dy_1^2} &= - \frac{d^2 \theta_n(y_1)}{dy_1^2} , \\
 \frac{\partial \Phi_n}{\partial t} &= -n\omega
 \end{aligned}$$

and

$$\frac{\partial^2 \Phi_n}{\partial t^2} = 0 .$$

Making use of these expressions in Eq. 3.31 one finds that

$$\sum_{n=1}^{\infty} \left\{ \frac{Z_{o1} I_o}{C_1} \frac{\omega^2 C_1^2}{u_o^2} \frac{d^2 A_n(y_1)}{dy_1^2} \cos \Phi_n - \frac{Z_{o1} I_o}{C_1} \frac{\omega^2 C_1^2}{u_o^2} A_n(y_1) \left[ - \frac{d^2 \theta_n(y_1)}{dy_1^2} \sin \Phi_n \right. \right. \\ \left. \left. + \left( \frac{n}{C_1} - \frac{d\theta_n(y_1)}{dy_1} \right)^2 \cos \Phi_n \right] - 2 \frac{Z_{o1} I_o}{C_1} \frac{\omega^2 C_1^2}{u_o^2} \frac{dA_n(y_1)}{dy_1} \left( \frac{n}{C_1} - \frac{d\theta_n(y_1)}{dy_1} \right) \right. \\ \left. \cdot \sin \Phi_n + \frac{Z_{o1} I_o}{C_1 v_{on}^2} A_n(y_1) n^2 \omega^2 \cos \Phi_n \right\} = - \sum_{n=1}^{\infty} \frac{Z_{on}}{v_{on}} \frac{n^2 \omega^2 I_o}{\pi L u_o} \\ \cdot \left( \int_0^{2\pi L} \frac{\cos \Phi_n(y_1, \Phi'_{o1}) d\Phi'_{o1}}{1 + 2C_1 u(y_1, \Phi'_{o1})} \cos \Phi_n + \int_0^{2\pi L} \frac{\sin \Phi_n(y_1, \Phi'_{o1}) d\Phi'_{o1}}{1 + 2C_1 u(y_1, \Phi'_{o1})} \sin \Phi_n \right) .$$

Since the coefficients of  $\sin \Phi_n$  and  $\cos \Phi_n$  on each side of the equal sign are independent of  $\Phi_n$  and since the sine and cosine are orthogonal, equating coefficients yields two circuit equations for each value of  $n$ .

Thus

$$\frac{Z_{o1} I_o}{C_1} \frac{\omega^2 C_1^2}{u_o^2} \frac{d^2 A_n(y_1)}{dy_1^2} - \frac{Z_{o1} I_o}{C_1} \frac{\omega^2 C_1^2}{u_o^2} A_n(y_1) \left( \frac{n}{C_1} - \frac{d\theta_n(y_1)}{dy_1} \right)^2 \\ + \frac{Z_{o1} I_o}{C_1 v_{on}^2} A_n(y_1) n^2 \omega^2 = - \frac{Z_{on}}{v_{on}} \frac{n^2 \omega^2 I_o}{\pi L u_o} \int_0^{2\pi L} \frac{\cos \Phi_n(y_1, \Phi'_{o1}) d\Phi'_{o1}}{1 + 2C_1 u(y_1, \Phi'_{o1})}$$

and

$$\begin{aligned} \frac{Z_{o1} I_o}{C_1} \frac{\omega^2 C^2}{u_o^2} A_n(y_1) \frac{d^2 \theta_n(y_1)}{dy_1^2} - 2 \frac{Z_{o1} I_o}{C_1} \frac{\omega^2 C^2}{u_o^2} \frac{dA_n(y_1)}{dy_1} \left( \frac{n}{C_1} - \frac{d\theta_n(y_1)}{dy_1} \right) \\ = - \frac{Z_{on}}{v_{on}} \frac{n^2 \omega^2 I_o}{\pi L u_o} \int_0^{2\pi L} \frac{\sin \Phi_n(y_1, \Phi'_{o1}) d\Phi'_{o1}}{1 + 2C_1 u(y_1, \Phi'_{o1})} . \end{aligned}$$

Rewriting the last two equations one obtains

$$\begin{aligned} \omega^2 \frac{d^2 A_n(y_1)}{dy_1^2} - \omega^2 A_n(y_1) \left( \frac{n}{C_1} - \frac{d\theta_n(y_1)}{dy_1} \right)^2 + \frac{1}{C_1^2} \frac{u_o^2}{v_{on}^2} A_n(y_1) n^2 \omega^2 \\ = - \frac{Z_{on} n^2 \omega^2 I_o}{v_{on} \pi L u_o} \frac{u_o^2}{Z_{o1} I_o C_1} \int_0^{2\pi L} \frac{\cos \Phi_n(y_1, \Phi'_{o1}) d\Phi'_{o1}}{1 + 2C_1 u(y_1, \Phi'_{o1})} \end{aligned}$$

and

$$\begin{aligned} \omega^2 A_n(y_1) \frac{d^2 \theta_n(y_1)}{dy_1^2} - 2\omega^2 \frac{dA_n(y_1)}{dy_1} \left( \frac{n}{C_1} - \frac{d\theta_n(y_1)}{dy_1} \right) \\ = - \frac{Z_{on} n^2 \omega^2 I_o}{v_{on} \pi L u_o} \frac{u_o^2}{Z_{o1} I_o C_1} \int_0^{2\pi L} \frac{\sin \Phi_n(y_1, \Phi'_{o1}) d\Phi'_{o1}}{1 + 2C_1 u(y_1, \Phi'_{o1})} . \end{aligned}$$

Simplifying further, the circuit equations finally become

$$\begin{aligned} \frac{d^2 A_n(y_1)}{dy_1^2} - A_n(y_1) \left( \frac{n}{C_1} - \frac{d\theta_n(y_1)}{dy_1} \right)^2 + \frac{n^2}{C_1^2} \left( \frac{u_o}{v_{on}} \right)^2 A_n(y_1) \\ = - \frac{n^2 \left( \frac{u_o}{v_{on}} \right) \left( \frac{Z_{on}}{Z_{o1}} \right)}{\pi L C_1} \int_0^{2\pi L} \frac{\cos \Phi_n(y_1, \Phi'_{o1}) d\Phi'_{o1}}{1 + 2C_1 u(y_1, \Phi'_{o1})} \quad (3.32) \end{aligned}$$

and

$$A_n(y_1) \frac{d^2\theta_n(y_1)}{dy_1^2} + 2 \frac{dA_n(y_1)}{dy_1} \left( \frac{d\theta_n(y_1)}{dy_1} - \frac{n}{C_1} \right) = - \frac{n^2 \left( \frac{u_o}{v_{on}} \right) \left( \frac{Z_{on}}{Z_{o1}} \right)}{\pi L C_1} \cdot \int_0^{2\pi L} \frac{\sin \Phi_n(y_1, \Phi'_{o1}) d\Phi'_{o1}}{1 + 2C_{n1} u(y_1, \Phi'_{o1})} \quad (3.33)$$

These are the circuit equations in Lagrangian coordinates and represent two additional working equations (actually there are  $2n$  of them, if all  $n$  harmonics are considered) in the large-signal analysis. Note that these equations appear in the same form as in the traveling-wave tube case. This is reasonable, because the plasma in this analysis is replaced by an equivalent circuit so that the plasma effects are hidden in  $Z_{on}$  and  $v_{on}$ . These latter quantities may of course be determined after a solution of the dispersion equation for the plasma column has been obtained.

### 3.3 The Lorentz Force Equation in Lagrangian Coordinates

In this analysis collisions between the beam electrons and the plasma particles will be included by adding a term including the collision frequency,  $\nu_c$ , to the usual Lorentz force equation. Thus

$$\frac{d\vec{v}}{dt} + \nu_c \vec{v} = -\eta(\vec{E} + \vec{v} \times \vec{B}) \quad (3.34)$$

The electric field in Eq. 3.34 is now separated into circuit and space-charge field components. Taking the one-dimensional case and neglecting relativistic effects one obtains

$$\frac{d^2z}{dt^2} + v_c \frac{dz}{dt} = \eta \left( \frac{\partial V_{nc}(z,t)}{\partial z} + \frac{\partial V_{nsc}(z,t)}{\partial z} \right), \quad (3.35)$$

where the subscript c denotes circuit terms and the subscript sc denotes space-charge terms. Since

$$\frac{dz}{dt} \triangleq u_o \left( 1 + 2C_1 u(y_1, \Phi_{o1}) \right),$$

Eq. 3.35 becomes

$$\frac{d^2z}{dt^2} + v_c u_o \left( 1 + 2C_1 u(y_1, \Phi_{o1}) \right) = \eta \left( \frac{\partial V_{nc}(z,t)}{\partial z} + \frac{\partial V_{nsc}(z,t)}{\partial z} \right).$$

From Eq. 3.12

$$\frac{d\Phi_n}{dy_1} = \frac{n}{C_1} - \frac{d\theta_n(y_1)}{dy_1},$$

and from Eq. 3.23

$$\frac{\partial V_{nc}(y_1, \Phi_{o1})}{\partial y_1} = \frac{Z_{o1} I_o}{C_1} \left( \frac{\partial A_n(y_1)}{\partial y_1} \cos \Phi_n - A_n(y_1) \sin \Phi_n \frac{\partial \Phi_n}{\partial y_1} \right).$$

In view of these results the following force equation in Lagrangian coordinates is obtained:

$$\begin{aligned} \frac{d^2z}{dt^2} + v_c u_o \left( 1 + 2C_1 u(y_1, \Phi_{o1}) \right) = & \eta \sum_{n=1}^{\infty} \frac{Z_{o1} I_o}{C_1} \frac{\omega C_1}{u_o} \left[ \frac{dA_n(y_1)}{dy_1} \right. \\ & \cdot \cos \Phi_n(y_1, \Phi_{o1}) - A_n(y_1) \sin \Phi_n(y_1, \Phi_{o1}) \left. \left( \frac{n}{C_1} - \frac{d\theta_n(y_1)}{dy_1} \right) \right] \\ & - \eta E_{nsc-z}(y_1, \Phi_n). \quad (3.36) \end{aligned}$$

This form of the force equation contains the acceleration, which needs to be eliminated for ease of solution of the final equations. Note that from Eq. 3.9

$$\frac{d^2z}{dt^2} = \frac{dv}{dt} = \frac{\partial v}{\partial y_1} \frac{dy_1}{dt} = 2C_1 u_0 \frac{\partial u}{\partial y_1} \frac{dy_1}{dt}$$

or

$$\frac{d^2z}{dt^2} = 2C_1^2 u_0 \omega \left( 1 + 2C_1 u(y_1, \Phi_{o1}) \right) \frac{\partial u(y_1, \Phi_{o1})}{\partial y_1} . \quad (3.37)$$

An expression for the space-charge field term of Eq. 3.36 must now be found. The harmonic method described in detail by Rowe<sup>46</sup> for the conventional traveling-wave amplifier may be used. A derivation of the space-charge field is outlined in Appendix C. Thus

$$E_{nsc-z}(y_1, \Phi_n) = - \frac{2\omega v_{on}}{L\eta} \left( \frac{\omega_b}{\omega} \right)^2 \int_0^{2\pi L} \frac{F_{1-z}(\Phi_n - \Phi'_n) d\Phi'_{o1}}{1 + 2C_1 u(y_1, \Phi'_{o1})} , \quad (3.38)$$

where  $\omega_b$  is the plasma frequency of the beam electrons and where  $F_{1-z}$  is the one-dimensional space-charge field weighting function relating the influence of an electron at  $\Phi'_n$  on an electron at  $\Phi_n$  in determining the space-charge field forces.

Now substitute Eqs. 3.37 and 3.38 into Eq. 3.36 to obtain the following form of the force equation:

$$\begin{aligned}
 & 2C_1^2 u_o \omega \left( 1 + 2C_1 u(y_1, \Phi_{o1}) \right) \frac{\partial u(y_1, \Phi_{o1})}{\partial y_1} + v_c u_o \left( 1 + 2C_1 u(y_1, \Phi_{o1}) \right) \\
 &= \eta \sum_{n=1}^{\infty} \frac{Z_{o1} I_o \omega}{u_o} \left[ \frac{dA_n(y_1)}{dy_1} \cos \Phi_n(y_1, \Phi_{o1}) - A_n(y_1) \sin \Phi_n(y_1, \Phi_{o1}) \right. \\
 &\quad \cdot \left. \left( \frac{n}{C_1} - \frac{d\theta_n(y_1)}{dy_1} \right) \right] + \eta \frac{2\omega v_{on}}{2C_1^2 L \eta u_o \omega} \left( \frac{\omega_b}{\omega} \right)^2 \int_0^{2\pi L} \frac{F_{1-z}(\Phi_n - \Phi'_n) d\Phi'_{o1}}{1 + 2C_1 u(y_1, \Phi'_{o1})} .
 \end{aligned}$$

This may be rewritten as

$$\begin{aligned}
 & \left( 1 + 2C_1 u(y_1, \Phi_{o1}) \right) \frac{\partial u(y_1, \Phi_{o1})}{\partial y_1} + \frac{1}{2C_1^2} \left( \frac{v_c}{\omega} \right) \left( 1 + 2C_1 u(y_1, \Phi_{o1}) \right) \\
 &= \sum_{n=1}^{\infty} \eta \frac{Z_{o1} I_o}{2C_1^2 u_o^2} \left[ \frac{dA_n(y_1)}{dy_1} \cos \Phi_n(y_1, \Phi_{o1}) - A_n(y_1) \sin \Phi_n(y_1, \Phi_{o1}) \right. \\
 &\quad \cdot \left. \left( \frac{n}{C_1} - \frac{d\theta_n(y_1)}{dy_1} \right) \right] + \frac{v_{on}}{LC_1^2 u_o} \left( \frac{\omega_b}{\omega} \right)^2 \int_0^{2\pi L} \frac{F_{1-z}(\Phi_n - \Phi'_n) d\Phi'_{o1}}{1 + 2C_1 u(y_1, \Phi'_{o1})}
 \end{aligned}$$

or

$$\begin{aligned}
 & \left( 1 + 2C_1 u(y_1, \Phi_{o1}) \right) \frac{\partial u(y_1, \Phi_{o1})}{\partial y_1} + \frac{1}{2C_1^2} \left( \frac{v_c}{\omega} \right) \left( 1 + 2C_1 u(y_1, \Phi_{o1}) \right) \\
 &= \eta \frac{Z_{o1} I_o}{2C_1^3 u_o^2} C_1 \sum_{n=1}^{\infty} \left[ \frac{dA_n(y_1)}{dy_1} \cos \Phi_n(y_1, \Phi_{o1}) - A_n(y_1) \sin \Phi_n(y_1, \Phi_{o1}) \right. \\
 &\quad \cdot \left. \left( \frac{n}{C_1} - \frac{d\theta_n(y_1)}{dy_1} \right) \right] + \frac{1}{LC_1^2} \left( \frac{v_{on}}{u_o} \right) \left( \frac{\omega_b}{\omega} \right)^2 \int_0^{2\pi L} \frac{F_{1-z}(\Phi_n - \Phi'_n) d\Phi'_{o1}}{1 + 2C_1 u(y_1, \Phi'_{o1})} .
 \end{aligned}$$



Making use of Eq. 3.7 and the fact that

$$u_o^2 = 2\eta V_o, \quad (3.39)$$

one obtains the final form of the force equation:

$$\begin{aligned} & \left[ \frac{\partial u(y_1, \Phi_{o1})}{\partial y_1} + \frac{1}{2C_1^2} \left( \frac{v_c}{\omega} \right) \right] \left( 1 + 2C_1 u(y_1, \Phi_{o1}) \right) \\ &= \sum_{n=1}^{\infty} \left[ C_1 \frac{dA_n(y_1)}{dy_1} \cos \Phi_n(y_1, \Phi_{o1}) - A_n(y_1) \sin \Phi_n(y_1, \Phi_{o1}) \right. \\ & \cdot \left. \left( n - C_1 \frac{d\theta_n(y_1)}{dy_1} \right) \right] + \frac{1}{LC_1^2} \left( \frac{v_{on}}{u_o} \right) \left( \frac{\omega_b}{\omega} \right)^2 \int_0^{2\pi L} \frac{F_{1-z}(\Phi_n - \Phi'_n) d\Phi'_{o1}}{1 + 2C_1 u(y_1, \Phi'_{o1})}. \end{aligned} \quad (3.40)$$

This form of the force equation is appropriate for solution in the large-signal analysis. It represents the last of the working equations needed. Thus the set of equations that must be solved consists of Eqs. 3.16, 3.32, 3.33 and 3.40.

#### 3.4 Inclusion of Loss Due to Plasma Particle Collisions in the Large-Signal Equations

If the plasma column in a beam-plasma interaction analysis is regarded as a lumped element transmission line, it turns out to be relatively straightforward to include losses due to plasma particle collisions. The interaction impedance used in the large-signal nonlinear interaction equations is then a complex number, and the analysis proceeds in much the same way as in the collisionless case. Major changes occur only in the circuit equations.

Recall that the field quantities along the plasma column were defined to vary as  $\exp[j(n\omega t - k_n z)]$ , where  $k_n$  is the complex propagation constant of the nth harmonic, in general given by

$$jk_n = \alpha_n + j\beta_n$$

or

$$k_n = \beta_n - j\alpha_n \quad (3.41)$$

Here  $\beta_n$  is the phase constant and  $\alpha_n$  is the attenuation constant. A positive value of  $\alpha_n$  implies a loss in the wave amplitude.

The dispersion equation for a plasma column contained in a dielectric-lined metallic cylinder was found in Chapter II and is shown here again for the nth harmonic.

$$1 = \frac{\kappa_{\perp}}{\kappa_e} \frac{T_{pn}}{k_n} \frac{J_1(T_{pn} b)}{J_0(T_{pn} b)} \left[ \frac{K_0(k_n b) I_0(k_n a) - K_0(k_n a) I_0(k_n b)}{I_0(k_n a) K_1(k_n b) + K_0(k_n a) I_1(k_n b)} \right], \quad (3.42)$$

where

$$T_{pn}^2 = k_n^2 \left( \frac{\kappa_{\parallel}}{\kappa_{\perp}} \right) = -k_n^2 \left[ \frac{1 - \frac{(\omega_p/n\omega)^2}{1 - j(\nu/n\omega)}}{1 - \frac{(\omega_p/n\omega)^2 [1 - j(\nu/n\omega)]}{[1 - j(\nu/n\omega)] - (\omega_c/n\omega)^2}} \right]. \quad (3.43)$$

The equivalent circuit elements at the nth harmonic are given by

$$L_{on} = \frac{T_{pn} [1 - j(\nu/n\omega)]}{2\pi\epsilon_o \omega_p^2 b} \frac{J_0(T_{pn} b)}{J_1(T_{pn} b)} \quad (3.44)$$

and

$$C_{on} = 2\pi b k_n \epsilon_o \kappa_e \left[ \frac{I_o(k_n a) K_1(k_n b) + K_o(k_n a) I_1(k_n b)}{K_o(k_n b) I_o(k_n a) - K_o(k_n a) I_o(k_n b)} \right] \left[ \frac{1}{1 - \frac{1 - j(v/n\omega)}{(\omega_p/n\omega)^2}} \right]. \quad (3.45)$$

Note that when collisions are present,  $L_o$  and  $C_o$  are complex numbers, the imaginary part representing a dissipation loss. For such an equivalent circuit the phase velocity is given by

$$v_{on} = \frac{n\omega}{\beta_n}, \quad (3.46)$$

and the characteristic impedance is given by

$$Z_{on} = \sqrt{\frac{L_{on}}{C_{on}}}. \quad (3.47)$$

The "circuit" equation is the same as Eq. 3.17, but  $Z_{on}$  is now complex. Thus define

$$Z_{on} \triangleq Z_{onr} + jZ_{oni}. \quad (3.48)$$

In terms of normalized variables the circuit voltage is given by

$$V(z,t) = \frac{|Z_{o1}| I_o}{C_1} \sum_{n=1}^{\infty} A_n(y_1) e^{-j\Phi_n(y_1, \Phi_{o1})}. \quad (3.49)$$

Proceeding as in Section 3.2 and expanding the charge density in a Fourier series one obtains

$$\rho(z,t) = \sum_{n=1}^{\infty} \rho_n(y_1) e^{-j\Phi_n(y_1, \Phi_{o1})}. \quad (3.50)$$

Thus the circuit equation may be written as

$$\begin{aligned} \frac{|Z_{o1}|I_o}{C_1} \sum_{n=1}^{\infty} \left[ \left( \frac{C_1 \omega}{u_o} \right)^2 \left\{ \frac{d^2 A_n(y_1)}{dy_1^2} - 2j \frac{dA_n(y_1)}{dy_1} \left( \frac{n}{C_1} - \frac{d\theta_n(y_1)}{dy_1} \right) \right. \right. \\ \left. \left. + A_n(y_1) \left[ j \frac{d^2 \theta_n(y_1)}{dy_1^2} - \left( \frac{n}{C_1} - \frac{d\theta_n(y_1)}{dy_1} \right)^2 \right] \right\} + \left( \frac{\omega v}{v_{on}} \right)^2 A_n(y_1) \right] \\ \cdot e^{-j\Phi_n(y_1, \Phi_{o1})} = \sum_{n=1}^{\infty} \frac{Z_{on}}{v_{on}} (\omega v)^2 \rho_n(y_1) e^{-j\Phi_n(y_1, \Phi_{o1})} \end{aligned}$$

or

$$\begin{aligned} \sum_{n=1}^{\infty} \left\{ \frac{d^2 A_n(y_1)}{dy_1^2} - 2j \frac{dA_n(y_1)}{dy_1} \left( \frac{n}{C_1} - \frac{d\theta_n(y_1)}{dy_1} \right) + A_n(y_1) \left[ j \frac{d^2 \theta_n(y_1)}{dy_1^2} \right. \right. \\ \left. \left. - \left( \frac{n}{C_1} - \frac{d\theta_n(y_1)}{dy_1} \right)^2 + \frac{n^2}{C_1^2} \left( \frac{u_o}{v_{on}} \right)^2 \right] \right\} e^{-j\Phi_n(y_1, \Phi_{o1})} = \sum_{n=1}^{\infty} \frac{n^2}{C_1} \frac{Z_{on}}{|Z_{o1}|} \\ \cdot \left( \frac{u_o}{v_{on}} \right) \left( \frac{u_o}{I_o} \right) \rho_n(y_1) e^{-j\Phi_n(y_1, \Phi_{o1})} \quad (3.51) \end{aligned}$$

Now the ratio of impedances is expanded as

$$\frac{Z_{on}}{|Z_{o1}|} = \frac{Z_{onr}}{|Z_{o1}|} + j \frac{Z_{oni}}{|Z_{o1}|} \triangleq \zeta_{nr} + j\zeta_{ni} \quad (3.52)$$

Then Eq. 3.51 may be written as

$$\begin{aligned}
 & \sum_{n=1}^{\infty} \left\{ \frac{d^2 A_n(y_1)}{dy_1^2} - 2j \frac{dA_n(y_1)}{dy_1} \left( \frac{n}{C_1} - \frac{d\theta_n(y_1)}{dy_1} \right) + A_n(y_1) \left[ j \frac{d^2 \theta_n(y_1)}{dy_1^2} \right. \right. \\
 & \left. \left. - \left( \frac{n}{C_1} - \frac{d\theta_n(y_1)}{dy_1} \right)^2 + \frac{n^2}{C_1^2} \left( \frac{u_o}{v_{on}} \right)^2 \right] \right\} e^{-j\Phi_n(y_1, \Phi_{o1})} \\
 & = \sum_{n=1}^{\infty} \frac{n^2}{C_1} \left( \frac{u_o}{v_{on}} \right) \left( \frac{u_o}{I_o} \right) (\xi_{nr} + j\xi_{ni}) \rho_n(y_1) e^{-j\Phi_n(y_1, \Phi_{o1})} \quad (3.53)
 \end{aligned}$$

The conservation of charge equation in normalized variables is

$$\rho_n(y_1, \Phi_{o1}) = - \frac{I_o}{u_o} \left| \frac{\partial \Phi_{o1}}{\partial \Phi_n} \right|_{y_1} \frac{n}{1 + 2C_1 u(y_1, \Phi_{o1})} \quad (3.54)$$

Since the fundamental frequency and its harmonics are assumed to have commensurate periods, the charge density may be written as

$$\rho_n(z) = \frac{2}{Tn\omega} \int_0^{T\omega} \rho_n(z, \Phi_n) e^{-j\Phi_n} d\Phi_n, \quad (3.55)$$

where

$$T = \frac{2\pi L}{\omega} \quad (3.56)$$

and L is an integer. Splitting the charge density into real and imaginary parts,

$$\rho_n(y_1) = \rho_{nr}(y_1) + j\rho_{ni}(y_1) \quad (3.57)$$

Then

$$\rho_{nr} = \frac{1}{n\pi L} \int_0^{2\pi L} \rho_n \cos \Phi_n d\Phi_n$$

and

$$\rho_{ni} = \frac{1}{n\pi L} \int_0^{2\pi L} \rho_n \sin \Phi_n d\Phi_n$$

Thus, in view of Eq. 3.54

$$\rho_{nr} = - \frac{I_o}{u_o \pi L} \int_0^{2\pi L} \frac{\cos \Phi_n(y_1, \Phi'_{o1}) d\Phi'_{o1}}{1 + 2C_1 u(y_1, \Phi'_{o1})} \quad (3.58a)$$

and

$$\rho_{ni} = - \frac{I_o}{u_o \pi L} \int_0^{2\pi L} \frac{\sin \Phi_n(y_1, \Phi'_{o1}) d\Phi'_{o1}}{1 + 2C_1 u(y_1, \Phi'_{o1})} \quad (3.58b)$$

Now Eqs. 3.53 and 3.57 are combined and the real and imaginary parts of the various terms of the series on the left- and right-hand sides of the equation are equated. Thus two circuit equations are obtained:

$$\begin{aligned} \frac{d^2 A_n(y_1)}{dy_1^2} + \left[ \frac{n^2}{C_1^2} \left( \frac{u_o}{v_{on}} \right)^2 - \left( \frac{n}{C_1} - \frac{d\theta_n(y_1)}{dy_1} \right)^2 \right] A_n(y_1) \\ = \frac{n^2}{C_1} \left( \frac{u_o}{v_{on}} \right) \left( \frac{u_o}{I_o} \right) (\zeta_{nr} \rho_{nr} - \zeta_{ni} \rho_{ni}) \end{aligned}$$

and

$$\begin{aligned} -2 \frac{dA_n(y_1)}{dy_1} \left( \frac{n}{C_1} - \frac{d\theta_n(y_1)}{dy_1} \right) + \frac{d^2 \theta_n(y_1)}{dy_1^2} A_n(y_1) \\ = \frac{n^2}{C_1} \left( \frac{u_o}{v_{on}} \right) \left( \frac{u_o}{I_o} \right) (\zeta_{nr} \rho_{ni} + \zeta_{ni} \rho_{nr}) \end{aligned}$$

Substituting from Eqs. 3.58, the final forms of the circuit equations are as follows:

$$\begin{aligned} \frac{d^2 A_n(y_1)}{dy_1^2} + \left[ \frac{n^2}{C_1^2} \left( \frac{u_o}{v_{on}} \right)^2 - \left( \frac{n}{C_1} - \frac{d\theta_n(y_1)}{dy_1} \right)^2 \right] A_n(y_1) = - \frac{n^2}{C_1 \pi L} \\ \cdot \left( \frac{u_o}{v_{on}} \right) \zeta_{nr} \int_0^{2\pi L} \frac{\cos \Phi_n(y_1, \Phi'_{o1}) d\Phi'_{o1}}{1 + 2C_1 u(y_1, \Phi'_{o1})} + \frac{n^2}{C_1 \pi L} \left( \frac{u_o}{v_{on}} \right) \zeta_{ni} \\ \cdot \int_0^{2\pi L} \frac{\sin \Phi_n(y_1, \Phi'_{o1}) d\Phi'_{o1}}{1 + 2C_1 u(y_1, \Phi'_{o1})} \quad (3.59) \end{aligned}$$

and

$$\begin{aligned} 2 \left( \frac{d\theta_n(y_1)}{dy_1} - \frac{n}{C_1} \right) \frac{dA_n(y_1)}{dy_1} + \frac{d^2 \theta_n(y_1)}{dy_1^2} A_n(y_1) = - \frac{n^2}{C_1 \pi L} \left( \frac{u_o}{v_{on}} \right) \zeta_{nr} \\ \cdot \int_0^{2\pi L} \frac{\sin \Phi_n(y_1, \Phi'_{o1}) d\Phi'_{o1}}{1 + 2C_1 u(y_1, \Phi'_{o1})} - \frac{n^2}{C_1 \pi L} \left( \frac{u_o}{v_{on}} \right) \zeta_{ni} \int_0^{2\pi L} \frac{\cos \Phi_n(y_1, \Phi'_{o1}) d\Phi'_{o1}}{1 + 2C_1 u(y_1, \Phi'_{o1})} \quad (3.60) \end{aligned}$$

The velocity phase equation, Eq. 3.16, and the force equation, Eq. 3.40, are unchanged when plasma collision effects are included.

The circuit equations derived in this section may be compared with the circuit equations derived by Rowe<sup>46</sup> for the traveling-wave amplifier when loss is included. Inspection reveals that the loss parameter for a traveling-wave amplifier is related to the imaginary part of the circuit impedance used in this study by

$$\zeta_{ni} = -2C_1 d_n, \quad (3.61)$$

where  $d_n$  is the traveling-wave tube loss parameter at the  $n$ th harmonic. Thus

$$d_n = -\frac{1}{2C_1} \frac{Z_{oni}}{|Z_{o1}|} . \quad (3.62)$$

Since  $Z_{oni}$  is negative, as was pointed out in Chapter II,  $d_n$  is a positive quantity, in agreement with traveling-wave tube theory.

### 3.5 Initial Conditions and Input Data

In the one-dimensional analysis of this chapter there are four equations in four unknowns. The unknown quantities are the dependent variables  $A_n(y_1)$ ,  $\theta_n(y_1)$ ,  $\Phi_n(y_1, \Phi_{o1})$  and  $u(y_1, \Phi_{o1})$ . These are given in terms of the two independent variables  $y_1$  and  $\Phi_{o1}$ . It is not convenient to solve the equations as a boundary value problem, because the conditions at the output of the interaction region are not known a priori. An initial value problem requires a knowledge of the dependent variables and some of their derivatives at the input only. A solution to the equations may thus be obtained by integrating along particle trajectories through the interaction region until saturation is reached. The following initial conditions need to be specified.

1. Define

$$A_n(0) \triangleq A_{no} , \quad (3.63)$$

the input signal level relative to  $C_1 I_o V_o$ .

2. Since the RF signal is applied at  $y_1 = 0$  and the electron stream also enters at  $y_1 = 0$ ,

$$\theta_n(0) = 0 \quad (3.64)$$

for all conditions.



3. From Eq. 3.32 one finds that for  $y_1 = 0$ ,

$$-A_n(0) \left[ \left( \frac{n}{C_1} - \frac{d\theta_n(0)}{dy_1} \right)^2 - \frac{n^2}{C_1^2} \left( \frac{u_o}{v_{on}} \right)^2 \right] = 0 .$$

It follows then that

$$\frac{n}{C_1} - \frac{d\theta_n(0)}{dy_1} = \frac{n}{C_1} \left( \frac{u_o}{v_{on}} \right)$$

or

$$\frac{d\theta_n(0)}{dy_1} = -\frac{n}{C_1} \left( \frac{u_o}{v_{on}} - 1 \right) = -nb_n \left( \frac{z_{onr}}{|z_{o1}|} \right)^{1/3} . \quad (3.65)$$

4. For an initially unbunched stream

$$\left. \frac{dA_n(y_1)}{dy_1} \right|_{y_1=0} = 0 , \quad (3.66)$$

which says that the stream cannot affect the signal until stream modulation has occurred. If the beam is prebunched, however, consider Eq. 3.33. Since

$$\frac{d^2\theta_n(0)}{dy_1^2} = 0$$

from Eq. 3.65, it follows that

$$2 \frac{dA_n(0)}{dy_1} \left( \frac{d\theta_n(0)}{dy_1} - \frac{n}{C_1} \right) = -\frac{n^2(u_o/v_{on})(z_{onr}/|z_{o1}|)}{\pi L C_1} \cdot \int_0^{2\pi L} \sin \Phi_n(y_1, \Phi'_{o1}) d\Phi'_{o1} .$$

Defining the bunch injection phase angle,  $\alpha_n$ , by

$$\frac{1}{2\pi L} \int_0^{2\pi L} \sin \Phi_n(y_1, \Phi'_{o1}) d\Phi'_{o1} \triangleq \sin \alpha_n, \quad (3.67)$$

one obtains after simplification of the above that

$$-2 \frac{dA_n(0)}{dy_1} \left[ nb_n \left( \frac{Z_{onr}}{|Z_{o1}|} \right)^{1/3} + \frac{n}{C_1} \right] = - \frac{2n^2(u_o/v_{on})(Z_{onr}/|Z_{o1}|)}{C_1} \sin \alpha_n$$

or

$$\frac{dA_n(0)}{dy_1} = n \left( \frac{Z_{onr}}{|Z_{o1}|} \right) \sin \alpha_n. \quad (3.68)$$

5. Beam bunching is specified in terms of

$$\Phi_n(0, \Phi_{o1,j}) = \Phi_{on,j}, \quad (3.69)$$

where  $j = 0, 1, 2, \dots, m$  denotes a particular charge group of electrons injected into the interaction region. For an unbunched stream input the charge groups are uniformly distributed in phase over one cycle of the RF wave at  $y_1 = 0$ . Thus for an unbunched stream

$$\Phi_{on,j} = \frac{2\pi j}{m}. \quad (3.70)$$

6. Equation 3.9 gives an expression for the electron velocity.

At the input plane the RF velocity of the  $j$ th charge group is given by

$$u(0, \Phi_{o1,j}) = 0 \quad (3.71)$$

for an unmodulated stream.

In order to obtain a solution to the large-signal equations the following input data must be given.

1.  $n$ , the harmonic number to be considered.
  2.  $C_1$ , the beam-"circuit" coupling parameter for the fundamental RF component.
  3.  $b_1 = (1/C_1)[(u_0/v_{01}) - 1]$ , the injection velocity parameter for the fundamental signal.
  4.  $v_{0n}/v_{01}$ , a normalized velocity ratio for the phase velocity of the  $n$ th harmonic RF wave.
  5.  $Z_{0nr}/|Z_{01}|$ , the normalized real part of the interaction impedance.
  6.  $Z_{0ni}/|Z_{01}|$ , the normalized imaginary part of the interaction impedance, if plasma collisions are included. Both the real and imaginary parts of the impedance are calculated for a solution of the dispersion equation, which is a separate program.
  7.  $v_c/\omega$ , the normalized beam-plasma collision frequency.
  8.  $B = \gamma b'$ , the space-charge force range parameter, where  $\gamma \cong \beta$  is the radial propagation constant and  $b'$  is the electron stream radius.
  9.  $\omega_p/\omega$ , the normalized plasma frequency for the beam electrons.
- The method of solution and the results obtained will be discussed in Chapter V.

#### 4.1 Introduction

From traveling-wave tube theory it is known that the radial variations of the circuit and space-charge fields tend to reduce the gain and the conversion efficiency. It is therefore desirable to take these effects into account theoretically in order to obtain better agreement with experimental observations. In this analysis the plasma "circuit" equation will be considered to be quasi-two-dimensional in nature. The circuit field term will be used directly from the one-dimensional analysis described in the previous chapter. The radial variation in the electric field will be taken into account by defining a weighting function which is proportional to the radial variation of the longitudinal electric field. It will be shown that for the frequency range of interest the effective circuit field at the electron stream is reduced from its value at the plasma edge.

Since the electron density and hence the plasma frequency in a typical electron stream used in amplifiers of the type considered in this study is very much less than in the plasma, the electron cyclotron frequency due to the applied magnetic field needed to focus the stream is usually considerably greater than the plasma frequency of the beam electrons. Thus many analyses assume to a fairly good approximation that the magnetic field is infinite as far as the beam electrons are concerned.<sup>67</sup> This in effect neglects the transverse motion of the stream electrons. In the present analysis this restriction will not be

made, and the electron stream will be treated essentially in two dimensions, i.e., the circuit RF potential and the space-charge potential are assumed to vary in the radial direction but are axisymmetric. The action of a finite axial magnetic focusing field will be included by considering electron motion, without bunching, around the axis. This inclusion of the magnetic field does not complicate the equations unduly; it merely introduces the angular velocity  $u_\phi$ . The coordinates of the model to be considered are shown in Fig. 4.1 and the analysis follows that of Rowe.<sup>46</sup>

The normalized independent space and phase Lagrangian variables are defined as

$$y_1 \triangleq \frac{C_1 \omega z}{u_0} = 2\pi C_1 N_s, \quad (4.1)$$

$$x \triangleq \frac{C_1 \omega r}{u_0}, \quad (4.2)$$

$$x_0 \triangleq \frac{C_1 \omega r_0}{u_0} \quad (4.3)$$

and

$$\Phi_{01} \triangleq \frac{\omega z_0}{u_0} = -\omega t_0, \quad (4.4)$$

where  $r_0$  is the mean radius of a charge ring at  $z = 0$  and the other quantities are as defined before. The RF voltage of the  $n$ th harmonic along the interaction region is written as the product of slowly varying amplitude and phase functions. Thus

$$V(y_1, x, \Phi_{01}) = \text{Re} \sum_{n=1}^{\infty} \left( \frac{Z_{01} I_0}{C_1} A_n(y_1) \psi_n(x) e^{-j\Phi_n + j\theta_{xn}} \right), \quad (4.5)$$

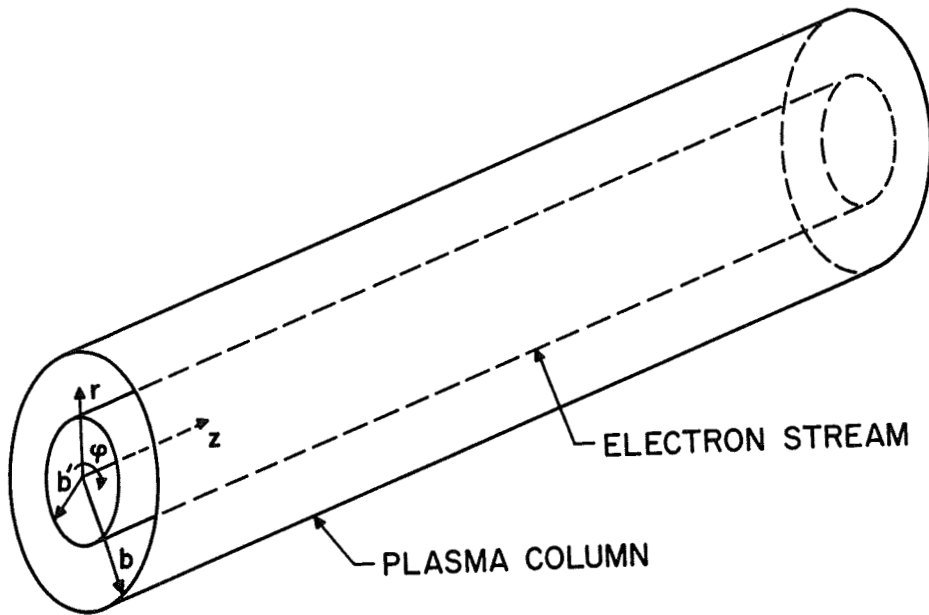


FIG. 4.1 MODEL FOR AN ELECTRON STREAM PASSING THROUGH A PLASMA COLUMN.

where it is assumed that  $\theta_{xn}$  is the radial phase shift and

$$\Phi_n = \Phi_n(y_1, x_0, \Phi_{o1}) = \frac{ny_1}{C_1} - n\omega t - \theta_n(y_1) \quad (4.6)$$

or

$$y_1 = \frac{C_1}{n} \left( \Phi_n(y_1, x_0, \Phi_{o1}) + \theta_n(y_1) + n\omega t \right) . \quad (4.7)$$

The quantity  $\psi_n(x)$  of Eq. 4.5 is proportional to the radial variation of the longitudinal electric field across the plasma column. At the edge of the plasma column,  $r = b$ , one may choose by an appropriate normalization that

$$\psi_n(b) = 1 . \quad (4.8)$$

#### 4.2 Variation of the Electric Field Across the Plasma Column

The longitudinal electric field variation inside a plasma column of uniform density is given by

$$E_{zn}(r) = A_n J_0(T_{pn} r) , \quad (4.9)$$

which has been obtained previously. Here  $J_0$  is the zero-order Bessel function of the first kind,  $T_{pn}$  is the radial propagation constant for the nth harmonic and  $A_n$  is an arbitrary constant. Recall that the radial propagation constant is given by

$$T_{pn}^2 = -k^2 \frac{\kappa_{||}}{\kappa_{\perp}} = -k^2 \left[ \frac{1 - \frac{\left(\frac{\omega_p}{n\omega}\right)^2}{\left(1 - j \frac{\nu}{n\omega}\right)}}{1 - \frac{\left(\frac{\omega_p}{n\omega}\right)^2 \left(1 - j \frac{\nu}{n\omega}\right)}{\left(1 - j \frac{\nu}{n\omega}\right)^2 - \left(\frac{\omega_c}{n\omega}\right)^2}} \right] . \quad (4.10)$$

Solution of the dispersion equation for a plasma column yields the  $\omega$ - $\beta$  diagram shown in Fig. 4.2. The cyclotron frequency is chosen to be below  $\omega_p$  because in a typical device operating in the 10-cm wavelength region a magnetic field ranging from a few hundred gauss to at most one kilogauss ( $f_c \cong 2.8$  GHz) is usually adequate for focusing the electron stream. For frequencies in Regions I and II of Fig. 4.2 a forward wave can propagate along the plasma column so that a traveling-wave tube type of interaction may take place between the wave on the plasma column and the electron beam space-charge waves. For frequencies in Region IV a backward wave can propagate along the plasma column, which may result in backward-wave amplification or backward-wave oscillation in the presence of an electron beam. The plasma waveguide is cut off for frequencies in Region III and does not support a wave. The dielectric constant is negative in this range. Therefore the plasma presents an inductive impedance to the electron beam. The electron beam traveling through the plasma column acts in cooperation with the plasma "circuit," which alone cannot support a propagating slow wave. Thus any charge bunching on the beam is enhanced, as in a multicavity klystron or in an Easitron<sup>68</sup> amplifier. This enhancement takes place through the induced charges formed in the plasma by the alternating fields of the modulated electron beam. The beam electrons are slowed down by the fields of these charges giving up some of their energy.

Solution of Eqs. 4.9 and 4.10 shows that  $E_{zn}$  has the distributions shown in Fig. 4.3 for different values of  $\omega$ . In the region between the



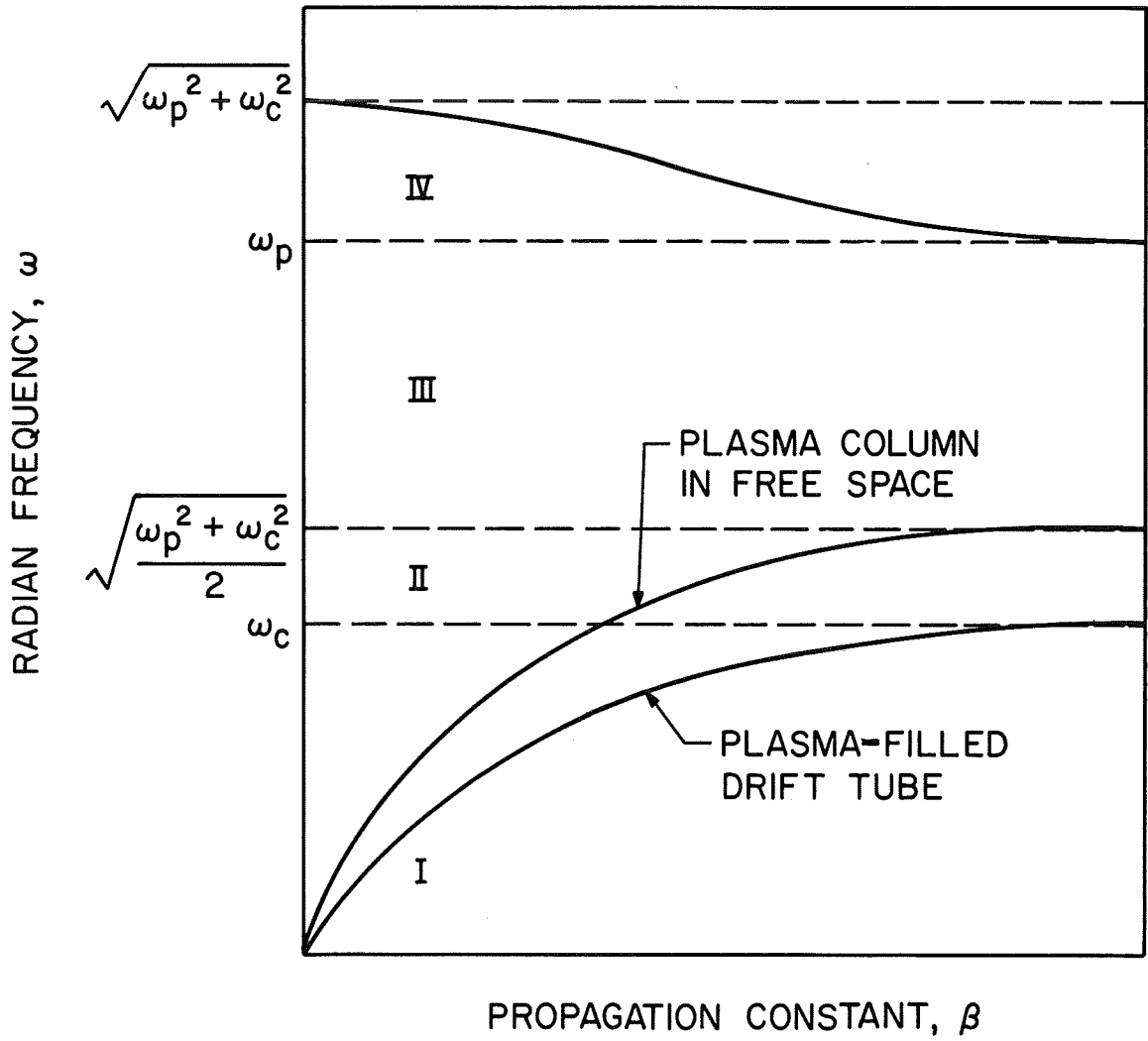


FIG. 4.2 DISPERSION CURVES FOR A PLASMA COLUMN.

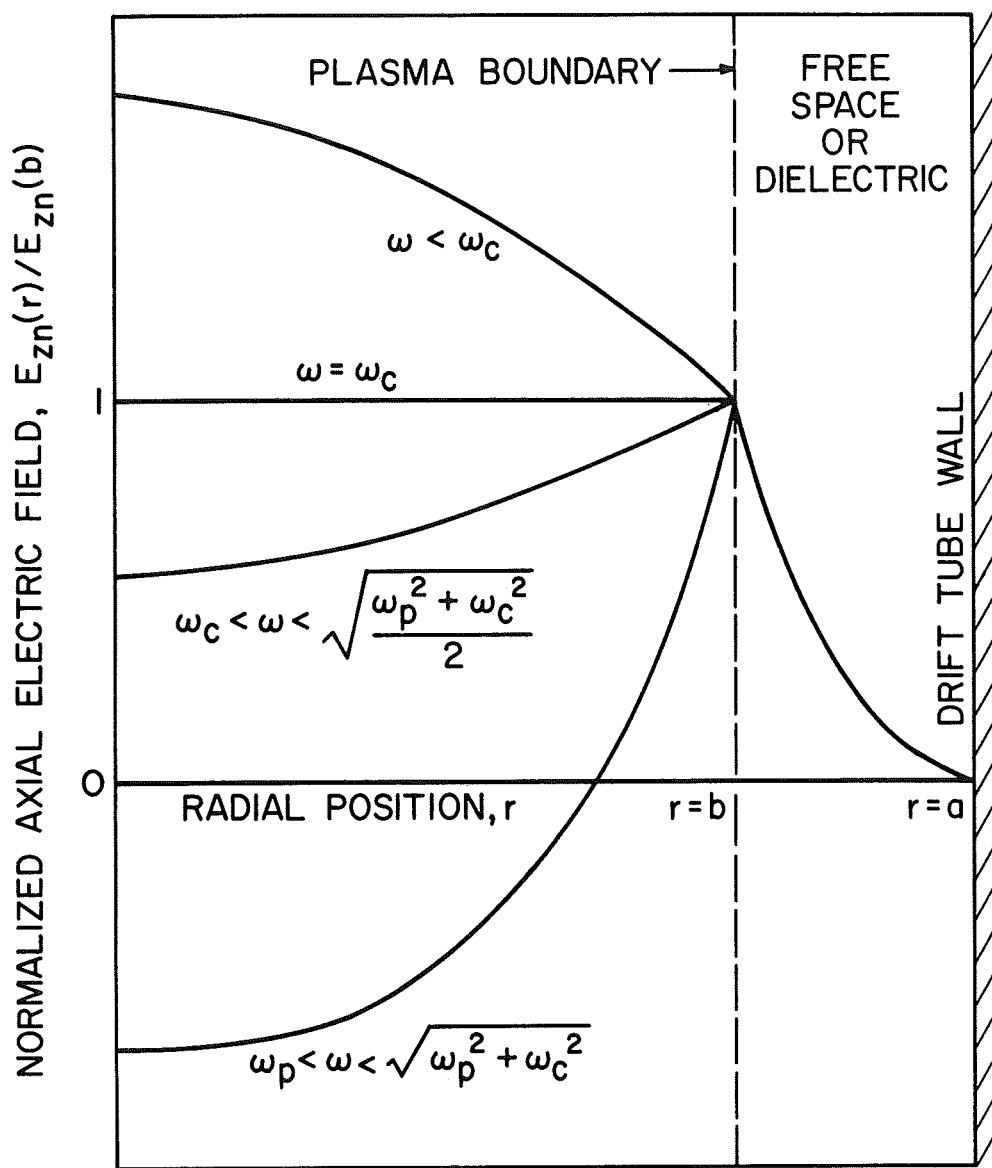


FIG. 4.3 AXIAL ELECTRIC FIELD VARIATION AS A FUNCTION OF RADIUS  
FOR THE CASE OF  $\omega_c < \omega_p$ .

plasma boundary at  $r = b$  and the conducting wall at  $r = a$  the fields go to zero exponentially in all cases, as shown. In the plasma region the field distribution is uniform for  $T_{pn} = 0$ , which occurs at  $\omega_c = \omega$ . By Eq. 4.10, for  $\nu = 0$  and  $k = \beta$ ,  $T_{pn}$  is either a positive real or a positive imaginary number. For  $T_{pn}$  real the RF field is highest along the axis of the plasma column and decreases as the Bessel function  $J_0$ . This corresponds to Region I of Fig. 4.2. If  $T_{pn}$  is imaginary, the RF field is lowest along the axis and increases as the modified Bessel function,  $I_0$ , due to the fact that

$$J_0(jT_{pn}r) = I_0(T_{pn}r) \quad (4.11)$$

This corresponds to Region II of Fig. 4.2. The wave propagating along the plasma column in this case is known as a surface wave, which has a resonance ( $\beta \rightarrow \infty$ ) in the range

$$\omega_c < \omega < \sqrt{\frac{\omega_p^2 + \omega_c^2}{2}}, \quad (4.12)$$

as was discussed in Chapter II. The resonance frequency in this range is determined by the geometry and the effective dielectric constant of the material surrounding the plasma column.

If the electric field distribution across the plasma column is known, it is straightforward to determine an appropriate field weighting function,  $\psi_n$ . For the case of a solid electron stream with radius  $r_{m1}$ , equal to or smaller than the radius  $b$  of the plasma column, the weighting function taking account of radial circuit field variations is

denoted by  $\psi_n(r_{m1})$ . Normalizing with respect to the electric field at the plasma column edge one obtains

$$\psi_n(r_{m1}) = \frac{\sqrt{J_0^2(T_{pn} r_{m1}) + J_1^2(T_{pn} r_{m1})}}{J_0(T_{pn} b)} . \quad (4.13)$$

On the other hand, for a thin, hollow electron stream with mean radius  $r_{m2} < b$ , the weighting function taking radial field variations into account is denoted by

$$\psi_n(r_{m2}) = \frac{J_0(T_{pn} r_{m2})}{J_0(T_{pn} b)} . \quad (4.14)$$

In the analysis to follow the appropriate field weighting function,  $\psi_n(r_m)$ , given by Eqs. 4.13 or 4.14 will be used. Note that  $T_{pn}$  and hence  $\psi_n$  must be found through a solution of the dispersion equation of the plasma column for the harmonic number  $n$  of interest.

### 4.3 Derivation of the Circuit Equations

A dependent axial velocity variable is defined as in the one-dimensional case. Here, however, radial and angular velocity variables are also needed. Thus

$$u_z = \frac{dz}{dt} = \frac{u_o}{C_1 \omega} \frac{dy_1}{dt} \triangleq u_o \left( 1 + 2C_1 u_y(y_1, x_o, \Phi_{o1}) \right) , \quad (4.15)$$

$$u_r = \frac{dr}{dt} = \frac{u_o}{C_1 \omega} \frac{dx}{dt} \triangleq 2C_1 u_o u_x(y_1, x_o, \Phi_{o1}) \quad (4.16)$$

and

$$u_\phi = \frac{d\phi}{dt} \triangleq 2C_1 u_o \frac{1}{r} u_\phi(y_1, x_o, \Phi_{o1}) . \quad (4.17)$$

From Eq. 4.15 it follows that

$$\frac{dy_1}{dt} = \frac{C_1 \omega}{u_o} \frac{dz}{dt} = C_1 \omega \left( 1 + 2C_1 u_y(y_1, x_o, \Phi_{o1}) \right) . \quad (4.18)$$

Also, from Eq. 4.7

$$\frac{dy_1}{dt} = \frac{C_1}{n} \left( \frac{d\theta_n}{dy_1} \frac{dy_1}{dt} + n\omega + \frac{\partial \Phi_n}{\partial y_1} \frac{dy_1}{dt} \right) . \quad (4.19)$$

Equating Eqs. 4.18 and 4.19 one obtains

$$2C_1 n\omega u_y = \frac{d\theta_n}{dy_1} \frac{dy_1}{dt} + \frac{\partial \Phi_n}{\partial y_1} \frac{dy_1}{dt} ,$$

or in view of Eq. 4.18,

$$2C_1 n\omega u_y = \left( \frac{d\theta_n}{dy_1} + \frac{\partial \Phi_n}{\partial y_1} \right) C_1 \omega (1 + 2C_1 u_y) .$$

After simplification,

$$\frac{d\theta_n(y_1)}{dy_1} + \frac{\partial \Phi_n(y_1, x_o, \Phi_{o1})}{\partial y_1} = \frac{2nu_y(y_1, x_o, \Phi_{o1})}{1 + 2C_1 u_y(y_1, x_o, \Phi_{o1})} . \quad (4.20)$$

This expression is one of the working equations in the two-dimensional large-signal analysis.

The dependent variable  $x$  is a function of  $y_1, x_o$  and  $\Phi_{o1}$ . A general expression for  $x$  may be written as

$$x(y_1, x_0, \Phi_{01}) = x_0 + \int_0^t \frac{dx}{dt} dt = x_0 + \int_0^z \frac{dx}{dt} \cdot \frac{dz}{u_0 [1 + 2C_1 u_y(y_1, x_0, \Phi_{01})]} , \quad (4.21)$$

which becomes, when Eq. 4.16 is substituted under the integral sign,

$$x(y_1, x_0, \Phi_{01}) = x_0 + 2C_1 \int_0^{y_1} \frac{u_x(y_1, x_0, \Phi_{01}) dy_1}{1 + 2C_1 u_y(y_1, x_0, \Phi_{01})} . \quad (4.22)$$

Equation 4.22 constitutes another one of the working equations.

The charge  $\rho_0$  entering the interaction region is conserved throughout so that for any point  $(z, r)$  the continuity of charge equation becomes (axial symmetry is assumed)

$$\rho r dr dz = \rho_0 r_0 dr_0 dz_0 . \quad (4.23)$$

Define a linear charge density  $\sigma$  at a given position  $z$  by

$$\sigma_n = 2\pi \int_0^{b'} \psi_n(b') \rho r dr , \quad (4.24)$$

where  $b'$  is the radius of the solid cylindrical electron stream considered here\* and  $\psi_n$  is given by Eq. 4.13. By Eq. 4.23 this can be written as

$$\sigma_n = 2\pi \int_0^{b'} \psi_n(b') \rho_0 r_0 \left| \frac{dz_0}{dz} \right| dr_0 , \quad (4.25)$$

where the entering dc charge density  $\rho_0$  is given by

\* For a discussion on the appropriate radius to use see Sec. 4.6.

$$\rho_o = - \frac{I_o}{\pi b'^2 u_o} . \quad (4.26)$$

The quantity  $|\partial z_o / \partial z|$  represents the electron phase displacement and is written as in the one-dimensional case as

$$\left| \frac{\partial z_o}{\partial z} \right| = \left| \frac{\frac{\partial z_o}{\partial t}}{\frac{\partial z}{\partial t}} \right| .$$

From Eq. 4.15

$$\frac{\partial z}{\partial t} = u_o \left( 1 + 2C_1 u_y(y_1, x_o, \Phi_{o1}) \right) .$$

Also, note that

$$\frac{\partial z_o}{\partial t} = \frac{\partial z_o}{\partial \Phi_{o1}} \frac{\partial \Phi_{o1}}{\partial \Phi_n} \frac{\partial \Phi_n}{\partial t} = -u_o n \frac{\partial \Phi_{o1}}{\partial \Phi_n} .$$

Thus the electron phase displacement becomes in Lagrangian variables

$$\left| \frac{\partial z_o}{\partial z} \right| = \left| \frac{\partial \Phi_{o1}}{\partial \Phi_n} \right| \frac{n}{1 + 2C_1 u_y(y_1, x_o, \Phi_{o1})} . \quad (4.27)$$

Substituting Eq. 4.27 into Eq. 4.25 and simplifying

$$\sigma_n = - \frac{2I_o n}{b'^2 u_o} \int_0^{b'} \left| \frac{\partial \Phi_{o1}}{\partial \Phi_n} \right| \frac{\psi_n(b') r_o}{1 + 2C_1 u_y(y_1, x_o, \Phi_{o1})} dr_o .$$

Defining a normalized stream radius by

$$x_{b'} = \frac{C \omega b'}{u_o} , \quad (4.28)$$

and making use of Eq. 4.3, one obtains

$$\sigma_n = - \frac{2I_o n}{x_{b',u_o}^2} \int_0^{x_{b'}} \left| \frac{\partial \Phi_{o1}}{\partial \Phi_n} \right| \frac{\psi_n(b') x_o dx_o}{1 + 2C_{1y}(y_1, x_o, \Phi_{o1})} . \quad (4.29)$$

The linear charge density may be expanded into a Fourier series of the phase variable  $\Phi_n$ . Thus

$$\sigma(z,r,t) = \sum_{n=1}^{\infty} \left( c_n \sin(-\Phi_n) + d_n \cos(-\Phi_n) \right) , \quad (4.30)$$

where the coefficients  $c_n$  and  $d_n$  are given by

$$c_n = \frac{1}{n\pi L} \int_0^{2\pi L} \int_0^{b'} \psi_n(b') \sigma_n(z,r,\Phi_n) \sin(-\Phi_n) r dr d\Phi_n$$

and

$$d_n = \frac{1}{n\pi L} \int_0^{2\pi L} \int_0^{b'} \psi_n(b') \sigma_n(z,r,\Phi_n) \cos(-\Phi_n) r dr d\Phi_n .$$

If these coefficients are substituted into Eq. 4.30, one obtains

$$\sigma(z,r,t) = \sum_{n=1}^{\infty} \frac{1}{n\pi L} \left[ \left( \int_0^{2\pi L} \int_0^{b'} \psi_n(b') \sigma_n(z,r,\Phi_n) \sin(-\Phi_n) r dr d\Phi_n \right) \cdot \sin(-\Phi_n) + \left( \int_0^{2\pi L} \int_0^{b'} \psi_n(b') \sigma_n(z,r,\Phi_n) \cos(-\Phi_n) r dr d\Phi_n \right) \cos(-\Phi_n) \right] .$$

Since  $\cos(-\Phi_n) + j \sin(-\Phi_n) = \exp(-j\Phi_n)$ , this expression may be expanded and then simplified to yield



$$\sigma(z,r,t) = \text{Re} \left[ \sum_{n=1}^{\infty} \frac{1}{n\pi L} e^{-j\Phi_n} \left( j \int_0^{2\pi L} \int_0^{b'} \psi_n(b') \sigma_n(z,r,\Phi_n) \cdot \sin \Phi_n r \, dr \, d\Phi_n + \int_0^{2\pi L} \int_0^{b'} \psi_n(b') \sigma_n(z,r,\Phi_n) \cos \Phi_n r \, dr \, d\Phi_n \right) \right] .$$

Substituting from the conservation of charge equation, Eq. 4.29, one obtains

$$\sigma(z,r,t) = -\text{Re} \left[ \frac{2I_o}{\pi L u_o x_{b'}^2} \sum_{n=1}^{\infty} e^{-j\Phi_n} \left( \int_0^{2\pi L} \int_0^{x_{b'}} \frac{\psi_n(b') \cos \Phi_n' x_o' \, dx_o' \, d\Phi_{o1}'}{1 + 2C_1 u_1(y_1, x_o', \Phi_{o1}') } + j \int_0^{2\pi L} \int_0^{x_{b'}} \frac{\psi_n(b') \sin \Phi_n' x_o' \, dx_o' \, d\Phi_{o1}'}{1 + 2C_1 u_1(y_1, x_o', \Phi_{o1}') } \right) \right] , \quad (4.31)$$

where the prime denotes the variable of integration. Note that Eq. 4.31 may be written as

$$\sigma_n = \sigma_{nc} \cos \Phi_n + \sigma_{ns} \sin \Phi_n , \quad (4.32)$$

where

$$\sigma_{nc} = - \frac{2I_o}{\pi L u_o x_{b'}^2} \int_0^{x_{b'}} \int_0^{2\pi L} \frac{\psi_n(b') \cos \Phi_n' x_o' \, dx_o' \, d\Phi_{o1}'}{1 + 2C_1 u_1(y_1, x_o', \Phi_{o1}') } \quad (4.33)$$

and

$$\sigma_{ns} = - \frac{2I_o}{\pi L u_o x_{b'}^2} \int_0^{x_{b'}} \int_0^{2\pi L} \frac{\psi_n(b') \sin \Phi_n' x_o' \, dx_o' \, d\Phi_{o1}'}{1 + 2C_1 u_1(y_1, x_o', \Phi_{o1}') } . \quad (4.34)$$

The "circuit" equation which describes the RF voltage variation along the equivalent transmission line may be written in general as follows:

$$\nabla^2 V_n(z,r,t) - \frac{1}{v_{on}^2} \frac{\partial^2 V_n(z,r,t)}{\partial t^2} = - \frac{Z_{on}}{v_{on}} \frac{\partial^2 \sigma_n(z,r,t)}{\partial t^2} . \quad (4.35)$$

The first term on the left-hand side for the present case, because of the quasi-two-dimensional treatment, simply becomes  $\partial^2 V_n(z,r,t)/\partial z^2$ .

Thus Eq. 4.35 is

$$\frac{\partial^2 V_n(z,r,t)}{\partial z^2} - \frac{1}{v_{on}^2} \frac{\partial^2 V_n(z,r,t)}{\partial t^2} = - \frac{Z_{on}}{v_{on}} \frac{\partial^2 \sigma_n(z,r,t)}{\partial t^2} . \quad (4.36)$$

The potential function was defined in Eq. 4.5. From Eq. 4.6 one finds that

$$\frac{\partial \Phi_n(y_1, x_0, \Phi_{01})}{\partial t} = -n\omega \quad (4.37)$$

and

$$\frac{\partial \Phi_n(y_1, x_0, \Phi_{01})}{\partial y_1} = \frac{n}{C_1} - \frac{d\theta_n(y_1)}{dy_1} . \quad (4.38)$$

The following derivatives of Eq. 4.5, which may be simplified by Eqs. 4.37 and 4.38, are needed for substitution into Eq. 4.36. Note that  $\theta_{xn} = 0$  for the quasi-two-dimensional treatment of the circuit equation.\*

$$\frac{\partial V}{\partial z} = \frac{Z_{o1} I_o}{C_1} \operatorname{Re} \sum_{n=1}^{\infty} \left[ \frac{dA_n(y_1)}{dz} \psi_n(b) e^{-j\Phi_n} - jA_n(y_1) \psi_n(b) \cdot \left( \frac{\omega}{u_o} - \frac{d\theta_n}{dz} \right) e^{-j\Phi_n} \right] , \quad (4.39)$$

\* For a discussion on the appropriate form of the weighting function see Sec. 4.6.

$$\begin{aligned} \frac{\partial^2 V}{\partial z^2} = & \frac{Z_{o1} I_o}{C_1} \operatorname{Re} \sum_{n=1}^{\infty} \left[ \frac{d^2 A_n(y_1)}{dz^2} \psi_n(b) e^{-j\Phi_n} - 2j \frac{dA_n(y_1)}{dz} \psi_n(b) \right. \\ & \cdot \left( \frac{\omega}{u_o} - \frac{d\theta_n}{dz} \right) e^{-j\Phi_n} + j \frac{d^2 \theta_n}{dz^2} A_n(y_1) \psi_n(b) e^{-j\Phi_n} - A_n(y_1) \psi_n(b) \\ & \left. \cdot \left( \frac{\omega}{u_o} - \frac{d\theta_n}{dz} \right)^2 e^{-j\Phi_n} \right] , \quad (4.40) \end{aligned}$$

$$\frac{\partial V}{\partial t} = \frac{Z_{o1} I_o}{C_1} \operatorname{Re} \sum_{n=1}^{\infty} \left( j n \omega A_n(y_1) \psi_n(b) e^{-j\Phi_n} \right) \quad (4.41)$$

and

$$\frac{\partial^2 V}{\partial t^2} = - \frac{Z_{o1} I_o}{C_1} \operatorname{Re} \sum_{n=1}^{\infty} \left( n^2 \omega^2 A_n(y_1) \psi_n(b) e^{-j\Phi_n} \right) . \quad (4.42)$$

Note that the above expressions are valid at the plasma column edge.

The right-hand side of Eq. 4.36 requires the second time derivative of the linear charge density. From Eq. 4.32,

$$\frac{\partial \sigma_n}{\partial t} = n \omega \sigma_{nc} \sin \Phi_n - n \omega \sigma_{ns} \cos \Phi_n \quad (4.43)$$

and

$$\frac{\partial^2 \sigma_n}{\partial t^2} = -n^2 \omega^2 \sigma_{nc} \cos \Phi_n - n^2 \omega^2 \sigma_{ns} \sin \Phi_n . \quad (4.44)$$

Substituting Eqs. 4.40, 4.42 and 4.44 into Eq. 4.36 and rearranging, one obtains

$$\begin{aligned}
 & \sum_{n=1}^{\infty} \psi_n(b) \left\{ \frac{d^2 A_n(y_1)}{dy_1^2} + A_n(y_1) \left[ \frac{n^2}{C_1^2} \left( \frac{u_o}{v_{on}} \right)^2 - \left( \frac{n}{C_1} - \frac{d\theta_n(y_1)}{dy_1} \right)^2 \right] \right\} \cos \Phi_n \\
 & + \sum_{n=1}^{\infty} \psi_n(b) \left[ A_n(y_1) n \frac{d^2 \theta_n(y_1)}{dy_1^2} + 2 \frac{dA_n(y_1)}{dy_1} \left( \frac{d\theta_n(y_1)}{dy_1} - \frac{n}{C_1} \right) \right] \sin \Phi_n \\
 & = - \sum_{n=1}^{\infty} \frac{2n^2 \left( \frac{u_o}{v_{on}} \right) \left( \frac{Z_{on}}{Z_{o1}} \right)}{\pi LC_1 x_b^2} \left( \int_0^{x_b'} \int_0^{2\pi L} \frac{\psi_n(b') \cos \Phi_n' x'_o dx'_o d\Phi'_{o1}}{1 + 2C_1 u(y_1, x'_o, \Phi'_{o1})} \cos \Phi_n \right. \\
 & \quad \left. + \int_0^{x_b'} \int_0^{2\pi L} \frac{\psi_n(b') \sin \Phi_n' x'_o dx'_o d\Phi'_{o1}}{1 + 2C_1 u(y_1, x'_o, \Phi'_{o1})} \sin \Phi_n \right) .
 \end{aligned}$$

Equating the coefficients of  $\sin \Phi_n$  and  $\cos \Phi_n$  separately on each side of the equal sign and noting that  $\psi_n(b) = 1$  by Eq. 4.8, one obtains the following two circuit equations:

$$\begin{aligned}
 & \frac{d^2 A_n(y_1)}{dy_1^2} + A_n(y_1) \left[ \frac{n^2}{C_1^2} \left( \frac{u_o}{v_{on}} \right)^2 - \left( \frac{n}{C_1} - \frac{d\theta_n(y_1)}{dy_1} \right)^2 \right] \\
 & = - \frac{2n^2 \left( \frac{u_o}{v_{on}} \right) \left( \frac{Z_{on}}{Z_{o1}} \right)}{\pi LC_1 x_b^2} \int_0^{x_b'} \int_0^{2\pi L} \frac{\psi_n(b') \cos \Phi_n' x'_o dx'_o d\Phi'_{o1}}{1 + 2C_1 u(y_1, x'_o, \Phi'_{o1})} \quad (4.45)
 \end{aligned}$$

and

$$A_n(y_1) \frac{d^2\theta_n(y_1)}{dy_1^2} + 2 \frac{dA_n(y_1)}{dy_1} \left( \frac{d\theta_n(y_1)}{dy_1} - \frac{n}{C_1} \right) =$$

$$- \frac{2n^2 \left( \frac{u_o}{v_{on}} \right) \left( \frac{Z_{on}}{Z_{o1}} \right)}{\pi L C_1 x_{b'}^2} \int_0^{x_{b'}} \int_0^{2\pi L} \frac{\psi_n(b') \sin \Phi_n' x_o' dx_o' d\Phi_{o1}'}{1 + 2C_1 u_y(y_1, x_o', \Phi_{o1}')} . \quad (4.46)$$

These are two more working equations in the large-signal analysis. It should be noted that the left-hand sides of Eqs. 4.45 and 4.46 are the same as in the one-dimensional case, while the driving terms on the right-hand sides are changed due to the modified coupling of the electron stream in a radially varying electric field.

#### 4.4 Derivation of the Force Equations

The Lorentz force equations are to be formulated now so as to include the effects of the electron stream and the space-charge forces within the stream on the waves propagating along the plasma column. As usual, low enough velocities are assumed so that relativistic effects are negligible. Hence RF magnetic fields need not be considered. In this two-dimensional analysis angular bunching of the beam is neglected, but the action of a finite axial magnetic field is included.

The various components of the Lorentz force equation are written as follows if the magnetic field,  $B_o$ , is assumed to be entirely axially directed in the RF interaction region:

$$\frac{d^2z}{dt^2} = \eta \left( \frac{\partial V_{nc}(z,r,t)}{\partial z} + \frac{\partial V_{nsc-z}(z,r,t)}{\partial z} \right) , \quad (4.47)$$

$$\frac{d^2 r}{dt^2} - r \left( \frac{d\phi}{dt} \right)^2 = \eta \left( -E_{o-r} + \frac{\partial V_{nsc-r}(z,r,t)}{\partial r} - B_o r \frac{d\phi}{dt} \right) \quad (4.48)$$

and

$$\frac{1}{r} \frac{d}{dt} \left( r^2 \frac{d\phi}{dt} \right) = \eta B_o \frac{dr}{dt} . \quad (4.49)$$

$E_{o-r}$  represents the radial field due to the dc space-charge. From a solution of Poisson's equation in cylindrical coordinates it may be found that

$$E_{o-r} = \frac{\rho_o}{2\epsilon_o} \frac{r_o^2}{r} .$$

Thus,

$$E_{o-r} = - \frac{1}{\eta} \frac{\omega_b^2}{2} \frac{r_o^2}{r} , \quad (4.50)$$

where  $\omega_b$  is the plasma frequency for the beam electrons. Introducing the normalized variables  $y_1$  and  $x$  from Eqs. 4.1 and 4.2 and defining the cyclotron frequency by  $\omega_c \triangleq \eta B_o$  as before, the force equations become

$$\frac{d^2 y_1}{dt^2} = \eta \left[ \left( \frac{C \omega}{u_o} \right)^2 \frac{\partial V_{nc}(y_1, x_o, \phi_{o1})}{\partial y_1} - \frac{C \omega}{u_o} E_{nsc-y} \right] ,$$

$$\frac{d^2 x}{dt^2} - x \left( \frac{d\phi}{dt} \right)^2 = \eta \left( - \frac{C \omega}{u_o} \frac{1}{\eta} \frac{\omega_b^2}{2} \frac{x_o^2}{x} \frac{u_o}{C \omega} - \frac{C \omega}{u_o} E_{nsc-x} - \frac{\omega_c}{\eta} x \frac{d\phi}{dt} \right)^*$$

and

$$\frac{1}{x} \frac{d}{dt} \left( x^2 \cdot 2C_1^2 \omega \frac{1}{x} u_\phi \right) = \omega_c \frac{dx}{dt} .$$

\*

There are no additional terms in the radial force equation because of the quasi-two-dimensional assumption. See Sec. 4.6.

Note that

$$\frac{d^2y_1}{dt^2} = \frac{dv_y}{dt} = \frac{\partial v_y}{\partial y_1} \frac{dy_1}{dt} ,$$

which, in view of Eq. 4.15 becomes

$$\frac{d^2y_1}{dt^2} = 2C_1^2 \omega \frac{\partial u_y}{\partial y_1} \frac{dy_1}{dt} .$$

Substituting from Eq. 4.18 for  $dy_1/dt$  yields

$$\frac{d^2y_1}{dt^2} = 2C_1^3 \omega^2 \frac{\partial u_y}{\partial y_1} (1 + 2C_1 u_y) . \quad (4.51)$$

Similarly one obtains

$$\frac{d^2x_1}{dt^2} = 2C_1^3 \omega^2 \frac{\partial u_x}{\partial y_1} (1 + 2C_1 u_y) . \quad (4.52)$$

Using the last two expressions, the force equations take the following form:

$$2C_1^3 \omega^2 \frac{\partial u_y}{\partial y_1} (1 + 2C_1 u_y) = \eta \left( \frac{C_1 \omega}{u_0} \right)^2 \frac{\partial V_{nc}(y_1, x_0, \Phi_{01})}{\partial y_1} - \eta \left( \frac{C_1 \omega}{u_0} \right) E_{nsc-y} ,$$

$$2C_1^3 \omega^2 \frac{\partial u_x}{\partial y_1} (1 + 2C_1 u_y) = 4 \frac{C_1^4 \omega^2}{x} u_\phi^2 + \frac{\omega_b^2}{2} \frac{x_0^2}{x} - \eta \left( \frac{C_1 \omega}{u_0} \right) E_{nsc-x} - 2\omega_c C_1^2 \omega u_\phi ,$$

$$2C_1^3 \omega^2 \frac{\partial u_\phi}{\partial y_1} (1 + 2C_1 u_y) = \omega_c \frac{dx}{dt} - \frac{2}{x} C_1^2 \omega u_\phi \frac{dx}{dt} .$$

Rearranging and substituting from Eq. 4.39 for  $(\partial V_{nc}/\partial y_1)$  one obtains the following:

$$\frac{\partial u_y}{\partial y_1} (1 + 2C_1 u_y) = \frac{\eta}{2u_0^2 C_1} \left( \frac{Z_{01} I_0}{C_1} \right) \sum_{n=1}^{\infty} \left[ \frac{dA_n(y_1)}{dy_1} \psi_n(b') \cos \Phi_n - A_n(y_1) \psi_n(b') \left( \frac{n}{C_1} - \frac{d\theta_n}{dy_1} \right) \sin \Phi_n \right] - \frac{\eta}{2C_1^2 \omega u_0} E_{nsc-y} ,$$

$$\frac{\partial u_x}{\partial y_1} (1 + 2C_1 u_y) = \frac{2C_1}{x} u_\phi^2 + \left( \frac{\omega_b}{\omega} \right)^2 \frac{1}{4C_1^3} \frac{x_0^2}{x} - \frac{\eta}{2C_1^2 \omega u_0} E_{nsc-x} - \frac{\omega_c}{C_1 \omega} u_\phi$$

and

$$\frac{\partial u_\phi}{\partial y_1} (1 + 2C_1 u_y) = \frac{\omega_c}{2C_1^3 \omega^2} \frac{dx}{dt} - \frac{2C_1^2 \omega}{2C_1^3 \omega^2 x} \frac{dx}{dt} u_\phi .$$

The space-charge field terms for the two-dimensional case are derived in Appendix C. They are

$$E_{nsc-y} = - \int_0^{x_b'} \left( \int_0^{2\pi L} \frac{C_1^2 \omega I_0}{u_0^2 \pi L \epsilon_0 x_b'^2 x_b'^2} \operatorname{sgn}(y_1 - y_1') F_{2-z} d\phi_{01}' \right) x_0' dx_0' \quad (4.53)$$

and

$$E_{nsc-x} = - \int_0^{x_b'} \left( \int_0^{2\pi L} \frac{C_1^2 \omega I_0}{u_0^2 \pi L \epsilon_0 x_b'^2 x_b'^2} F_{2-r} d\phi_{01}' \right) x_0' dx_0' . \quad (4.54)$$

The two-dimensional space-charge field weighting functions are defined by

$$F_{2-z} \triangleq \sum_{\ell=1}^{\infty} e^{-v_\ell |y_1 - y_1'|} \frac{J_0(v_\ell x_0') J_0(v_\ell x_0)}{[J_1(v_\ell x_b)]^2} \quad (4.55)$$

and



$$F_{2-r} \triangleq \sum_{\ell=1}^{\infty} e^{-v_{\ell} |y_1 - y_1'|} \frac{J_0(v_{\ell} x') J_1(v_{\ell} x)}{[J_1(v_{\ell} x_b)]^2} . \quad (4.56)$$

Equations 4.53 and 4.54 may be substituted into the force equations, which then become

$$\frac{\partial u_y}{\partial y_1} (1 + 2C_1 u_y) = \eta \frac{Z_{o1} I_o}{2u_o^2 C_1^2} \sum_{n=1}^{\infty} \left[ \frac{dA_n(y_1)}{dy_1} \psi_n(b') \cos \Phi_n - A_n(y_1) \psi_n(b') \left( \frac{n}{C_1} - \frac{d\theta_n}{dy_1} \right) \sin \Phi_n \right] + \frac{\eta u_o}{2C_1^2 u_o \omega} \frac{C_1^2 \omega I_o}{u_o^2 \pi L \epsilon_o x_b^2 x_b'^2} \int_0^{x_b'} \left( \int_0^{2\pi L} \text{sgn}(y_1 - y_1') \cdot F_{2-z} d\Phi'_{o1} \right) x'_o dx'_o ,$$

$$\frac{\partial u_x}{\partial y_1} (1 + 2C_1 u_y) = \frac{2C_1}{x} u_{\phi}^2 - \left( \frac{\omega_c}{\omega C_1} \right) u_{\phi} + \left( \frac{\omega_b}{\omega} \right)^2 \frac{1}{4C_1^3} \frac{x_o^2}{x} + \frac{\eta u_o}{2C_1^2 u_o \omega} \frac{C_1^2 \omega I_o}{u_o^2 \pi L \epsilon_o x_b^2 x_b'^2} \int_0^{x_b'} \left( \int_0^{2\pi L} F_{2-r} d\Phi'_{o1} \right) x'_o dx'_o$$

and

$$\frac{\partial u_{\phi}}{\partial y_1} (1 + 2C_1 u_y) = \frac{\omega_c}{2C_1^3 \omega^2} 2C_1^2 \omega u_x - \frac{1}{C_1 \omega x} u_{\phi} 2C_1^2 \omega u_x .$$

After further simplification one obtains the following final forms of the Lorentz force equations:

$$\begin{aligned} \frac{\partial u_y(y_1, x_0, \Phi_{01})}{\partial y_1} \left( 1 + 2C_1 u_y(y_1, x_0, \Phi_{01}) \right) &= \sum_{n=1}^{\infty} \left[ C_1 \psi_n(b') \frac{dA_n(y_1)}{dy_1} \cos \Phi_n \right. \\ &- A_n(y_1) \psi_n(b') \left( n - C_1 \frac{d\theta_n}{dy_1} \right) \sin \Phi_n \left. \right] - \frac{1}{2C_1^2 L x_b^2} \left( \frac{\omega_b}{\omega} \right)^2 \\ &\cdot \int_0^{x_b'} \left( \int_0^{2\pi L} \text{sgn}(y_1 - y_1') F_{2-z} d\Phi'_{01} \right) x'_0 dx'_0, \quad (4.57) \end{aligned}$$

$$\begin{aligned} \frac{\partial u_x(y_1, x_0, \Phi_{01})}{\partial y_1} \left( 1 + 2C_1 u_y(y_1, x_0, \Phi_{01}) \right) &= \frac{2C_1}{x} u_\varphi^2(y_1, x_0, \Phi_{01}) \\ &- \frac{1}{C_1} \left( \frac{\omega_c}{\omega} \right) u_\varphi(y_1, x_0, \Phi_{01}) + \left( \frac{\omega_b}{\omega} \right)^2 \frac{1}{4C_1^3} \frac{x_0^2}{x} - \frac{1}{2C_1^2 L x_b^2} \left( \frac{\omega_b}{\omega} \right)^2 \\ &\cdot \int_0^{x_b'} \left( \int_0^{2\pi L} F_{2-r} d\Phi'_{01} \right) x'_0 dx'_0 \quad (4.58) \end{aligned}$$

and

$$\begin{aligned} \frac{\partial u_\varphi(y_1, x_0, \Phi_{01})}{\partial y_1} \left( 1 + 2C_1 u_y(y_1, x_0, \Phi_{01}) \right) &= \frac{1}{C_1} \left( \frac{\omega_c}{\omega} \right) u_x(y_1, x_0, \Phi_{01}) \\ &- \frac{2C_1}{x} u_x(y_1, x_0, \Phi_{01}) u_\varphi(y_1, x_0, \Phi_{01}) \quad (4.59) \end{aligned}$$

It is possible to obtain a simpler form of the angular force equation from Busch's theorem.<sup>69</sup> It was assumed above that the magnetic field  $B_0$  is entirely axially directed throughout the interaction region. If the magnetic field at the electron beam cathode of radius  $r_c$  is  $B_c$ , then one may write

$$mr_o^2 \frac{d\phi}{dt} = \frac{e}{2\pi} \left( \pi r_o^2 B_o - \frac{r_o^2}{r^2} \pi r_c^2 B_c \right)$$

or

$$\frac{d\phi}{dt} = \frac{\omega_c}{2} \left( 1 - \frac{r_o^2}{r^2} \frac{r_c^2}{r_o^2} \frac{B_c}{B_o} \right) \quad (4.60)$$

If one defines

$$K^{1/2} \triangleq \frac{r_c^2}{r_o^2} \frac{B_c}{B_o} \quad , \quad (4.61)$$

then

$$\frac{d\phi}{dt} = \frac{\omega_c}{2} \left( 1 - \frac{r_o^2}{r^2} K^{1/2} \right) \quad (4.62)$$

Combining Eqs. 4.17 and 4.62 the following angular force equation is obtained:

$$\frac{2C_1 u_\phi}{x} = \frac{1}{2C_1} \left( \frac{\omega_c}{\omega} \right) \left[ 1 - \left( \frac{x_o}{x} \right)^2 K^{1/2} \right] \quad (4.63)$$

For the special case of constant magnetic field everywhere (immersed flow)  $K = 1$ . For shielded Brillouin flow, for which

$$\frac{d\phi}{dt} = \frac{\eta B_o}{2} \quad , \quad (4.64)$$

there is assumed to be no magnetic field at the beam cathode and  $K = 0$ .

If a fraction of the focusing field threads the cathode region, the beam electron trajectories ripple in going through the interaction region.

In practice this problem is overcome and balanced flow is obtained

by increasing the focusing field above the Brillouin value and placing a bucking coil around the gun region so as to reduce the fringing field.

In that case

$$K = 1 - 2 \left( \frac{\omega_b}{\omega_c} \right)^2 . \quad (4.65)$$

Solving Eq. 4.63 for  $u_\phi$  and substituting into Eq. 4.58, one obtains the following simplified form of the radial force equation:

$$\frac{\partial u_x(y_1, x_o, \Phi_{o1})}{\partial y_1} \left( 1 + 2C_1 u_y(y_1, x_o, \Phi_{o1}) \right) = - \frac{x}{8C_1^3} \left( \frac{\omega_c}{\omega} \right)^2 \left[ 1 - \left( \frac{x_o}{x} \right)^4 \right. \\ \left. \cdot K - 2 \left( \frac{\omega_b}{\omega} \right)^2 \left( \frac{x_o}{x} \right)^2 \right] - \frac{1}{2C_1^2 x_b^2} \left( \frac{\omega_b}{\omega} \right)^2 \int_0^{x_b'} \left( \int_0^{2\pi L} F_{z-r} d\Phi_{o1}' \right) x_o' dx_o' . \quad (4.66)$$

#### 4.5 Initial Conditions and Input Data

In the two-dimensional case it is in general necessary to solve seven equations (Eqs. 4.20, 4.22, 4.45, 4.46, 4.57, 4.58 and 4.59) in seven unknowns. The seven unknown quantities are the dependent variables  $A_n(y_1)$ ,  $\theta_n(y_1)$ ,  $\Phi_n(y_1, x_o, \Phi_{o1})$ ,  $x$ ,  $u_y(y_1, x_o, \Phi_{o1})$ ,  $u_x(y_1, x_o, \Phi_{o1})$  and  $u_\phi(y_1, x_o, \Phi_{o1})$ . These are given in terms of the independent variables  $y_1$ ,  $x_o$ , and  $\Phi_{o1}$ . The equations are solved just as in the one-dimensional case. It is again necessary to specify the initial conditions on the dependent variables. Thus at  $y_1 = 0$  the following conditions are required:

$$1. \quad A_n(0) = A_{no} . \quad (4.67)$$

$$2. \quad \theta_n(0) = 0 . \quad (4.68)$$

3.

$$\left. \frac{d\theta_n(y_1)}{dy_1} \right|_{y_1=0} = - \frac{n}{C_1} \left( \frac{u_o}{v_{o1}} - 1 \right) = -nb_n \left( \frac{Z_{onr}}{|Z_{o1}|} \right)^{1/3} . \quad (4.69)$$

$$4. \quad \left. \frac{dA_n(y_1)}{dy_1} \right|_{y_1=0} = 0, \quad (4.70)$$

for an unbunched stream. For a stream bunched in the longitudinal direction, but with negligible bunching in the radial direction,

$$\left. \frac{dA_n(y_1)}{dy_1} \right|_{y_1=0} = n \left( \frac{Z_{onr}}{|Z_{o1}|} \right) \sin \alpha_n, \quad (4.71)$$

where  $\alpha_n$  is the injection phase angle defined in Chapter III.

$$5. \quad \Phi_n(0, x_o, \Phi_{o1, j}) = \frac{2\pi j}{m} \quad (j = 0, 1, 2, \dots, m), \quad (4.72)$$

where  $j$  denotes a particular charge group and the stream is unbunched so that the charge groups are injected uniformly distributed in phase over one cycle of the RF wave. Other distributions may be specified when taking prebunched streams into account. In the two-dimensional analysis one must not only take the entering charge per ring as distributed over  $\Phi_n$  into account, but one must also consider layers or rings of charge.

$$6. \quad u_y(0, x_o, \Phi_{o1, j}) = 0, \quad (4.73a)$$

$$u_x(0, x_o, \Phi_{o1, j}) = 0, \quad (4.73b)$$

$$u_\phi(0, x_o, \Phi_{o1, j}) = 0. \quad (4.73c)$$

These expressions state that the RF velocity components of the  $j$ th charge group are zero for an unmodulated stream.

As in the one-dimensional case, the input data consists of  $n$ ,  $C_1$ ,  $b_1$ ,  $v_{on}/v_{o1}$ ,  $Z_{on}/|Z_{o1}|$ ,  $\gamma b'$  and  $\omega_b/\omega$ . Here, however, the axial magnetic field must be specified in the form of the normalized cyclotron

frequency,  $\omega_c/\omega$ . In addition, the equivalent circuit radius must be given by  $b/b'$  and the radial circuit field function,  $\psi_n(b')$ , must be specified.

#### 4.6 Discussion on the Quasi-Two-Dimensional Model Used

If the full two-dimensional treatment had been used for both the stream and the circuit there would appear additional terms in the radial force equations following Eq. 4.48 due to the differentiation of the circuit field expression with respect to  $r$ , and also  $\psi_n$  would be a function of  $x$  in the circuit equations. In that case one must use an expression for  $\psi(x)$  obtained from the field solution and depicted in Fig. 4.3.

As an alternative one could employ a two-dimensional treatment for the stream but subdivide the stream into layers and use that value of  $\psi(r)$  that is an average for that layer. One would then have to assume that the radial positions of the layers do not appreciably change during saturation. This is probably justified as long as the device is operated with a magnetic field greater than 50 percent above the Brillouin field. In practice this is usually the case.

As a third alternative one could take an effective value for the field across the beam in accordance with Eq. 4.13. The same restrictions as in the previous case apply. This case was carried through in the derivation of the equations of this chapter.

### 5.1 Introduction

Due to the complexity of the large-signal equations derived in Chapters III and IV, it is necessary to solve them on a digital computer. The two circuit equations for each harmonic can be used to eliminate the voltage amplitude in favor of the phase variable. The force equations and the velocity-phase equations allow the calculation of the electron velocities and the phases. Once the phases are known, the amplitudes can then be calculated readily.

Since the wave amplitude at the end of a beam-plasma interaction region is not a priori known for a given input signal, this large-signal analysis is treated as an initial value problem. The working equations must be written in difference form to be suitable for machine computation. A set of discrete  $\Phi_{01,j}$  are chosen so that they represent the entering phases of a set of representative charge groups at the beginning of the interaction region. Numerical integration then proceeds in the y-direction in finite steps.

An important factor that affects the accuracy of computation and the execution time is the magnitude of the integration increment  $\Delta y$ . This quantity must be chosen to be small enough so that the change of any signal quantity over  $\Delta y$  is small. A difficulty with very small  $\Delta y$  is that in addition to increasing the computing time the round-off error increases due to the increased number of iterations and the limited number of significant figures used in the computer arithmetic. For

the results to be presented in the present chapter a value of  $\Delta y = 0.01$  was found to give reasonable accuracy.

## 5.2 Solution of the One-Dimensional Equations

The working equations for the one-dimensional case are Eqs. 3.16, 3.32, 3.33 and 3.40. If plasma particle collisions are to be included, the circuit equations, Eqs. 3.32 and 3.33, are replaced by Eqs. 3.59 and 3.60. The phase velocities and the impedance values occurring in these equations are known once the appropriate dispersion equation of Chapter II has been solved. The initial conditions and the input data required to solve the large-signal equations are listed in Section 3.5.

It should be noted that in a practical situation only a finite number of harmonics can be included in the analysis, due to the finite number of charge groups (500 in this particular case) distributed over phase that can be tracked through the interaction region. Thus in the working equations the summation is terminated at a value in accordance with this restriction. In particular, the one-dimensional program was set up to handle a fundamental input signal and up to three harmonics. Beam space-charge effects were not included in the one-dimensional case.

The experimental work of the present study to be described in Chapter VI was conducted in the L-band and S-band frequency regions. In order to insure that the calculations are useful for later comparison with experiment, some of the parameters needed for the computations will be calculated here and listed below in tabular form.

The fundamental RF frequency was chosen to be 1.7 GHz and the electron cyclotron frequency corresponded to a reasonable axial magnetic



field for focusing the electron beam. For the particular beam optics to be employed,  $B_o > B_{Br}$ , where the Brillouin magnetic field is given by<sup>69</sup>

$$B_{Br} = \left( \frac{\sqrt{2} I_o}{b'^2 \pi \eta^{3/2} \epsilon_o \sqrt{V_o}} \right)^{1/2} = \frac{8.3 \cdot 10^{-4}}{b'} \left( \frac{I_o}{\sqrt{V_o}} \right)^{1/2} . \quad (5.1)$$

In the present case  $B_{Br} \cong 200$  G. The effective dielectric constant of the space between the beam or the plasma column and the surrounding metallic cylinder determines the value of  $\kappa_e$ . It was chosen to be 2.0 for the present calculations. The plasma frequency was measured or calculated, as described in Chapter VI. There was no way of measuring the collision frequencies either directly or indirectly; hence they were calculated as follows.

The collision frequency between electrons and heavy particles in the plasma is given in rad/s by

$$\nu = 2\pi \frac{\bar{v}}{\lambda_e} , \quad (5.2)$$

where  $\bar{v}$  is the average electron velocity and  $\lambda_e$  is the mean-free-path of the electrons.

$$\bar{v} = \sqrt{\frac{8kT_e}{\pi m_e}} \quad (5.3)$$

for a Maxwellian velocity distribution.<sup>70</sup> Here  $T_e$  is the electron temperature,  $m_e$  is the electron mass, and  $k$  is the Boltzmann constant. The electron mean-free-path is given by<sup>70</sup>

$$\lambda_e \cong 4\sqrt{2} \lambda , \quad (5.4)$$

where  $\lambda$  is the mean-free-path for the background gas particles when a hard-sphere collision model is assumed. For example, in xenon at  $50^\circ\text{C}$  and a pressure of  $1 \cdot 10^{-3}$  Torr,  $\lambda = 6.61$  cm. Thus  $\lambda_e = 37.4$  cm. In a magnetic field of a few hundred gauss the plasma electron temperature was measured to be approximately  $15,000^\circ\text{K}$ . Thus  $\bar{v} = 7.6 \cdot 10^5$  m/s. These values yield a collision frequency of  $2.03$  MHz in the plasma. In the absence of a magnetic field or for a slightly higher pressure this value could be somewhat larger. The effect of collisions in the plasma column may therefore be expected to be quite small for the range of parameters applicable to the experimental work of the present study.

The effect of collisions due to the beam electrons may be shown to be substantially larger, however. For beam electrons above several hundred volts the probability for an elastic collision is considerably less than for an ionizing collision.<sup>70</sup> Thus for beam electrons at  $520$  V ( $u_0 = 1.35 \cdot 10^7$  m/s) and a beam current of  $8.8$  mA passing through the xenon plasma at a pressure of  $1 \cdot 10^{-3}$  Torr the collision frequency is estimated to be  $6.4$  MHz. Thus  $\nu_c/\omega_s = 0.00376$ . Inspection of the force equation, Eq. 3.40, reveals that the term containing  $\nu_c/\omega_s$  may not be expected to be negligible due to the presence of the  $1/C_1^2$  factor. Since  $C_1$  is ordinarily in the order of  $0.1$ , the collision term in the force equation is in the order of unity, which is comparable to the magnitude of the other terms. Table 5.1 lists the parameters needed to specify the input to the large-signal program.

Table 5.1

Plasma Device Parameters

Signal Frequency, $f_s = \omega_s / 2\pi$	1.7 GHz
$\kappa_e$	2.0
Outer Shield Radius, a	0.952 cm
"Circuit" Radius, b	0.152 cm
Beam Radius, b'	0.125 cm
Magnetic Field, $B_0$	260 G
Electron Cyclotron Frequency, $f_c$	728 MHz
$\omega_c / \omega_s$	0.428
$\omega_p / \omega_s$	2.49
Plasma Frequency, $f_p$	4.24 GHz
Pressure	$1.10^{-3}$ Torr
Mean-Free-Path for Xenon	6.61 cm
Plasma Collision Frequency, $\nu$	$12.7 \cdot 10^6$ rad/s
Beam Collision Frequency, $\nu_c$	$40.7 \cdot 10^6$ rad/s
$\nu / \omega_s$	0.0012
$\nu_c / \omega_s$	0.0038

The interaction impedance values for the fundamental and the first three harmonics were calculated from the above data and the solution to the dispersion equation. The results are shown in Table 5.2.

Table 5.2

Equivalent Circuit Impedance Values

$Z_{01r}$	=	340 $\Omega$	$Z_{01i}$	=	-11.3 $\Omega$
$Z_{02r}$	=	175 $\Omega$	$Z_{02i}$	=	-5.82 $\Omega$
$Z_{03r}$	=	103 $\Omega$	$Z_{03i}$	=	-3.42 $\Omega$
$Z_{04r}$	=	74 $\Omega$	$Z_{04i}$	=	-2.46 $\Omega$

In Fig. 5.1, the variation of some of the important parameters for a beam-plasma amplifier in the vicinity of the signal frequency is shown. The gain parameter,  $C_1$ , is 0.113 at 1.7 GHz for the above conditions. The plasma characteristics are assumed to be so adjusted that beam-wave synchronism ( $b_1 = 0$ ) occurs at 1.7 GHz. From one-dimensional linear traveling-wave tube theory<sup>71</sup> it may be expected that gain occurs between  $b_1 = -1.5$  and  $b_1 = 2.3$ . This corresponds to a frequency range of 1.44 to 1.94 GHz, as shown in Fig. 5.1.

The one-dimensional program was written in Fortran IV and was solved on an IBM 360/67 digital computer. A typical run with one signal present required an execution time of two minutes, if 16 charge groups distributed over phase were injected into the interaction region. A four-signal run usually required 64 charge groups for reasonable accuracy and a computing time of approximately 8 minutes.

### 5.3 One-Dimensional Results

5.3.1 No Collisions. Figure 5.2 shows the voltage amplitude and the power level relative to  $C_1 I_0 V_0$  along the beam-plasma interaction region when only one signal, the fundamental frequency, was assumed to

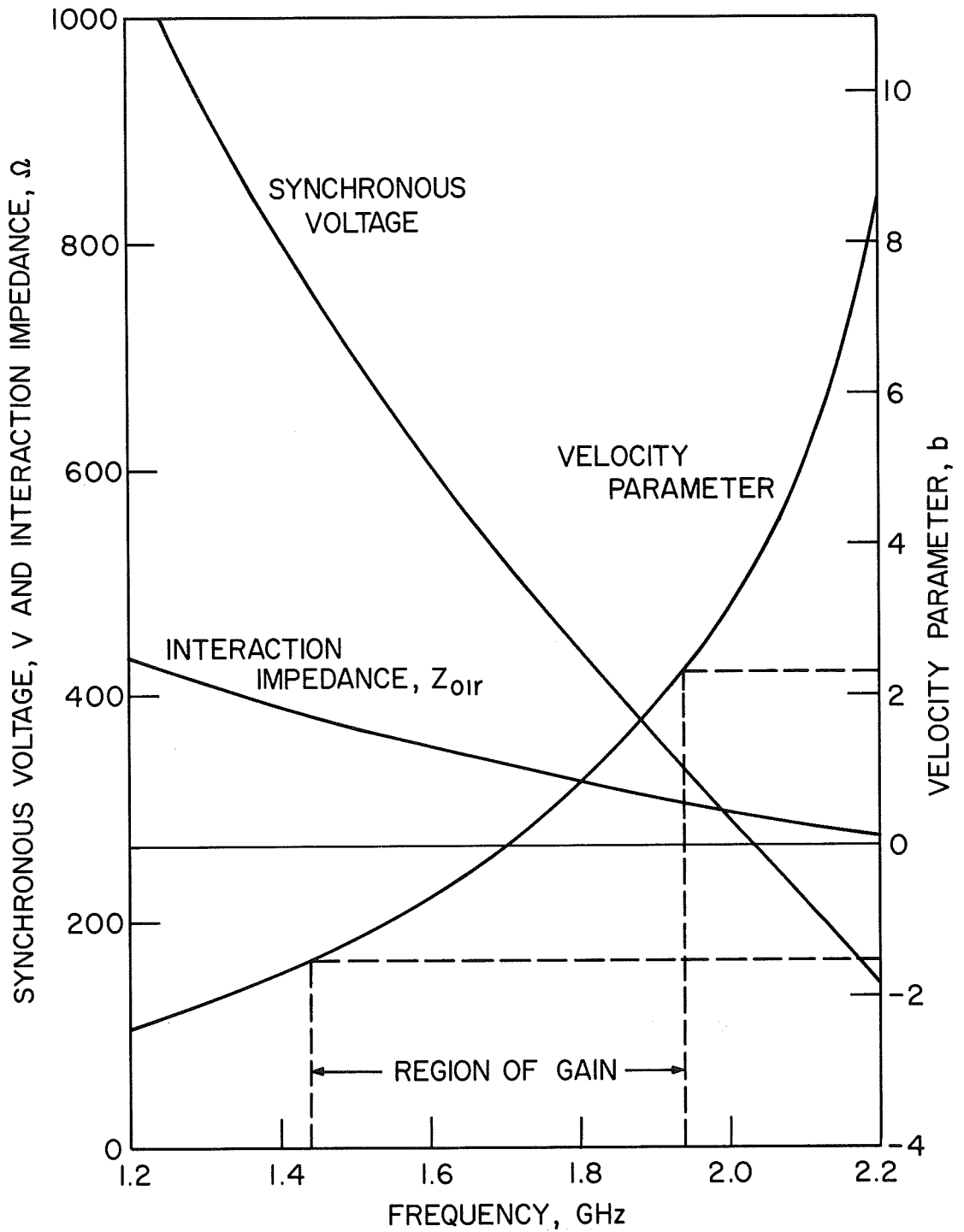


FIG. 5.1 OPERATING PARAMETERS FOR THE BEAM-CONFINED MODE OF A BEAM-GENERATED PLASMA COLUMN INTERACTING WITH THE ELECTRON BEAM.

$(f_p = 4.24 \text{ GHz}, f_c = 728 \text{ MHz}, a/b = 6.26, b/b' = 1.217)$

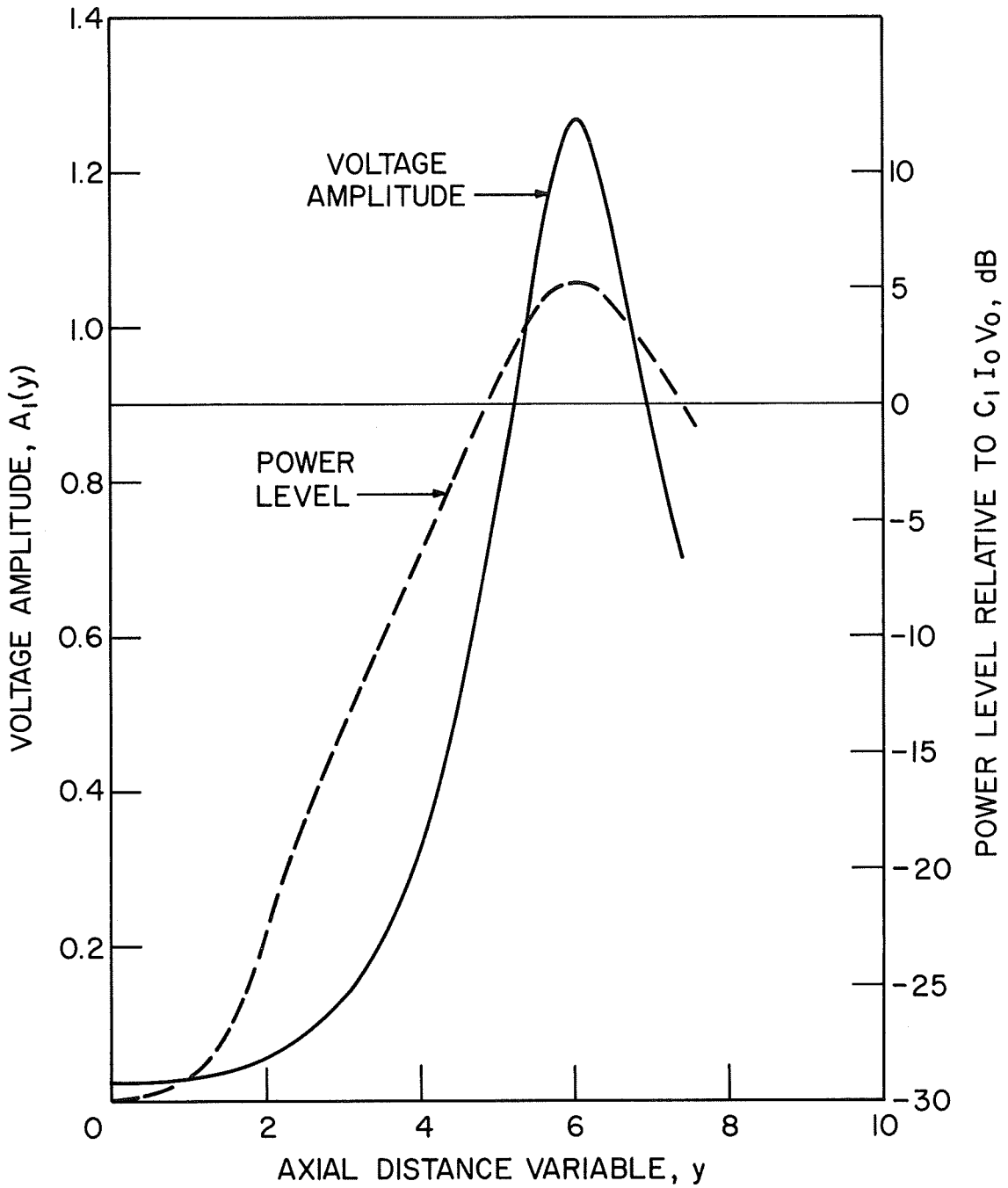


FIG. 5.2 VOLTAGE AMPLITUDE AND POWER LEVEL OF THE FUNDAMENTAL AS A FUNCTION OF DISTANCE ALONG A BEAM-PLASMA AMPLIFIER. ( $C_1 = 0.111$ ,  $b_1 = 0.8$ ,  $Z_{o1} = 324 \Omega$ ,  $v_c/\omega = 0$ ,  $f_p = 4.24$  GHz,  $f_c = 728$  MHz,  $f_s = 1.79$  GHz)

interact with the beam space-charge waves. This, as well as most subsequent one-dimensional results, applies to a beam voltage of 520 V and a beam current of 8.8 mA. The plasma column is assumed to be generated by the electron beam, which corresponds to a large portion of the experimental data to be presented in Chapter VI. The input level of the fundamental signal was normalized with respect to the beam power and was almost always chosen to be 30 dB below  $C_1 I_0 V_0$ . This value corresponds approximately to the gain obtained in the beam-plasma interaction and therefore is convenient for comparing the saturation lengths of the various theoretical and experimental cases. Figure 5.2 shows that the device saturates at a distance  $y = 6.1$ , or  $8.75$  electronic wavelengths, corresponding to an actual distance of 7.23 cm, with a gain of 35 dB.

The initial amplitude of the harmonics could not be set identically equal to zero because singularities would then have resulted in the difference equations; however, the initial harmonic amplitudes were chosen sufficiently small to have no effect on the manner in which saturation occurred. It was found that, if the input level of the harmonics was at least 80 dB below  $C_1 I_0 V_0$ , the voltage amplitudes as a function of axial distance did not depend on the initial levels of the harmonics. Thus a value of 90 dB below  $C_1 I_0 V_0$  was ordinarily used. In Figs. 5.3 through 5.5 the results for conditions identical to those for Fig. 5.2 are shown, but with harmonics through the second, third and fourth, respectively, assumed to be coupled out of the device. Note that the presence of higher harmonics reduces the amplitude of the fundamental because a fraction of the beam power converted to RF power

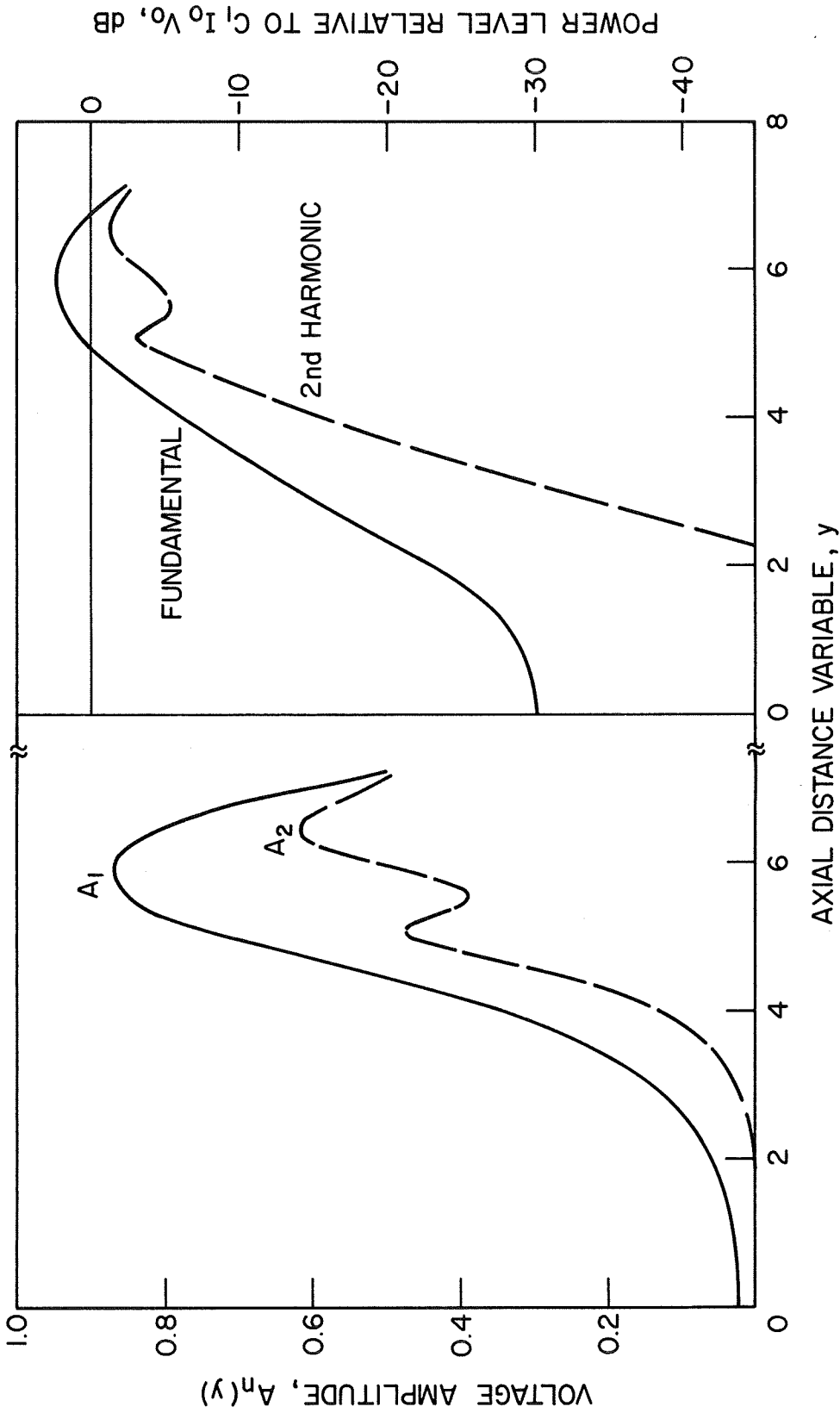


FIG. 5.3 VOLTAGE AMPLITUDE AND POWER LEVEL OF THE FUNDAMENTAL AND THE SECOND HARMONIC AS A FUNCTION OF DISTANCE ALONG A BEAM-PLASMA AMPLIFIER. ( $c_1 = 0.111$ ,  $b_1 = 0.8$ ,  $Z_{01} = 324 \Omega$ ,  $v_c/\omega = 0$ ,  $f_p = 4.24$  GHz,  $f_c = 728$  MHz,  $f_s = 1.79$  GHz)



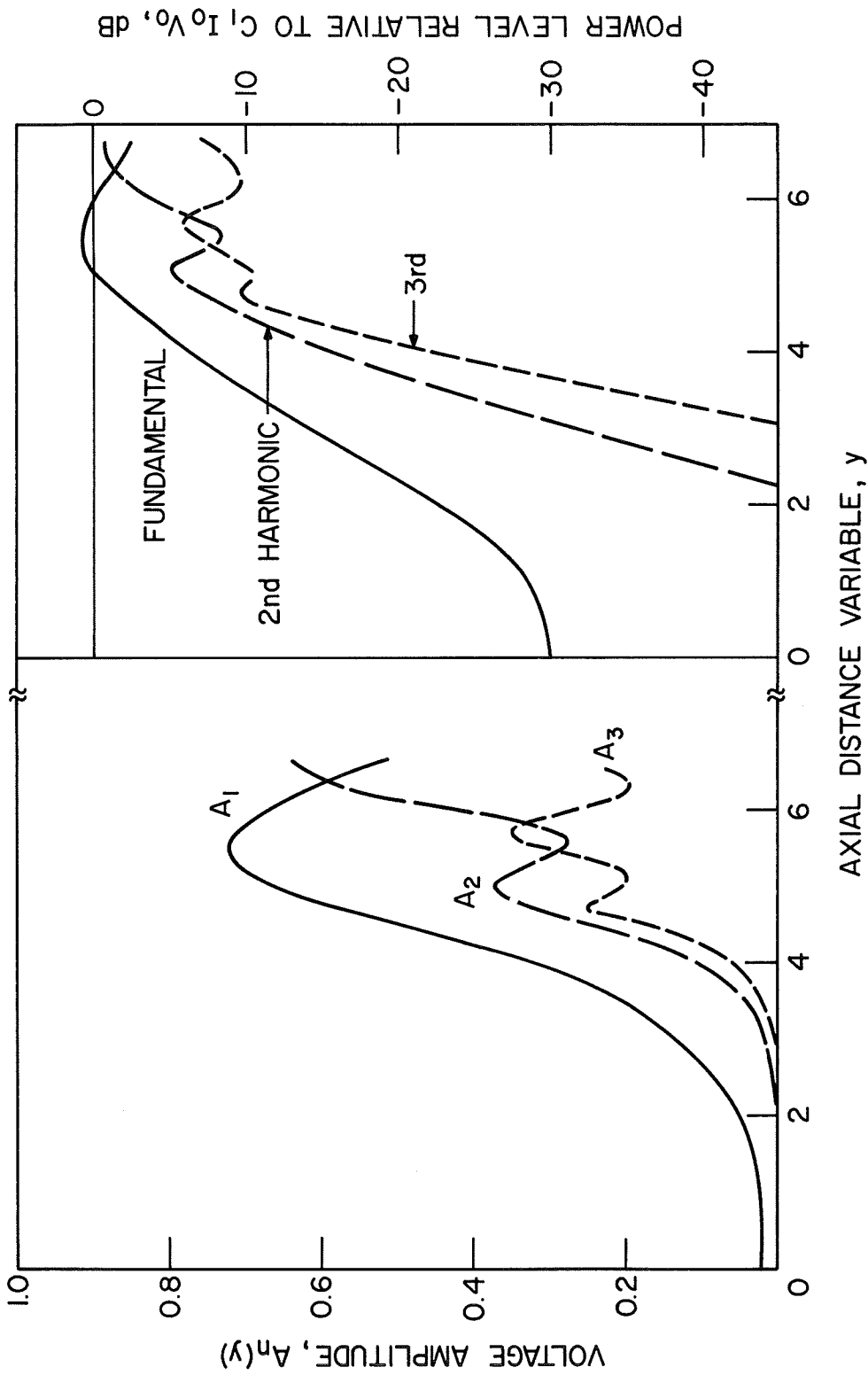


FIG. 5.4 VOLTAGE AMPLITUDE AND POWER LEVEL OF THE FUNDAMENTAL AND THE FIRST TWO HARMONICS AS A FUNCTION OF DISTANCE ALONG A BEAM-PLASMA AMPLIFIER. ( $C_1 = 0.111$ ,  $b_1 = 0.8$ ,  $Z_{01} = 324 \Omega$ ,  $v_c/\omega = 0$ ,  $f_p = 4.24$  GHz,  $f_c = 728$  MHz,  $f_s = 1.79$  GHz)

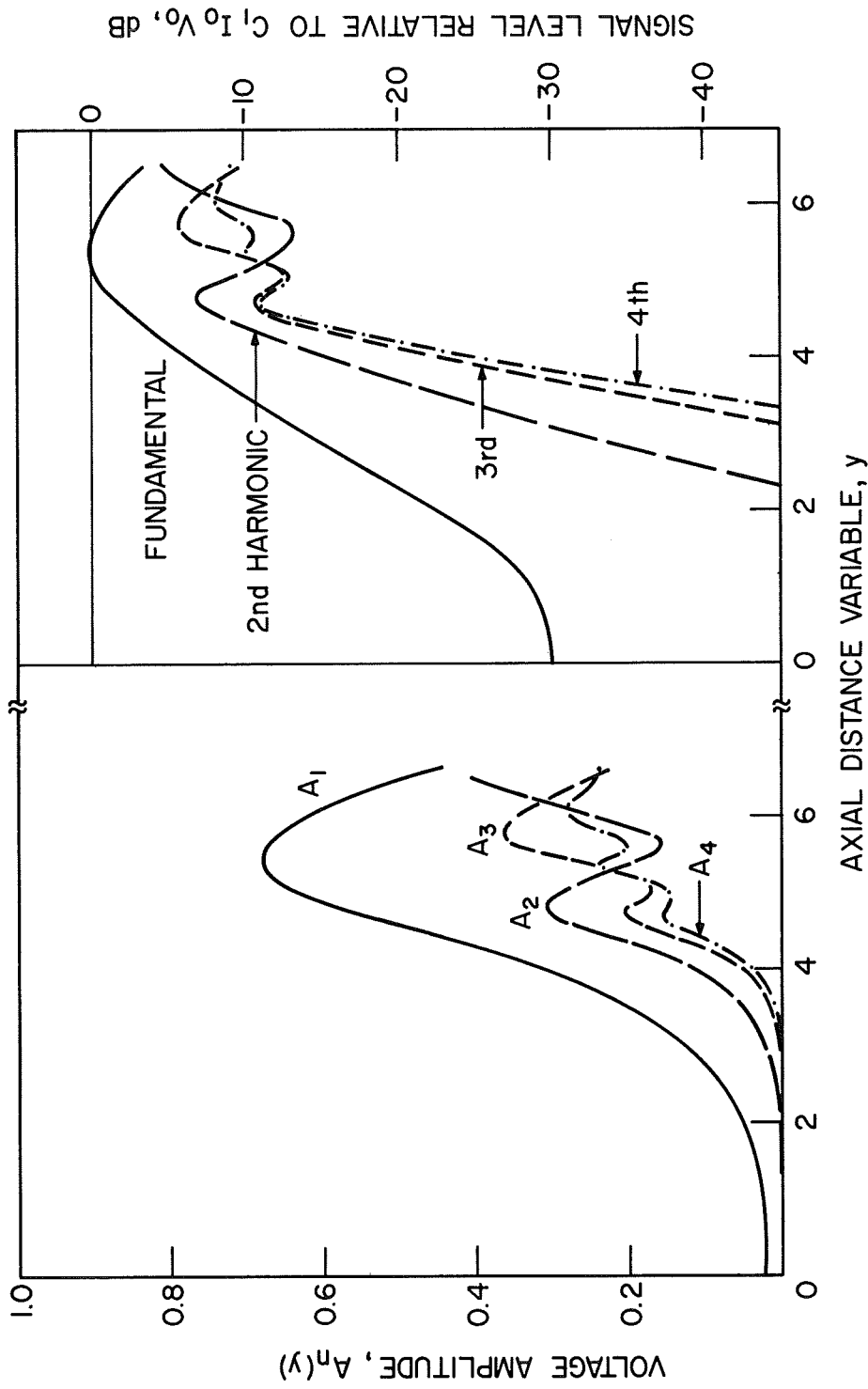


FIG. 5.5 VOLTAGE AMPLITUDE AND SIGNAL LEVEL OF THE FUNDAMENTAL AND THE FIRST THREE HARMONICS AS A FUNCTION OF DISTANCE ALONG A BEAM-PLASMA AMPLIFIER. ( $c_1 = 0.111$ ,  $b_1 = 0.8$ ,  $Z_{o1} = 324 \Omega$ ,  $v_c/\omega = 0$ ,  $f_p = 4.24$  GHz,  $f_c = 728$  MHz,  $f_s = 1.79$  GHz)

is converted into harmonic power. For example, the figures show that the presence of three harmonics reduces the power level in the fundamental signal by approximately 6 dB. For a uniform plasma column calculations indicate that the fundamental and only the second harmonic should exist, because the other harmonics are well above the plasma frequency. In actual practice, as the experimental results show, higher harmonics could be detected. This is believed to be due to nonuniformities in the plasma column, such that the plasma frequency near the center of the column is considerably greater than the estimated value of 4.24 GHz.

Figures 5.6 and 5.7 give an overview of the variation of the maximum signal amplitudes and the saturation length as the velocity and gain parameters are varied. These results were obtained from a large number of computer runs. The fundamental and the next two harmonics only were assumed to exist in the beam-plasma device. The range of values for  $b_1$  and  $C_1$  is reasonable in a beam-plasma amplifier of the type useful for the present study. Figure 5.6 indicates that the minimum distance for saturation occurs for  $b_1 \approx 0.7$ , even though more power output can be obtained when a larger value of  $b_1$  and a longer interaction distance is used. For values of  $b_1 > 2.0$  the output from the device falls off very sharply due to the electron stream being too far out of synchronism with respect to the RF wave. In Fig. 5.7 the signal level at the output decreases with an increase in the gain parameter. This is so because the value of  $b_1$  is kept fixed. If  $b_1$  would be increased appropriately as  $C_1$  is increased in order to maximize the output, then there would be a rise in the voltage amplitude curves as  $C_1$  increases.

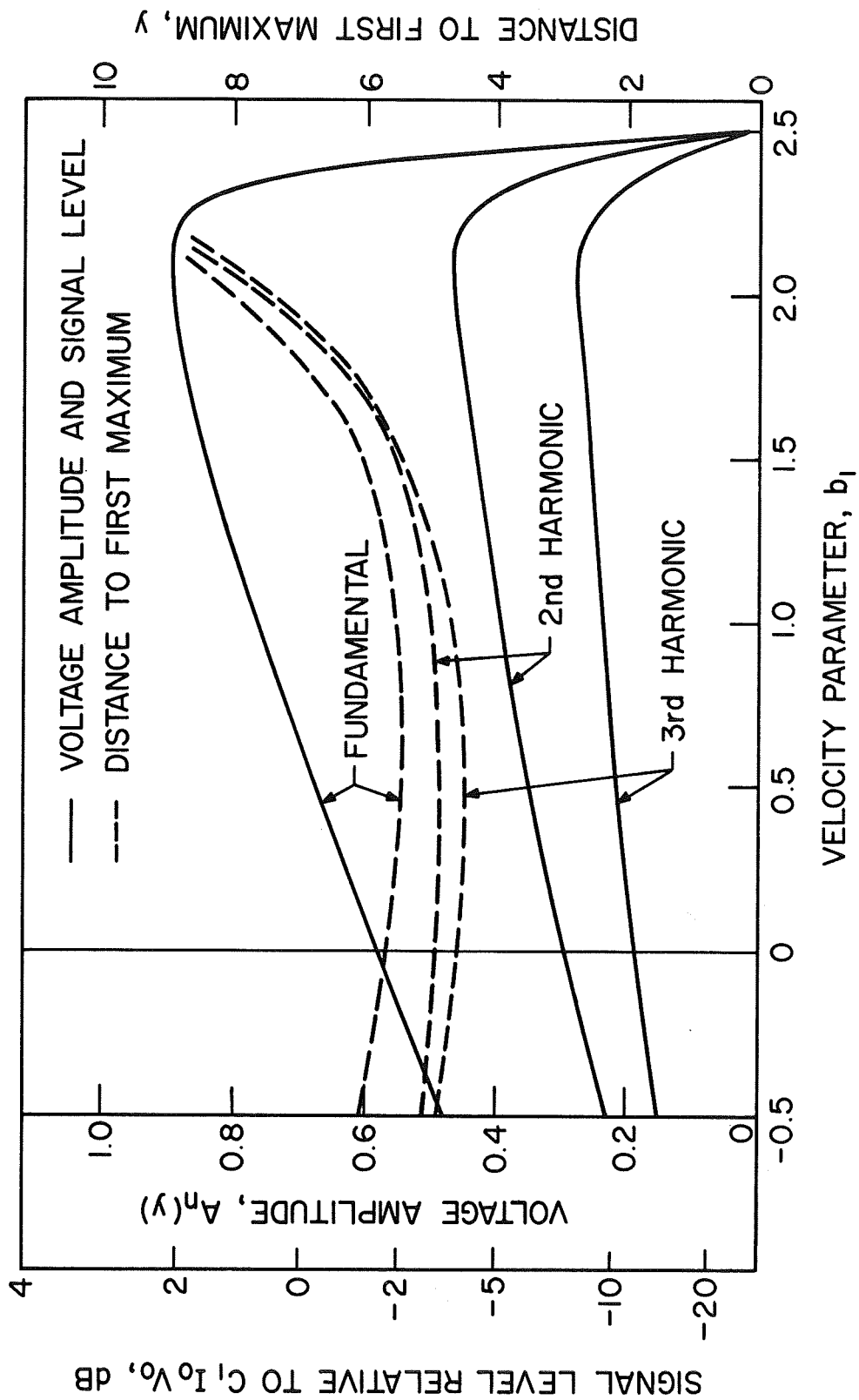


FIG. 5.6 SATURATION CHARACTERISTICS FOR A BEAM-PLASMA INTERACTION AS A FUNCTION OF THE VELOCITY PARAMETER.

$$(c_1 = 0.113, z_{01} = 324 \Omega, v_c/\omega = 0)$$

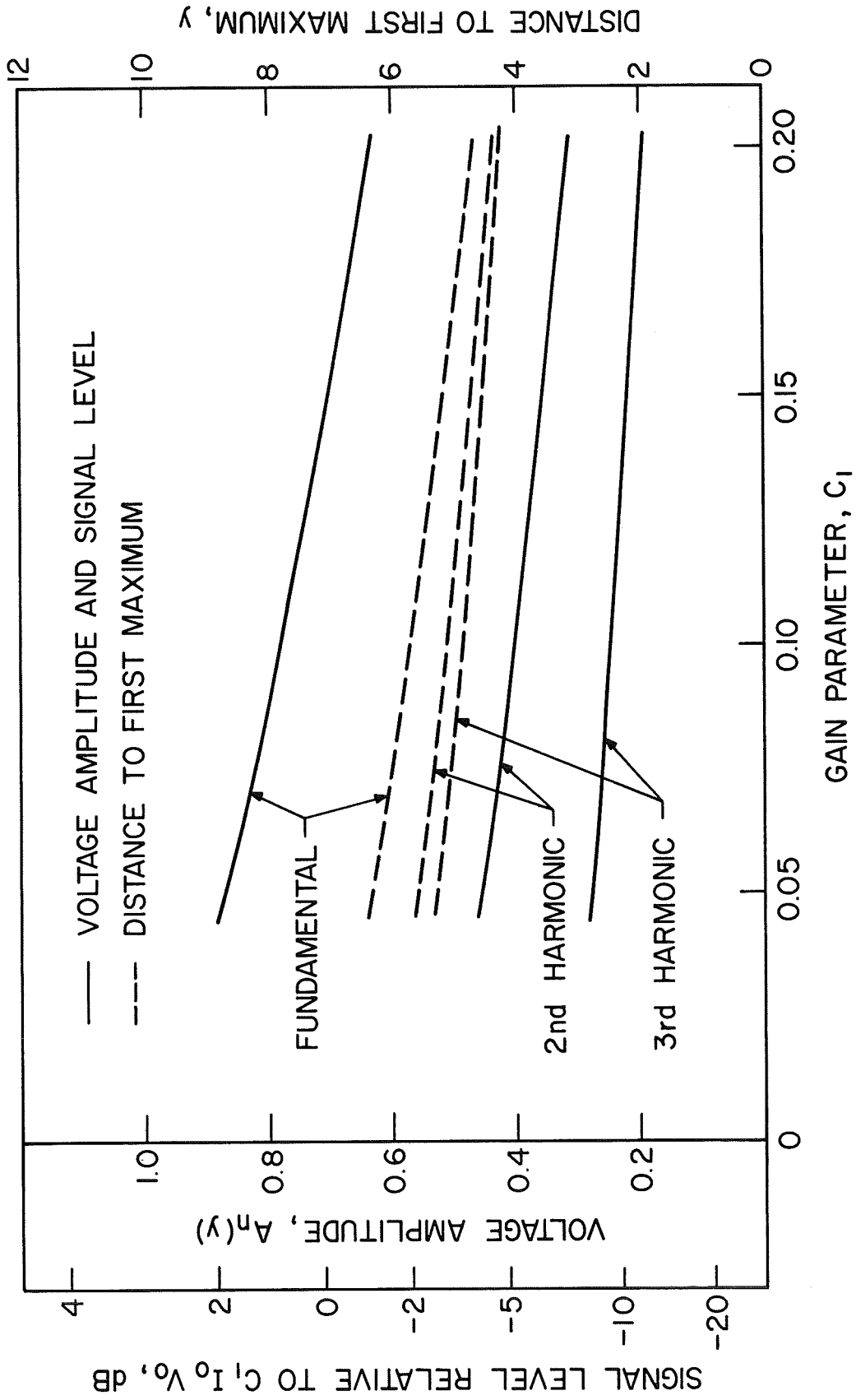


FIG. 5.7 SATURATION CHARACTERISTICS FOR A BEAM-PLASMA INTERACTION AS A FUNCTION OF THE GAIN PARAMETER.

$$(b_1 = 1.0, Z_{o1} = 324 \Omega, v_c/\omega = 0)$$

5.3.2 Effect of Beam Collisions. Figures 5.8 and 5.9 show the voltage amplitude and the signal level of the fundamental for various collision frequency values. Figure 5.8 is for synchronism between beam and wave,  $b_1 = 0$ , while Fig. 5.9 is for  $b_1 = 1.4$ . In the latter figure an increase in the collision frequency causes a more rapid rise in the voltage amplitude and considerably earlier saturation. This is due to the fact that for a value of  $b_1 = 1.4$  the beam travels considerably faster than the wave, and maximum gain occurs later than for lower values of  $b_1$ . The collision term in the force equation, however, represents a slowing contribution to the velocity. Thus a lower value of  $b_1$  actually applies when beam collision effects are included, resulting in the more rapid saturation seen in Fig. 5.9. In most of the experimental cases to be discussed in Chapter VI,  $v_c/\omega$  was between 0.001 and 0.003.

When the fundamental and the next three harmonics were assumed to exist in the device, the voltage amplitudes and signal levels shown in Fig. 5.10 were calculated for the case  $b_1 = 0.8$  and  $v_c/\omega = 0.001$ . Comparing this with the corresponding no-collision case of Fig. 5.5 a reduction in saturation gain of nearly 1 dB may be found due to beam collision effects.

5.3.3 Effect of Plasma Collisions. The effect of plasma collisions on the gain of a beam-plasma amplifier when only the fundamental signal is present is shown in Fig. 5.11. For a collision frequency estimated to apply to the experimental device of this study  $v/\omega \cong 0.0012$ , which yields an impedance ratio  $Z_{o1i}/|Z_{o1}| = -0.0303$ .

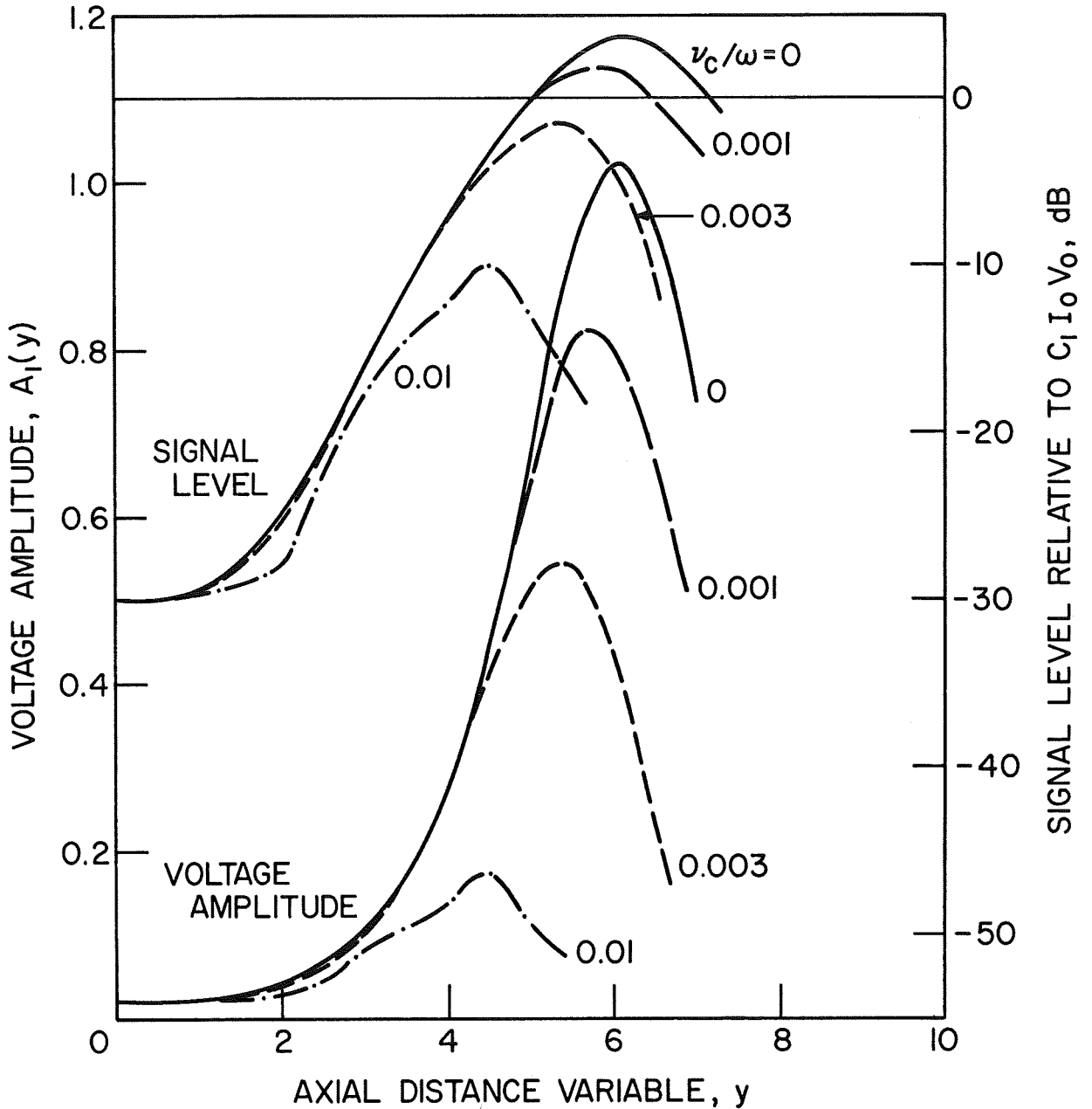


FIG. 5.8 VOLTAGE AMPLITUDE AND SIGNAL LEVEL OF THE FUNDAMENTAL AS A FUNCTION OF DISTANCE ALONG A BEAM-PLASMA AMPLIFIER, WITH BEAM-PLASMA COLLISIONS INCLUDED. ( $c_1 = 0.113$ ,  $b_1 = 0$ ,  $Z_{o1} = 340 \Omega$ ,  $f_p = 4.24$  GHz,  $f_c = 728$  MHz,  $f_s = 1.70$  GHz)

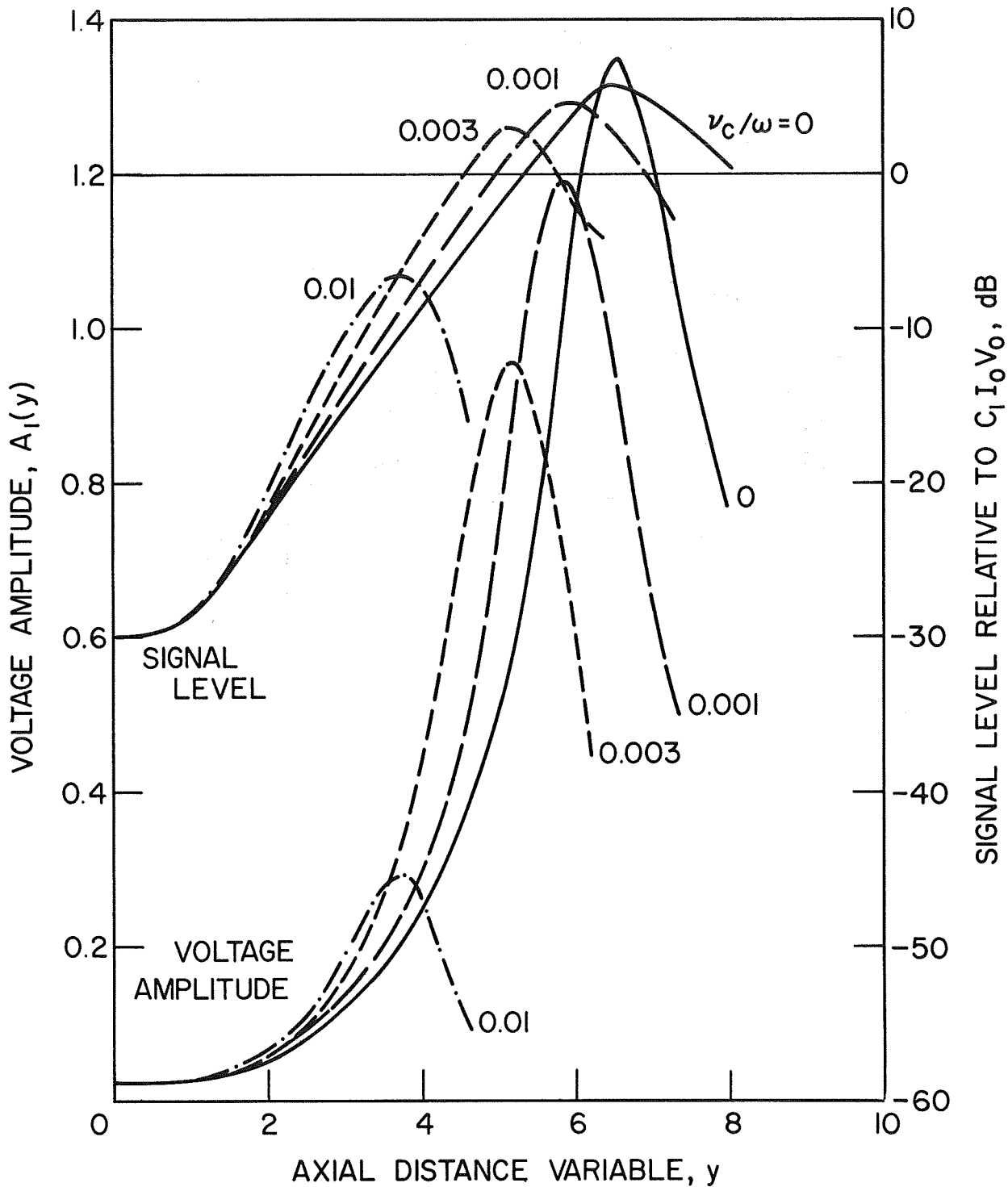


FIG. 5.9 VOLTAGE AMPLITUDE AND SIGNAL LEVEL OF THE FUNDAMENTAL AS A FUNCTION OF DISTANCE ALONG A BEAM-PLASMA AMPLIFIER, WITH BEAM-PLASMA COLLISIONS INCLUDED. ( $C_1 = 0.110$ ,  $b_1 = 1.4$ ,  $Z_{o1} = 312 \Omega$ ,  $f_p = 4.24 \text{ GHz}$ ,  $f_c = 728 \text{ MHz}$ ,  $f_s = 1.85 \text{ GHz}$ )



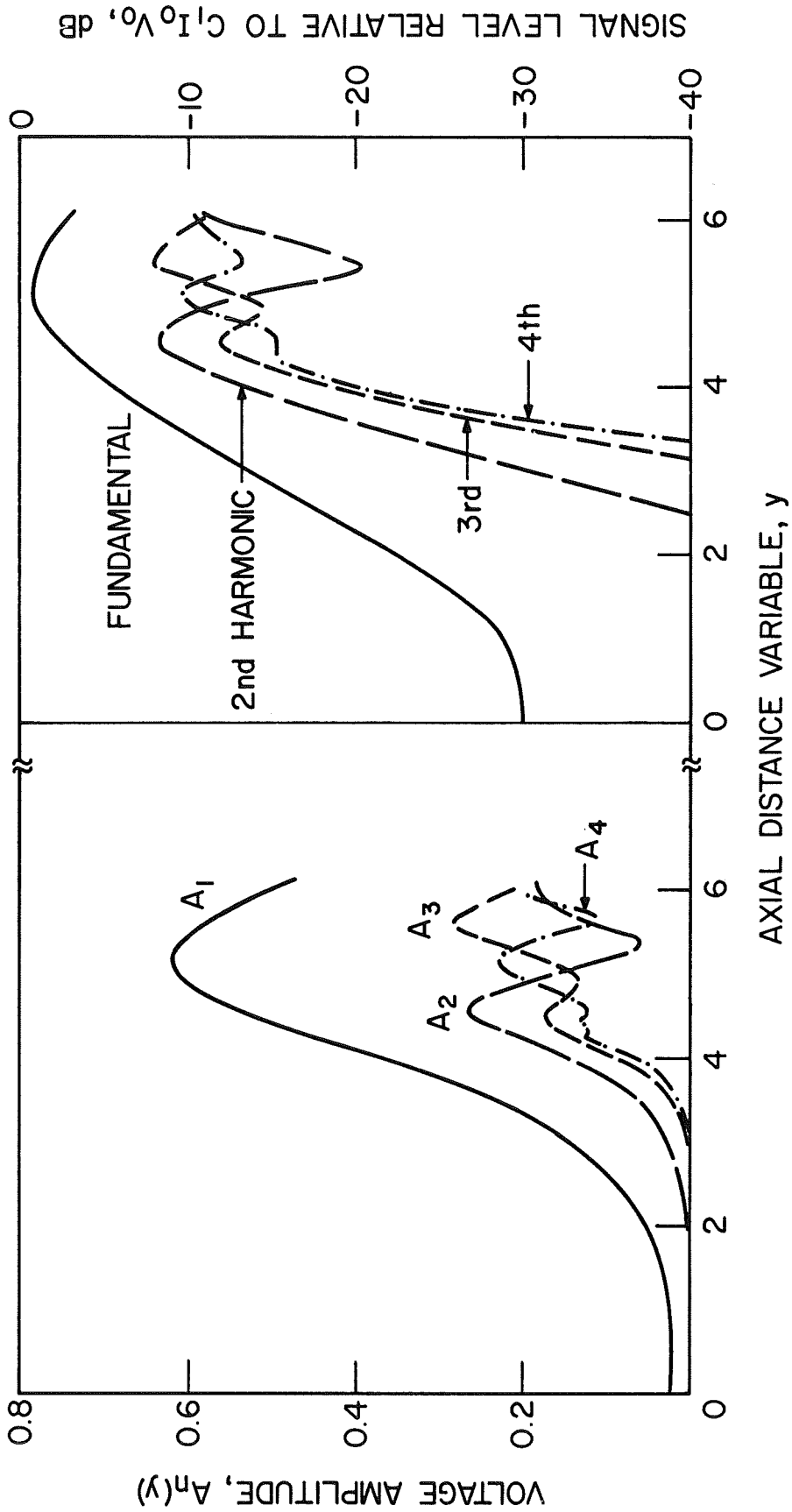


FIG. 5.10 VOLTAGE AMPLITUDE AND SIGNAL LEVEL OF THE FUNDAMENTAL AND FIRST THREE HARMONICS AS A FUNCTION OF DISTANCE ALONG A BEAM-PLASMA AMPLIFIER. ( $C_1 = 0.111$ ,  $b_1 = 0.8$ ,  $Z_{01} = 324 \Omega$ ,  $v_c/\omega = 0.001$ ,  $f_p = 4.24$  GHz,  $f_c = 728$  MHz,  $f_s = 1.79$  GHz)

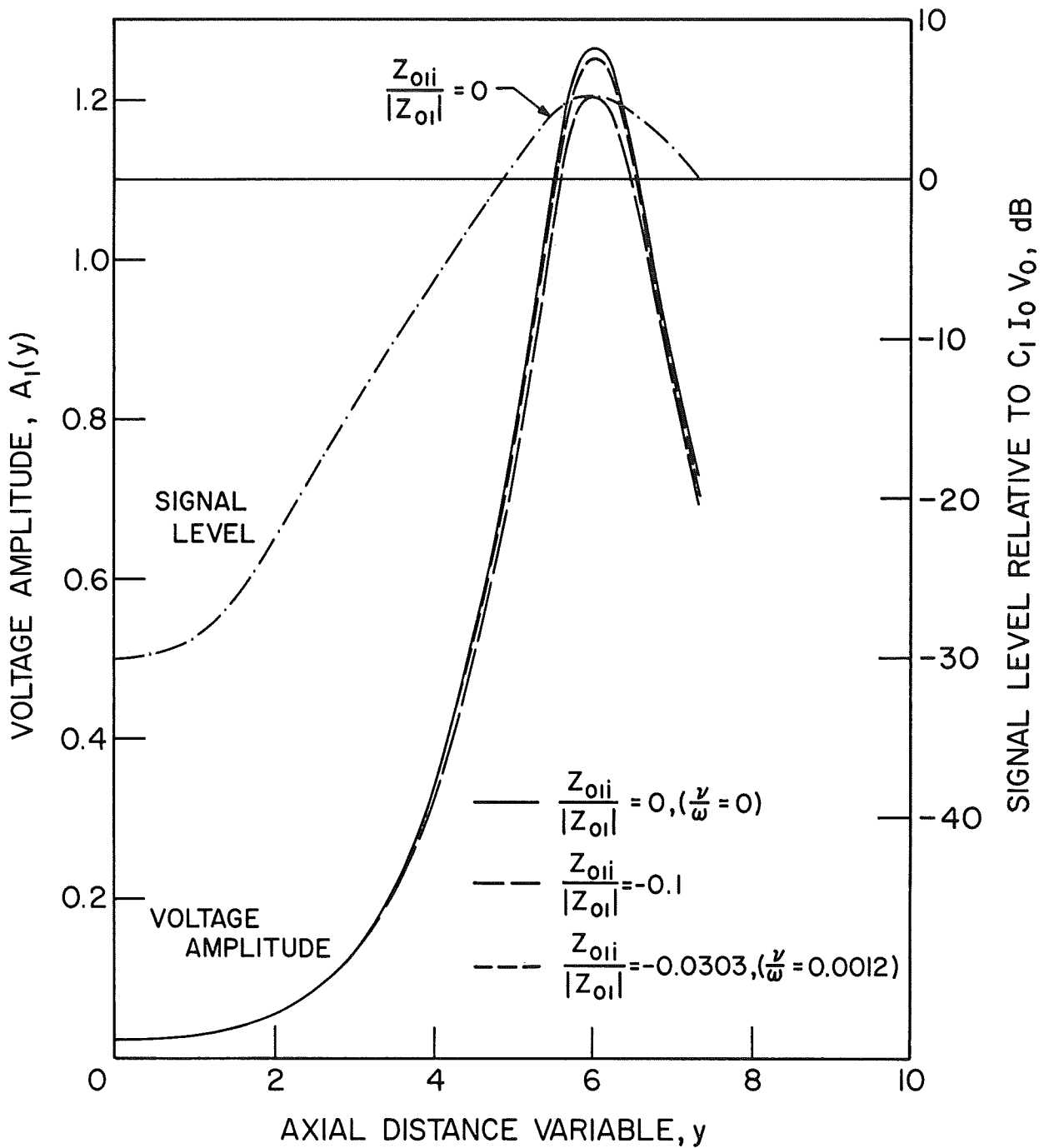


FIG. 5.11 VOLTAGE AMPLITUDE AND SIGNAL LEVEL OF THE FUNDAMENTAL AS A FUNCTION OF DISTANCE ALONG A BEAM-PLASMA AMPLIFIER SHOWING THE EFFECT OF PLASMA COLLISIONS. ( $C_1 = 0.111$ ,  $b_1 = 0.8$ ,  $Z_{01r} = 324 \Omega$ ,  $v_c/\omega = 0$ ,  $f_p = 4.24$  GHz,  $f_c = 728$  MHz,  $f_s = 1.79$  GHz)

The reduction in gain amounts to less than 0.1 dB. Thus the effect is very small, as was already anticipated in Section 5.2. Comparing the case for the fundamental and three harmonics depicted in Fig. 5.12 with the case for no plasma collisions of Fig. 5.5, the differences are again seen to be almost negligible.

5.3.4 Two-Signal Operation. The computer program used for the one-dimensional calculations was written in a sufficiently general way so that not only harmonic frequencies but also fairly closely spaced signals could be analyzed. This makes the program suitable for multisignal studies on traveling-wave tubes<sup>72</sup> and similar devices. When two signals are introduced in a beam-plasma device and the dispersion of the plasma column is sufficiently small, intermodulation products at  $mf_a - nf_b$ , where  $m = 2, 3, \dots$  and  $n = 1, 2, 3, \dots$ , ( $m > n$ ), may be generated. In addition, crossmodulation resulting in interference between the input signals,  $f_a$  and  $f_b$ , may take place. These considerations are of importance when the device is to be used in a multichannel communication system, for example.

One of the problems encountered when multisignal operation is to be analyzed is the increase of the number of charge groups that have to be followed through the interaction region and the resulting increase in computer time. This increase is due to the fact that the integration over the entering charge groups has to be carried out over a complete period of the input, which is generally longer than the period of each single signal. For example, for two input signals with frequencies spaced five percent apart, the period of the combined input is 20 times the period of a single signal. Thus it was not possible to make calculations

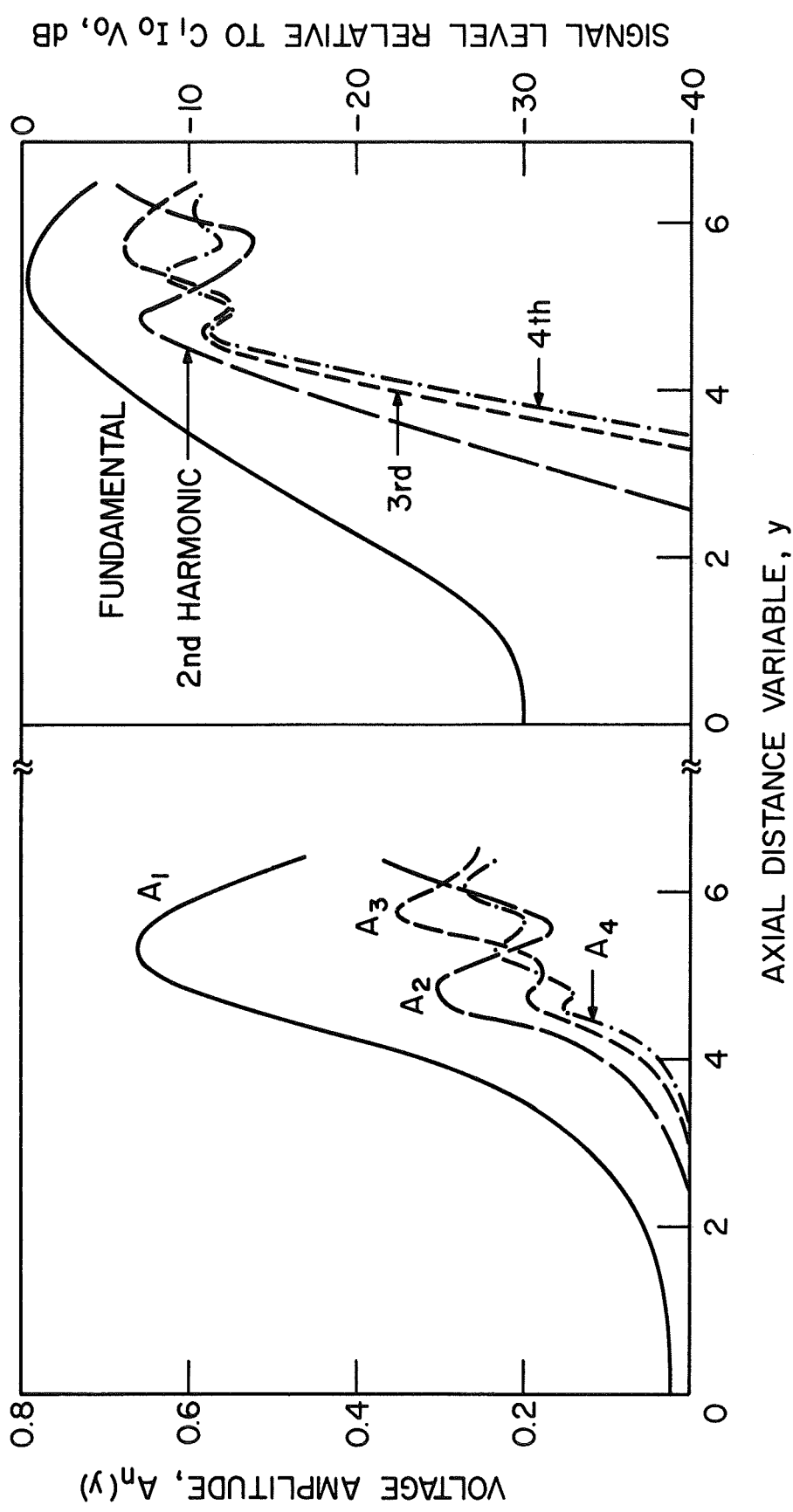


FIG. 5.12 VOLTAGE AMPLITUDE AND SIGNAL LEVEL OF THE FUNDAMENTAL AND THE FIRST THREE HARMONICS AS A FUNCTION OF DISTANCE ALONG A BEAM-PLASMA AMPLIFIER WITH PLASMA COLLISIONS INCLUDED. ( $c_1 = 0.111$ ,  $b_1 = 0.8$ ,  $Z_{01r} = 324 \Omega$ ,  $Z_{01i} / |Z_{01}| = -0.0303$ ,  $v_c / \omega = 0$ ,  $f_p = 4.24$  GHz,  $f_c = 728$  MHz,  $f_s = 1.79$  GHz)

for input signals spaced appreciably closer than 100 MHz apart. For the case of Fig. 5.13, where  $f_a = 1.7$  GHz and  $f_b = 1.8$  GHz, 305 charge groups had to be tracked through the interaction region for reasonable accuracy. The program was set up to handle at most 500. For example, for a spacing of 6 MHz between  $f_a$  and  $f_b$ , more than 4600 charge groups would have been required. This would have made a computation entirely impractical from a standpoint of computing time used.

The two input signals of equal magnitude shown in Fig. 5.13 were chosen to be approximately 6 dB below the saturation value in order to insure a short interaction length and thus conserve computing time. Approximately seven minutes of execution time was required for the case shown. Signal  $f_b$  is seen to grow more rapidly, even though it is the higher frequency signal, because its velocity parameter is closer to the value corresponding to maximum saturation gain than is the case for  $f_a$ . Thus the dominance of the lower frequency signal frequently seen in less dispersive devices, such as a helix-type traveling-wave tube, is masked in this case. In Fig. 5.14 the lower frequency signal does dominate, but this is due to the fact that it is approximately 6 dB larger at the input. In general it can be said that the signal with the largest initial strength or the most rapid growth rate is likely to dominate, unless the circuit is quite nondispersive. In that case, for signals that have an approximately equal initial magnitude, the lower frequency signal may dominate. This is found to be true in the experimental part of this study, where the frequency difference between the input signals was only a few MHz.

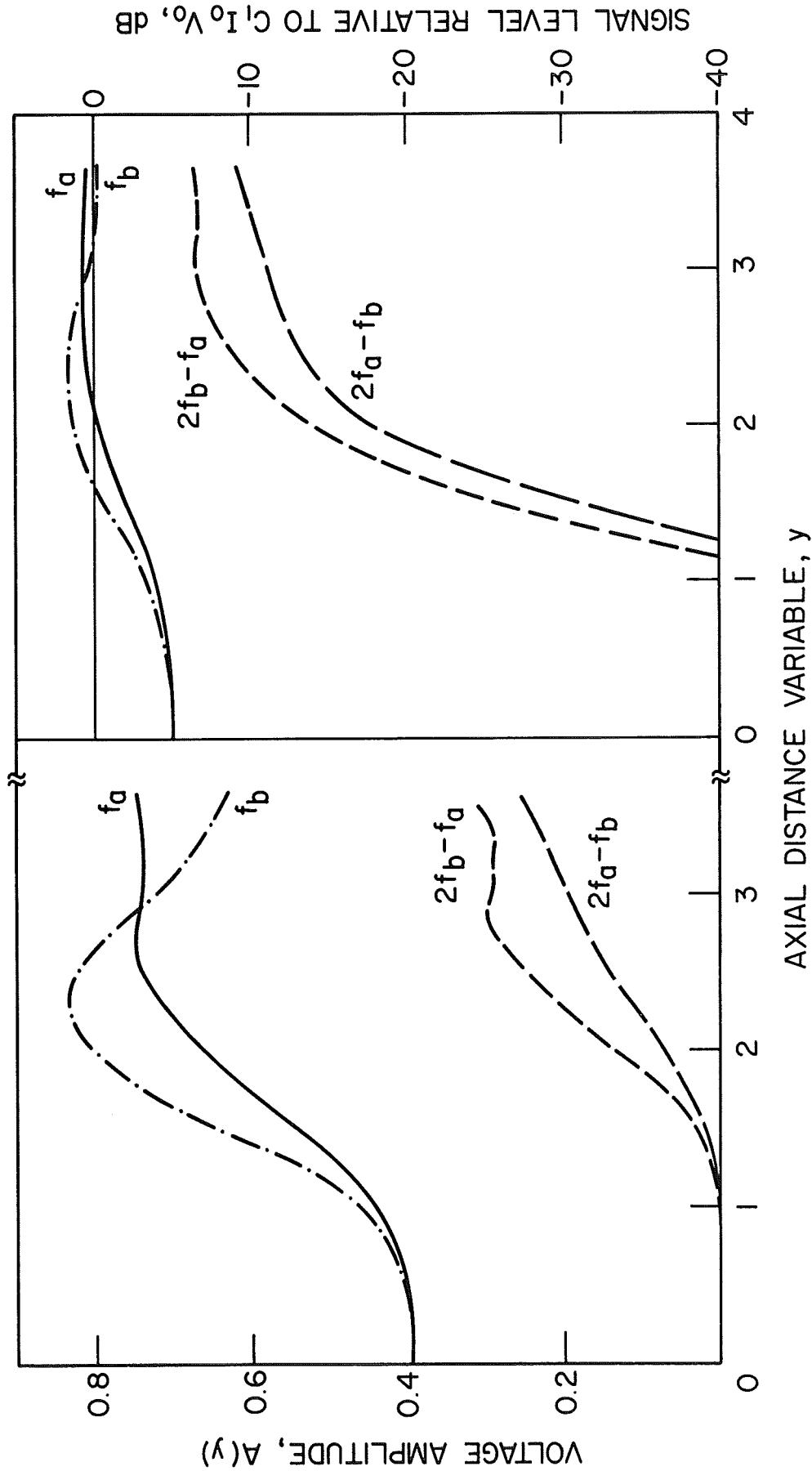


FIG. 5.13 TWO-SIGNAL OPERATION OF A BEAM-PLASMA AMPLIFIER SHOWING TWO INTERMODULATION COMPONENTS. ( $C_a = 0.111$ ,  $b_a = 0.8$ ,  $Z_{oa} = 358 \Omega$ ,  $f_p = 4.24$  GHz,  $f_c = 728$  MHz,  $f_a = 1.7$  GHz,  $f_b = 1.8$  GHz)

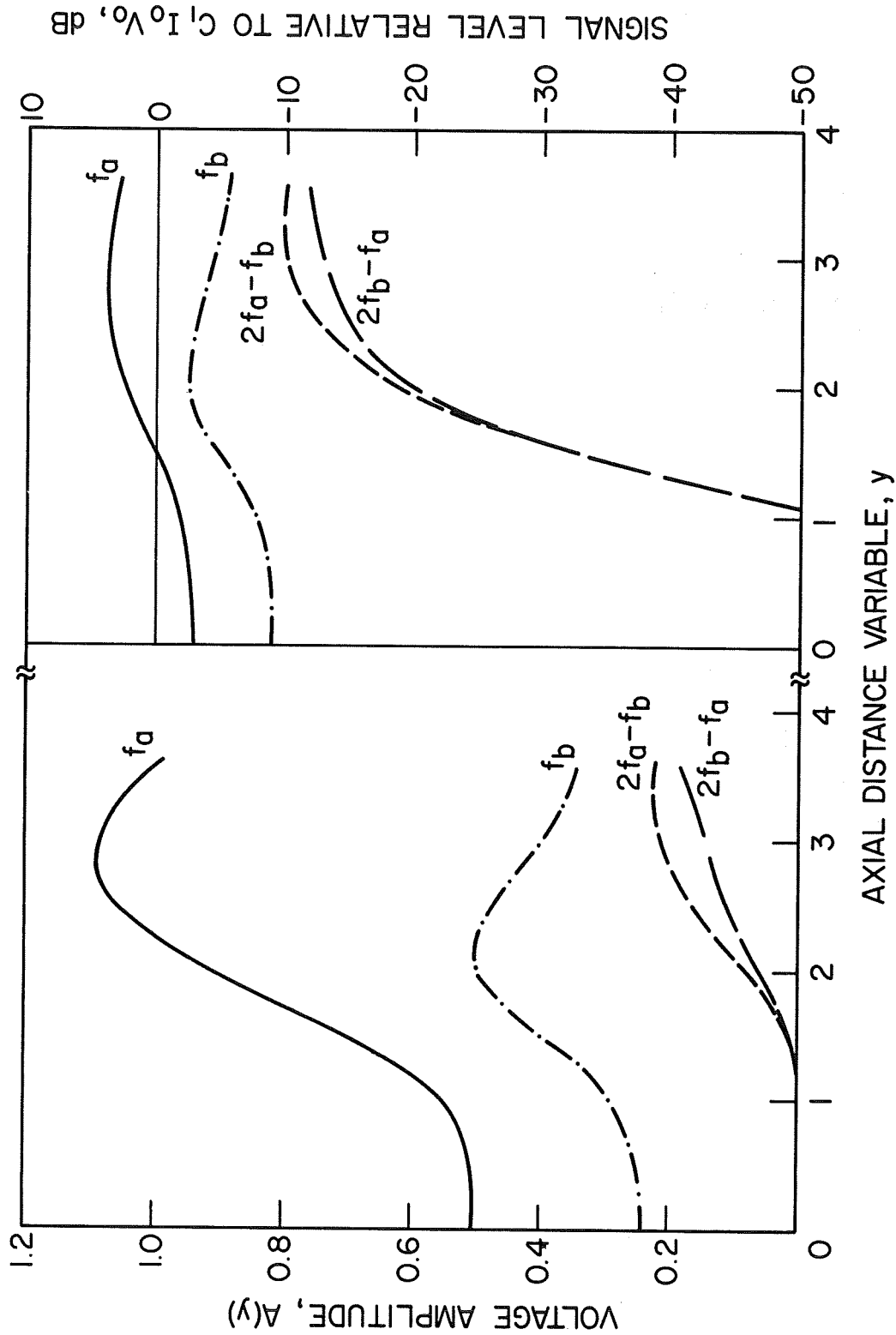


FIG. 5.14 TWO-SIGNAL OPERATION OF A BEAM-PLASMA AMPLIFIER SHOWING TWO INTERMODULATION COMPONENTS. ( $c_a = 0.111$ ,  $b_a = 0.8$ ,  $Z_{oa} = 338 \Omega$ ,  $f_p = 4.24$  GHz,  $f_c = 728$  MHz,  $f_a = 1.7$  GHz,  $f_b = 1.8$  GHz)

#### 5.4 Solution of the Two-Dimensional Equations

The working equations for the two-dimensional case are Eqs. 4.20, 4.22, 4.45, 4.46 and 4.57 through 4.59. The equations are solved as in the one-dimensional case. The initial conditions and the required input data were discussed in Section 4.5. The following additional information is required for the two-dimensional case.

The cyclotron frequency not only appears in the dispersion equation in this case, but also in the beam force equations. When beam space-charge effects are included in the calculations, the plasma frequency of the beam electrons,  $f_b$ , is required. It is given by<sup>73</sup>

$$f_b = \frac{\eta I_D}{2\pi\epsilon_0 u_0} = \frac{1}{2\pi} \cdot 1.83 \cdot 10^8 \left( \frac{I_D}{\sqrt{V_0}} \right)^{1/2}, \quad (5.5)$$

where  $I_D$  is the current density in the electron beam. For a 520 V beam carrying a current of 8.8 mA and a beam radius of 0.125 cm,  $f_b$  is 259 MHz.

In the two-dimensional analysis the entering electron stream is divided radially into three annular layers and within each layer 32 charge groups are injected into the interaction region. Because charge groups are followed at various radial positions, the axial velocity can vary over the beam cross section. The program was set up to handle only one signal, namely the fundamental. Thus only  $A_1(y)$  could be obtained in the two-dimensional case; however, the normalized RF currents,  $i_n/I_0$ , for the fundamental and harmonics through the fifth were computed. If  $I_0$  and the interaction impedance at the harmonics are known, the harmonic output power can easily be computed to a fair approximation.



The program for the two-dimensional case was written directly in machine language for the IBM 7090 computer. A typical run neglecting beam space-charge effects required an execution time of eight to twelve minutes, depending on the interaction length. When space-charge effects were included, the execution time for a similar run was 1-1/2 to 2 hours. For that reason only a few space-charge runs were obtained.

### 5.5 Two-Dimensional Results

In Fig. 5.15 the results obtained from the one-dimensional model are compared with those for two-dimensional theory, both without and with space-charge effects included. The gain at saturation is approximately 0.6 dB less when two-dimensional effects are included. Saturation occurs at a position approximately 33 percent farther along the device when compared with the one-dimensional case. In particular, it should be noted that beam space-charge effects do not make a very drastic difference in the gain and power output level, justifying the neglect of space-charge effects in many of the calculations.

Figures 5.16 and 5.17 show the trajectories of the 32 charge groups in each layer of the electron stream. As saturation is approached the electrons make ever wider excursions from their radial starting positions. Comparing Figs. 5.16 and 5.17 it may be seen that when space-charge effects are included, these excursions are much greater due to the space-charge repulsion forces. The line labeled "plasma boundary" is more meaningful in a traveling-wave tube than it is here. Some of the electrons of Fig. 5.17 are seen to be intercepted on the boundary. The digital computer program is set up so that these electrons are

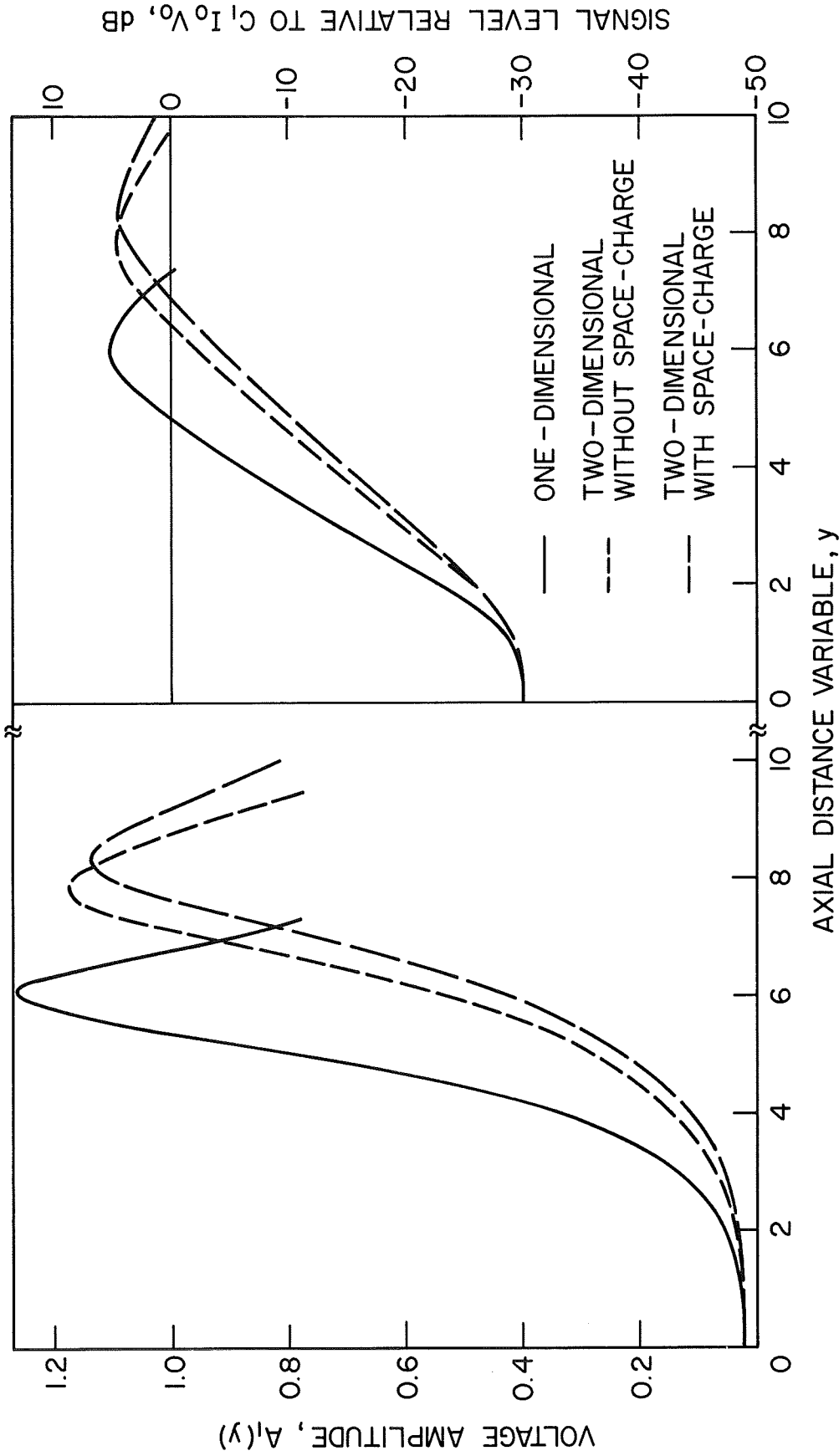


FIG. 5.15 COMPARISON OF ONE-DIMENSIONAL AND TWO-DIMENSIONAL ANALYSES OF A BEAM-PLASMA SYSTEM. ( $c_1 = 0.111$ ,  $b_1 = 0.8$ ,  $Z_{01} = 324 \Omega$ ,  $v_c/\omega = 0$ ,  $f_p = 4.24$  GHz,  $f_b = 259$  MHz,  $f_c = 728$  MHz,  $f_s = 1.79$  GHz)

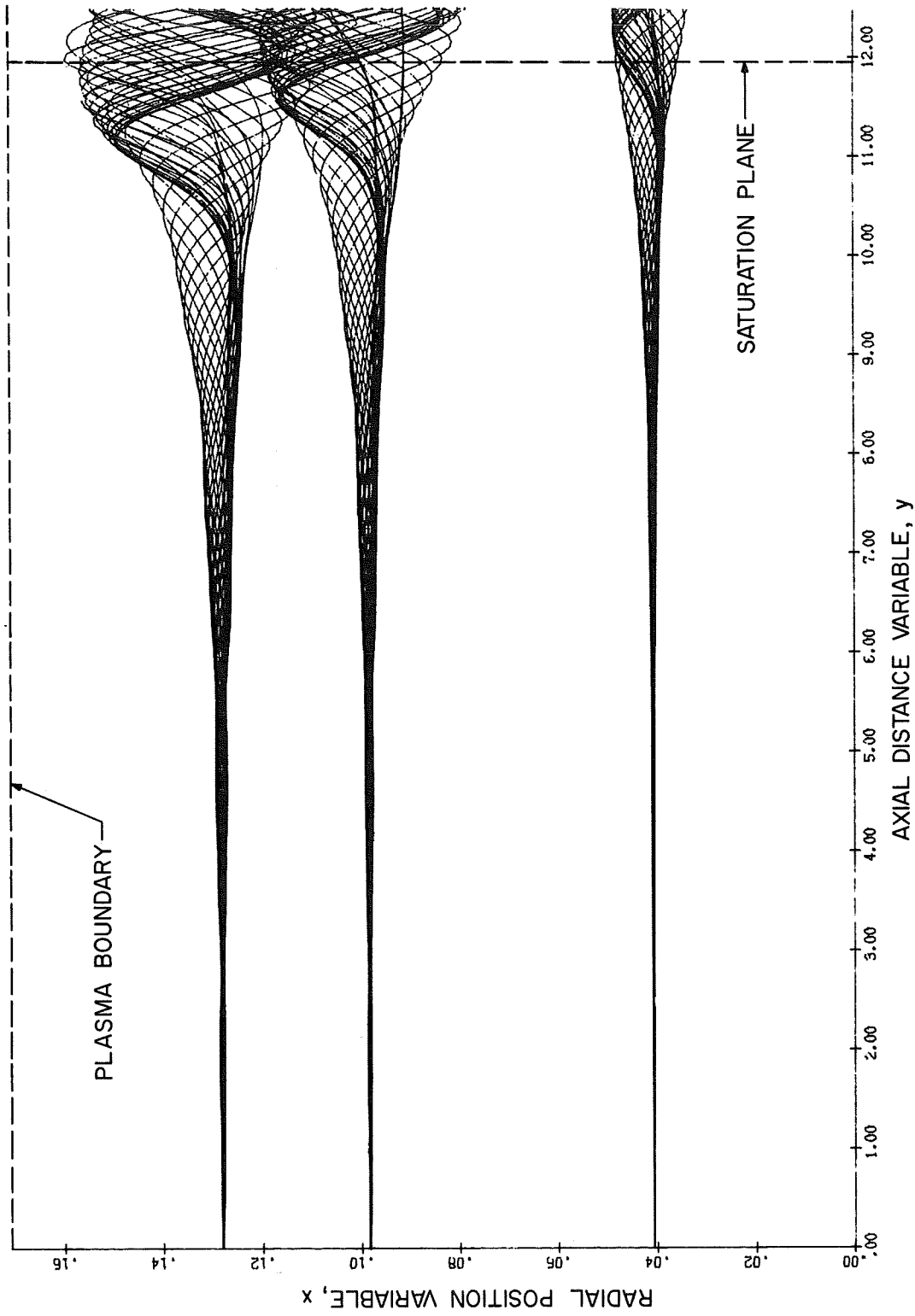


FIG. 5.16 ELECTRON TRAJECTORIES IN A BEAM-PLASMA AMPLIFIER WHEN BEAM SPACE-CHARGE EFFECTS ARE NEGLECTED.

( $c_1 = 0.110$ ,  $b_1 = 1.4$ ,  $Z_{01} = 312 \Omega$ ,  $v_c/\omega = 0$ ,  $f_p = 4.24$  GHz,  $f_b = 259$  MHz,  $f_c = 728$  MHz,  $f_s = 1.85$  GHz)

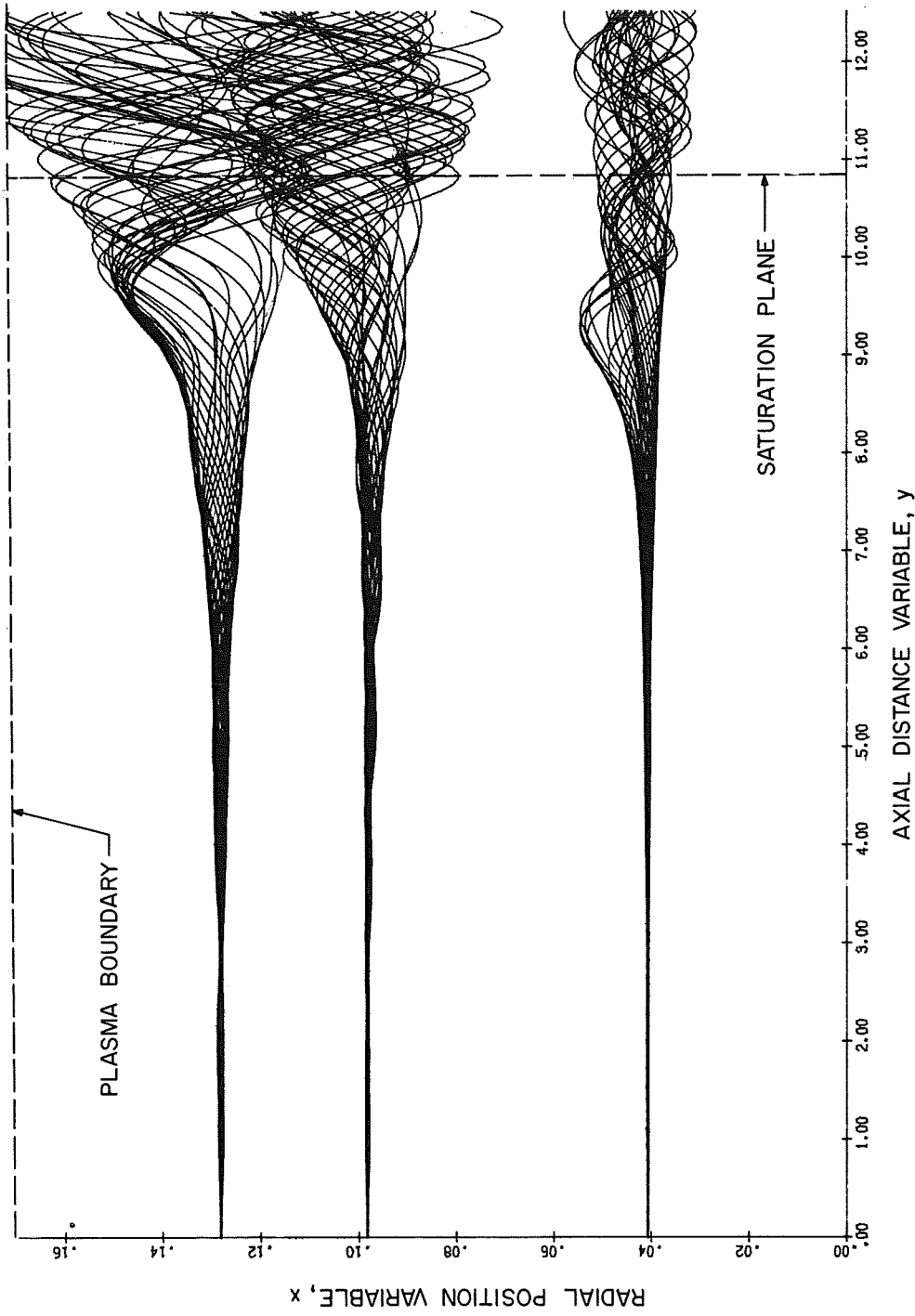


FIG. 5.17 ELECTRON TRAJECTORIES IN A BEAM-PLASMA AMPLIFIER WHEN BEAM SPACE-CHARGE EFFECTS ARE INCLUDED.

$(c_1 = 0.110, b_1 = 1.4, Z_{01} = 312 \Omega, v_c/\omega = 0, f_p = 4.24 \text{ GHz}, f_b = 259 \text{ MHz}, f_c = 728 \text{ MHz}, f_s = 1.85 \text{ GHz})$

removed from further interaction. In the beam-plasma amplifier the plasma boundary position is at the effective radius of the equivalent circuit. In an actual device making use of a beam-generated plasma there is nothing at this position except ionized and un-ionized gas particles. Thus an electron could readily cross and recross the "circuit" line. The two figures of the trajectory plots, as well as Fig. 5.18, were obtained directly from the computer through the use of a plotting routine.

Figure 5.18 shows the normalized RF velocity variables of the 32 charge groups in each stream layer as a function of phase with respect to the RF wave. Beam space-charge effects were included. Initially all electrons should be uniformly distributed over velocity space near  $1 + 2C_1 u(y) = 1$ . As RF interaction takes place some electrons are speeded up and some are slowed down to give up a part of their kinetic energy to the wave. For efficient RF amplification there should be more of the latter. The figure in the upper left of Fig. 5.18 shows the velocity distribution at an axial position 10 dB below saturation. The figures in the upper right and lower left are for 6 and 3 dB below saturation, respectively. At the saturation plane, depicted in the lower right figure, it may be seen that relatively more electrons have slowed down than have been speeded up. This means they have given up some of their kinetic energy. If a similar figure were obtained beyond the saturation plane, some electrons would move again to the upper half of the figure, taking RF energy away from the wave.

The fundamental and the harmonic RF currents are shown in Figs. 5.19 through 5.21. Figure 5.19 shows the total normalized RF currents, while Figs. 5.20 and 5.21 show the RF layer currents

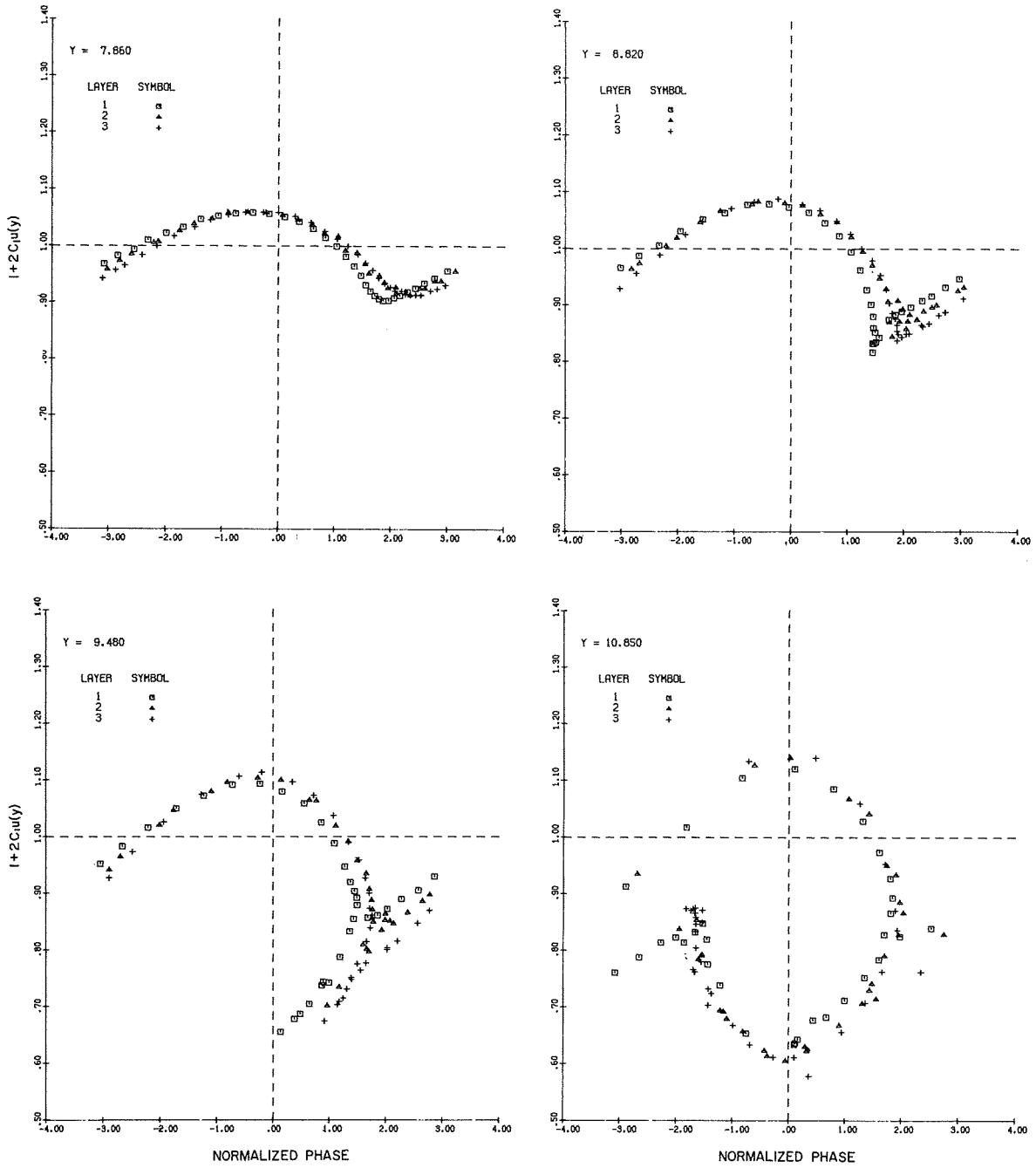


FIG. 5.18 RF VELOCITY OF THE BEAM ELECTRONS AS A FUNCTION OF NORMALIZED PHASE AT FOUR POSITIONS ALONG A BEAM-PLASMA AMPLIFIER. ( $C_1 = 0.110$ ,  $b_1 = 1.4$ ,  $Z_{01} = 312 \Omega$ ,  $v_c/\omega = 0$ ,  $f_p = 4.24$  GHz,  $f_b = 259$  MHz,  $f_c = 728$  MHz,  $f_s = 1.85$  GHz)

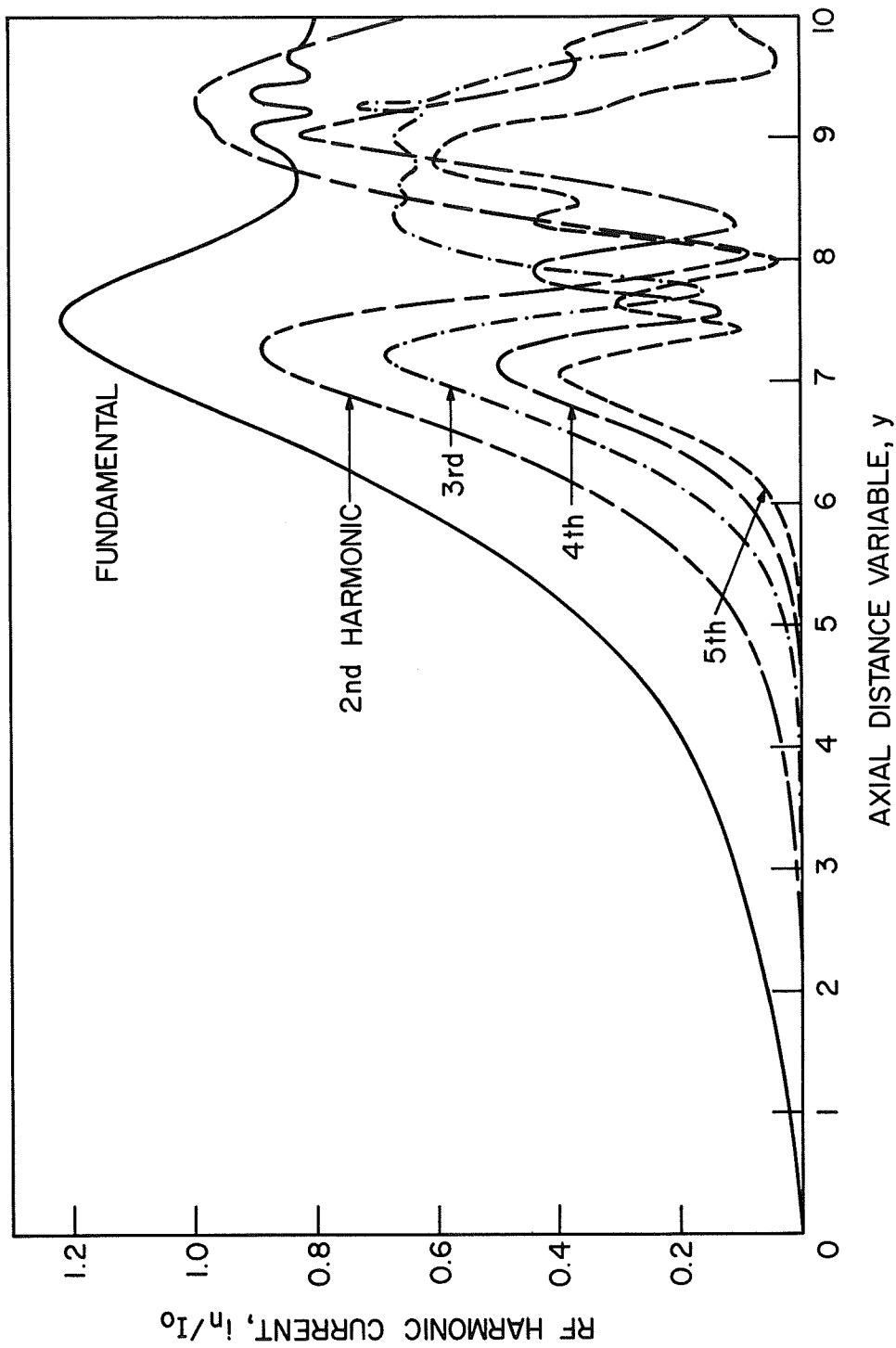


FIG. 5.19 RF HARMONIC CURRENTS AS A FUNCTION OF DISTANCE ALONG A BEAM-PLASMA AMPLIFIER WITH BEAM SPACE-CHARGE EFFECTS INCLUDED. ( $c_1 = 0.111$ ,  $b_1 = 0.8$ ,  $Z_{01} = 324 \Omega$ ,  $v_c/\omega = 0$ ,  $f_p = 4.24$  GHz,  $f_b = 259$  MHz,  $f_c = 728$  MHz,  $f_s = 1.79$  GHz)

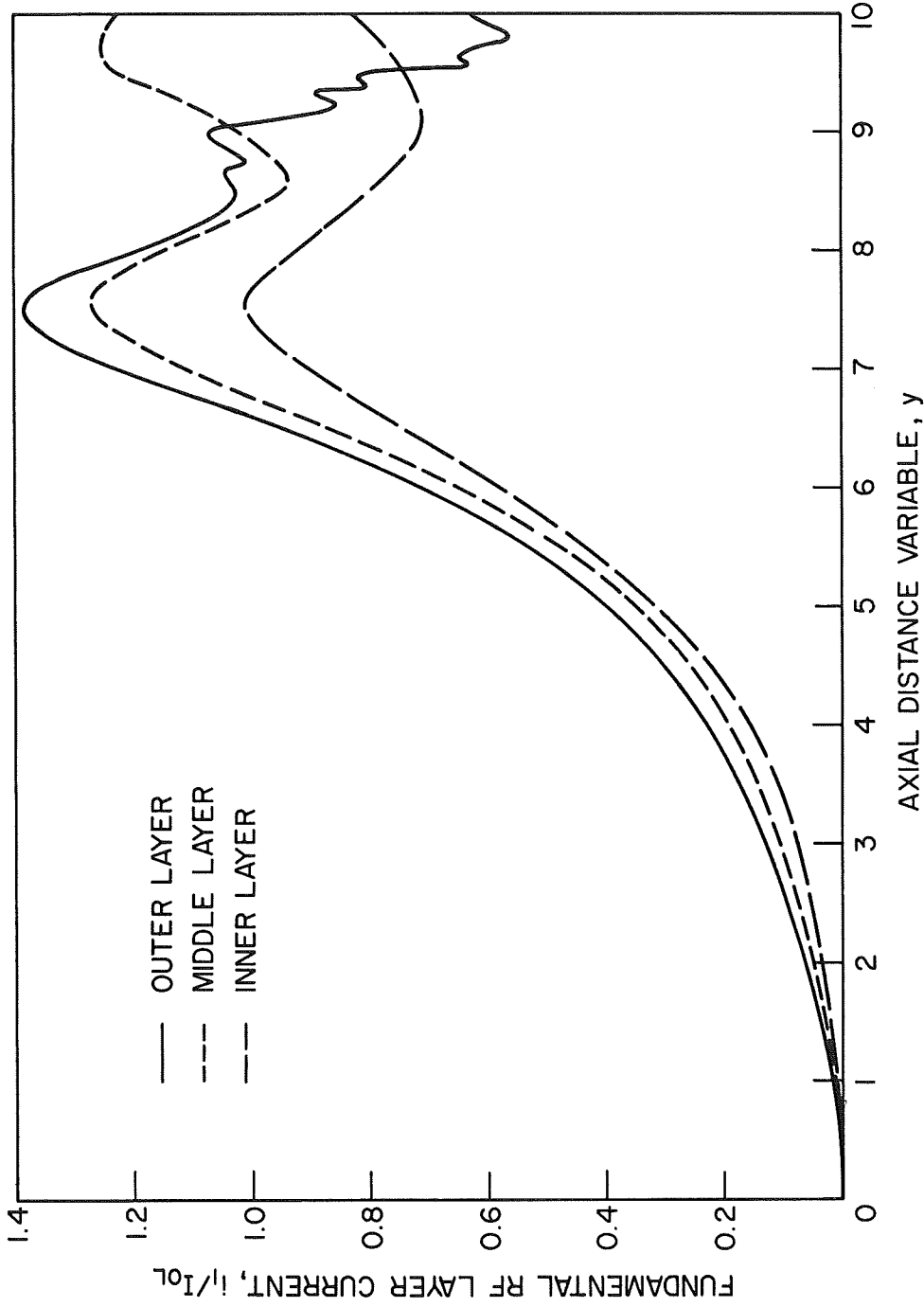


FIG. 5.20 FUNDAMENTAL RF CURRENTS IN THE THREE BEAM LAYERS AS A FUNCTION OF DISTANCE ALONG A BEAM-PLASMA

AMPLIFIER WITH BEAM SPACE-CHARGE EFFECTS INCLUDED. ( $c_1 = 0.111$ ,  $b_1 = 0.8$ ,  $Z_{o1} = 324 \Omega$ ,  $v_c/\omega = 0$ ,

$f_p = 4.24$  GHz,  $f_b = 259$  MHz,  $f_c = 728$  MHz,  $f_s = 1.79$  GHz)



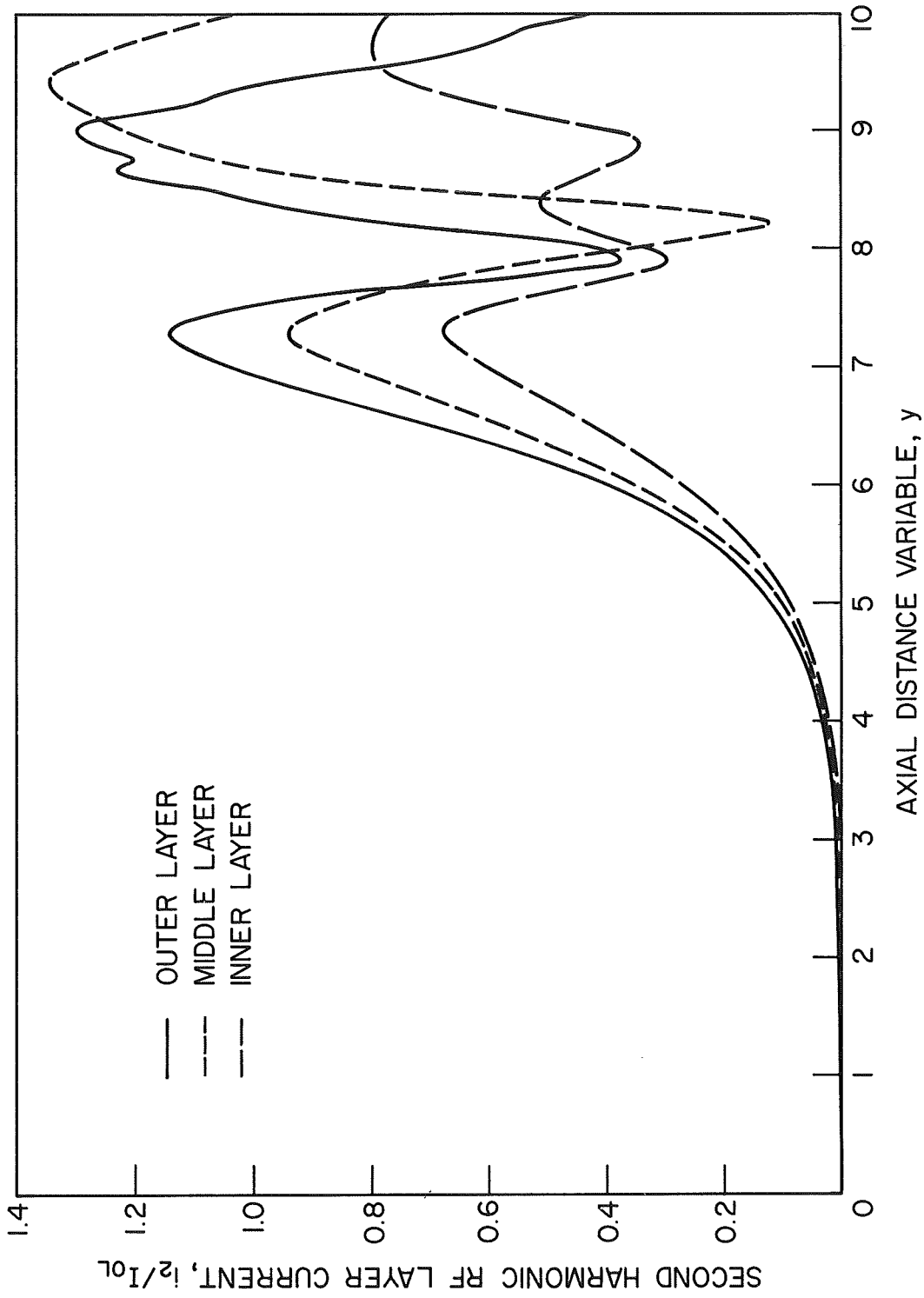


FIG. 5.21 SECOND HARMONIC CURRENTS IN THE THREE BEAM LAYERS AS A FUNCTION OF DISTANCE ALONG A BEAM-PLASMA

AMPLIFIER WITH BEAM SPACE-CHARGE EFFECTS INCLUDED. ( $c_1 = 0.111$ ,  $b_1 = 0.8$ ,  $Z_{01} = 324 \Omega$ ,  $v_c/\omega = 0$ ,  
 $f_p = 4.24$  GHz,  $f_b = 259$  MHz,  $f_c = 728$  MHz,  $f_s = 1.79$  GHz)

normalized with respect to their respective dc layer currents for the fundamental and the second harmonic, respectively. It should be noted that each harmonic has its first peak at a slightly larger interaction length than the next higher harmonic. There are subsequent peaks which may be higher than the first one or even those of lower harmonics. The significant observation from Figs. 5.20 and 5.21 is that the largest portion of the RF currents is near the surface of the electron beam until well past saturation.

Figure 5.22 shows the saturation gain and the conversion efficiency expected in a beam-plasma amplifier over the frequency range of 1.6 to 1.85 GHz. The effects of beam space charge are also shown.

All previous and subsequent figures, except Fig. 5.23, pertaining to the two-dimensional analysis apply to the previously stated operating conditions of  $V_0 = 520$  V,  $I_0 = 8.8$  mA and an axial magnetic field of 260 G, which is approximately 1.3 times the Brillouin field. Figure 5.23, however, is for  $V_0 = 570$  V,  $I_0 = 8.4$  mA and a magnetic focusing field of 485 G, which is approximately 2.4 times the Brillouin field. By comparing with Fig. 5.22 it may be noticed that the gain is not much different but that the conversion efficiency is a few percent less. Inspection of electron trajectory plots similar to Fig. 5.16 reveals that for this higher focusing field the beam electrons have smaller excursions from their radial starting positions. With the interaction being with the surface wave on the plasma column, the beam electrons remain in a lower "circuit" field, and hence a weaker dc to RF conversion results.

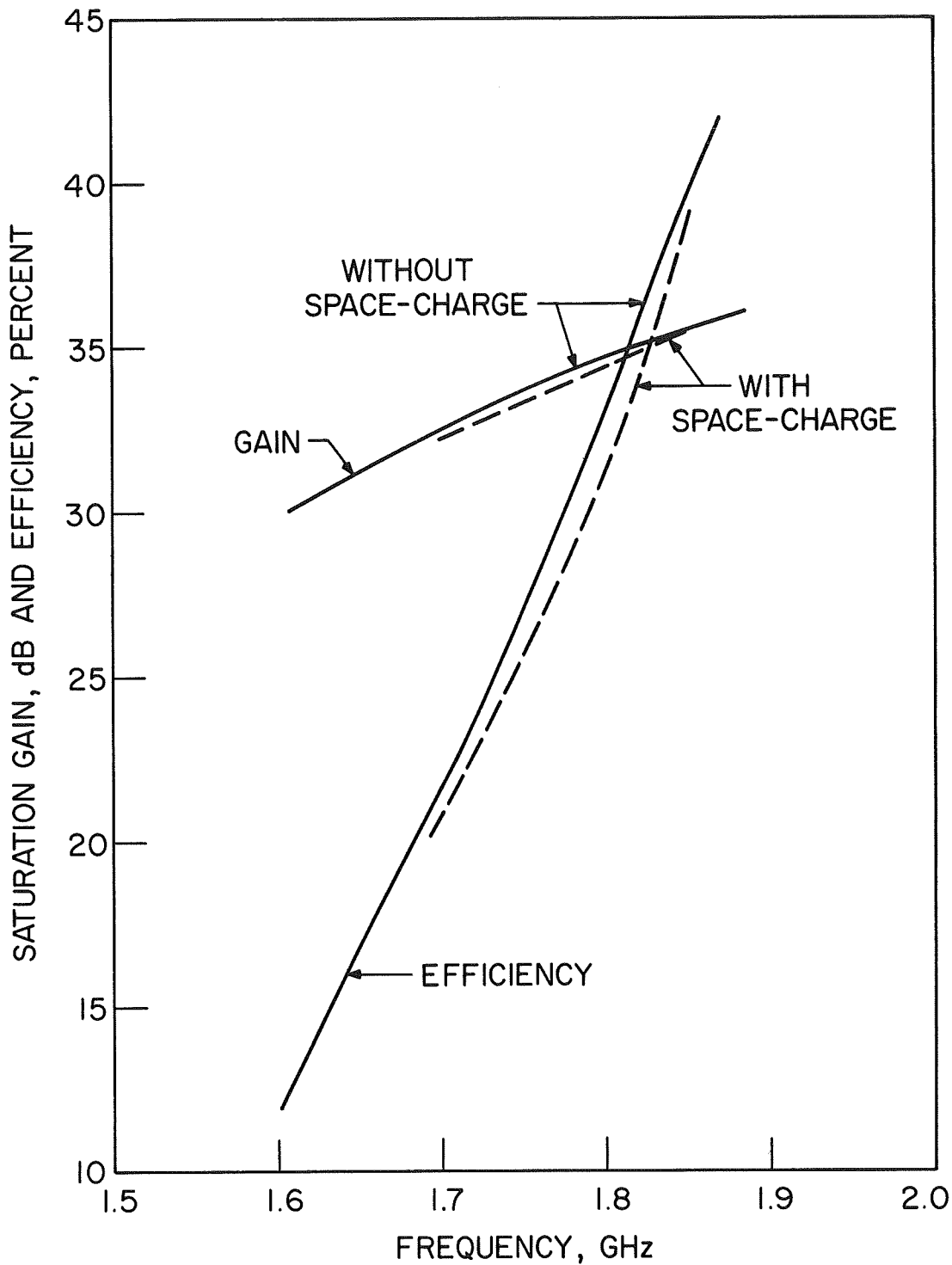


FIG. 5.22 SATURATION GAIN AND EFFICIENCY AS A FUNCTION OF FREQUENCY IN A BEAM-PLASMA AMPLIFIER. ( $v_c/\omega = 0$ ,  $f_p = 4.24$  GHz,  $f_b = 259$  MHz,  $f_c = 728$  MHz)

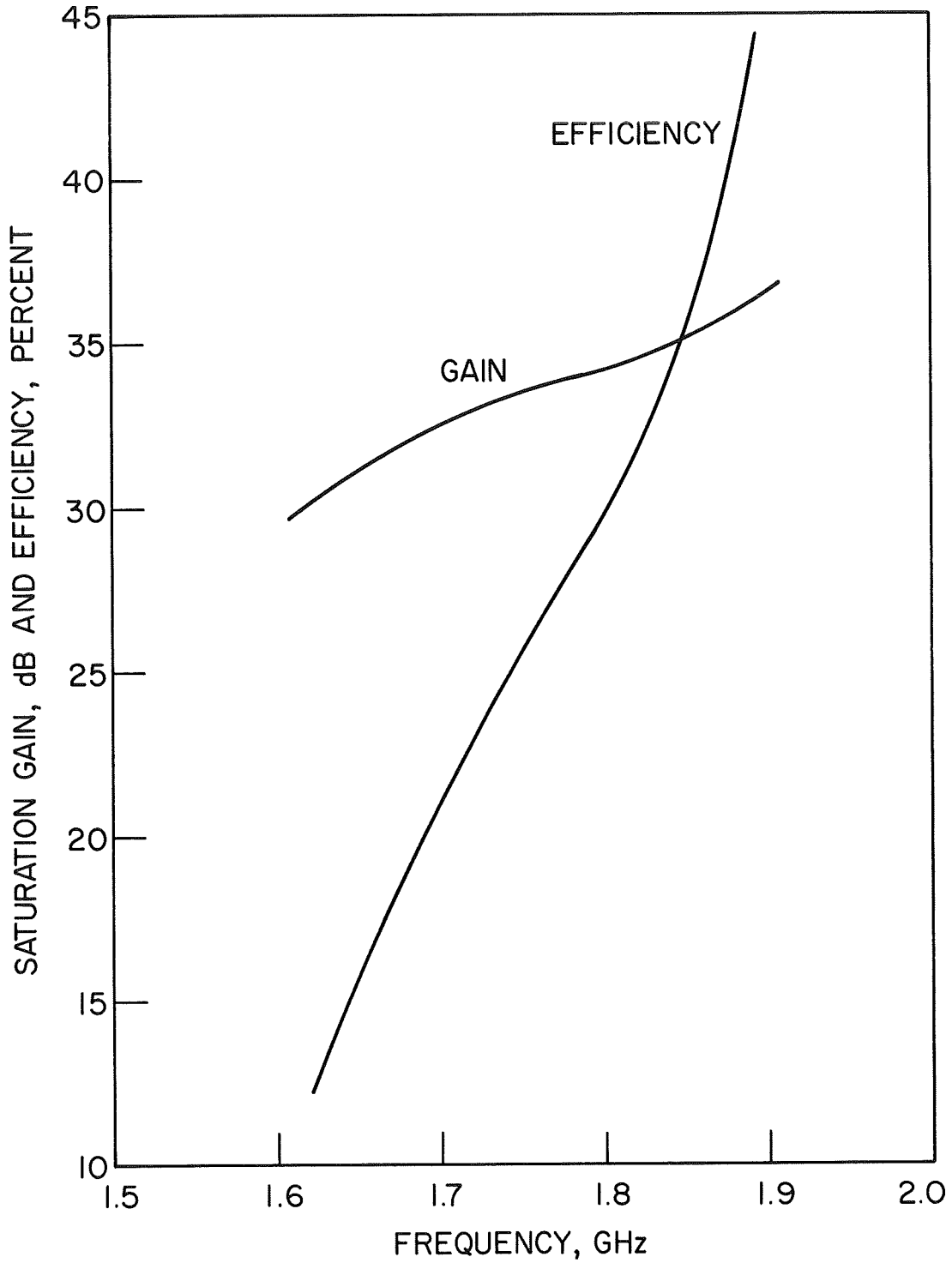


FIG. 5.23 SATURATION GAIN AND EFFICIENCY AS A FUNCTION OF FREQUENCY IN A BEAM-PLASMA AMPLIFIER. ( $\nu_c/\omega = 0$ ,  $f_p = 4.17$  GHz,  $f_b = 247$  MHz,  $f_c = 1.357$  GHz)

In Fig. 5.24 the results of many computer runs similar to that for Fig. 5.19 are summarized. The harmonic currents for the higher values of  $n$  peak within a shorter interaction distance; however, all RF currents peak before the circuit voltage amplitude does. This is explained by the fact that saturation of the device actually occurs when in addition to the initial electron bunch, which gives energy to the wave, a second bunch is formed, which is in the accelerating phase of the circuit wave, taking energy from the wave. At saturation the transfer of energy between these bunches and the wave is balanced so that there is no net transfer of energy between the stream and the wave. At that point the circuit voltage amplitude has its maximum. The current maxima, however, are expected to be at the position where the initial bunch is tightest, which occurs somewhat sooner.

Figure 5.25 is again a composite of a number of computer runs. It shows that the RF currents are highest in the vicinity of beam-wave synchronism, where the tightest bunches occur. As the beam voltage is increased above synchronism the RF current maxima are seen to fall off markedly. This is directly connected with the explanation given in the previous paragraph, where it was pointed out that the maximum RF current amplitude occurs for tightest electron bunching and not necessarily for maximum stream nonlinearity. As Fig. 5.26 shows, the voltage amplitude, gain and efficiency increase with  $b_1$  due to the fact that the initial bunch can slow down more and hence give up more energy before it reaches the optimum position in the decelerating phase, if it initially traveled somewhat faster than the wave. When  $b_1$  is increased, however, the

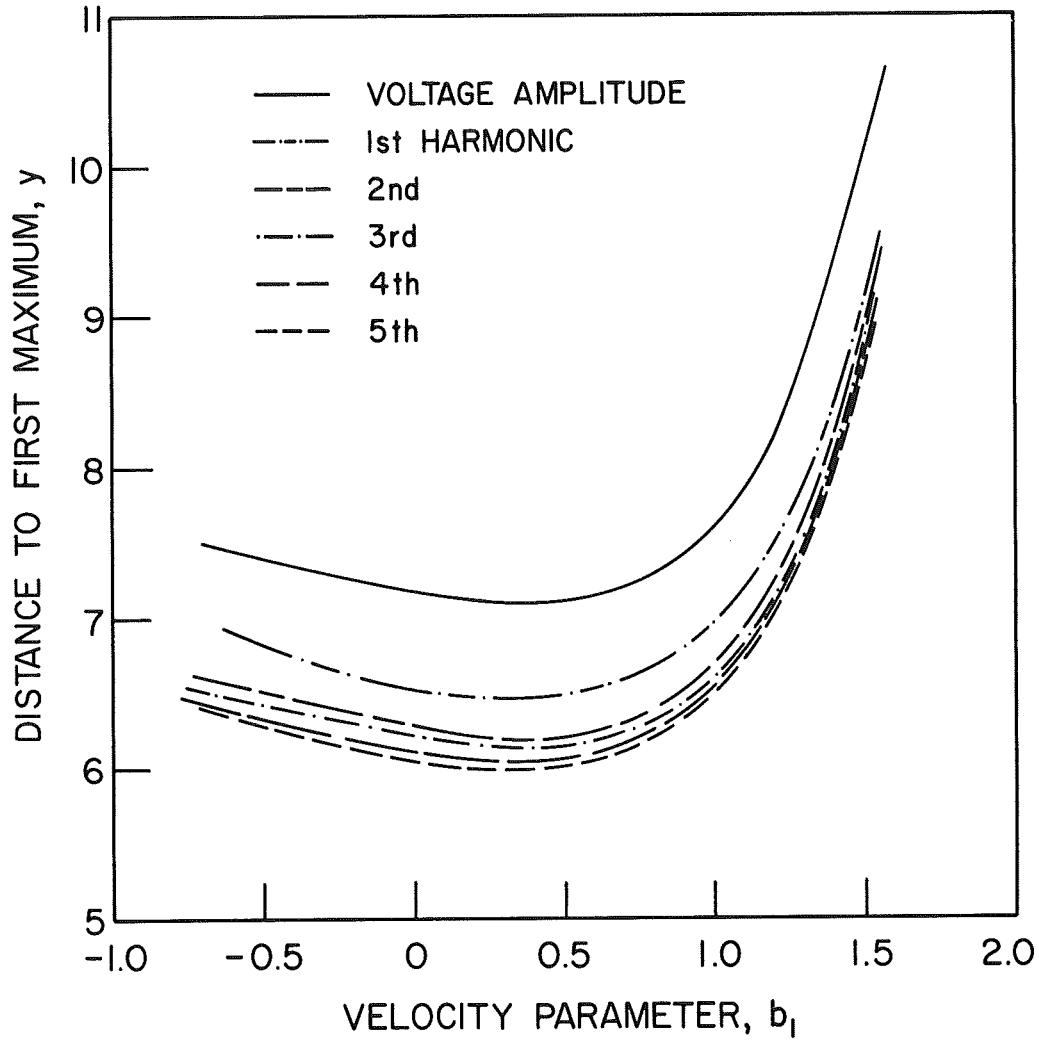


FIG. 5.24 POSITION OF FIRST MAXIMA IN THE VOLTAGE AMPLITUDE,  $A_1(y)$ , AND THE HARMONIC CURRENTS AS A FUNCTION OF  $b_1$ . ( $C_1 = 0.113$ ,  $Z_{o1} = 340 \Omega$ ,  $v_c/\omega = 0$ ,  $f_p = 4.24$  GHz,  $f_b = 259$  MHz,  $f_c = 728$  MHz,  $f_s = 1.7$  GHz)

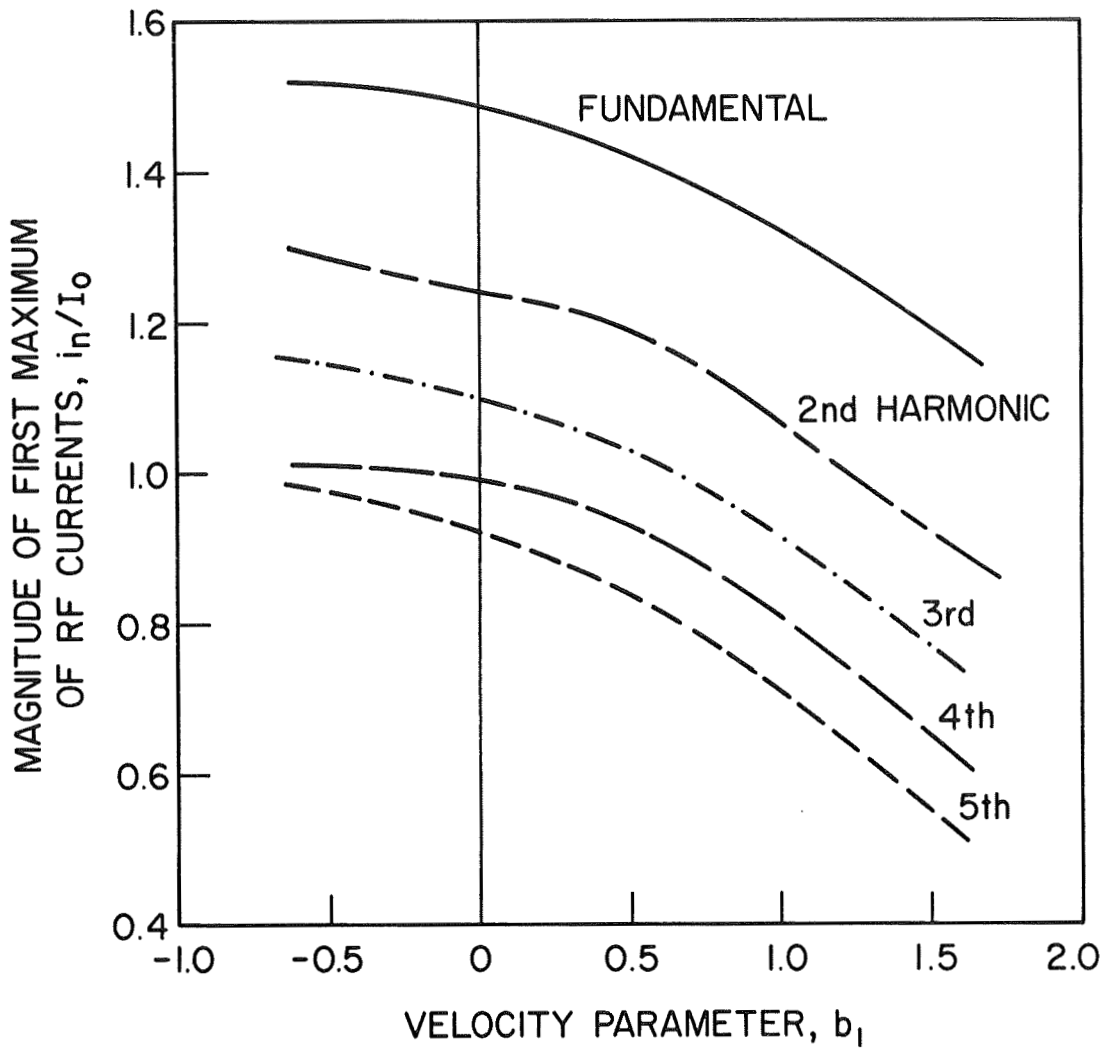


FIG. 5.25 MAXIMUM VALUES OF THE RF CURRENTS AS A FUNCTION OF  $b_1$ . ( $C_1 = 0.113$ ,  $Z_{o1} = 340 \Omega$ ,  $v_c/\omega = 0$ ,  $f_p = 4.24$  GHz,  $f_b = 259$  MHz,  $f_c = 728$  MHz,  $f_s = 1.7$  GHz)

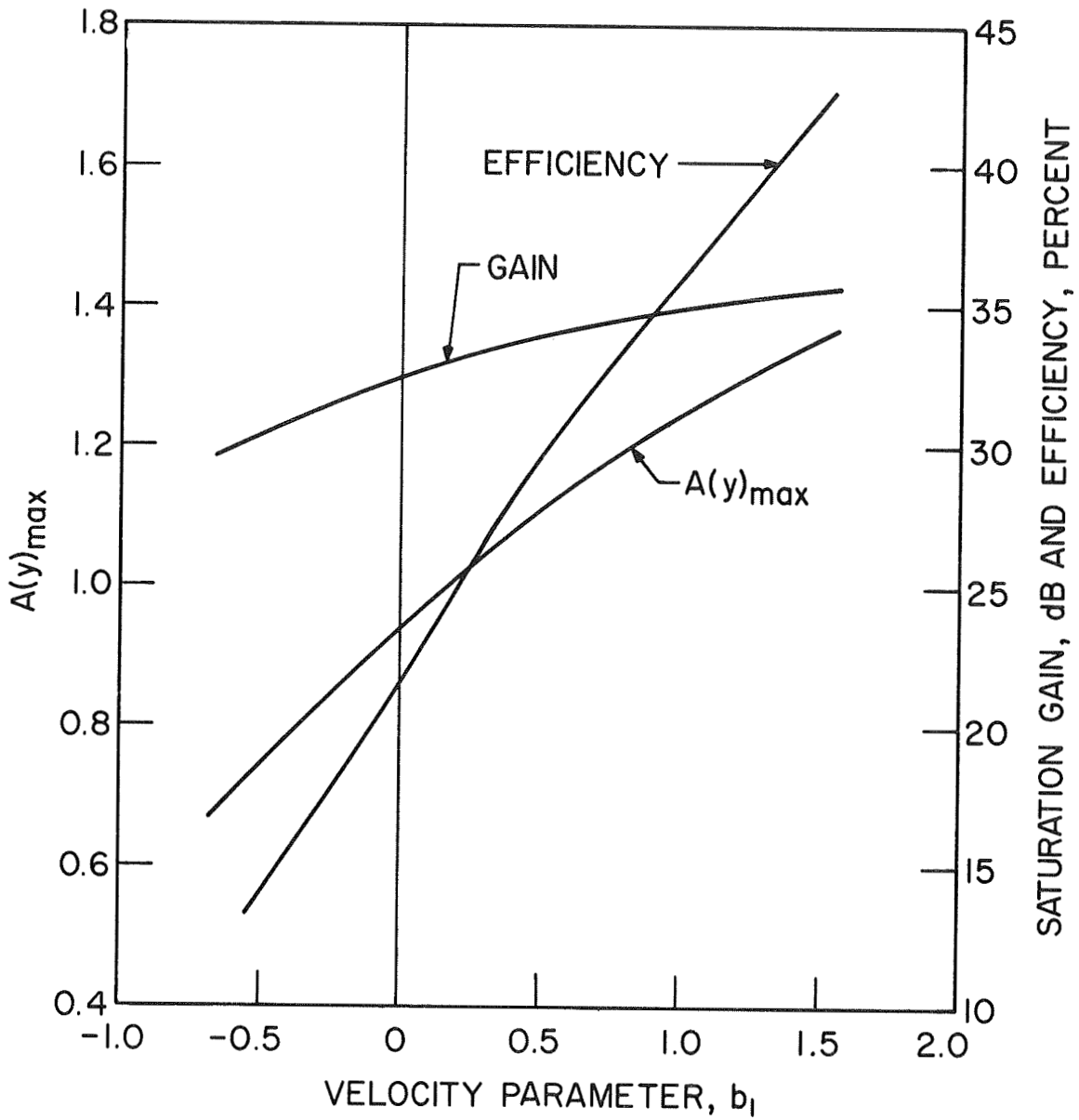


FIG. 5.26 MAXIMUM VALUES OF THE VOLTAGE AMPLITUDE, SATURATION GAIN AND EFFICIENCY AS A FUNCTION OF  $b_1$ . ( $C_1 = 0.113$ ,  $Z_{o1} = 340 \Omega$ ,  $v_c/\omega = 0$ ,  $f_p = 4.24$  GHz,  $f_b = 259$  MHz,  $f_c = 728$  MHz,  $f_s = 1.7$  GHz)



individual stream electrons stay out of synchronism longer. Consequently, the bunching is not as efficient and the RF currents are not as high for larger values of  $b_1$ , as Fig. 5.25 shows.

In comparing these results with those for the one-dimensional calculations two facts should be noted. First, maximum values of gain and efficiency are predicted for lower values of  $b_1$  in the two-dimensional analysis. This is attributed to the importance of radial effects in the model analyzed. Second, the RF currents shown in Fig. 5.25 are seen to decrease as  $b_1$  is raised, while the voltage amplitudes shown in Figs. 5.6 and 5.26 increase as  $b_1$  is raised. It should be noted that the maxima in the RF currents do not occur at the same y-position as the maxima in the voltage amplitudes. Thus these results are not inconsistent with each other in view of the explanations given in the two previous paragraphs.

### 6.1 Description of the Experimental Apparatus

In the theoretical considerations described so far many simplifying assumptions were made, such as the equivalent circuit representation of a plasma, linearity of the plasma, neglect of angular or radial variations, and neglect of nonuniformities. The only reliable check on the validity of these assumptions is an experimental study. To this end a fairly versatile test vehicle was constructed and tested.

6.1.1 Vacuum System. A diagram showing the vacuum system and the location of the beam-plasma device may be seen in Fig. 6.1. A 750 l/s NRC oil diffusion pump was used along with a Welch Model 1397 mechanical pump. A liquid nitrogen trap prevented oil from the diffusion pump from backstreaming into the device. A pressure of approximately  $2 \cdot 10^{-8}$  Torr could be maintained above the cold trap. Pressure measurements were made using a Varian Dual Range Ionization Control Unit. The ultrahigh vacuum (UHV) gauge was located immediately above the cold trap, whereas the millitorr (MT) gauge was located close to the device under test. During operation of the device the valve located in the upper right-hand corner of Fig. 6.1 was kept closed and gas was introduced from the xenon gas supply and regulated by means of a Granville-Phillips variable leak valve. Thus pressures in the range from  $5 \cdot 10^{-7}$  Torr to  $1 \cdot 10^{-1}$  Torr could be maintained in the device and monitored fairly accurately with the MT gauge. The vacuum in the electron gun region was approximately one order of magnitude better than in the rest of the

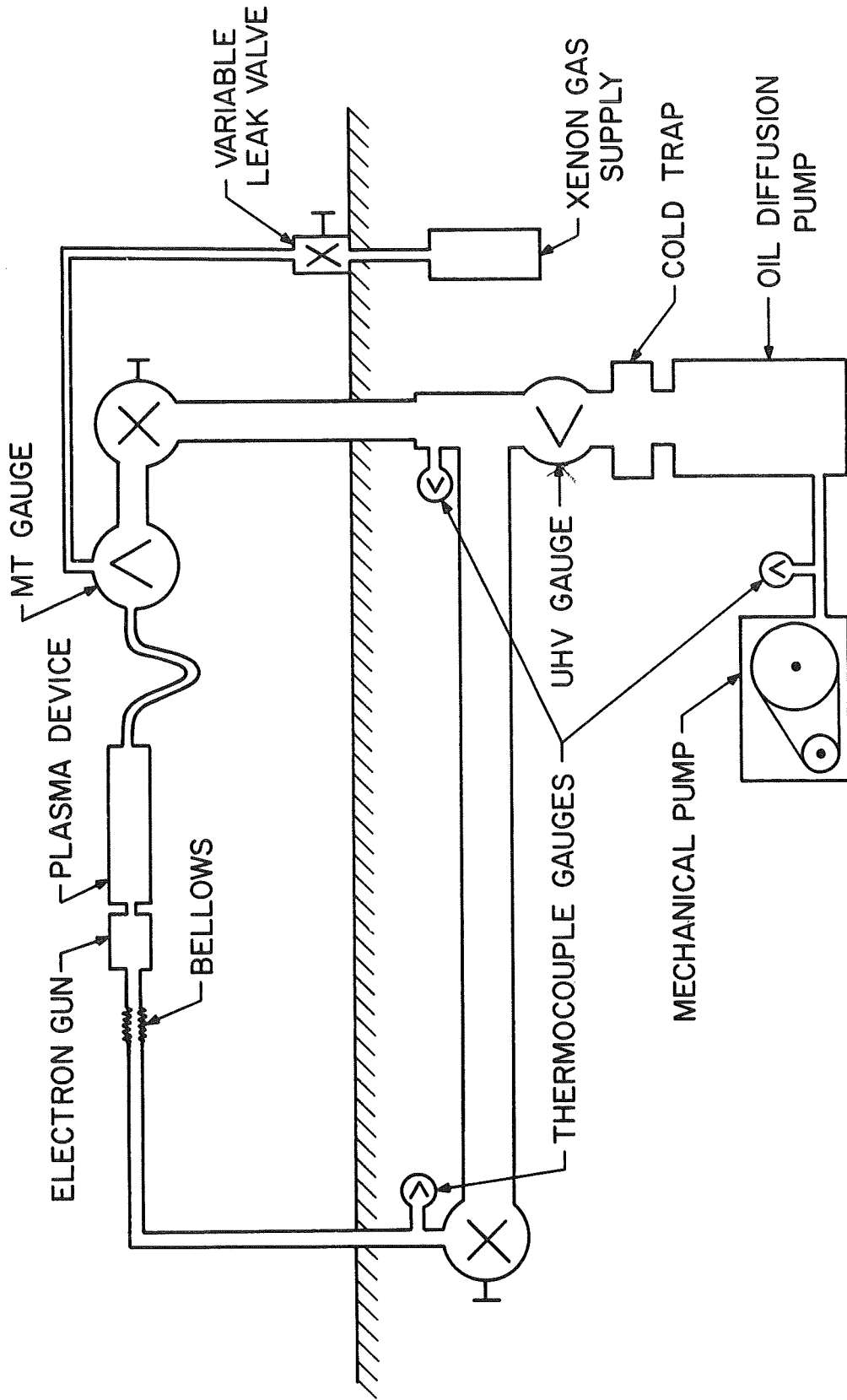


FIG. 6.1 VACUUM SYSTEM.

plasma device due to differential pumping through the small beam tunnel between the gun and the plasma region. The stainless steel bellows and the small copper tubing at the opposite end of the device allowed the device to be moved slightly under vacuum for purposes of alignment with the magnetic field. Since the beam-plasma device was of metal-ceramic construction, the whole system could be baked prior to operation. In view of this and since the test vehicle was continuously pumped, there did not appear to be any contamination of the xenon gas during operation. Research grade xenon with a purity of 99.995 percent by volume was used.

6.1.2 Test Vehicle. Figure 6.2 is a diagram of the beam-plasma device, while Fig. 6.3 shows a photograph of the completely assembled device. As mentioned above, metal-ceramic construction was used. In construction the metal-ceramic brazes were made first and small units containing the gun, plasma cathodes and collector were assembled. These are pictured in Fig. 6.4. As the final assembly step these units were heliarc welded together.

The electron gun was a conventional Pierce-type gun with a dispenser cathode. It could operate up to voltages of several kV with unity microperveance. The design diameter of the electron beam was 2.5 mm. The gun envelope and the pole piece in front of the gun were made of kovar in order to exclude the magnetic field from the gun region. In spite of this some flux did apparently penetrate and could not be compensated for. As a result of this and mechanical misalignments the electron beam was found to ripple and the interception on subsequent electrodes was found to be substantial under some conditions.

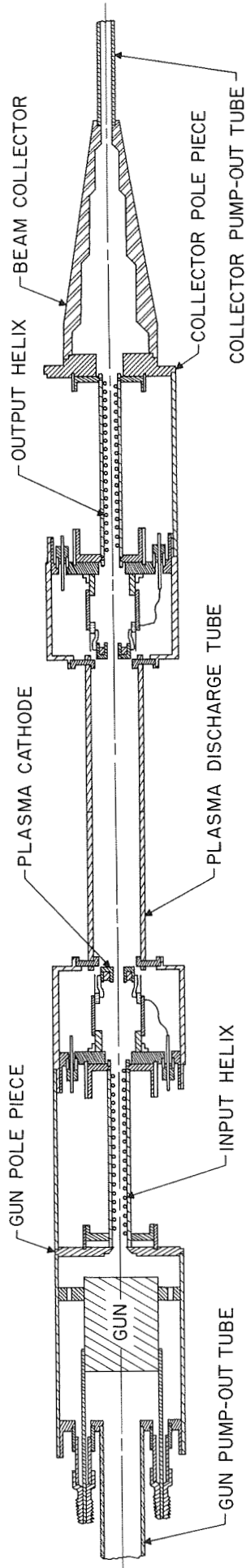


FIG. 6.2 DIAGRAM OF THE BEAM-PLASMA DEVICE.

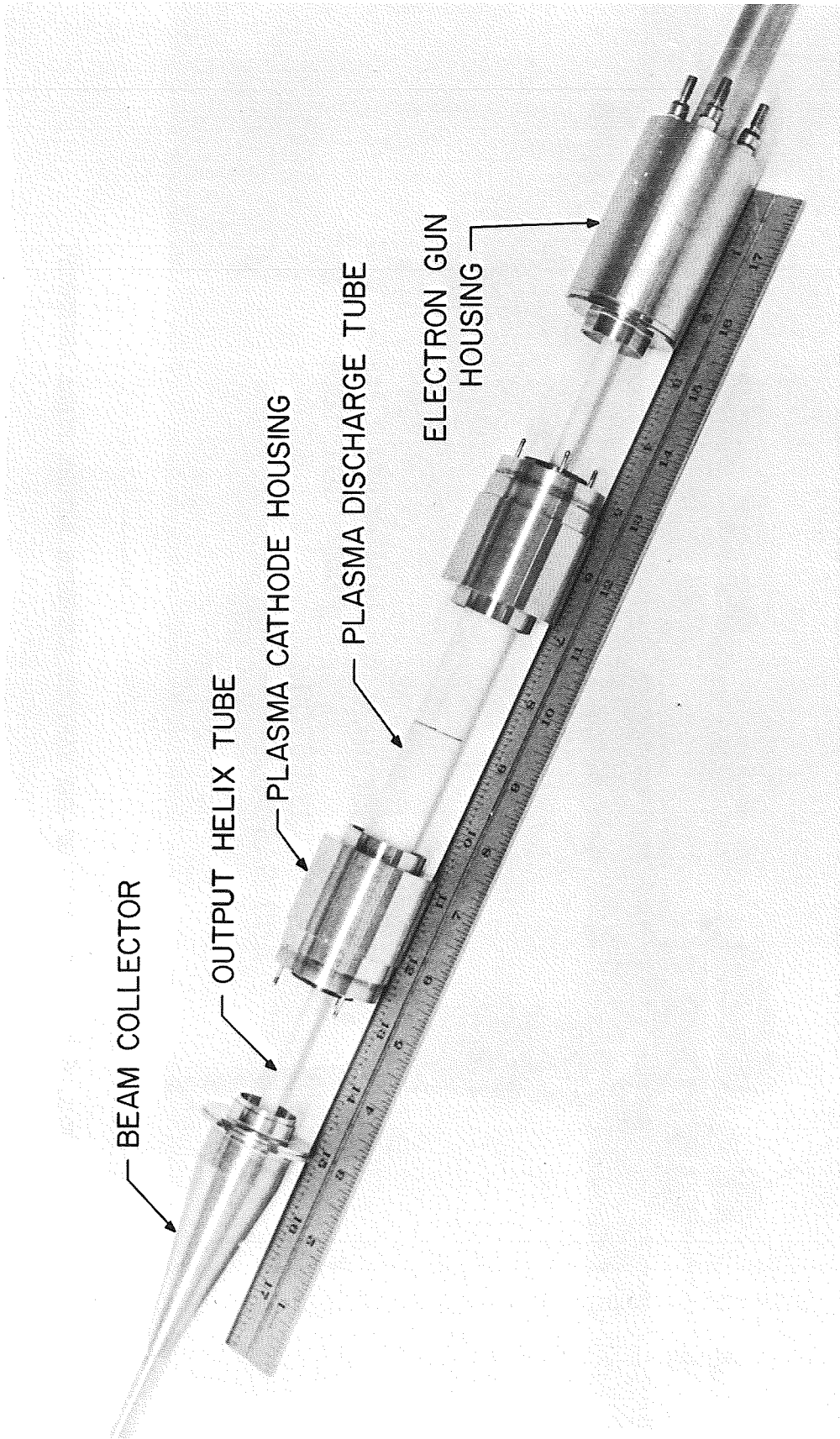


FIG. 6.3 PHOTOGRAPH OF THE COMPLETED BEAM-PLASMA DEVICE.

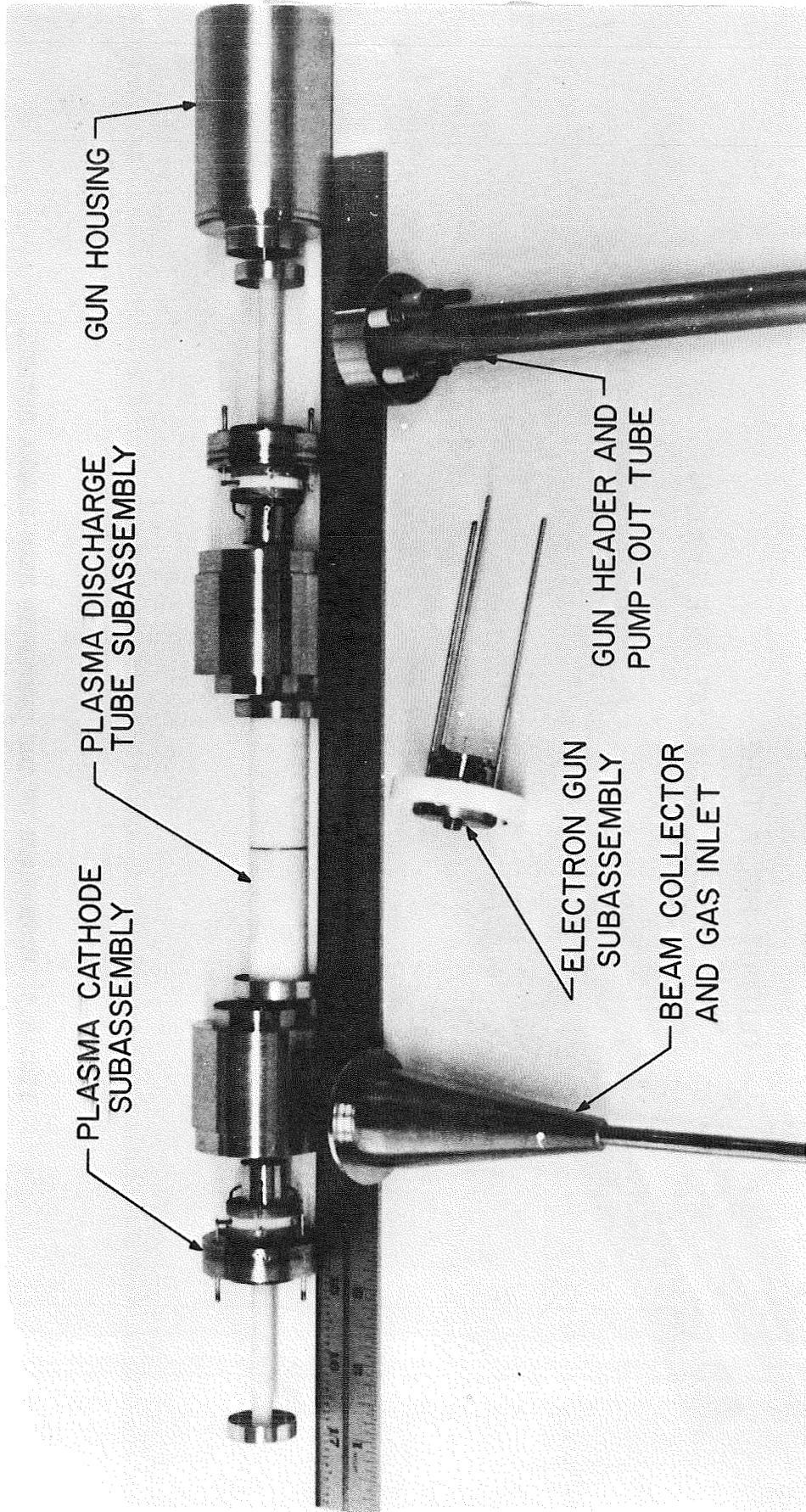


FIG. 6.4 PHOTOGRAPH OF THE VARIOUS SUBUNITS BEFORE FINAL ASSEMBLY.

In order to premodulate the electron beam before entering the plasma region, a short section of helical RF structure was placed immediately following the gun. This helix was of the type commonly used in traveling-wave tubes. Some of its characteristics are shown in Table 6.1. The dielectric loading factor (DLF) is quite low. This is due to the fact that the helix is placed in direct contact with the ceramic cylinder containing it. Even though this method of mounting the helix would not be desirable in a traveling-wave amplifier due to the high loss, it is acceptable here where little gain is desired in the helix sections.

Table 6.1

RF Helix Parameters

I.D.	3.91 mm
O.D.	4.93 mm
Pitch	1.37 mm
DLF	0.65
Synchronous Voltage	~1000 V
$\lambda_g$ at 2 GHz	1.0 cm
Interaction Length	5.0 cm

The plasma cathodes were dispenser cathodes with a fairly porous tungsten matrix (Semicon Associates, Type S-75). The high porosity insured a copious supply of barium at the emitting surface, even when poisoning might be expected to be quite high at the higher pressures. At a temperature of 1050°C a hot-cathode Penning discharge of several



hundred milliamperes could be created by a voltage of 25 to 30 V applied between the cathode and the ground electrode adjacent to it with the xenon pressure in the  $10^{-2}$  Torr region. A double-ended discharge was used to insure a more uniform axial plasma density. The plasma region was approximately 10.5 cm long.

An output helix identical to the input helix was used for demodulating the electron beam after emerging from the plasma interaction region. A beam collector surrounded by a water jacket was used for dissipating the spent electron beam.

6.1.3 RF Couplers. Two means of coupling RF energy into and out of the beam-plasma device were employed. One made use of coupled-helix couplers<sup>74</sup> which are employed extensively in traveling-wave tubes. The coupler is a short section of helix, about two to three turns long and wound in the direction opposite to that of the helix in the beam-plasma device. It is essentially an impedance transformer that can be adjusted to match the  $50 \Omega$  impedance of a coaxial line to the substantially higher impedance of the interaction helix. Two such couplers are shown in Fig. 6.5. Since they could not be slipped over the helix from either end after the beam-plasma device was assembled, it was necessary to make the couplers demountable so they could be assembled and disassembled on the device. Measurements indicated that a good RF match ( $VSWR < 3.0$ ) could be obtained from 1.5 to 3.6 GHz. The coupling loss was approximately 1.5 dB per coupler.

The other means of coupling consisted of elliptic cavity couplers which could be placed directly around the plasma discharge region of Fig. 6.2. The RF energy launched by an antenna at one focus of an

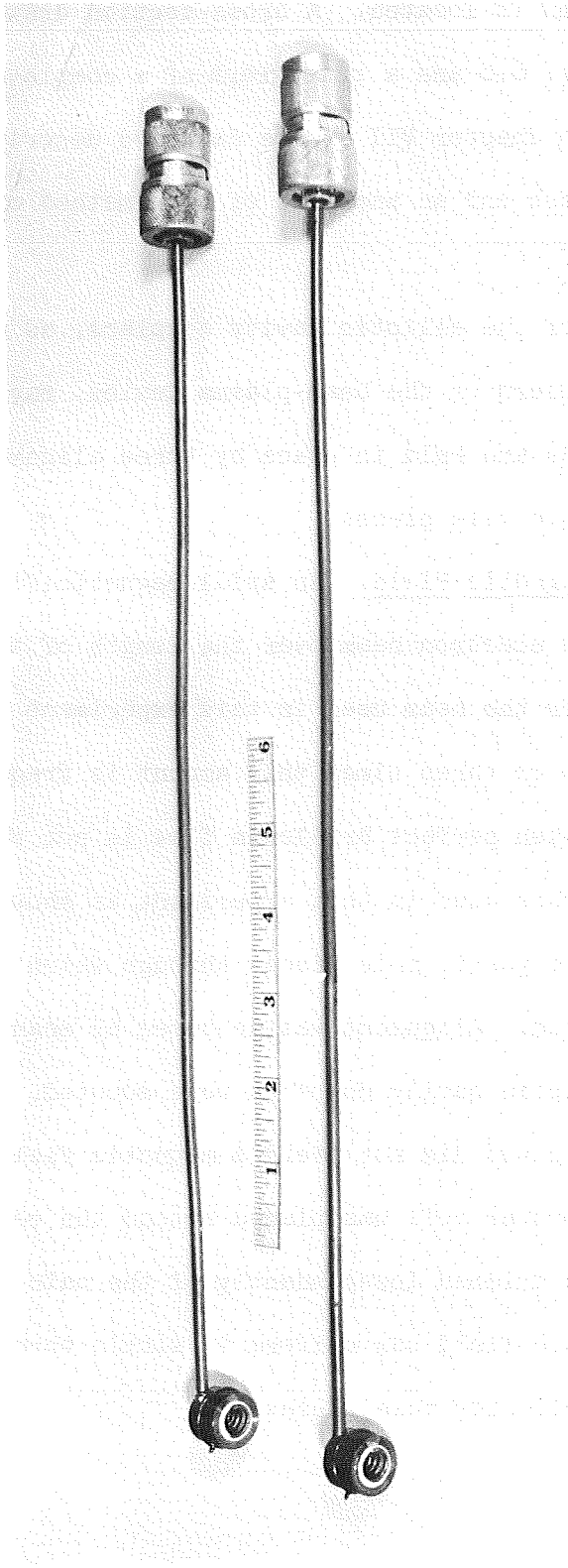


FIG. 6.5 COUPLED-HELIX COUPLERS.

elliptic cavity is transferred phase coherently to the other focus, where the plasma column is located. A cross-section drawing of such a cavity is shown in Fig. 6.6 and a photograph of a completed cavity is shown in Fig. 6.7. In Chapter VII a more detailed description of elliptic cavity couplers and an analysis of this method of coupling will be given.

The placement of the elliptic cavity couplers, as well as one of the coupled-helix couplers on the beam-plasma device, may be seen in Fig. 6.8. The cavities are held in place by three alignment rods inserted in the magnetic pole pieces.

6.1.4 Axial Magnetic Field. An axial magnetic field is necessary to focus the electron beam over the length of the device. The Brillouin field for the beam used in this experiment is approximately 200 G. A value of two or three times this amount is frequently necessary in experimental work when perfect Brillouin flow is not obtainable. Three magnetic coils were used in this experiment, as shown in Fig. 6.9. The two end coils had magnetic pole pieces through which the beam-plasma device could be inserted. Alignment was achieved by means of the three rods on which the elliptic cavity couplers were mounted. Use of the two end coils by themselves did not yield a magnetic field of sufficient uniformity. Thus a booster coil was placed around the center of the device. Its field was trimmed independently of the main field so that the total axial magnetic field was uniform to within three or four percent between the gun and collector pole pieces.

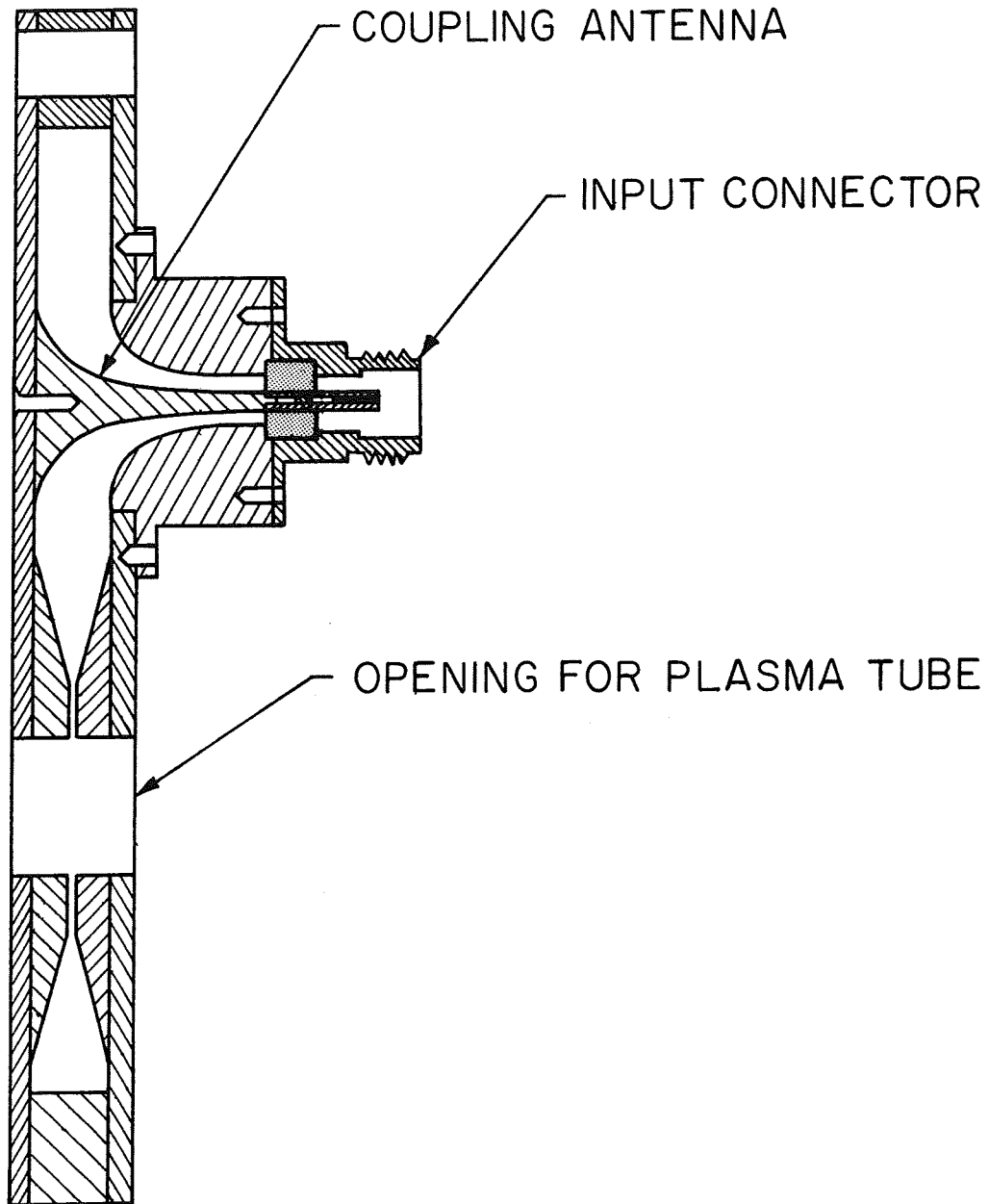


FIG. 6.6 DIAGRAM OF AN ELLIPTIC CAVITY COUPLER.

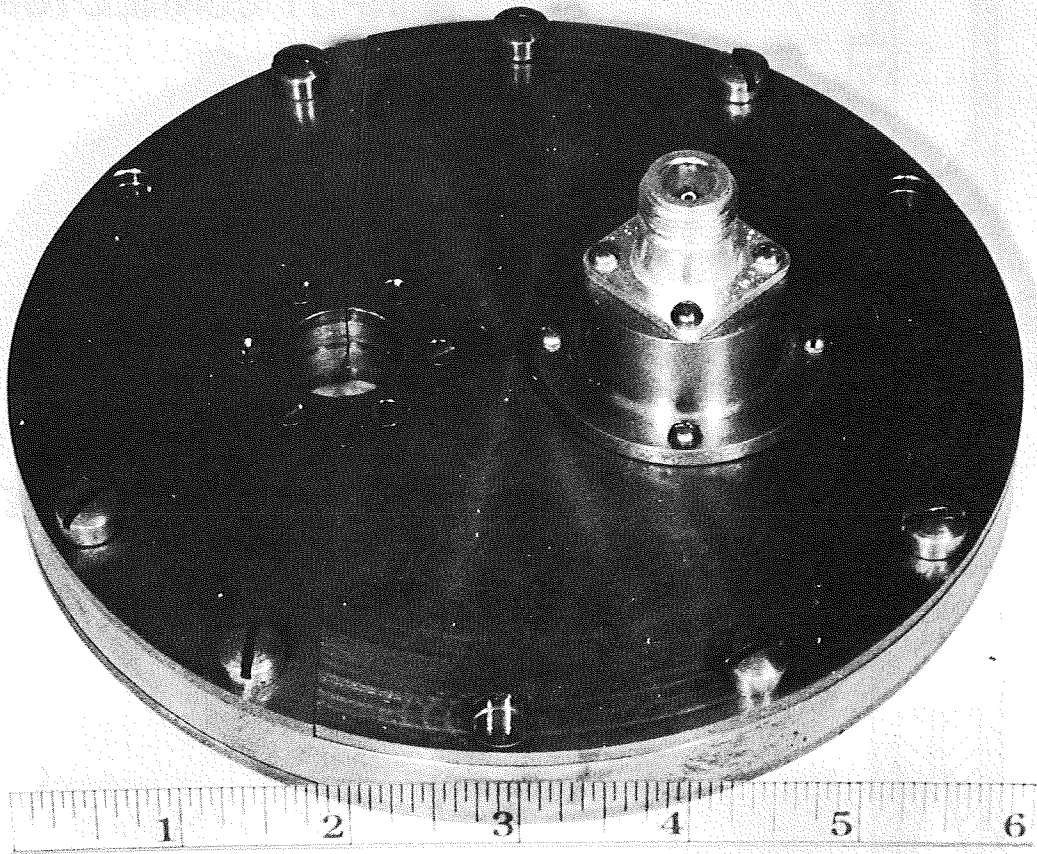


FIG. 6.7 PHOTOGRAPH OF AN ELLIPTIC CAVITY COUPLER.

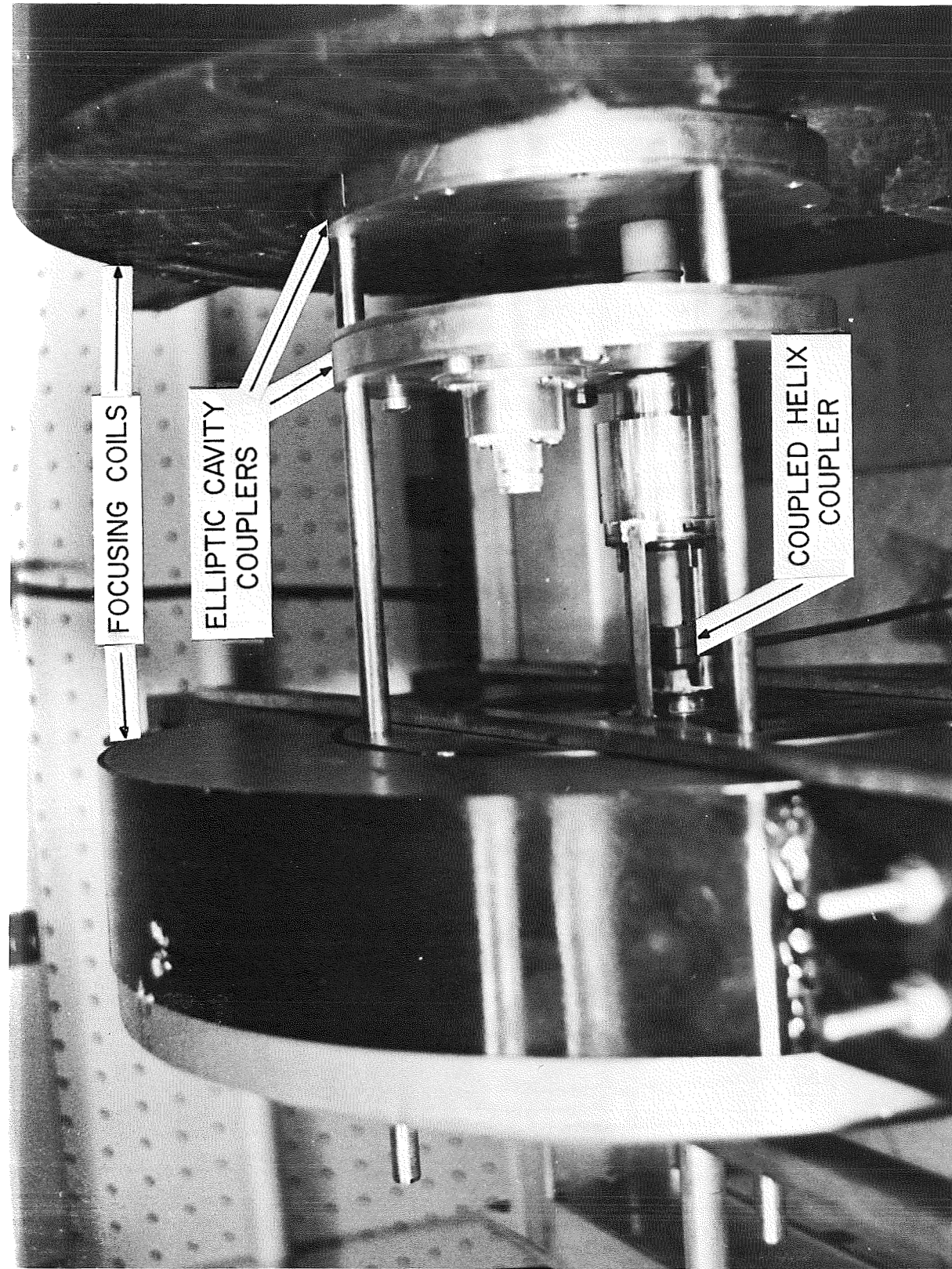


FIG. 6.8 PLACEMENT OF RF COUPLERS ON THE BEAM-PLASMA DEVICE.



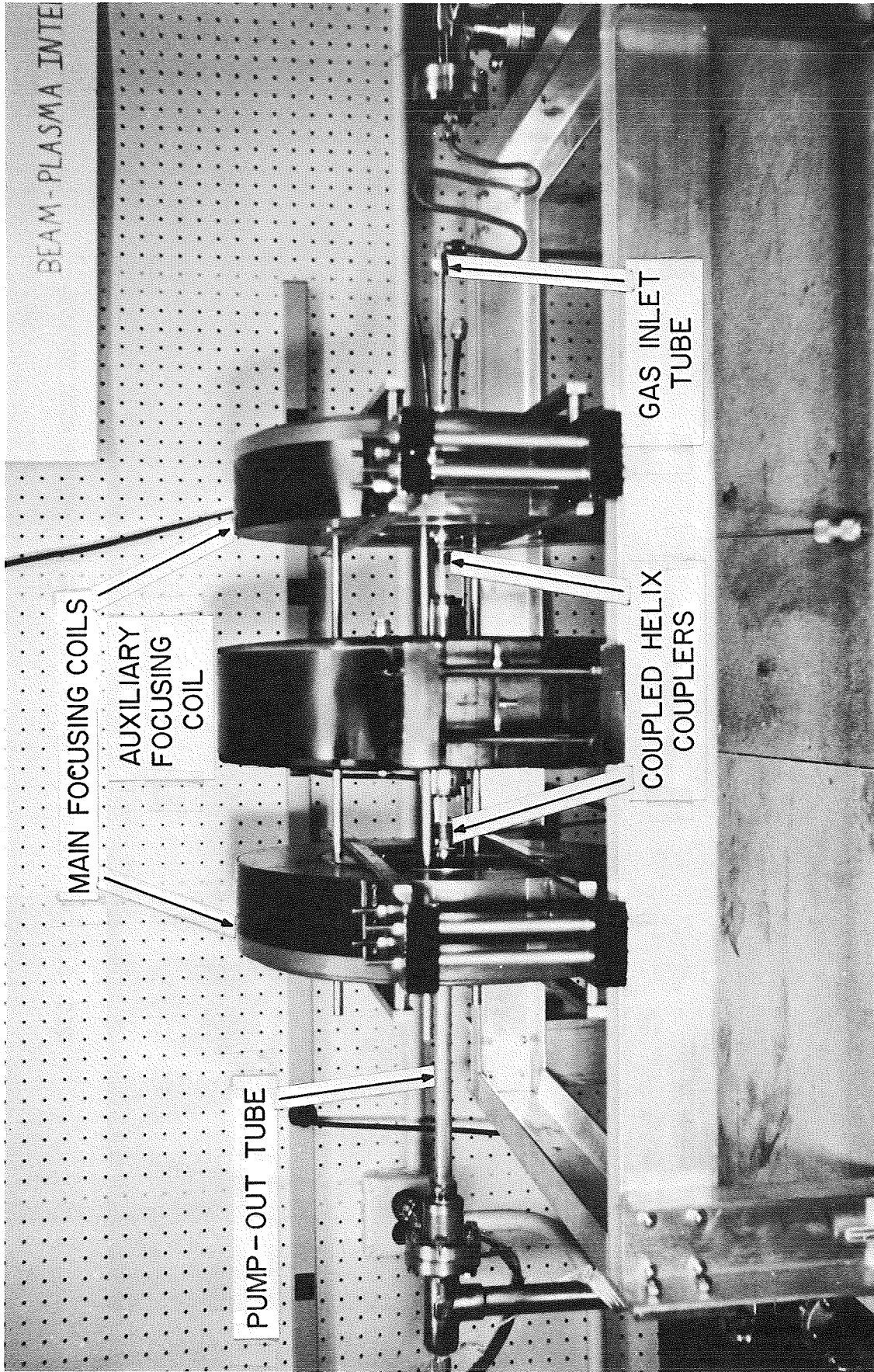


FIG. 6.9 MAGNETIC FIELD COILS FOR FOCUSING THE ELECTRON BEAM.

## 6.2 Characteristics of the Xenon Plasma Column

The gas to be used in the beam-plasma experiments was chosen to be xenon. The reason for the choice was that xenon is a noble gas with a quite high ionization cross section.<sup>70</sup> This may be expected to yield a sufficiently dense plasma at relatively low pressures. Thus cathode poisoning would be minimized.

In the course of the experimental work two methods of generating a plasma were employed: hot-cathode discharge and beam-generated plasma. It was anticipated at the beginning of the experimental work that the hot-cathode discharge plasma would be used almost exclusively. During the course of the experimental work it was found, however, that the beam-generated plasma had certain features that recommended it for extensive use in many of the large-signal measurements. One of the important considerations was that the beam-generated plasma could be maintained at lower gas pressures. This in turn yielded considerably better RF performance.

6.2.1 Measurement of Plasma Density in the Plasma Tester. Before the final beam-plasma device was constructed, the plasma tester shown in Fig. 6.10 was constructed out of glass. It consisted only of the center section of the beam-plasma device shown in Fig. 6.2 without gun, collector and the two helices. The electrode configuration in the plasma discharge section was, however, simulated as closely as possible. Figure 6.11 shows a diagram of the plasma tester. A double probe was placed at the middle of the plasma column near the point where the highest plasma density along the radial direction was expected. The results of measurements with the double probe are shown in Fig. 6.12



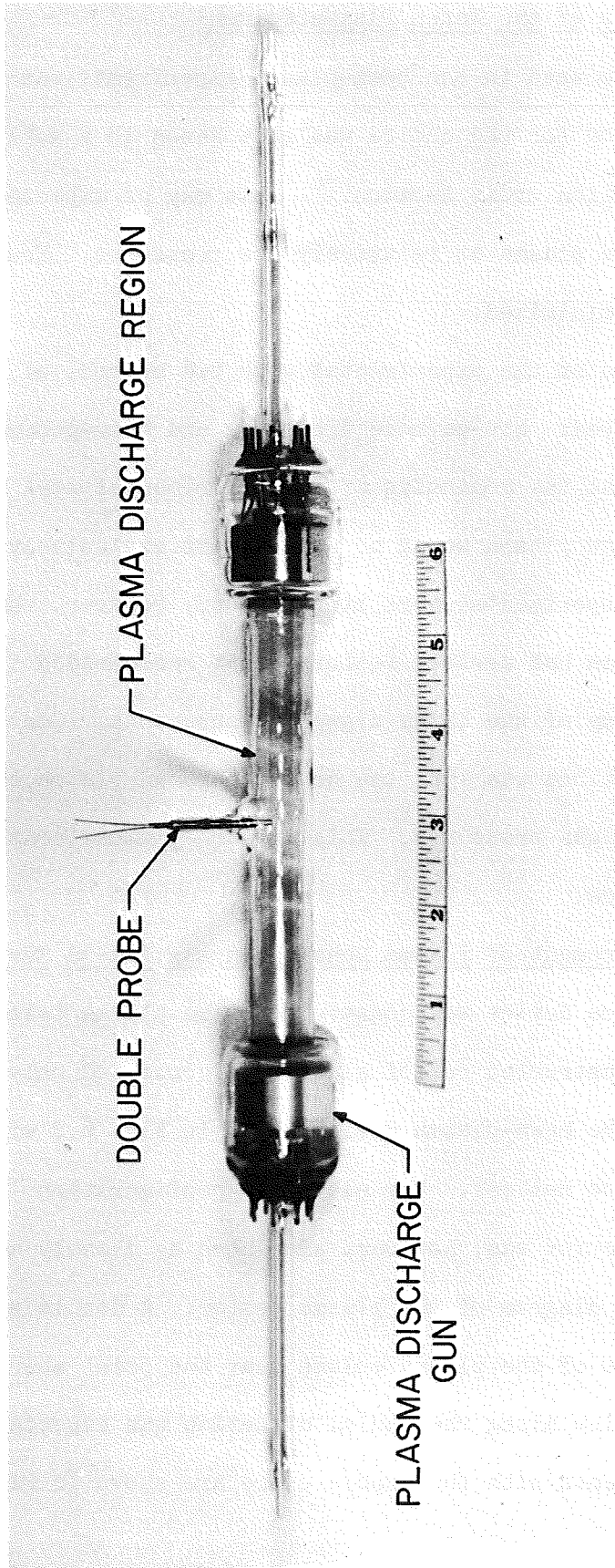


FIG. 6.10 PHOTOGRAPH OF THE PLASMA TESTER.

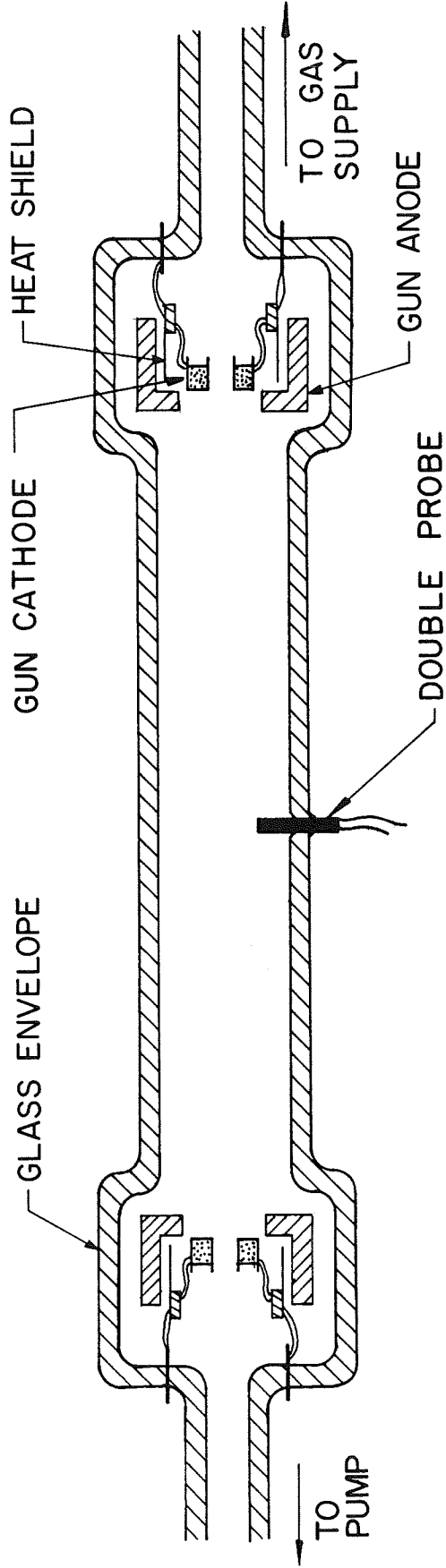


FIG. 6.1.1 DIAGRAM OF THE PLASMA TESTER.

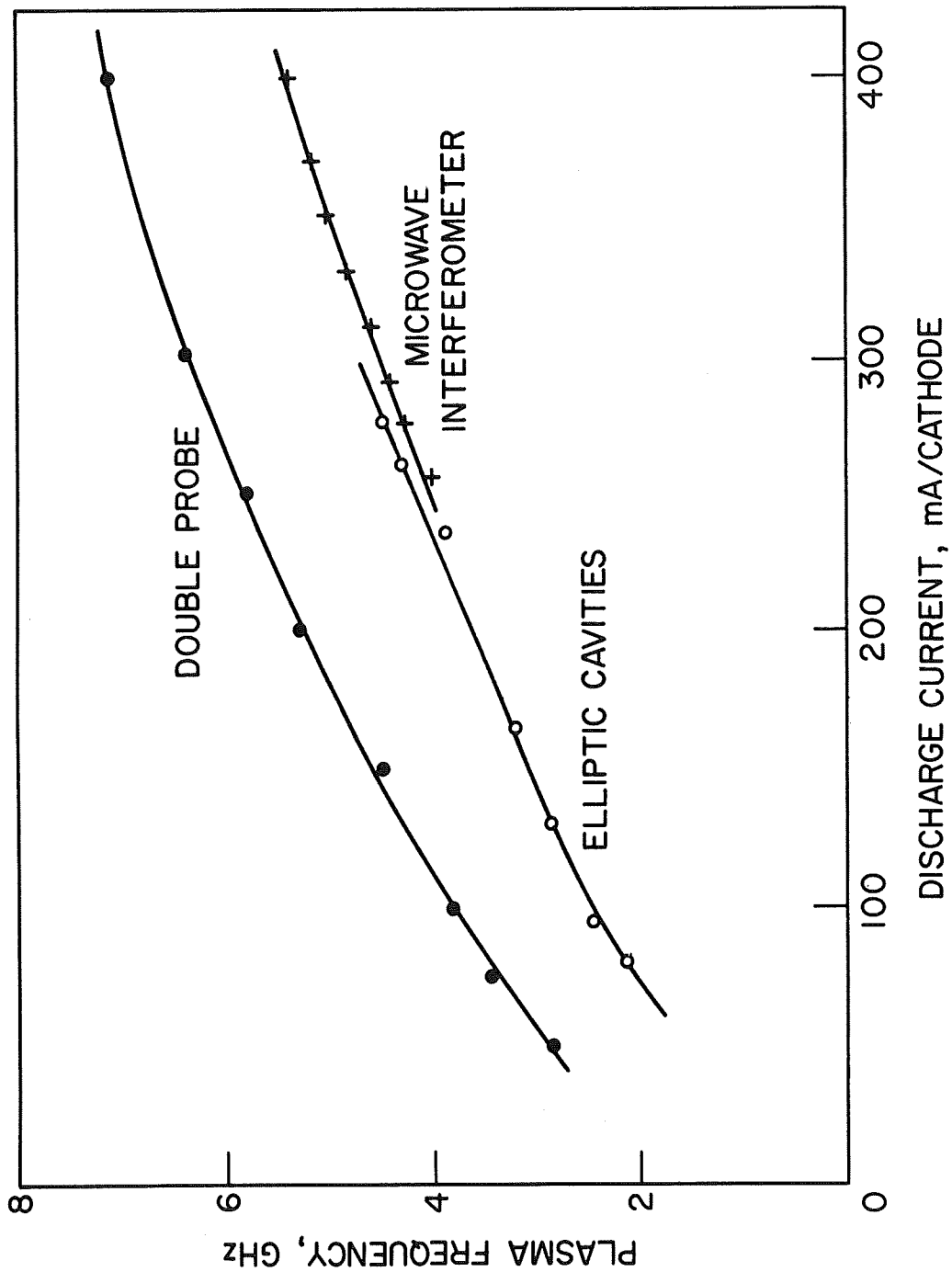


FIG. 6.12 PLASMA FREQUENCY VS. DISCHARGE CURRENT MEASURED IN A XENON PLASMA COLUMN WITH ZERO MAGNETIC FIELD.  
( $P = 2 \cdot 10^{-2}$  TORR)

as a function of the discharge current. An ionization efficiency in the order of 0.1 percent was obtained. Two other methods of measurement are shown in the same figure. One made use of two S-band waveguide horns placed across the plasma column, forming an interferometer. The plasma frequency could be calculated from the shift in phase through the interferometer when the discharge was switched on and off. This method may be expected to be the least accurate because of the size of the horns being comparable to the whole plasma column. Thus only an average plasma frequency could be obtained in this way.

The other method of determining the plasma frequency made use of wave propagation along the plasma column. A surface wave could be launched and received by the set of elliptic cavity couplers which were placed around the plasma column. At the resonant frequency given by

$$\omega_r = \frac{\omega_p}{\sqrt{1 + \kappa_e}} , \quad (6.1)$$

where  $\kappa_e$  is the effective dielectric constant of the material surrounding the plasma column, a strong signal could be detected at the receiving cavity. Since the effective dielectric constant is somewhat less than that for the glass tube surrounding the plasma (because of the finite radial extent of the glass) a value of  $\kappa_e = 3.0$  was chosen. The results of these measurements are also shown in Fig. 6.12.

The probe measurements are taken at the most dense plasma region. Chorney and Madore<sup>75</sup> considered axial and radial plasma density variations for an annular cathode geometry of the type used in these experiments. Near the outside edge of the plasma column they obtained an approximately parabolic density variation, which may be expressed by

$$\rho(r) = \rho_m \left[ 1 - \alpha \left( \frac{r}{b} \right)^2 \right] . \quad (6.2)$$

Here  $\rho_m$  is the maximum plasma density in the column of radius  $b$ , and  $\alpha$  is a parameter between zero and unity, which determines the degree of radial charge variation. Since the surface wave along the plasma column sees the edge plasma density, it is possible to determine  $\alpha$  from the measurements of Fig. 6.12 by

$$\omega_{pe} = \sqrt{1 - \alpha} \omega_{pm} , \quad (6.3)$$

where  $\omega_{pe}$  is the edge plasma frequency obtained by the elliptic cavity data. The values of  $\omega_{pm}$  were obtained from the probe data. Thus in this case  $\alpha$  was found to be approximately 0.5. A similar procedure was pointed out by Trivelpiece,<sup>76</sup> who suggested a low-frequency phase velocity measurement for determining  $\omega_{pm}$  and a measurement of the frequency where  $\beta b = \infty$  for determining  $\omega_{pe}$ .

When a longitudinal magnetic field was applied, the plasma frequency and the electron temperature in the plasma tester were found to vary as shown in Fig. 6.13. The data were obtained by use of the double probe. The initial increase in plasma frequency is due to the fact that the electrons begin to spiral slightly as the magnetic field is increased a small amount from the zero value. Hence the electrons have a higher probability of colliding with a gas particle and ionizing it. As the magnetic field is increased further the Larmor radius of the electrons becomes comparable to the plasma tube radius, enhancing recombination at the tube wall and hence decreasing the plasma density. Further increase in the magnetic field tends to confine the plasma, and

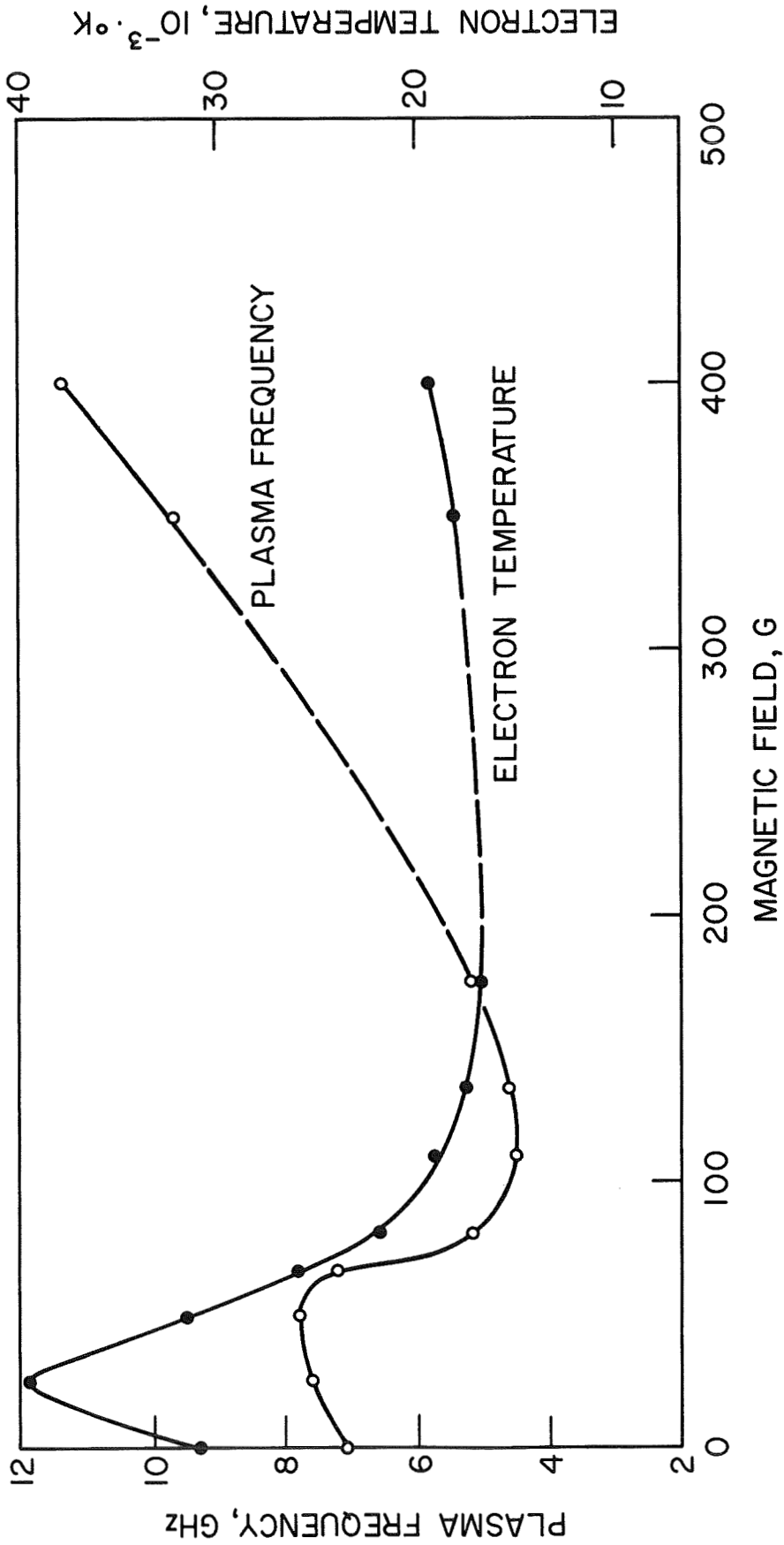


FIG. 6.13 PLASMA FREQUENCY AND ELECTRON TEMPERATURE AT THE CENTER OF THE XENON PLASMA COLUMN AS MEASURED WITH THE DOUBLE PROBE. ( $P = 2 \cdot 10^{-2}$  TORR, DISCHARGE CURRENT = 400 mA/CATHODE)

diffusion to the walls decreases as  $1/B^2$  for ambipolar diffusion or as  $1/B$  for the so-called anomalous diffusion<sup>77</sup> to be discussed below. Note that for the pressure of  $2 \cdot 10^{-2}$  Torr used in these experiments the mean-free-path of the electrons is on the order of the tube diameter and the mean-free-path of the xenon ions is less by a factor of  $4\sqrt{2}$ . Thus the operation is in a transition region between ambipolar and free diffusion where most diffusion theories break down.<sup>78</sup>

The dashed portion of the curves in Fig. 6.13 indicates that for those values of magnetic field measurements were difficult to take because of discharge current fluctuations accompanied by instabilities in the plasma density. For the highest values of magnetic field these instabilities still persisted, but they were much less violent, so that meaningful data could be taken readily. Other workers<sup>26,77</sup> have found these fluctuations to exist above a critical magnetic field,  $B_c$ , which increases with pressure and with the mass of the positive ions in the plasma. An important observation is that the quantity  $B_c b$ , where  $b$  is the radius of the discharge, is essentially constant for a particular set of discharge parameters. The instabilities are thought to accompany anomalous diffusion across the magnetic field lines. This type of diffusion involves microelectric fields set up in the plasma due to density fluctuations. These electric fields give rise to drift motion across the magnetic field, increasing the diffusion rate so that it is proportional to  $1/B$  rather than  $1/B^2$ .

6.2.2 Plasma Generation in the Beam-Plasma Device. As noted above, the plasma tester hot-cathode discharge was operated in the low  $10^{-2}$  Torr pressure range. Identical results could be obtained with the

final beam-plasma device. In attempting to obtain an electron beam in this pressure range, the electron emission from the beam cathode very quickly dropped to a fraction of one tenth or less of its rated value. This could have been due to cathode poisoning by the impurity gases in the device. Even though differential pumping maintained the pressure in the gun region approximately one order of magnitude lower than in the plasma region, there may have been a high enough partial pressure of  $O_2$  or hydrocarbons for poisoning. Most likely, however, the drop in beam emission was due to bombardment of the beam cathode by the positive xenon ions. This caused the barium layer to be sputtered from the cathode surface as quickly as it could be replenished. Attempts to trap the ions in the plasma discharge region proved to be unsuccessful.

To obtain an electron beam it was therefore necessary to operate in the  $10^{-3}$  Torr range or lower. In addition to the problem with the critical magnetic field decreasing with pressure, as described above, an extinguishing pressure was reached in the upper  $10^{-3}$  Torr region. As shown in Fig. 6.14, as the pressure was decreased, the discharge voltage drop rose very rapidly. The flattening of the curves near 50 V was merely due to the maximum voltage limit of the constant current supplies used to maintain the discharge. The extinguishing pressure is probably due to the fact that, as the voltage increases, the ions can be accelerated into the plasma cathodes to be sputter pumped. Thus at a voltage between 25 to 30 V the pressure in the tube dropped rapidly increasing the voltage drop further and finally extinguishing the discharge.



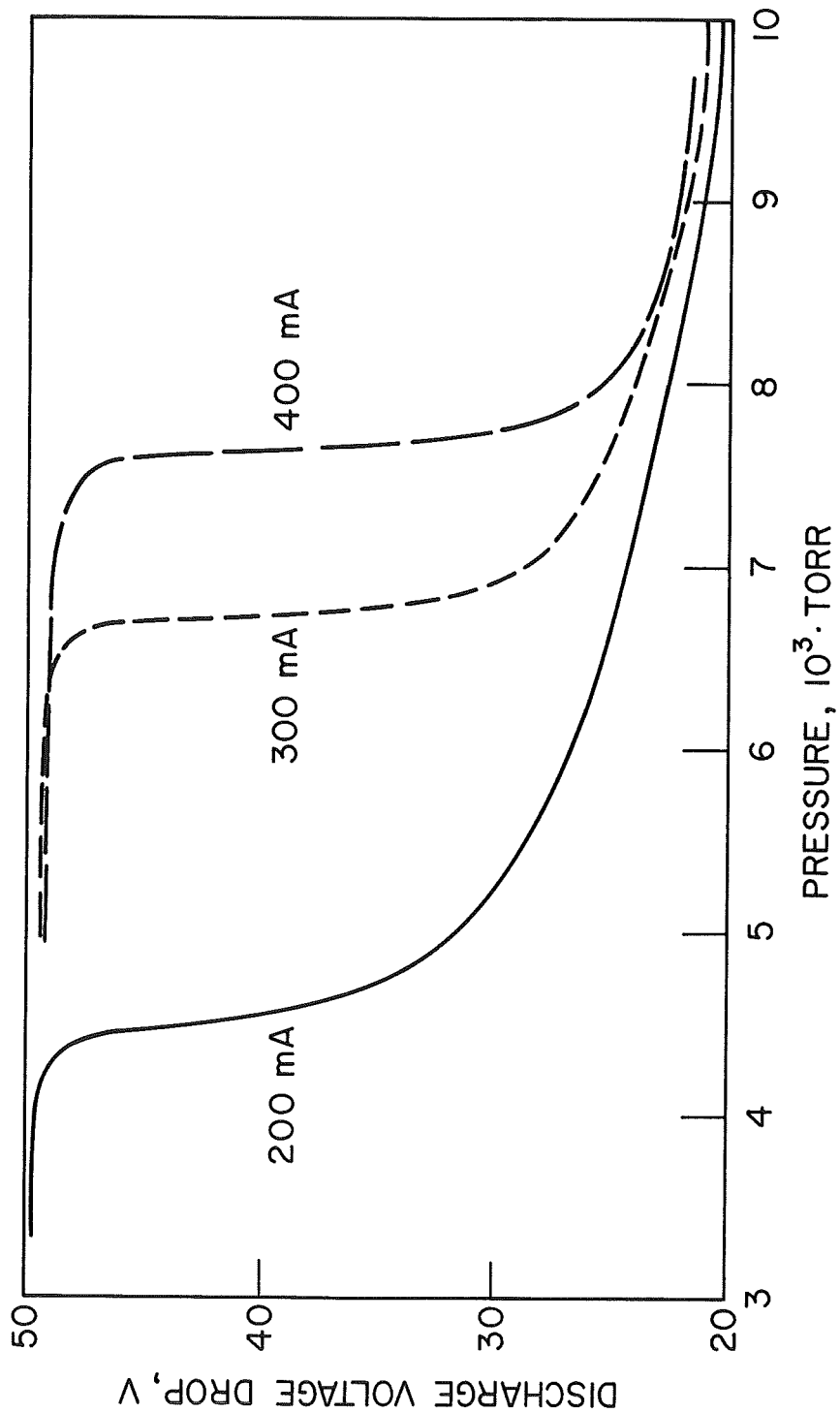


FIG. 6.14 DISCHARGE VOLTAGE DROP VS. PRESSURE FOR VARIOUS VALUES OF DISCHARGE CURRENT. ( $B_0 = 485 \text{ G}$ )

In view of these difficulties a different way of obtaining a plasma was desirable. It was found that a plasma could be obtained by making use of collisions between the beam electrons and the gas particles at pressures as low as  $1 \cdot 10^{-5}$  Torr. This method of plasma generation has been used extensively. See, for example, References 23 through 25 and 39. Getty and Smullin<sup>23</sup> explained the processes in a beam-generated plasma as follows. The electron beam, when first turned on, ionizes the background gas by inelastic collisions between the beam electrons and the gas particles. If the pressure is sufficiently high so that the plasma so formed is dense enough, the excited plasma electrons become the dominant ionization source after a few microseconds. Nonconvective instabilities initiate RF oscillations which first appear at the cyclotron frequency. Then a convective instability at the plasma frequency generates the oscillations that sustain the discharge.

For a fixed beam voltage the beam-generated plasma can exist in two distinct modes for different beam currents or pressures. The mode for lower values of pressure or beam current has been called the "beam confined mode" by Dunn et al.<sup>79</sup>, while the mode at higher values of pressure or beam current has been called the "total glow mode." The former is so called because the plasma column is confined to the approximate size of the electron beam, with the plasma density at the beam edge having dropped to approximately half of its value at the center, as some of Hedvall's<sup>25</sup> measurements indicate. Above a critical pressure the total glow mode exists. It fills the entire diameter of the tube and in that respect it is similar to the hot-cathode discharge plasma. The total glow mode is accompanied by a larger noise level at the output

couplers of the device, as may be detected with a spectrum analyzer. The transition from one mode to the other is quite abrupt and occurred in the pressure range of  $2 \cdot 10^{-3}$  to  $4 \cdot 10^{-3}$  Torr for typical operating conditions of the beam-plasma device tested in this study.

There was no provision to measure the density of the beam-generated plasma in the final test vehicle. For that reason it was necessary to calculate it from a knowledge of the pressure and the beam density. Cavity measurements by Hedvall<sup>25</sup> indicate that plasma densities of many times the beam density can be obtained in the  $10^{-4}$  to  $10^{-3}$  Torr region, for example. At lower pressures there is very little scattering of the beam electrons and it appears that the predominant ionization source is the electron beam itself rather than secondary ionization by the plasma electrons. It has been found experimentally<sup>25,80</sup> that the plasma density varies slowly with pressure but is proportional to the square of the longitudinal magnetic field. Above a pressure of approximately  $10^{-4}$  Torr, with the exact value depending on the type of gas, secondary ionization by the plasma electrons becomes predominant. Under those conditions the density is nearly independent of magnetic field for high enough values of B, but is proportional to the square of the pressure. Frey<sup>81</sup> has carried out a one-dimensional analysis that yields the ratio of plasma density to beam density in a beam-generated plasma. He assumed an infinite magnetic field so that the beam-generated ions and electrons can leave the system by recombination or one-dimensional ambipolar diffusion only. His results are for hydrogen, nitrogen and argon, but may easily be extended to xenon. His agreement with Hedvall's experimental results is excellent in the region where the density varies with the square of the gas pressure. On the basis of Frey's calculations

along with the experimental results of Hedvall the data for Table 6.2 were calculated for beam parameters appropriate to this study.

Table 6.2

Characteristics of a Beam-Generated Plasma in Xenon

Beam Voltage (V)	Beam Current (mA)	Pressure (Torr)	Beam Electron Density (particles/cm <sup>3</sup> )	$n_{eb}/n_{ep}$	Plasma Frequency (GHz)
400	6	$2 \cdot 10^{-4}$	$6.2 \cdot 10^8$	300	4.0
600	10	$2 \cdot 10^{-4}$	$8.6 \cdot 10^8$	250	4.25
600	10	$2 \cdot 10^{-3}$	$8.6 \cdot 10^8$	1500	10.1
600	6	$2 \cdot 10^{-3}$	$7.7 \cdot 10^8$	1500	9.5

### 6.3 RF Test Results

The RF test data to be presented in this section were obtained with the beam-plasma interaction device described above. The coupled-helix couplers and short sections of the helical slow-wave structure were used to couple RF energy into and out of the system. Work done with the elliptic cavity couplers will be described in Chapter VII. The complete experimental test facility is shown in Fig. 6.15. The plasma device is located behind the meter panels near the top of the photograph. The cold loss of the beam-plasma device between the input and output coupled-helix couplers was very high, as Fig. 6.16 shows, and was not appreciably different when the plasma was either present or absent. This indicates that the RF leakage in the absence of the beam and plasma and the transmission through the plasma in the absence of the beam are approximately the same due to the dominance of the coupling losses in the absence of the beam. A Hewlett-Packard Model 851A/8551A spectrum analyzer was used for all RF measurements so that the various signals, harmonics and spurious oscillations could be ascertained simultaneously.

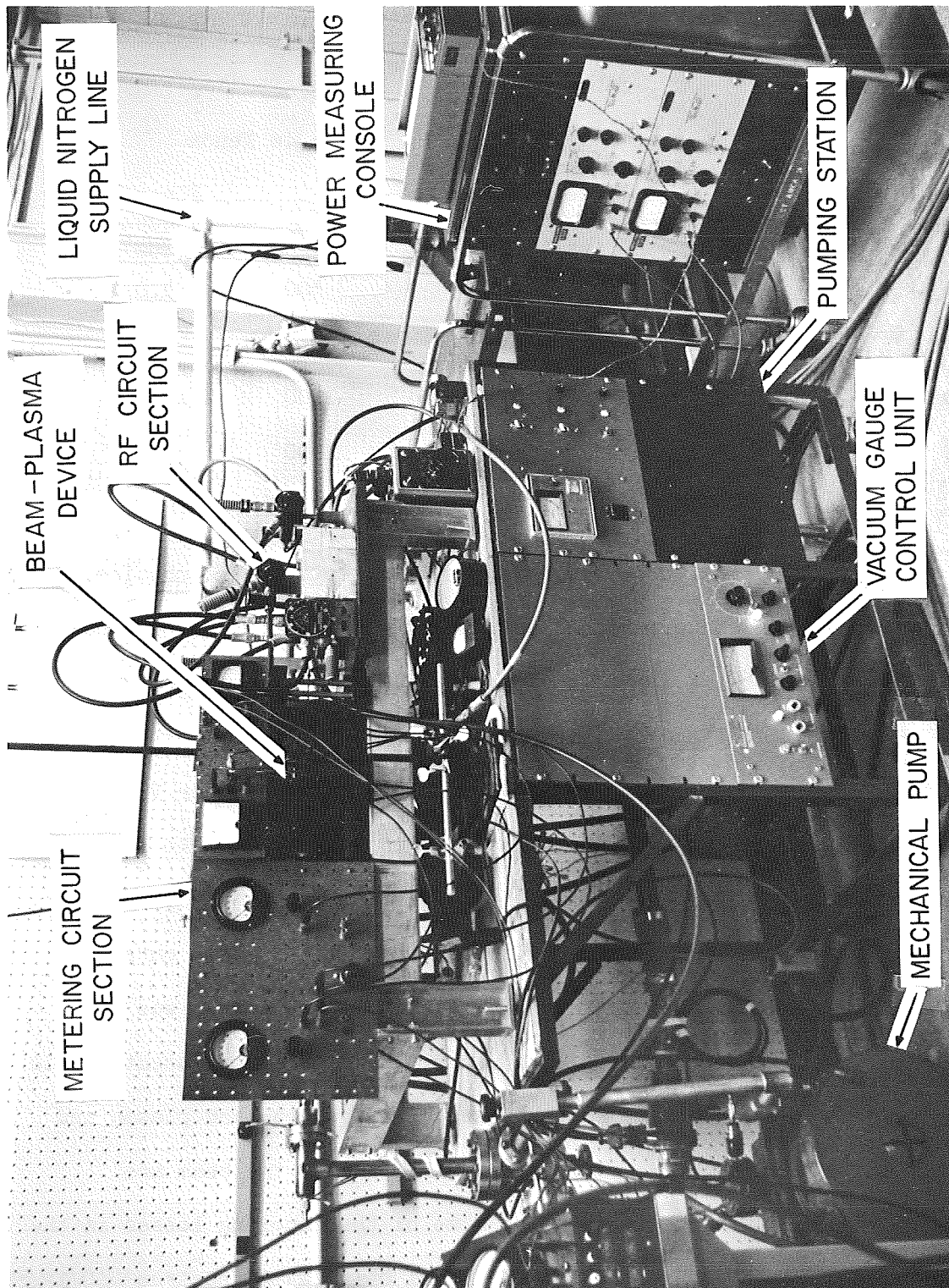


FIG. 6.15 EXPERIMENTAL TEST FACILITY.

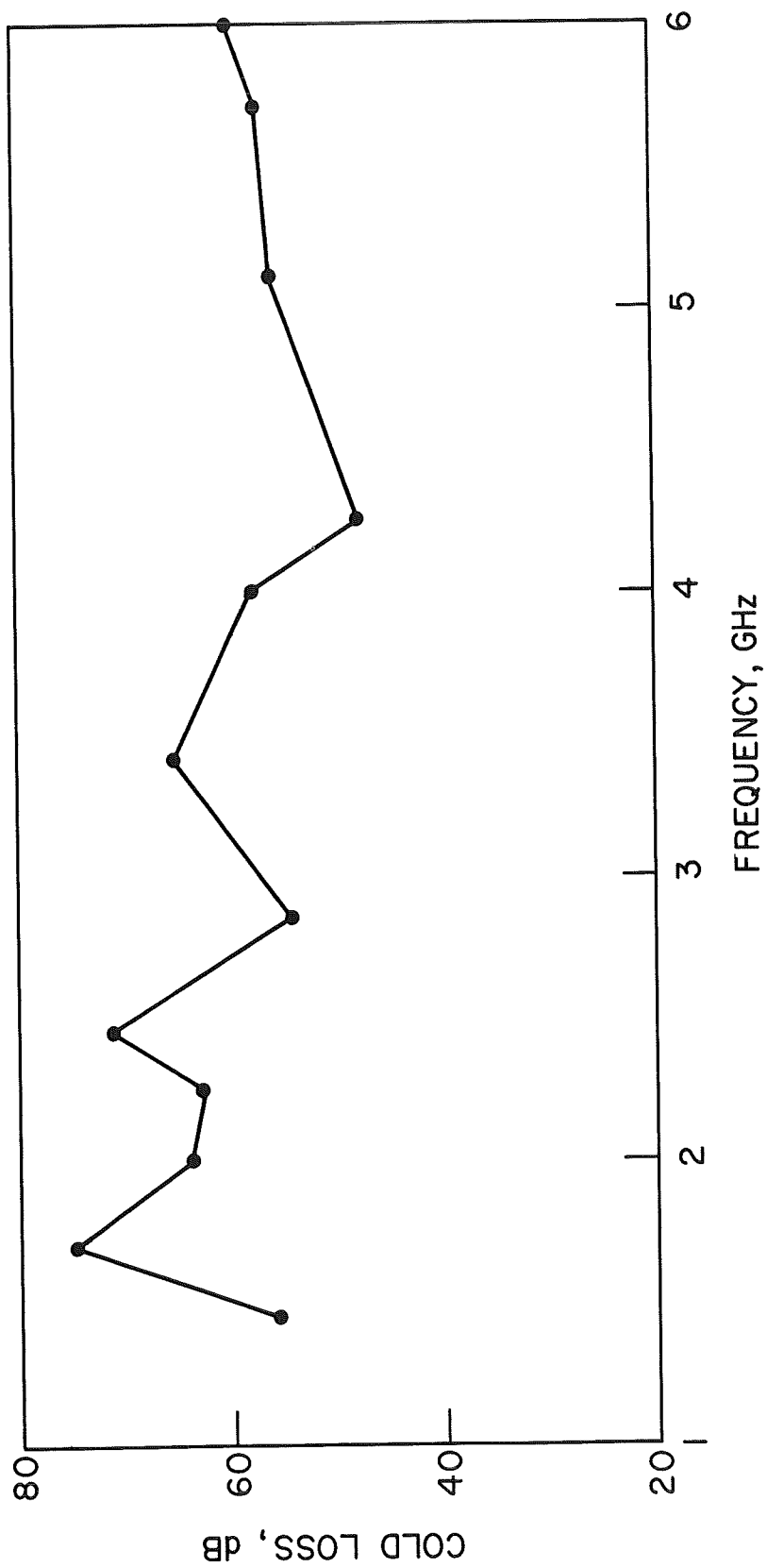


FIG. 6.16 COLD LOSS OF THE BEAM-PLASMA DEVICE THROUGH THE COUPLED-HELIX COUPLERS WITH NEITHER BEAM NOR PLASMA PRESENT.

Most RF data were taken at beam voltages in the range of 400 to 600 V. Figure 6.17 shows the beam transmission through the device as a function of voltage for two different values of magnetic focusing field. The first case corresponds to approximately 1.3 and the second to 2.5 times the Brillouin field at 500 V. Balanced flow could be attained in neither case. The cathode current was adequate to furnish a beam current well above the design perveance of 1 microperv but the current entering the plasma region is seen to be roughly one half the cathode current due to interception on the gun pole piece and the first helix. The location of these various components may be seen in Fig. 6.2. After traversing the plasma, further beam interception took place on the second helix so that only 20 to 25 percent of the cathode current finally reached the beam collector. The interception is believed to be due to small misalignments, particularly of the electron gun and the second plasma cathode. As already mentioned, magnetic flux lines fringing into the electron gun region caused the beam to ripple quite severely as it traversed the device. The erratic behavior of the two lower solid curves of Fig. 6.17 is due to the fact that the focusing field was slightly below the Brillouin field for voltages above 600 V.

Figure 6.18 shows the beam interception on the first helix and the gun anode as the pressure was raised from below  $2 \cdot 10^{-4}$  Torr through the  $10^{-3}$  Torr region. At first the first helix current is seen to decrease due to ion focusing of the beam. It reached a minimum near a pressure of  $1 \cdot 10^{-3}$  Torr. As the pressure was increased above this value the interception currents rose due to scattering of the beam electrons as a result of collisions. The apparent drop in helix current above a pressure of  $7 \cdot 10^{-3}$  Torr was due to a decrease in cathode emission

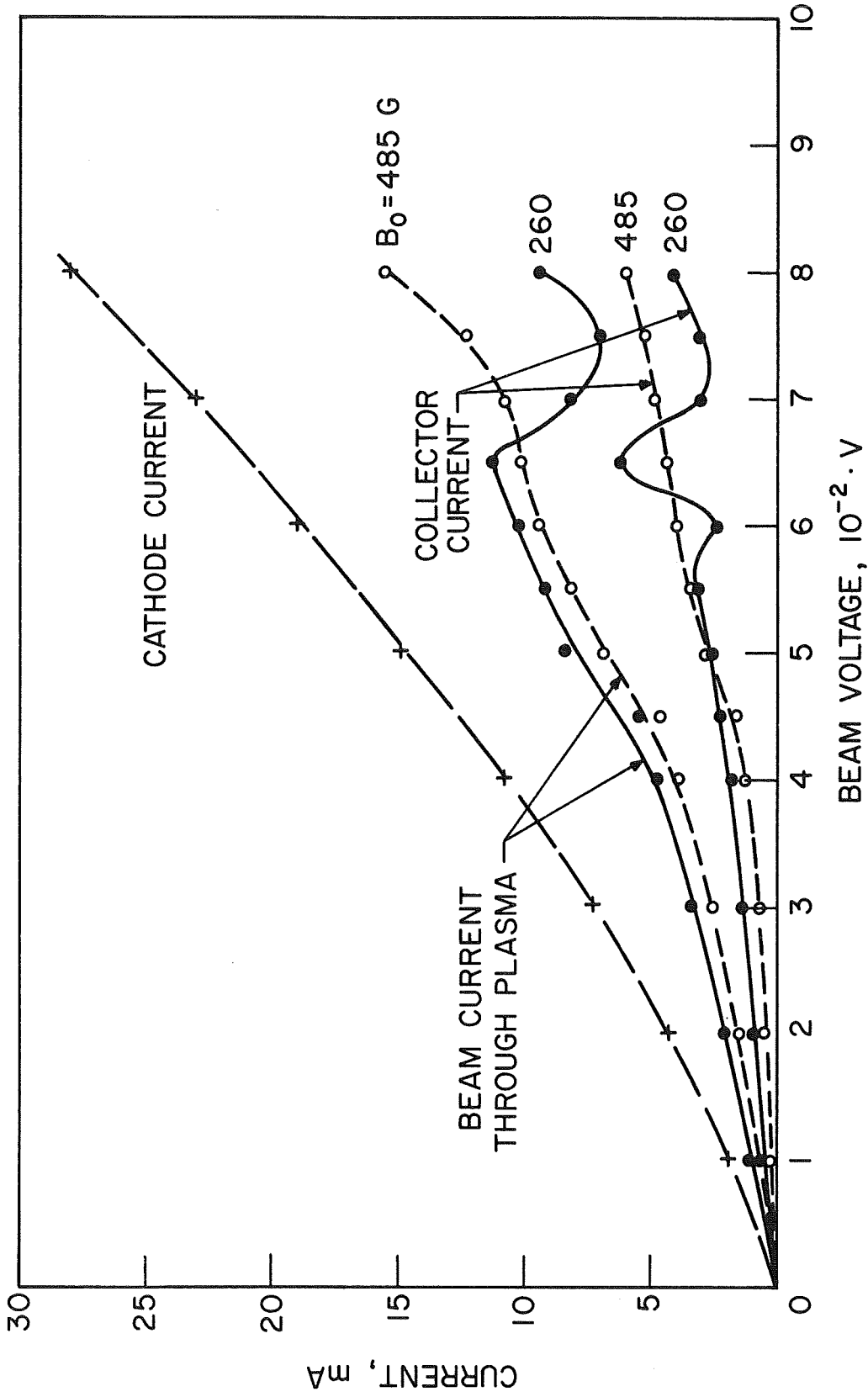


FIG. 6.17 BEAM TRANSMISSION THROUGH THE BEAM-PLASMA DEVICE AT PRESSURES LESS THAN APPROXIMATELY  $2 \cdot 10^{-4}$  TORR FOR FOCUSING FIELD VALUES OF 260 AND 485 G.



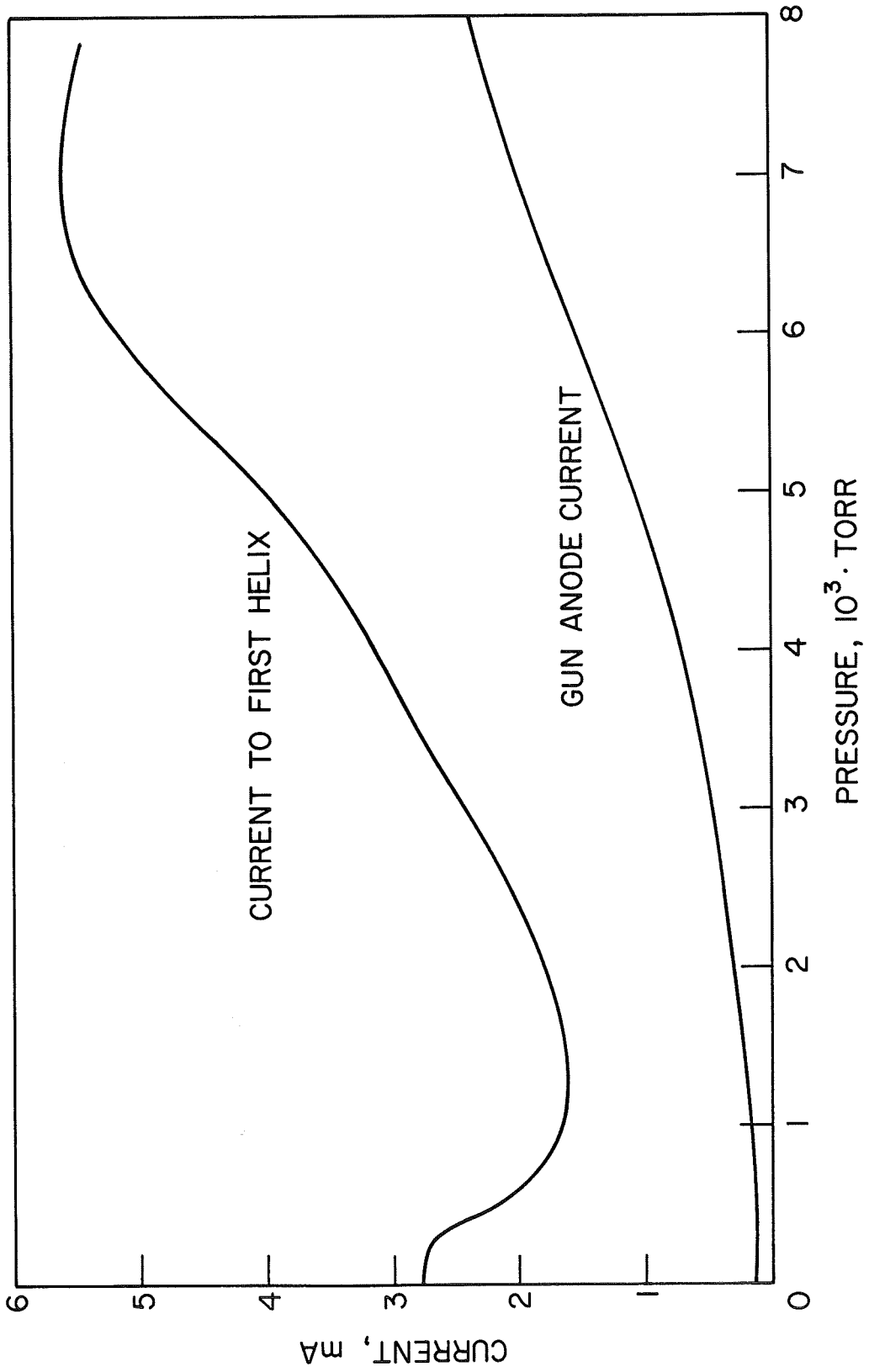


FIG. 6.18 VARIATION OF VARIOUS ELECTRODE CURRENTS IN THE MILLITORR PRESSURE RANGE. ( $B_0 = 485$  G,  $V_0 = 600$  V)

as a result of poisoning or sputtering. The transition from the beam confined mode to the total glow mode in the beam generated plasma occurred at  $2 \cdot 10^{-3}$  Torr in this case.

6.3.1 Gain and Harmonic Generation Tests. In Fig. 6.19 the small-signal electronic gain as a function of beam voltage may be seen. The maximum value of electronic gain was found to be 36 dB for the parameters indicated. The beam-generated plasma operated in the beam confined mode in this case. It should be noted that there was no net gain from the device due to the very high value of cold loss shown in Fig. 6.16. The large variations in the gain curve can be explained as follows.

Since there is an abrupt discontinuity in the plasma at the ends of the interaction region, RF waves set up in the plasma are almost totally reflected at both ends of the plasma unless good coupling to the plasma column can be achieved. A wave propagating back and forth along the plasma column can grow whenever the round-trip gain from end to end along the column is greater than unity. Thus a gain curve with sharp peaks, as the voltage or the frequency are varied, may be expected.

Figure 6.20 shows some spectrum analyzer patterns of the output from the beam-plasma device operating under the same conditions as those for Fig. 6.19, except that the drive power was sufficient to nearly saturate the device. In Figs. 6.20a and b the fundamental is shown, with the frequency scale expanded ten times in Fig. 6.20b. The noise level is seen to be at least 20 dB below the signal. The second harmonic output is shown in Fig. 6.20c and is seen to be approximately 10 dB below the fundamental. Note that in these, as well as in all subsequent spectrum analyzer patterns, the frequency increases from right to left.

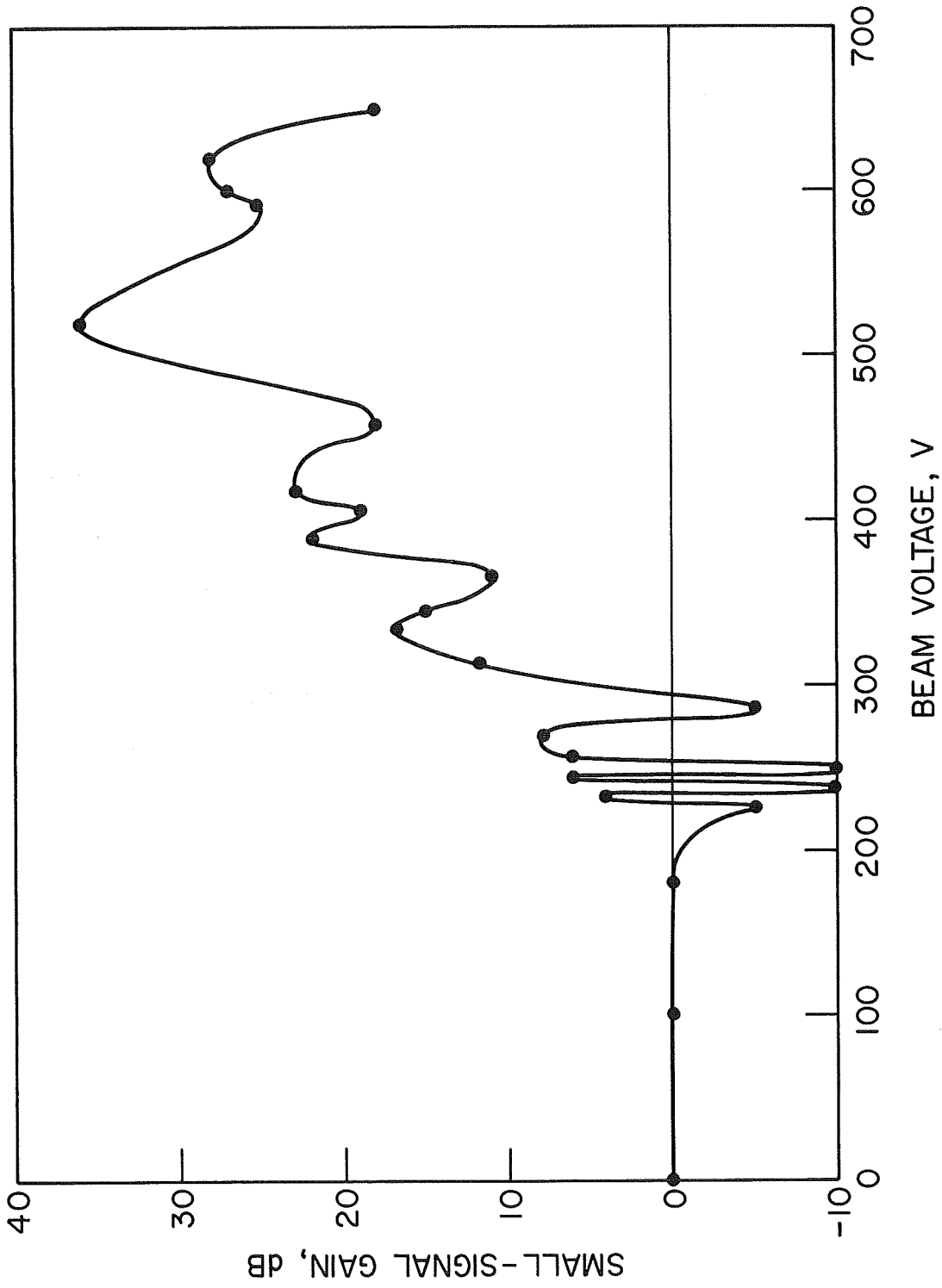
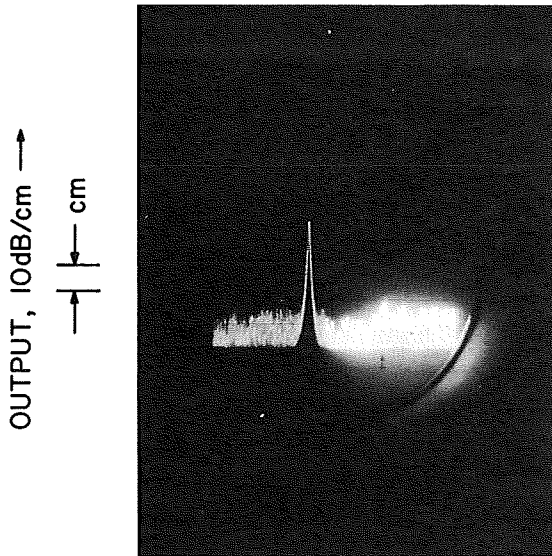


FIG. 6.19 SMALL-SIGNAL GAIN VS. BEAM VOLTAGE FOR A BEAM-PLASMA DEVICE USING COUPLED-HELIX COUPLERS. ( $B_0 = 260$  G,  $f_c = 728$  MHz,  $f_s = 2.0$  GHz,  $f_p \approx 4.3$  GHz,  $P = 2 \cdot 10^{-4}$  TORR)



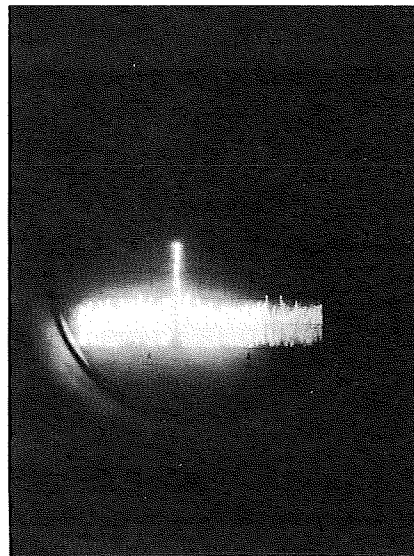
← FREQUENCY, 3MHz/cm

(a) FUNDAMENTAL



← FREQUENCY, 300KHz/cm

(b) FUNDAMENTAL



← FREQUENCY, 300KHz/cm

(c) SECOND HARMONIC

FIG. 6.20 TYPICAL SPECTRUM ANALYZER PATTERNS OF THE OUTPUT FROM A BEAM-PLASMA DEVICE. ( $f_s = 2.0$  GHz, DRIVE POWER = 250 mW,  $P = 2 \cdot 10^{-4}$  TORR,  $f_c = 728$  MHz,  $f_p \cong 4.3$  GHz,  $I_o = 10$  mA,  $V_o = 585$  V)

In Figs. 6.21 through 6.26 the performance of the beam-plasma device operating in the beam-confined mode is summarized. Figure 6.21 shows the small-signal electronic gain at a number of frequencies for two different voltages and with the magnetic field set at 260 G. The maximum of 36 dB was found at 2.0 GHz for 520 V. Comparing these results with Fig. 5.1, it should be noted that experimentally gain occurred over a considerably wider frequency range. As pointed out in Chapter V this is believed to be due to nonuniformities in the density across the plasma column. The saturation characteristics of the device are shown in Figs. 6.22 and 6.23, where the output of the fundamental signal and the harmonics that could be detected on the spectrum analyzer are plotted. At a frequency of 1.045 GHz the device is obviously saturating, but for a frequency of 1.7 GHz sufficient drive power was available just to approach saturation. In Fig. 6.23 the second harmonic comes to within 5 dB of the fundamental at saturation. At no time was it possible to detect harmonic signals above 6.0 GHz. Harmonic signals between 5.0 and 6.0 GHz were usually so small that they could be seen only in a few instances. This was due to the rapid deterioration of the coupler VSWR above 5.0 GHz and the very low value of interaction impedance near the plasma frequency. The plasma frequency was estimated to be slightly above 4.0 GHz for these conditions, as explained in Section 6.2; however, due to nonuniformities in the plasma column harmonics above this frequency were observed experimentally.

Figure 6.24 summarizes a large amount of experimental data, such as is shown in Figs. 6.22 and 6.23. The harmonic power output below the fundamental power level is shown at saturation.

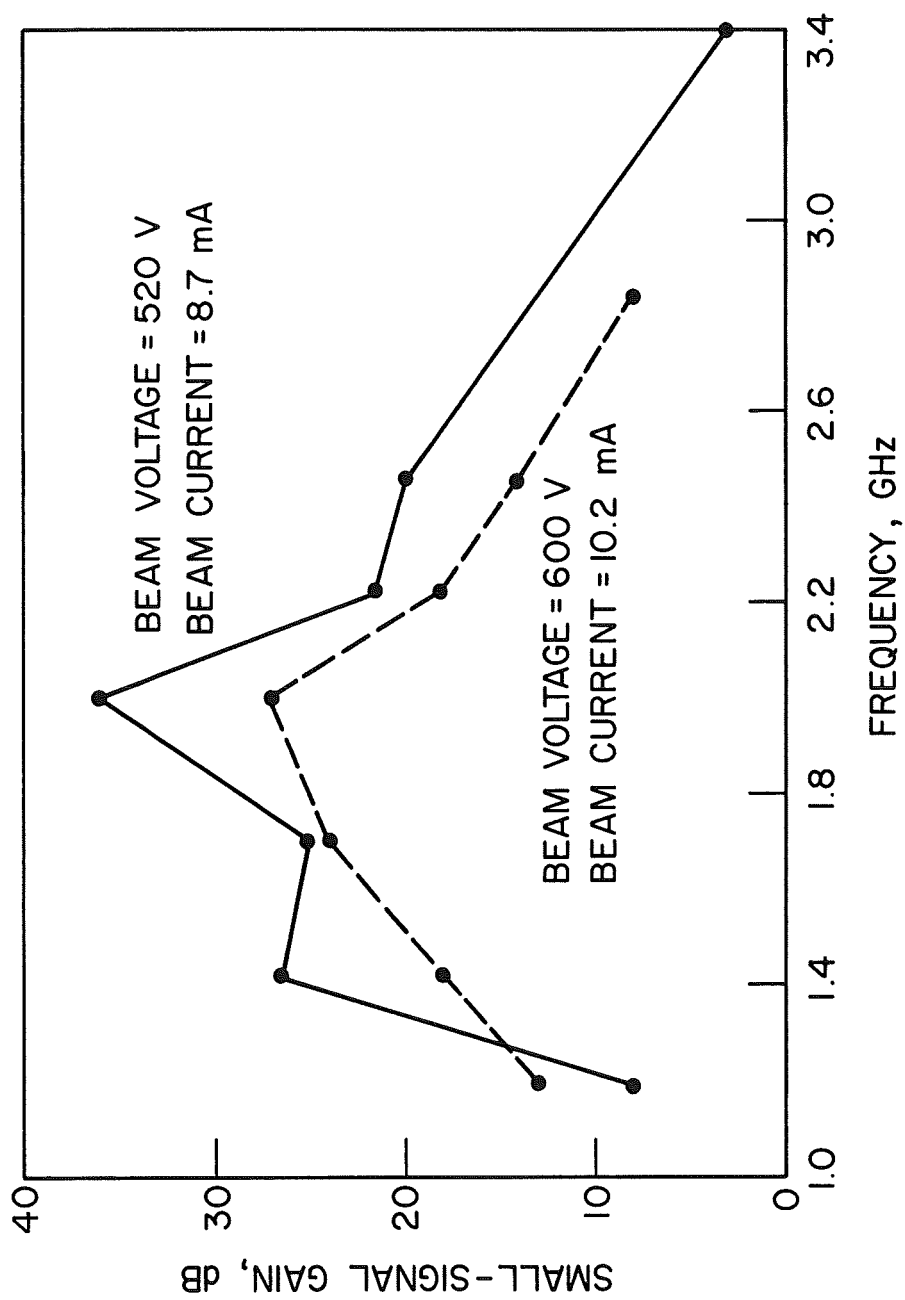


FIG. 6.21 SMALL-SIGNAL ELECTRONIC GAIN IN A BEAM-PLASMA SYSTEM USING COUPLED-HELIX COUPLERS. ( $B_0 = 260$  G,  $f_c = 728$  MHz,  $f_p \approx 4.3$  GHz,  $P = 2 \cdot 10^{-4}$  TORR)

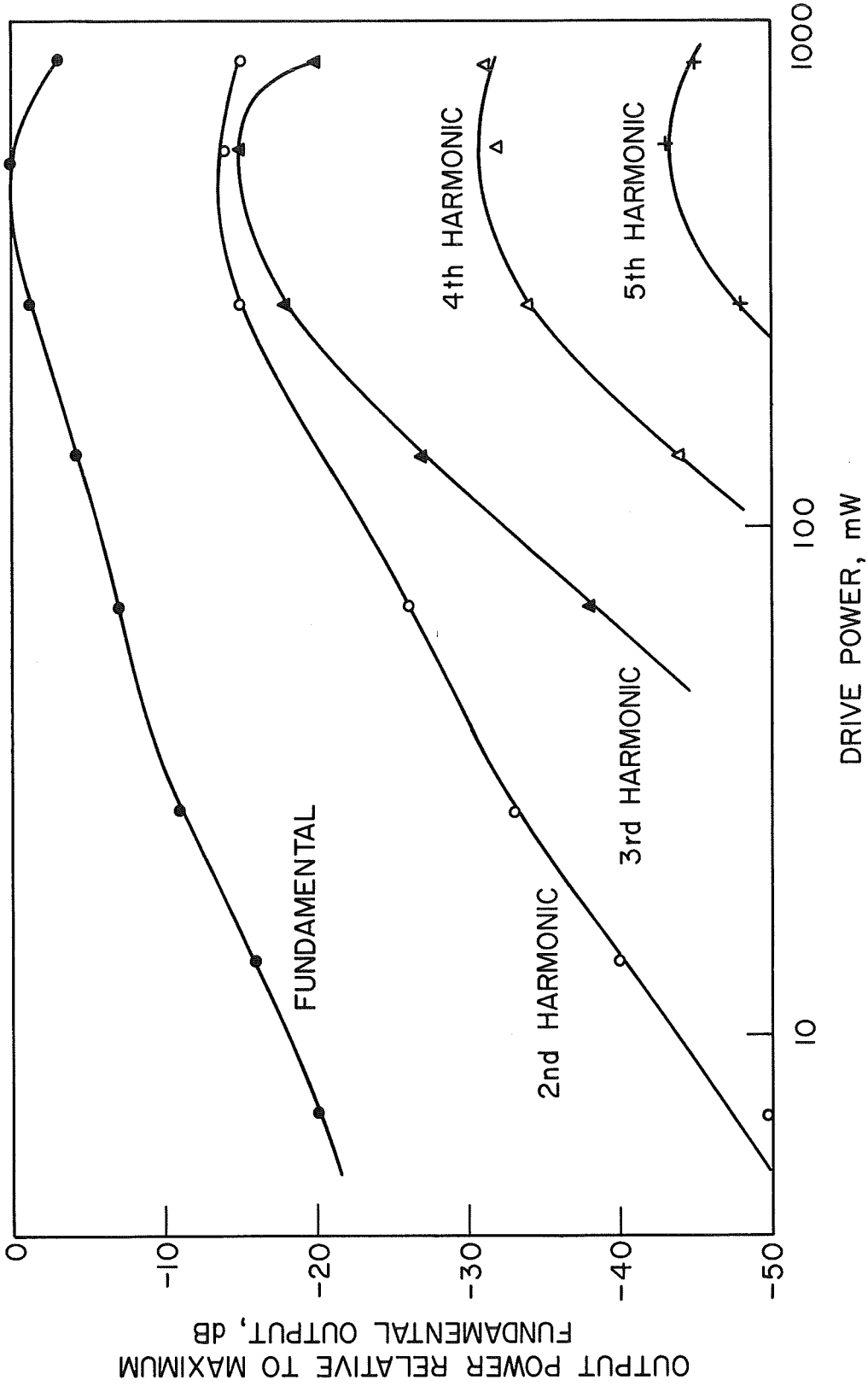


FIG. 6.22 SATURATION DATA FOR A BEAM-PLASMA DEVICE USING COUPLED-HELIX COUPLERS. ( $f_s = 1.045$  GHz,  $V_0 = 770$  V,  $I_0 = 7.1$  mA,  $B_0 = 260$  G,  $f_c = 728$  MHz,  $f_p \approx 4.3$  GHz,  $P = 2 \cdot 10^{-4}$  TORR, SMALL-SIGNAL GAIN = 6 dB)

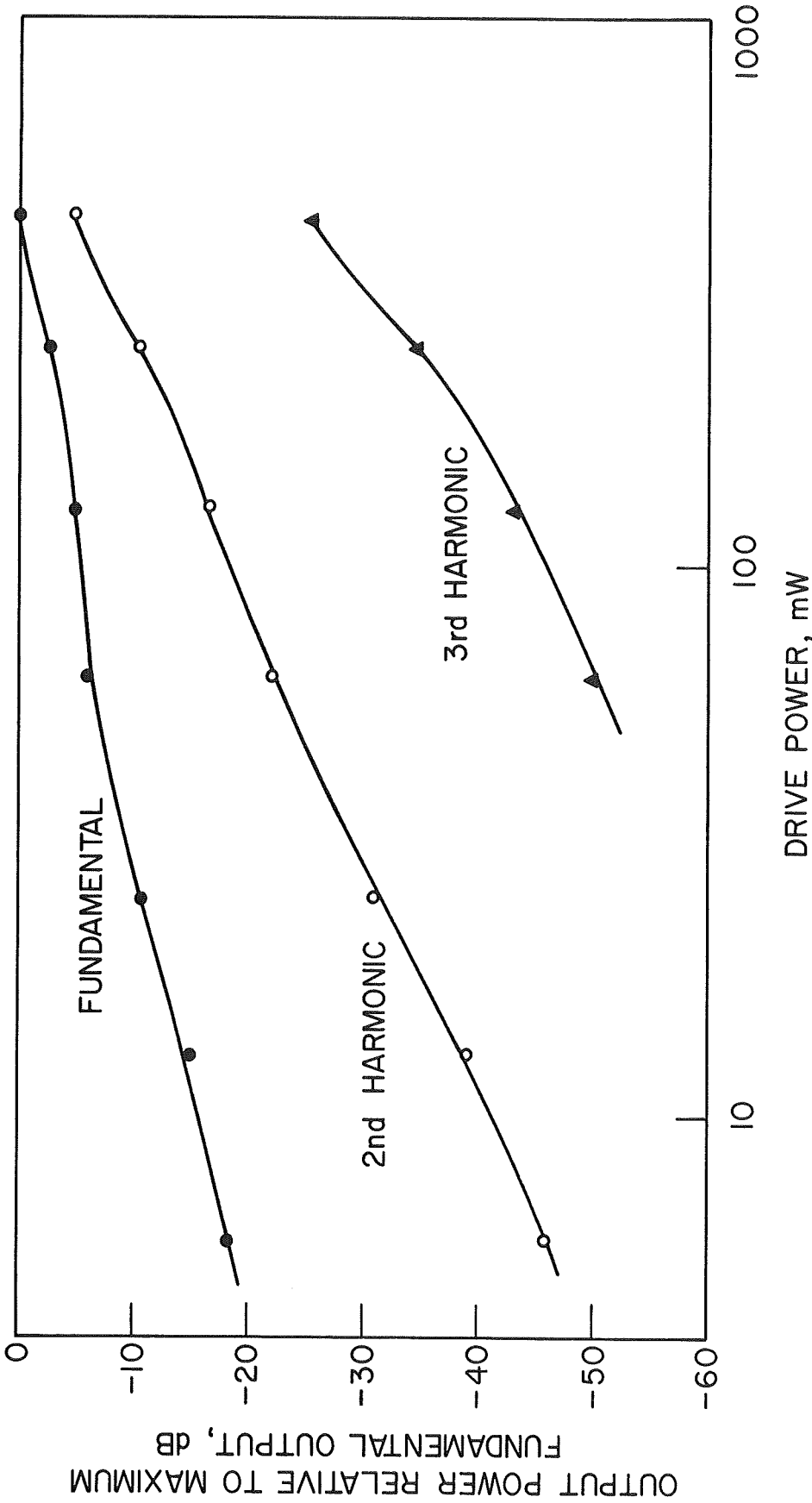


FIG. 6.23 SATURATION DATA FOR A BEAM-PLASMA DEVICE USING COUPLED-HELIX COUPLERS. ( $f_s = 1.7$  GHz,  $V_o = 600$  V,  $I_o = 10.2$  mA,  $B_o = 260$  G,  $f_c = 728$  MHz,  $f_p \approx 4.3$  GHz,  $P = 2 \cdot 10^{-4}$  TORR, SMALL-SIGNAL GAIN = 24 dB)



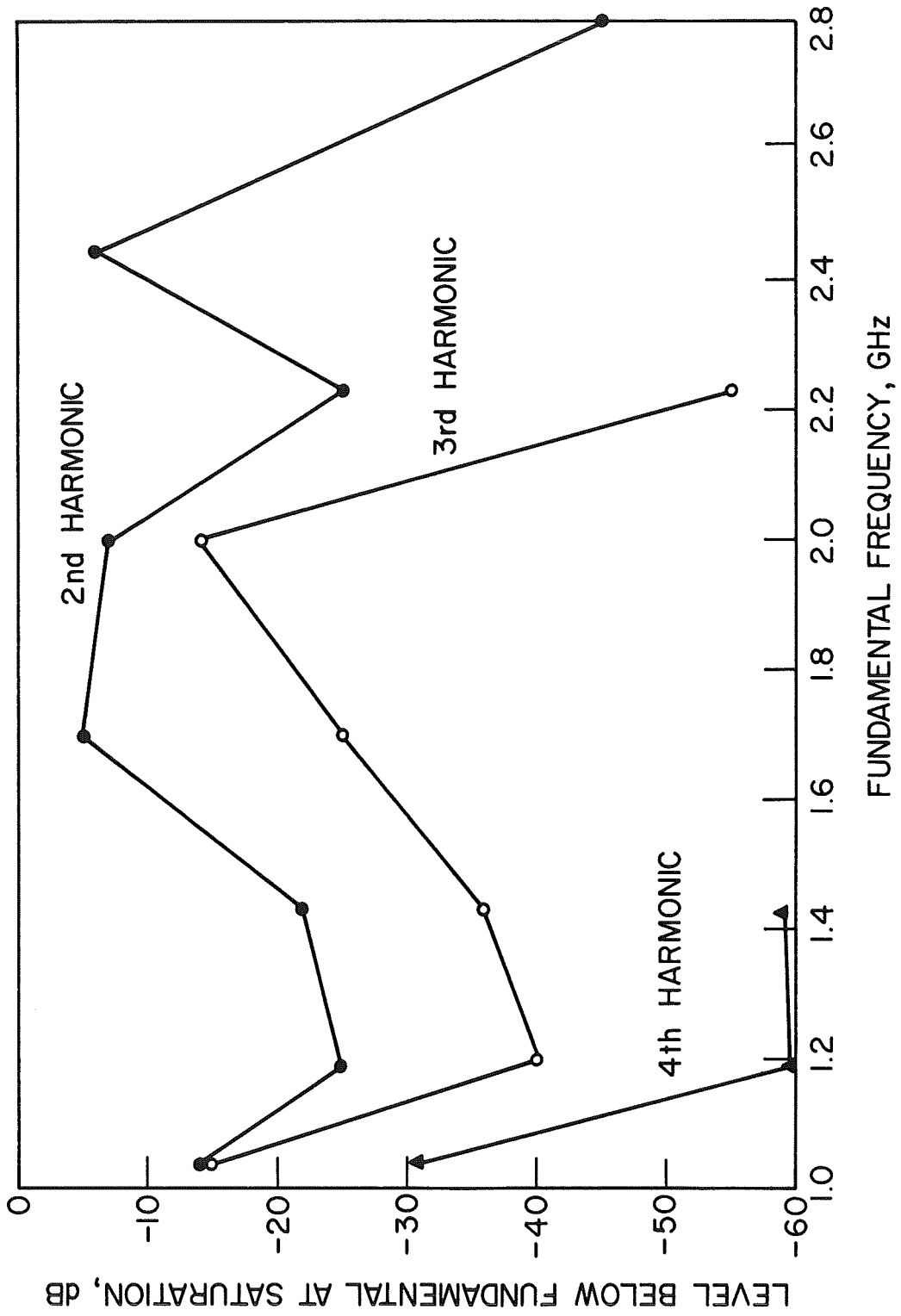


FIG. 6.24 HARMONIC LEVEL BELOW THE FUNDAMENTAL AT SATURATION IN A BEAM-PLASMA AMPLIFIER. ( $V_0 \approx 600$  V,  $I_0 \approx 10.2$  mA,  $B_0 = 260$  G,  $f_p \approx 4.3$  GHz,  $P = 2 \cdot 10^{-4}$  TORR)

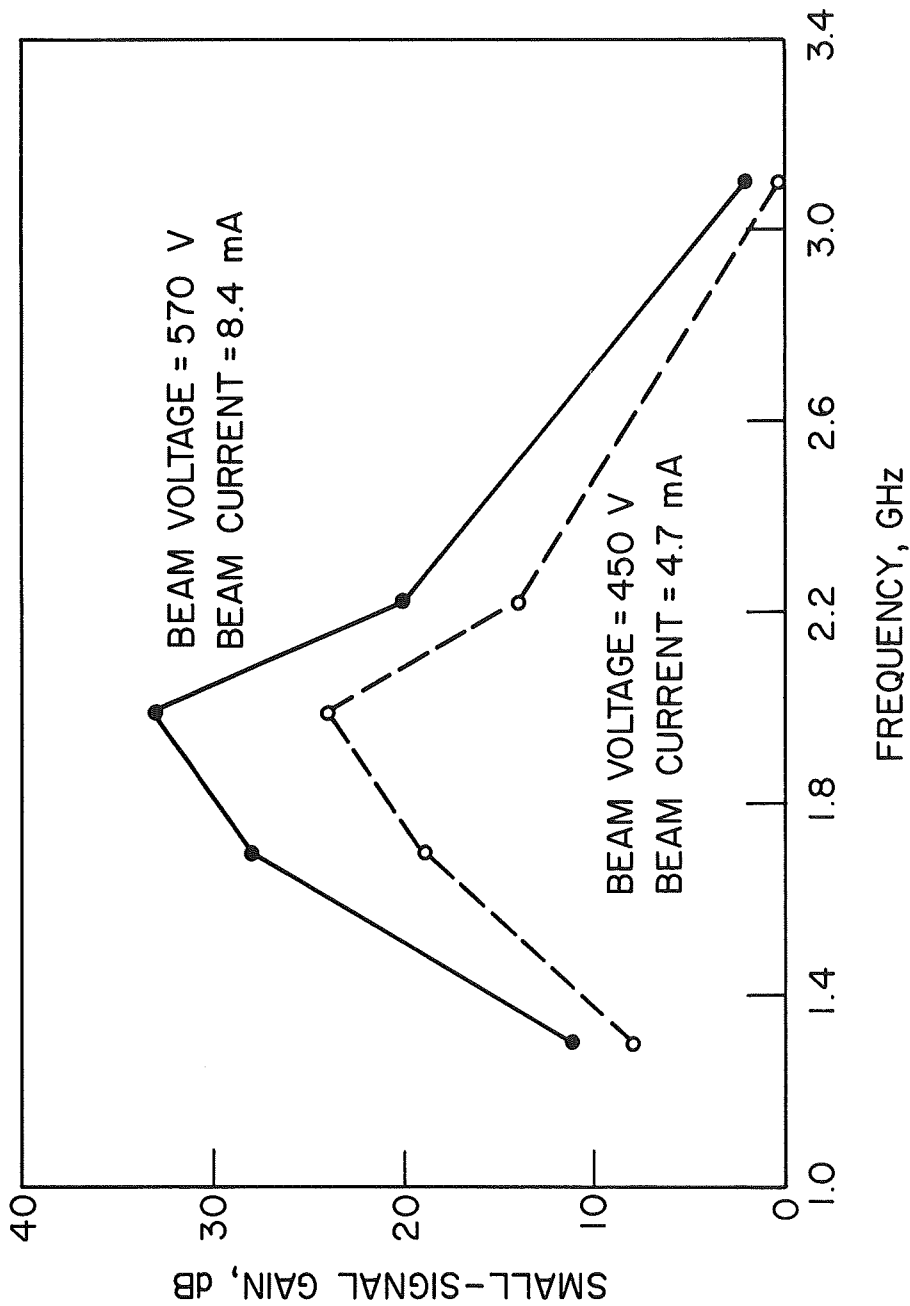


FIG. 6.25 SMALL-SIGNAL ELECTRONIC GAIN IN A BEAM-PLASMA SYSTEM USING COUPLED-HELIX COUPLERS. ( $B_0 = 485$  G,  $f_c = 1.357$  GHz,  $f_p \approx 4.2$  GHz,  $P = 2 \cdot 10^{-4}$  TORR)

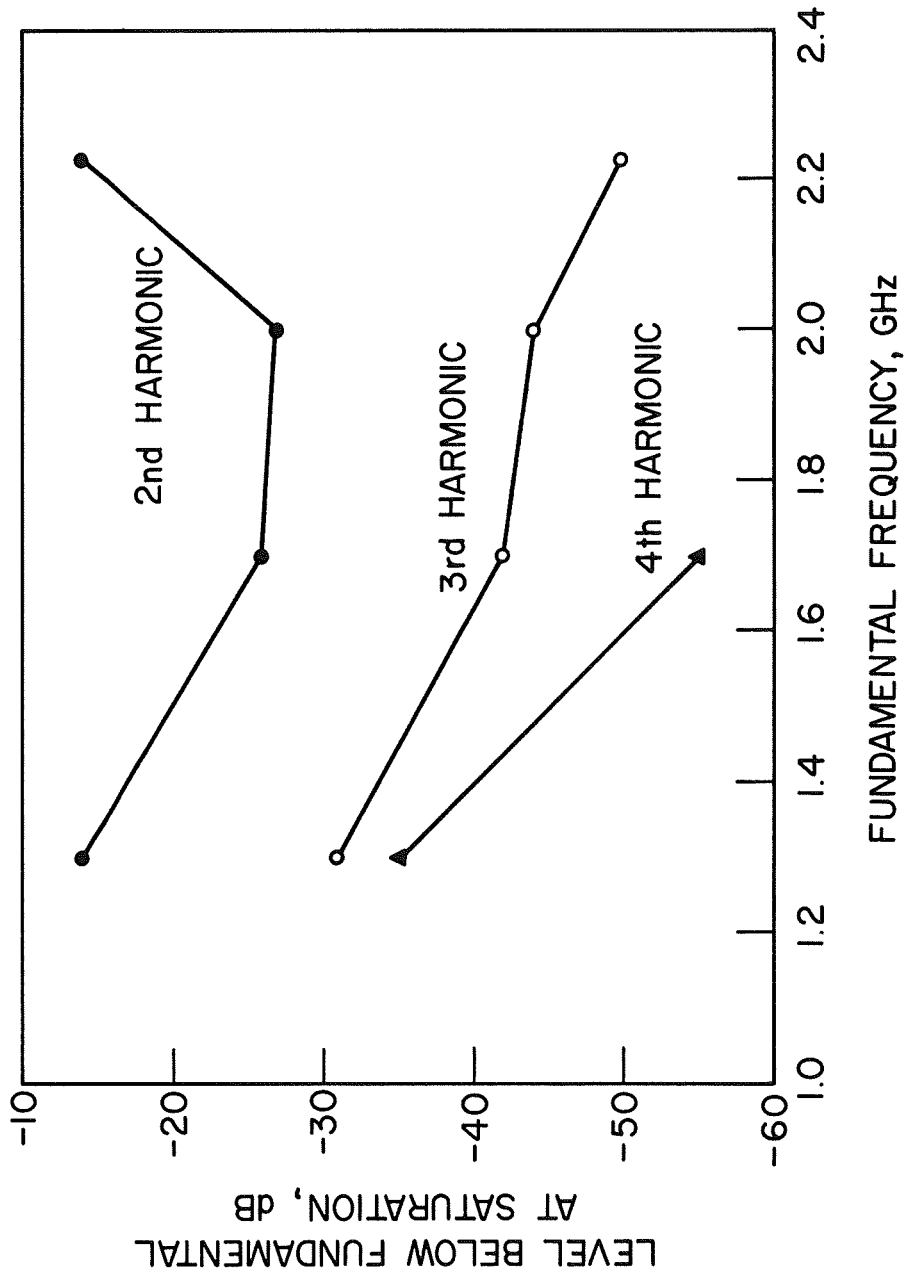


FIG. 6.26 HARMONIC LEVEL BELOW THE FUNDAMENTAL AT SATURATION IN A BEAM-PLASMA AMPLIFIER. ( $V_0 \approx 570$  V,  $I_0 = 8.4$  mA,  $B_0 = 260$  G,  $f_p \approx 4.3$  GHz,  $P = 2 \cdot 10^{-4}$  TORR)

Figure 6.25 is similar to Fig. 6.21 except that the axial magnetic field in this case was 485 G. A maximum small-signal gain of 35 dB was observed at 570 V and 2.0 GHz. In Fig. 6.26 the level of the harmonics that could be observed is again compared with the fundamental output power.

Table 6.3 lists the gain, interaction length and the first two harmonic levels obtained experimentally and by use of the various theoretical models. For the theoretical calculations the input level of the fundamental signal was chosen to be 30 dB below  $C_1 I_0 V_0$ , which insures that small-signal conditions prevail at the input and that the experimental and theoretical values of gain are comparable for an easy comparison of interaction length. The gain predicted by the two-dimensional analysis is too high because beam collision effects were neglected. The distance for saturation from the one-dimensional theory is too low because radial effects are not negligible. In addition, nonuniformities in an actual plasma may result in a larger saturation length. The discrepancies between experiment and theory in the harmonic levels can be easily understood from an inspection of any of the graphs of Chapter V showing the circuit voltage amplitudes or RF currents as a function of axial distance. It may be noted that these quantities vary substantially within a short axial distance in the vicinity of the saturation plane. Thus small position changes of the output coupler of the device could result in large variations of the harmonic power output. It is also likely that the plasma extended into the helix regions in a highly nonuniform fashion so that the coupling could be enhanced, resulting in the unexpectedly high harmonic output at the second harmonic.

Table 6.3

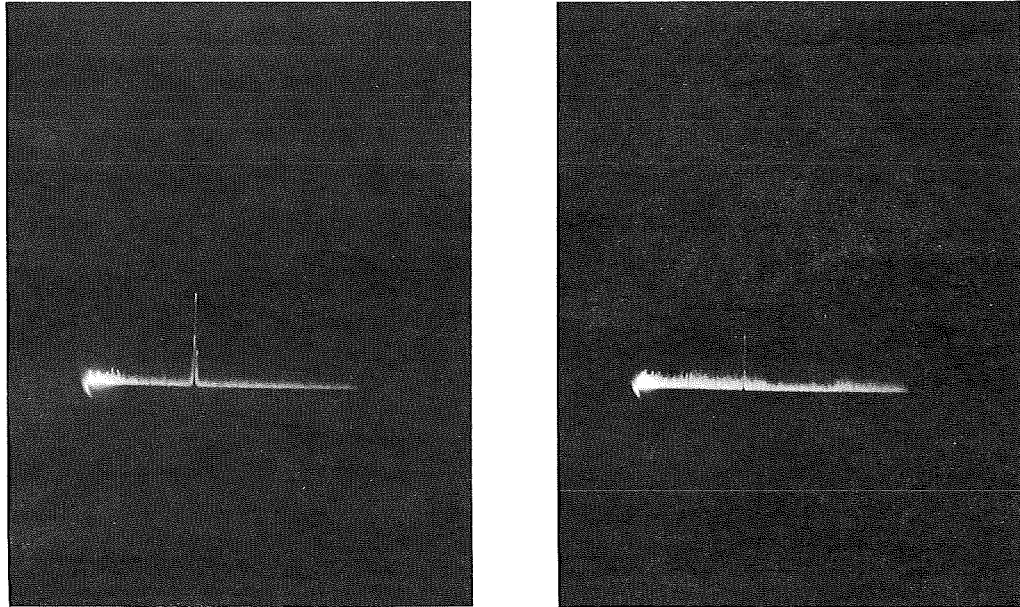
Comparison of Experimental and Theoretical Results

$b_1 = 0, C_1 = 0.113, V_0 = 520 \text{ V}, I_0 = 8.8 \text{ mA}$   
 $f_p = 4.24 \text{ GHz}, f_c = 728 \text{ MHz}, f_s = 1.7 \text{ GHz}$

	Experiment	One-Dimensional Theory $v_c/\omega = 0 \mid v_c/\omega = 0.003$	Two-Dimensional Theory Without Space Charge $(v_c/\omega = 0)$	Two-Dimensional Theory with Space Charge $(v_c/\omega = 0)$
Electronic Gain	25 dB	35.5 dB	32.3 dB	32.1 dB
Interaction Length	10.5 cm	6.2 cm	8.6 cm	9.4 cm
Second Harmonic Level Below Fundamental at Saturation	5 dB	14.4 dB	15.8 dB	13.1 dB
Third Harmonic Level Below Fundamental at Saturation	25 dB	17.3 dB	20.2 dB	18.7 dB

Deterioration of the coupler VSWR on the other hand could prevent some of the higher harmonic components from being coupled out effectively. This may have been the case for the third harmonic. In view of these sources of error the agreement of the results shown in Table 6.3 is seen to be quite reasonable. It has been found experimentally that the magnitudes of the harmonic components in this beam-plasma amplifier are comparable to those in a conventional traveling-wave amplifier with similar operating parameters, except in those cases where plasma nonuniformities enhance the coupling at certain frequencies.

Operation of the beam-plasma device in the beam confined mode is compared with operation in the total glow mode in Fig. 6.27. Here  $I_K$  is the cathode current and  $I_O$  is the current through the plasma region. Transition from one mode to the other occurred quite suddenly in the region between  $2 \cdot 10^{-3}$  and  $3 \cdot 10^{-3}$  Torr. Note the higher noise level in the total glow mode and the reduced power output. The reduction in power is attributed to (1) reduced beam current through the plasma region due to higher pressure and (2) increased collision frequency, which increases the loss through the plasma. In Fig. 6.28 operation in the total glow mode is studied in more detail with the RF input signal separated from the cyclotron frequency by 90 MHz. The first spectrum analyzer photograph shows the background noise level at the output of the device along with oscillations at the electron cyclotron frequency with no input signal applied. The second photograph shows an output signal with the input drive level slightly below saturation. When the device was driven well into saturation, as shown in the third photograph of Fig. 6.28, the cyclotron oscillations were completely suppressed and



→ | | ← cm  
← 10MHz/cm

→ | | ← cm  
← 10MHz/cm

(a) BEAM CONFINED MODE

$V_0 = 553 \text{ V}$   
 $I_K = 16.3 \text{ mA}$   
 $I_0 = 8.0 \text{ mA}$   
 $P = 2 \cdot 10^{-4} \text{ TORR}$

(b) TOTAL GLOW MODE

$V_0 = 553 \text{ V}$   
 $I_K = 16.2 \text{ mA}$   
 $I_0 = 6.0 \text{ mA}$   
 $P = 3 \cdot 10^{-3} \text{ TORR}$

FIG. 6.27 COMPARISON OF BEAM CONFINED AND TOTAL GLOW MODES. ( $f_s = 2.013$  GHz,  $f_c = 1.357$  GHz)

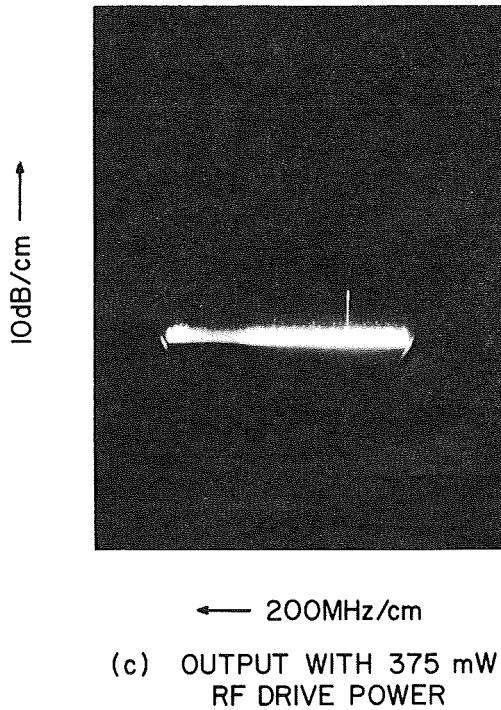
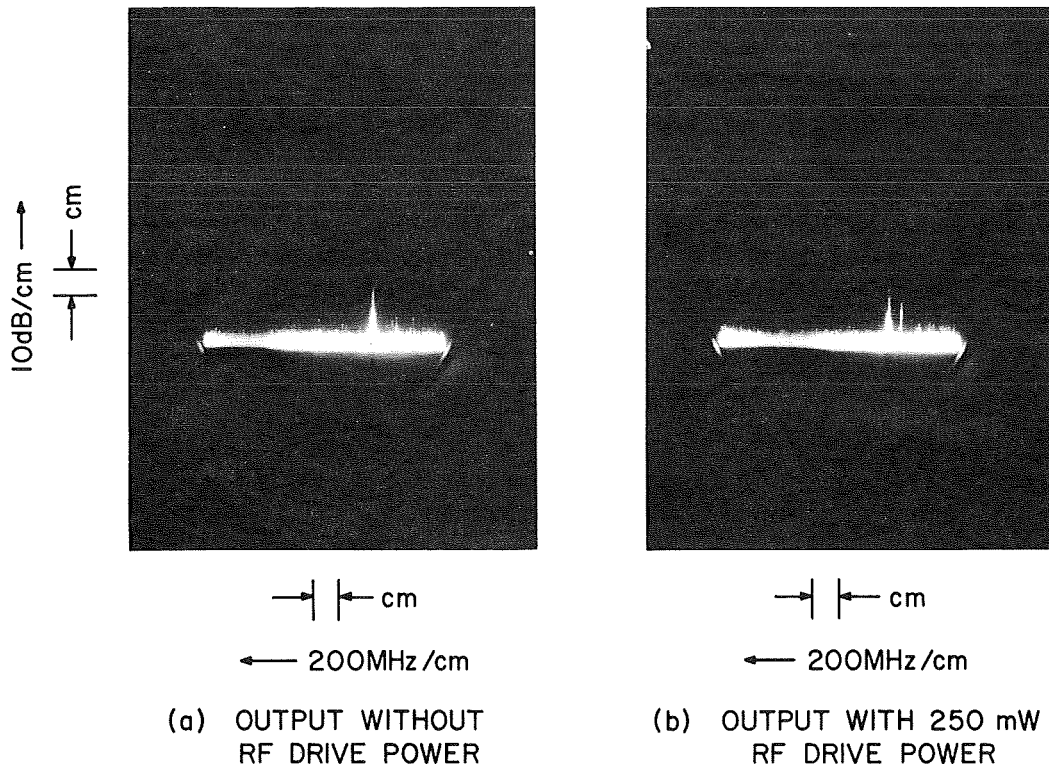


FIG. 6.28 OUTPUT CHARACTERISTICS OF A BEAM-PLASMA DEVICE OPERATING IN THE TOTAL GLOW MODE WITH THE INPUT SIGNAL CLOSE TO THE CYCLOTRON FREQUENCY. ( $V_o = 580$  V,  $I_o = 7.2$  mA,  $f_c = 1260$  MHz,  $f_s = 1150$  MHz,  $f_p \cong 9.56$  GHz)



the second harmonic is just barely visible at a level approximately 15 dB below the fundamental.

In Fig. 6.29 the saturation characteristics for the beam-plasma device operating in the total glow mode with a small-signal electronic gain of 20 dB are shown. Note that in this case the third harmonic was greater than the second by as much as 8 dB at saturation. Figure 6.30 depicts this situation in the form of a spectrum analyzer photograph. Cyclotron oscillations were suppressed in this case because the cyclotron frequency and the fundamental signal were separated by only 35 MHz. Figures 6.31 and 6.32 show total glow mode operation at a higher magnetic field and with the separation between signal and cyclotron frequencies much greater than in the two previous figures. Here saturation was just barely reached due to a lack of adequate drive power, the second and third harmonics were 14 and 20 dB below the fundamental, respectively, and the cyclotron oscillations were not suppressed.

6.3.2 Intermodulation and Cross-Modulation Tests Using Two RF Signals. Both of these phenomena may be expected to take place when a beam-plasma device is operated in the nonlinear regime. Since the one-dimensional computer program used for calculating the harmonic components was general enough to handle closely spaced signals as well, a few results showing two-signal operation of a beam-plasma device will be included in this study. All data was obtained for operation in the beam confined mode at a pressure of  $2 \cdot 10^{-4}$  Torr.

Let  $f_a$  be the lower frequency signal and  $f_b$  be the higher frequency signal. The two intermodulation products which are closest to

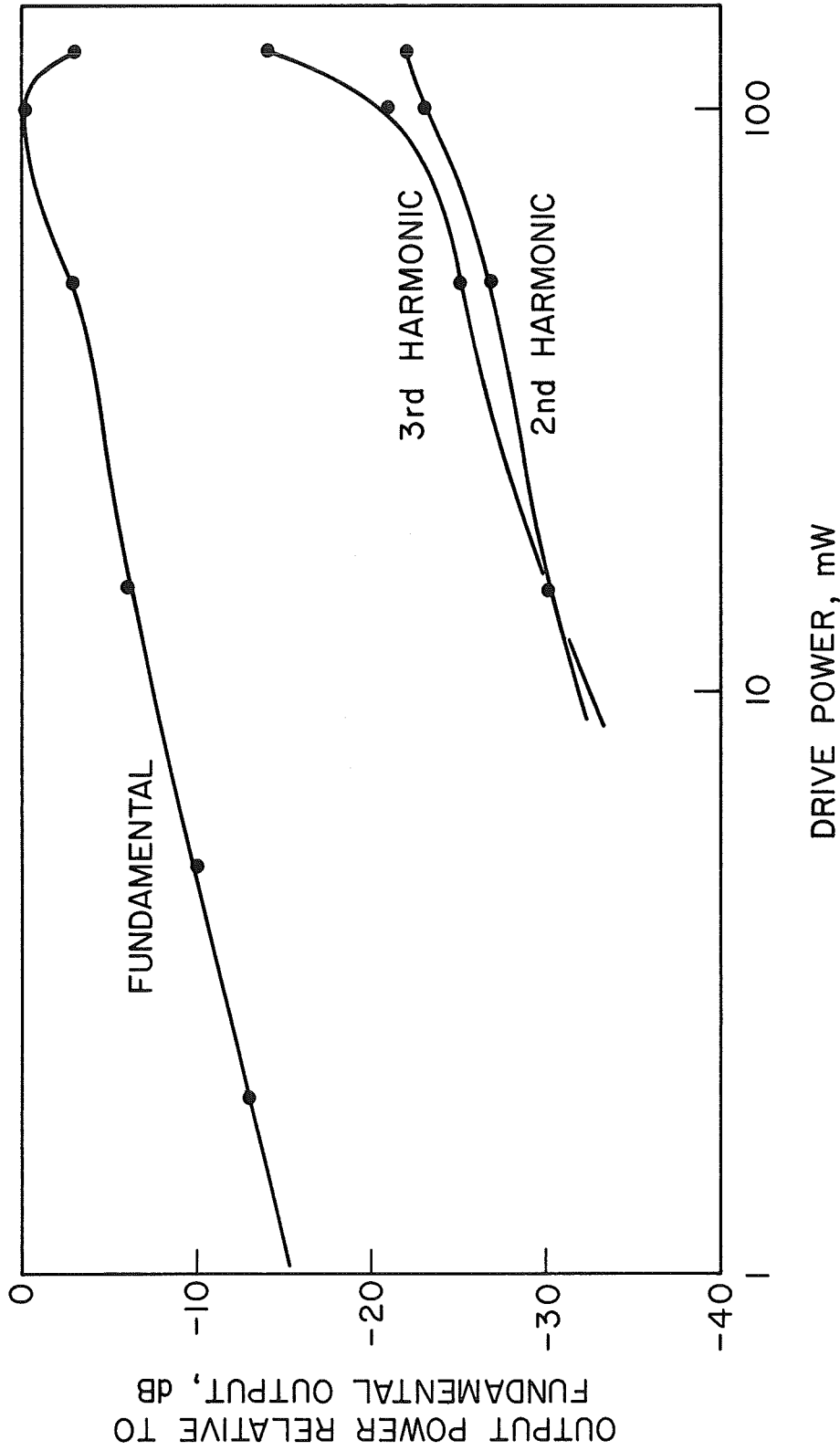


FIG. 6.29 OUTPUT AS A FUNCTION OF THE INPUT DRIVE LEVEL FOR THE BEAM-PLASMA DEVICE OPERATING IN THE TOTAL GLOW MODE AT A FREQUENCY OF 745 MHz. ( $V_o = 580$  V,  $I_o = 7.8$  mA,  $B_o = 280$  G,  $f_c = 780$  MHz,  $P = 3 \cdot 10^{-8}$  TORR,  $f_p \approx 9.5$  GHz)

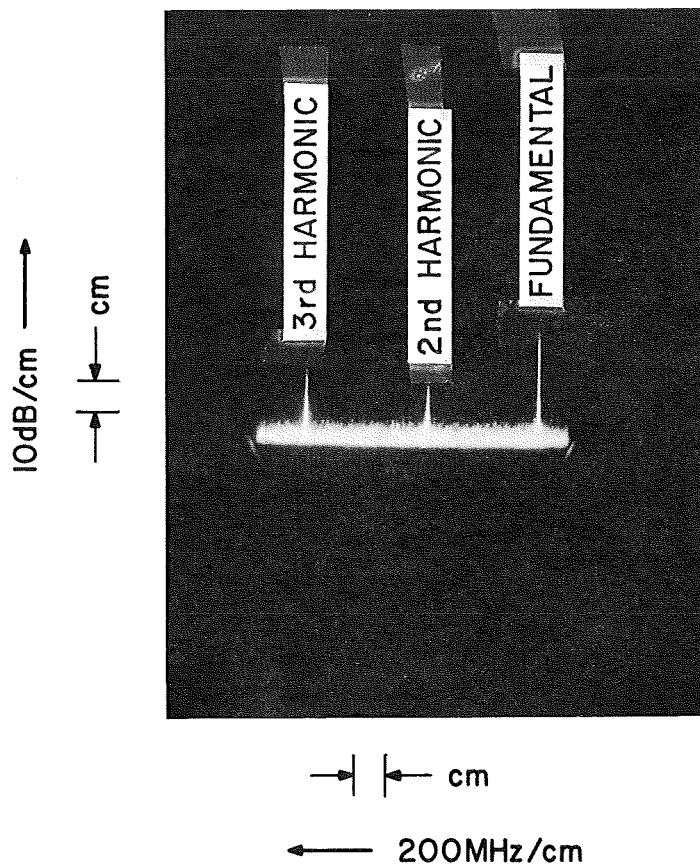


FIG. 6.30 SPECTRUM ANALYZER DISPLAY OF THE FUNDAMENTAL AND ITS FIRST TWO HARMONICS IN THE OUTPUT FROM A BEAM-PLASMA DEVICE OPERATING IN THE TOTAL GLOW MODE. ( $V_o = 580$  V,  $I_o = 7.8$  mA,  $f_c = 780$  MHz,  $f_s = 745$  MHz)

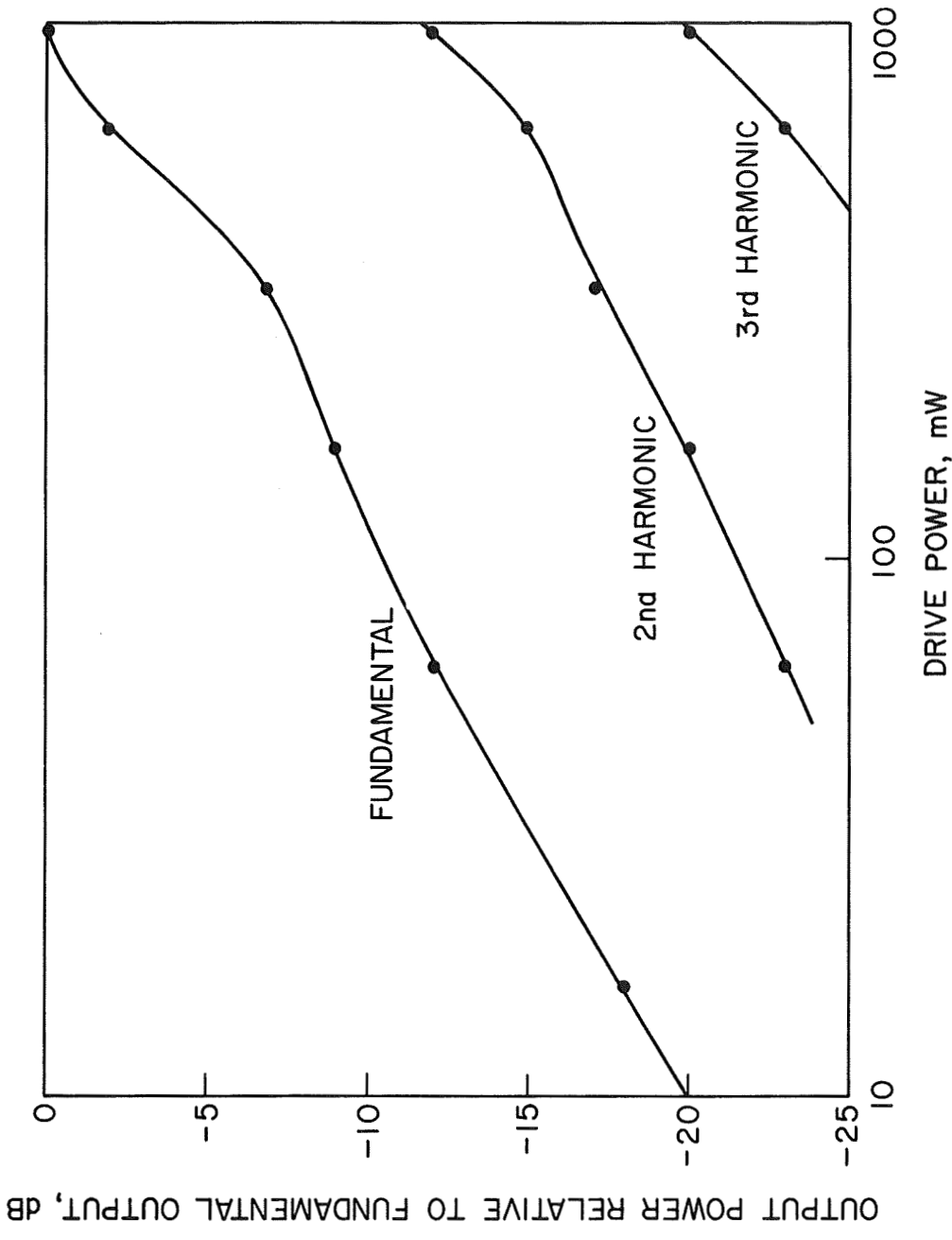


FIG. 6.31 OUTPUT AS A FUNCTION OF THE INPUT DRIVE LEVEL FOR THE BEAM-PLASMA DEVICE OPERATING IN THE TOTAL GLOW MODE AT A FREQUENCY OF 924 MHz. ( $V_0 = 580$  V,  $I_0 = 7.2$  mA,  $B_0 = 450$  G,  $f_c = 1260$  MHz,  $P = 3 \cdot 10^{-3}$ ,  $f_p \approx 9.5$  GHz)

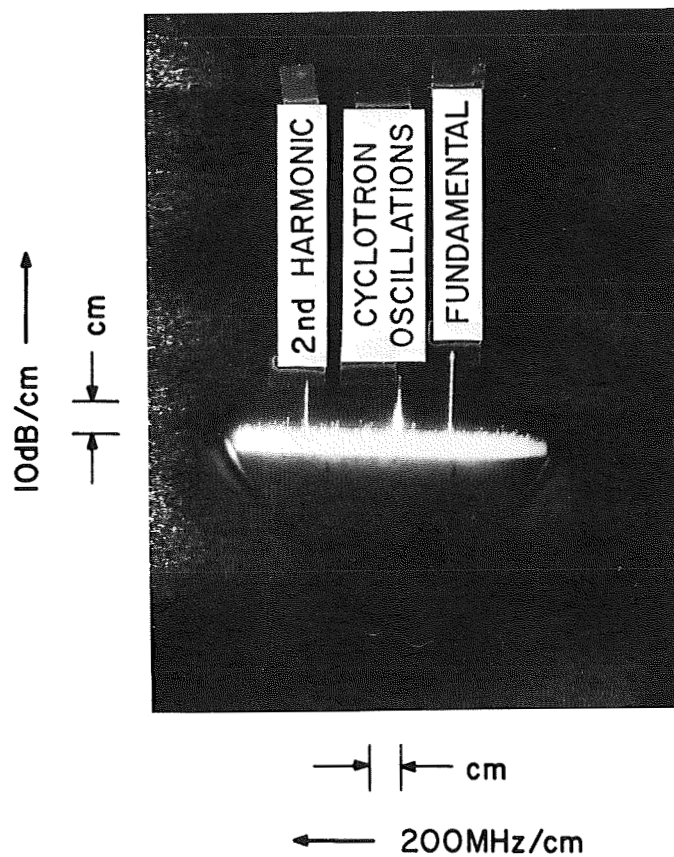


FIG. 6.32 SPECTRUM ANALYZER DISPLAY OF THE FUNDAMENTAL AND THE SECOND HARMONIC AT THE OUTPUT OF A BEAM-PLASMA DEVICE OPERATING IN THE TOTAL GLOW MODE. ( $V_o = 580$  V,  $I_o = 7.2$  mA,  $f_c = 1260$  MHz,  $f_s = 924$  MHz)

the input signals are  $2f_a - f_b$  and  $2f_b - f_a$ . Holding the input signal level of  $f_b$  fixed, Fig. 6.33 shows a drop in  $f_b$  at the output of the device due to cross-modulation as  $f_a$  is increased to saturation and slightly beyond. The small-signal gain of the device was approximately 33 dB. The drive level was so chosen that when  $f_a$  of comparable magnitude was applied the device was saturating, even though  $f_b$  alone was not sufficient for saturation. The magnitude of the intermodulation components is also shown in Fig. 6.33. Their level comes to within approximately 15 dB of the drive signals. For the frequency spacing of 6 MHz chosen for this run only two modulation components were detected. Figure 6.34 shows the corresponding results for the case when the lower frequency input signal,  $f_a$ , was held fixed while the upper frequency signal,  $f_b$ , was increased. The intermodulation components were comparable in magnitude to the previous case, but there was a negligible decrease in the output of  $f_a$ . This shows that the lower frequency signal dominates when closely spaced signals of approximately equal strength are applied to the device. Similar results are obtained for a conventional traveling-wave amplifier, but were not apparent in the theoretical calculations for the beam-plasma amplifier. This is due to the fact that, for the frequency difference of 100 MHz that had to be used in the calculations, the variation in the velocity parameter and hence the gain completely masked this effect. Figure 6.35 shows a series of spectrum analyzer photographs of the behavior of the intermodulation components as  $f_b$  was held fixed while  $f_a$  was increased until the device saturated. All parameters are the same as for the two previous figures. Note that the intermodulation components are approximately 15 dB below the primary output signals.

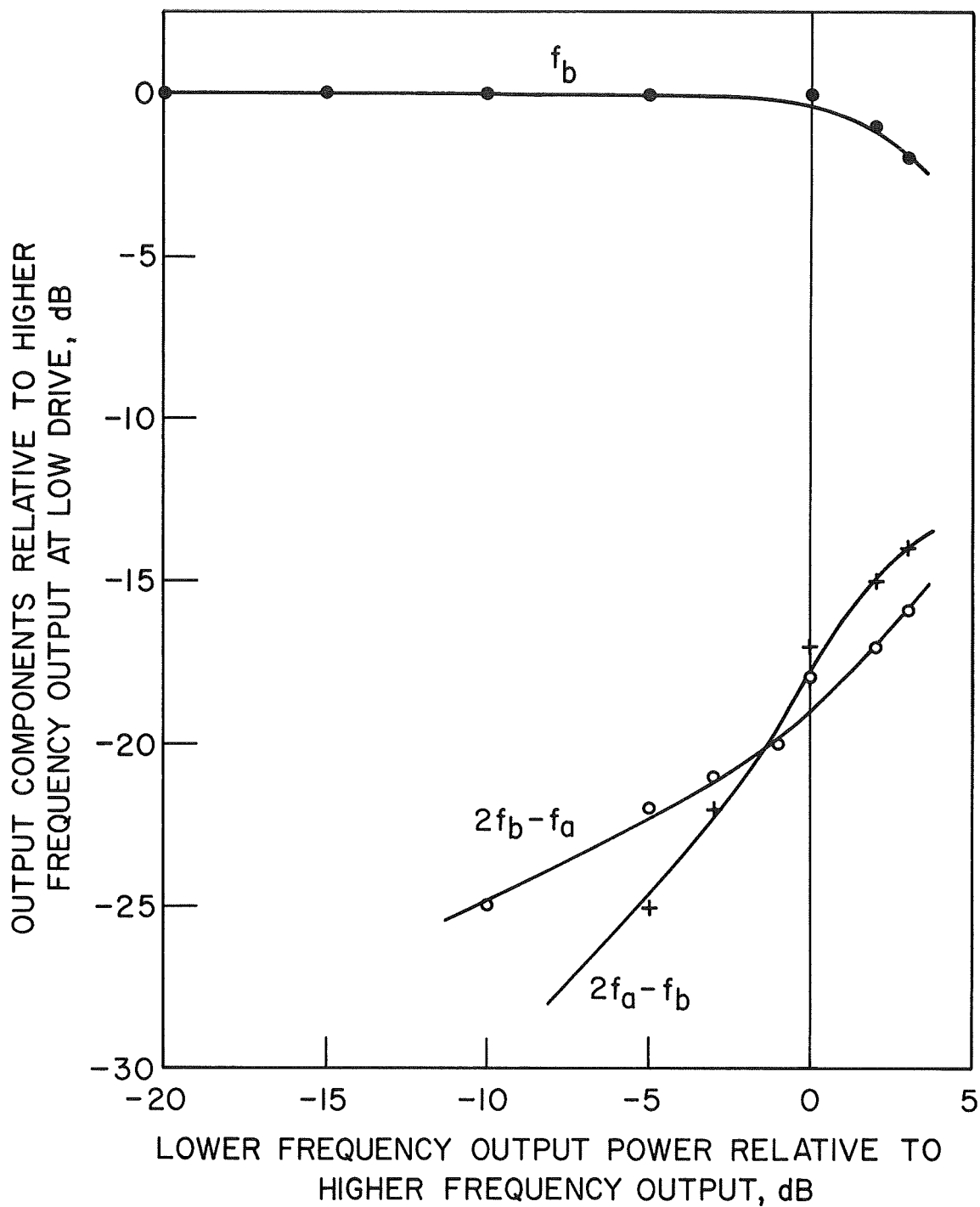


FIG. 6.33 INTERMODULATION COMPONENTS AND HIGHER FREQUENCY OUTPUT AS THE LOWER FREQUENCY INPUT LEVEL IS VARIED. [ $f_a = 1.994$  GHz,  $f_b = 2.000$  GHz (140 mW DRIVE POWER), SMALL-SIGNAL GAIN = 33 dB,  $V_o = 573$  V,  $I_o = 8.9$  mA,  $B_o = 485$  G,  $f_p \cong 4.2$  GHz,  $P = 2 \cdot 10^{-4}$  TORR]

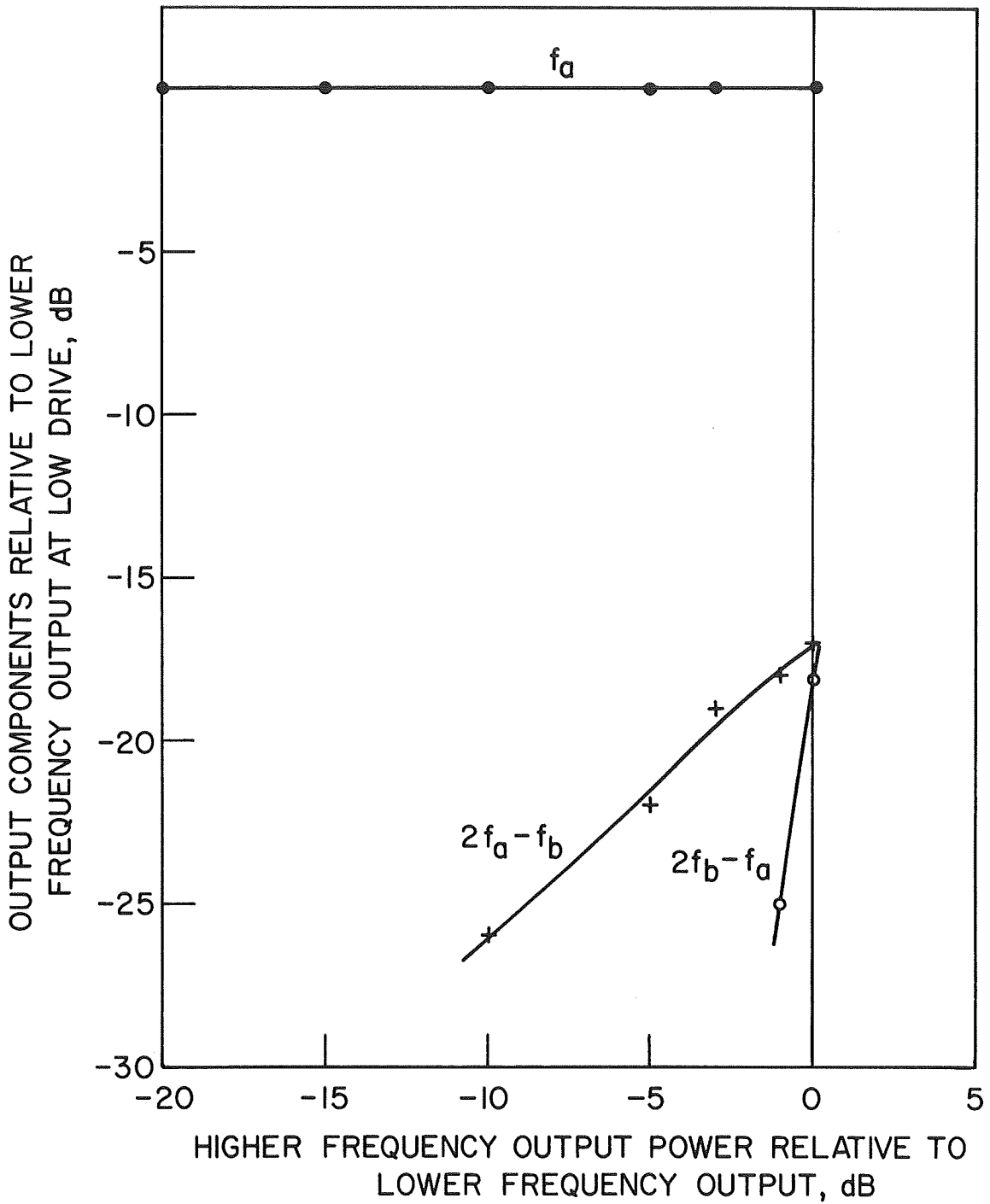


FIG. 6.34 INTERMODULATION COMPONENTS AND LOWER FREQUENCY OUTPUT AS THE HIGHER FREQUENCY INPUT LEVEL IS VARIED. [ $f_a = 1.994$  GHz (140 mW DRIVE POWER),  $f_b = 2.000$  GHz, SMALL-SIGNAL GAIN = 33 dB,  $V_o = 573$  V,  $I_o = 8.9$  mA,  $B_o = 485$  G,  $f_p \cong 4.2$  GHz,  $P = 2 \cdot 10^{-4}$  TORR]



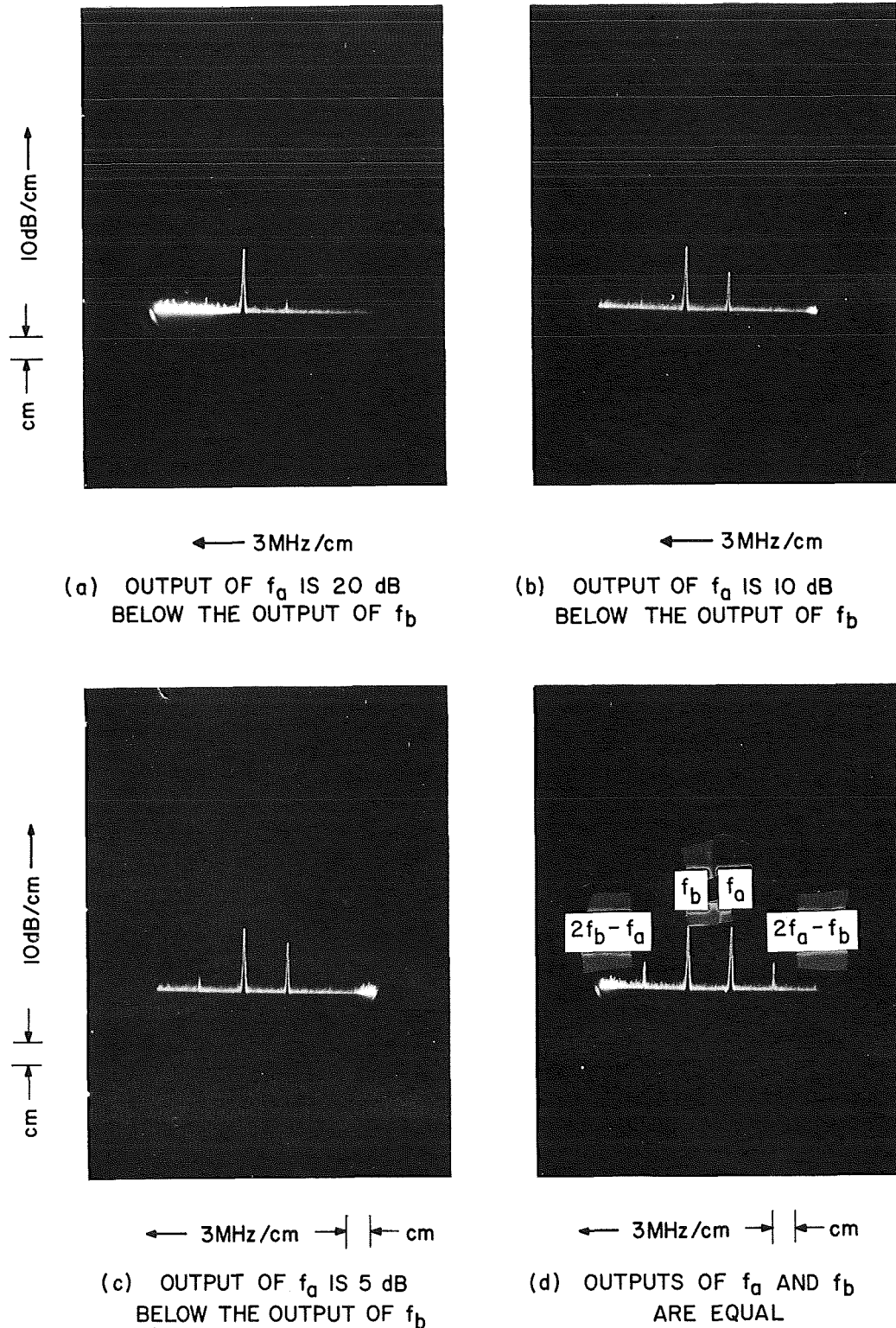


FIG. 6.35 SPECTRUM ANALYZER DISPLAY OF THE OUTPUT OF A BEAM-PLASMA DEVICE WITH TWO INPUT SIGNALS. ( $f_a = 1.994$  GHz,  $f_b = 2.000$  GHz,  $V_o = 573$  V,  $I_o = 8.9$  mA,  $B_o = 485$  G)

The next two figures are similar to the previous ones, except that the input signals are more closely spaced. They are only 1 MHz apart in Figs. 6.36 and 6.37. Consequently, two additional intermodulation components could be seen at  $3f_a - 2f_b$  and  $3f_b - 2f_a$ . The output from the device is shown in Fig. 6.36 as the higher frequency signal amplitude was held fixed, while the lower frequency amplitude was increased until saturation set in. Figure 6.37 shows a spectrum analyzer display of the various signals in the saturation region. Note that the higher frequency output signal has been slightly suppressed by the lower frequency one. Signals  $2f_a - f_b$  and  $2f_b - f_a$  appear approximately 20 dB below the primary signals,  $3f_b - 2f_a$  appears approximately 25 dB below the primary signals, while  $3f_a - 2f_b$  is just barely visible.

In summary, it can be said that the experimentally observed intermodulation components agreed within a few dB with the results calculated in Chapter V. A detailed comparison is not possible because a far greater frequency separation had to be used for the computations than for the experiments. As was pointed out in Section 5.3.4, this was necessitated by the limit in the number of charge groups that could be tracked through the interaction region.

Comparing the results of this study with El-Shandwily's data<sup>72</sup> for a Sperry STX-297 traveling-wave amplifier, one finds that the intermodulation components appear slightly higher in this beam-plasma device. This is probably due to a higher value of interaction impedance, which results in a higher value of the gain parameter,  $C_1$ .

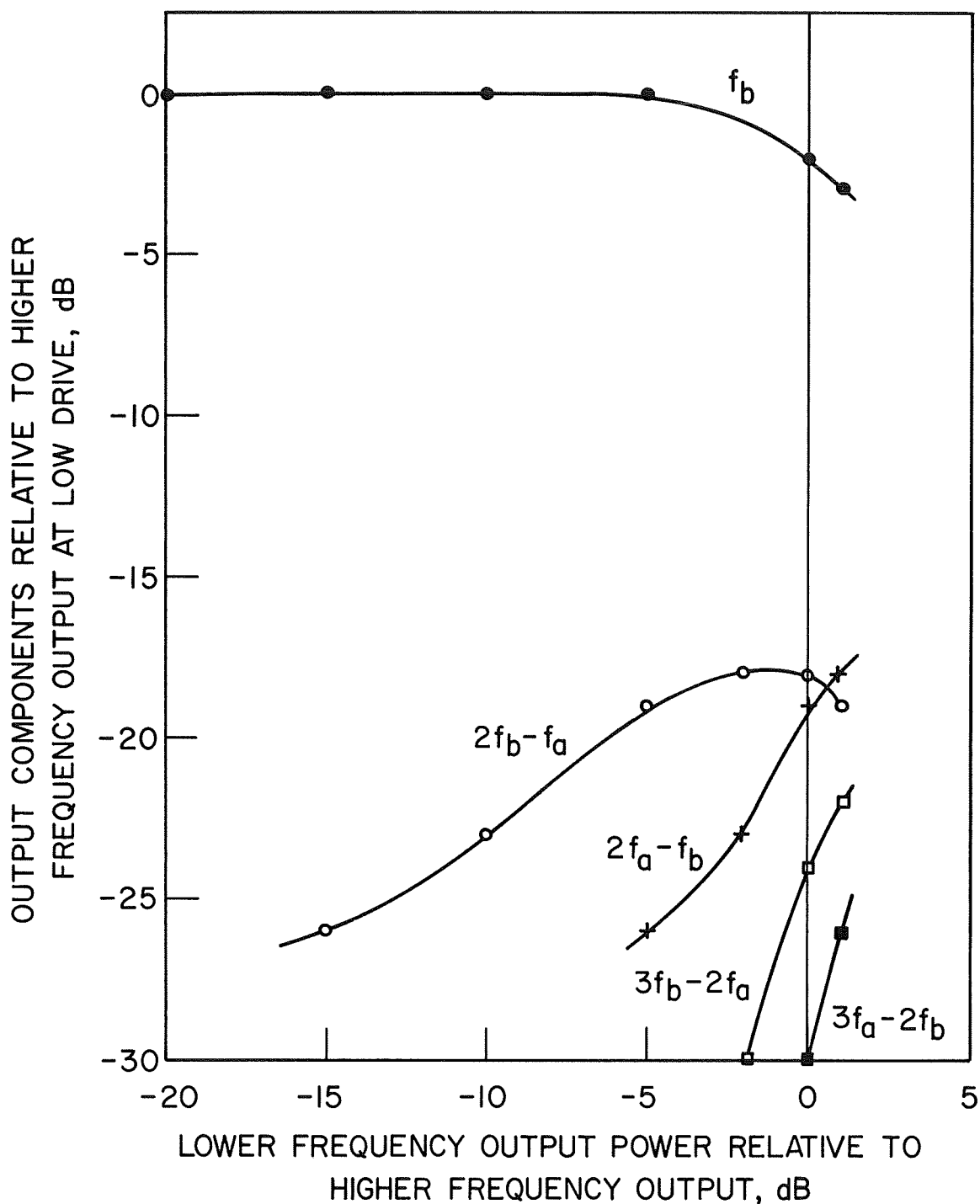


FIG. 6.36 INTERMODULATION COMPONENTS AND HIGHER FREQUENCY OUTPUT AS THE LOWER FREQUENCY INPUT LEVEL IS VARIED. [ $f_a = 2.009$  GHz,  $f_b = 2.010$  GHz (150 mW DRIVE POWER), SMALL-SIGNAL GAIN = 33 dB,  $V_o = 573$  V,  $I_o = 8.9$  mA,  $B_o = 485$  G,  $f_p \cong 4.2$  GHz,  $P = 2 \cdot 10^{-4}$  TORR]

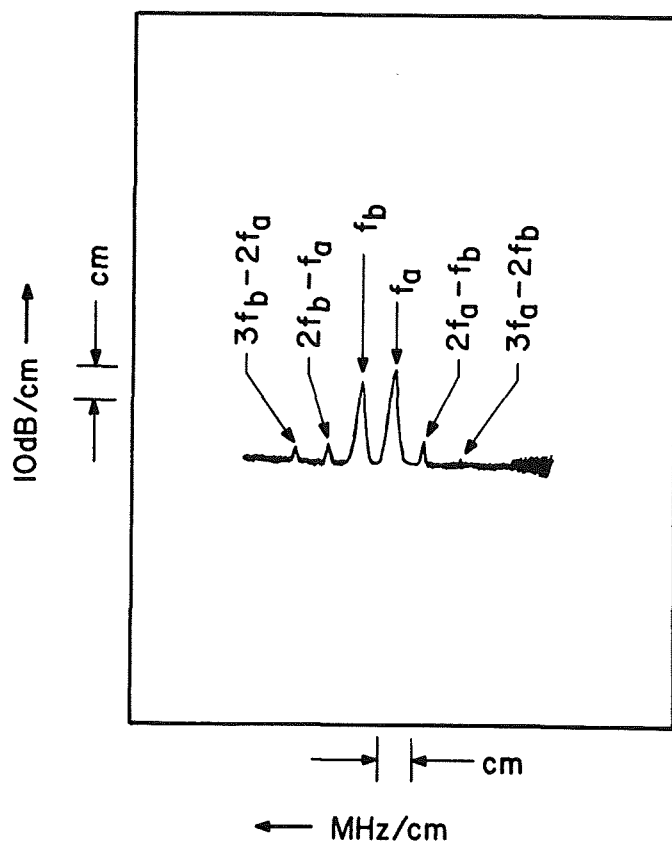


FIG. 6.37 SPECTRUM ANALYZER DISPLAY OF THE FIRST TWO SETS OF INTER-MODULATION COMPONENTS AT THE OUTPUT OF A BEAM-PLASMA DEVICE.

( $f_a = 2.009$  GHz,  $f_b = 2.010$  GHz,  $V_o = 573$  V,  $I_o = 8.9$  mA,  
 $B_o = 485$  G)

## CHAPTER VII. COUPLING TO BEAM-PLASMA SYSTEMS

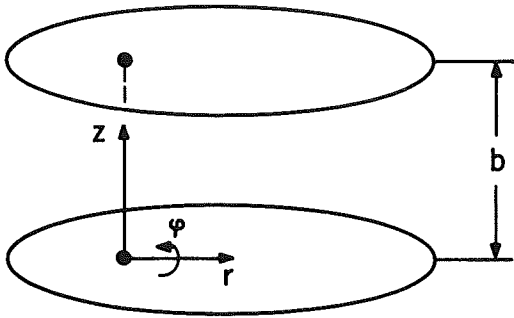
### 7.1 Introduction

One of the principal advantages of a beam-plasma device compared with a conventional microwave tube is that the slow-wave structure is replaced by the plasma column. Thus the problems inherent in manufacturing the fragile slow-wave structure are eliminated. Unfortunately the problem of coupling into the device is still present. The experimental data of Chapter VI, for example, were obtained with a beam-plasma device that made use of short sections of slow-wave structure to which RF energy could be coupled. These were located outside of the actual plasma, but were just as limited in size as the slow-wave structure of a comparable traveling-wave tube.

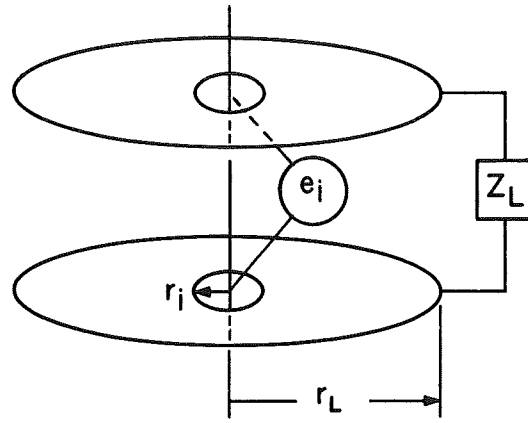
Elliptic cavity couplers represent a quasi-optical approach to coupling to a beam-plasma system. They were mentioned briefly in Chapter VI and will be analyzed more fully below. There are no stringent restrictions on the size of such a coupler other than those dictated by impedance considerations. Of course, wall losses increase with physical size, but these are ordinarily small compared to the coupling losses between the cavity and the plasma. Thus, if the impedance of an elliptic cavity can be matched to the impedance of the plasma column, an excellent coupling scheme should result.

### 7.2 Analysis of Elliptic Cavity Couplers

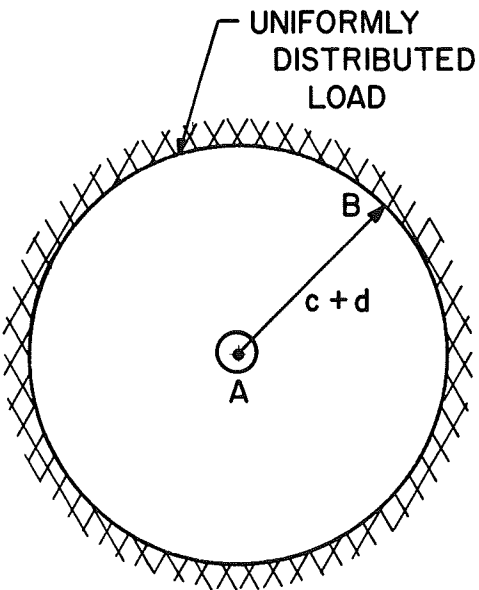
Consider the radial transmission line depicted in Fig. 7.1a consisting of two parallel plane conductors with a spacing,  $b$ , between



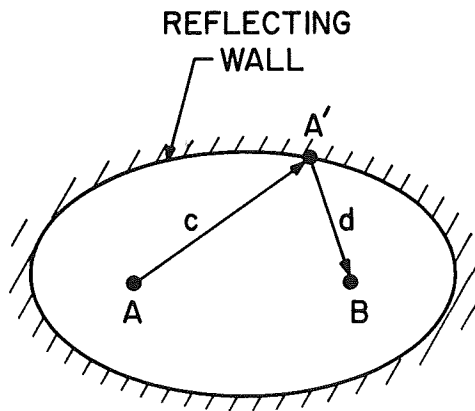
(a) RADIAL TRANSMISSION LINE COORDINATES



(b) TERMINATED RADIAL TRANSMISSION LINE



(c) TOP VIEW OF TERMINATED RADIAL TRANSMISSION LINE



(d) ELLIPTIC DEVELOPMENT OF RADIAL TRANSMISSION LINE (TOP VIEW)

FIG. 7.1 DEVELOPMENT OF AN ELLIPTIC CAVITY COUPLER.

them. Solving the wave equation for such a system one finds that the dominant E-type mode is a TEM mode.<sup>82</sup> The excitation geometry and guide dimensions will later be chosen so that the dominant mode characterizes the field everywhere. The nonvanishing field components of this mode are the  $E_z$ -component, which has no variation in the z-direction, and the  $H_\phi$ -component, which corresponds to a total radial current  $2\pi r H_\phi$ , directed outward in one plate and inward in the other. The component  $E_z$  corresponds to a total voltage  $E_z b$  between the plates. Thus

$$E_z = -V(r)/b \quad (7.1)$$

and

$$H_\phi = I(r)/2\pi r \quad (7.2)$$

The corresponding characteristic impedance is then

$$Z = \zeta b/2\pi r \quad , \quad (7.3)$$

where

$$\zeta = (\mu_0/\epsilon_0)^{1/2} = 377 \Omega \quad (7.4)$$

when the space between the radial waveguide planes is empty. For computation of power flow the input impedance of a matched line is not in general equal to its characteristic impedance.

In a radial waveguide the concept of guide wavelength loses its customary meaning because of the nonperiodic nature of the field variation in the transmission direction. Consequently the usual relation between guide wavelength and cutoff wavelength is not valid. However, the cutoff wavelength, defined as the wavelength at which the

propagation constant is zero, is useful as an indication of the propagating or nonpropagating character of a mode. For an E-type mode the cutoff wavelength is given by<sup>82</sup>

$$\lambda_c = [(n/2b)^2 + (m/2\pi r)^2]^{-1/2} . \quad (7.5)$$

Thus for the dominant mode, for which  $m = n = 0$ , there is no lower frequency cutoff.

Instead of letting the radial transmission line extend to infinity, it is assumed to be terminated in an impedance  $Z_L$  uniformly distributed around a radius  $r_L$ , as shown in Fig. 7.1b. Assume also that an input signal is applied at  $r_i$ . For such a case Ramo and Whinnery<sup>83</sup> derived an expression for the input impedance,  $Z_i$ , defined by

$$Z_i = \left. \frac{E_z}{H_\phi} \right|_i . \quad (7.6)$$

For arbitrary values of  $Z_L$  the result is

$$Z_i = Z_{oi} \frac{Z_L \cos(\theta_i - \psi_L) + jZ_{oL} \sin(\theta_i - \theta_L)}{Z_{oL} \cos(\psi_i - \theta_L) + jZ_L \sin(\psi_i - \psi_L)} , \quad (7.7)$$

where

$$Z_o(k_o r) = \zeta \frac{G_o(k_o r)}{G_1(k_o r)} , \quad (7.8)$$

$$\theta(k_o r) = \tan^{-1} \frac{N_o(k_o r)}{J_o(k_o r)} , \quad (7.9)$$

$$\psi(k_o r) = \tan^{-1} \frac{J_1(k_o r)}{-N_1(k_o r)} , \quad (7.10)$$



$$G_0(k_0 r) = \sqrt{J_0^2(k_0 r) + N_0^2(k_0 r)} \quad (7.11)$$

and

$$G_1(k_0 r) = \sqrt{J_1^2(k_0 r) + N_1^2(k_0 r)} \quad (7.12)$$

Here  $k_0$  is the propagation constant of free space and the J's and N's are Bessel functions of the first and second kind, respectively.

Choosing  $Z_L = 50 \Omega$  for a reason which will be apparent shortly, Eq. 7.7 was used to calculate the input impedance as a function of  $k_0 r_L$  with  $k_0 r_i = 0.416$ . The results are shown in Fig. 7.2.

Knowing the characteristics of a terminated radial transmission line the final step in the development of an elliptic cavity coupler is depicted in Figs. 7.1c and d. The transmission line of height  $b$  and radius  $r_L$  is replaced by an elliptic line of height  $b$  such that  $c + d = r_L$ . A perfectly reflecting surface is assumed to be located at A' and the  $50 \Omega$  load is at B. The foci of the ellipse are at A and B. The final geometry of the elliptic cavity is shown in Fig. 7.3. It is a characteristic of an ellipse that the lengths of the rays between one focus, the wall and the other focus are all equal. In particular, in Fig. 7.3,

$$\overline{F_1 A F_2} = \overline{F_1 B F_2} = r_L \quad (7.13)$$

One may now place a transition to a  $50 \Omega$  coaxial transmission line at  $F_2$  and a plasma column of radius  $r_i$  at  $F_1$ . Then RF energy launched in the cavity at  $F_2$  is transmitted in phase to the plasma at  $F_1$  due to the equal path lengths between the two foci. The electric field in the cavity is such that it lies along the longitudinal direction of

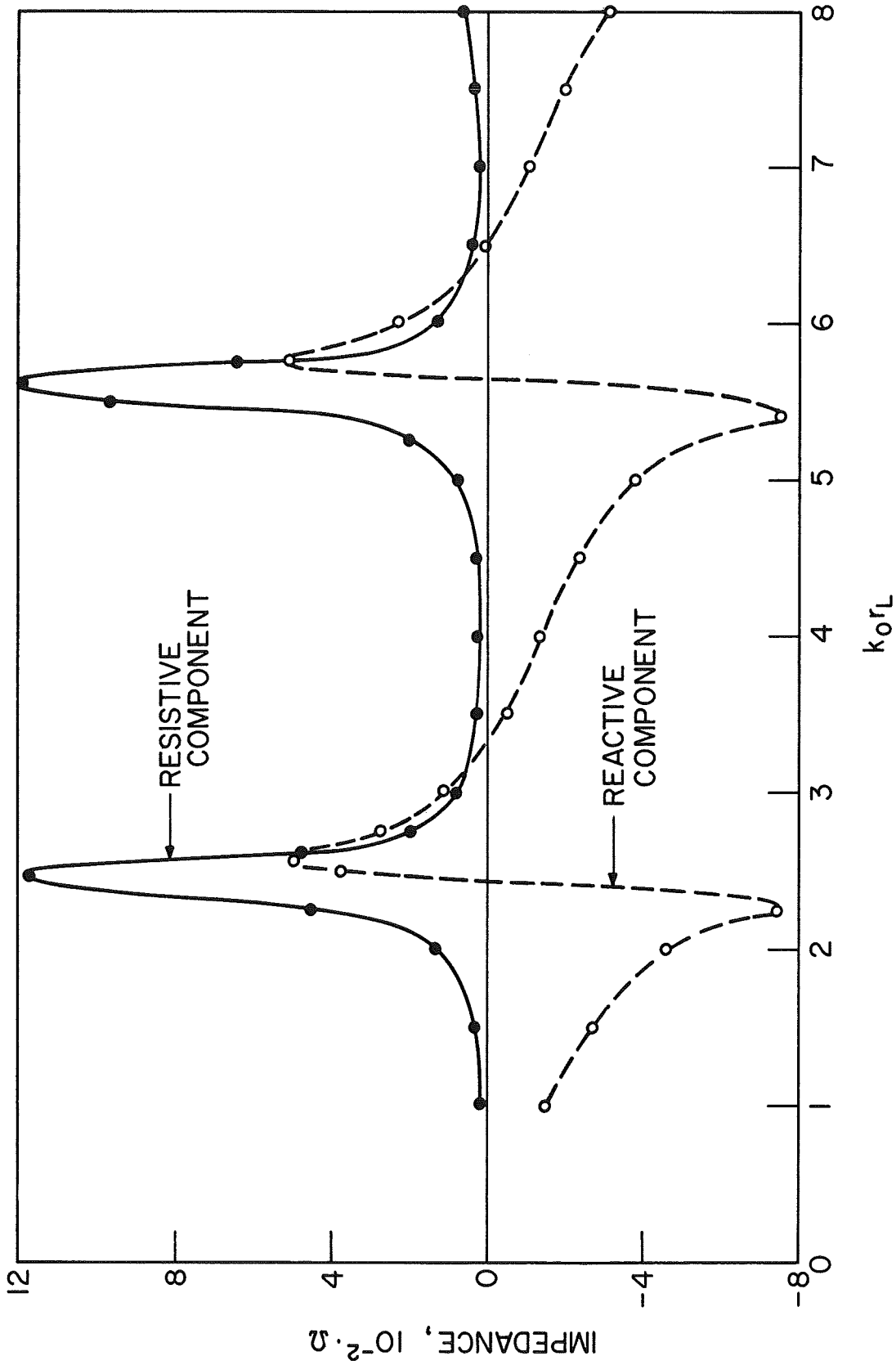


FIG. 7.2 INPUT IMPEDANCE OF A RADIAL TRANSMISSION LINE TERMINATED IN  $50 \Omega$ . ( $k_0 r_1 = 0.416$ )

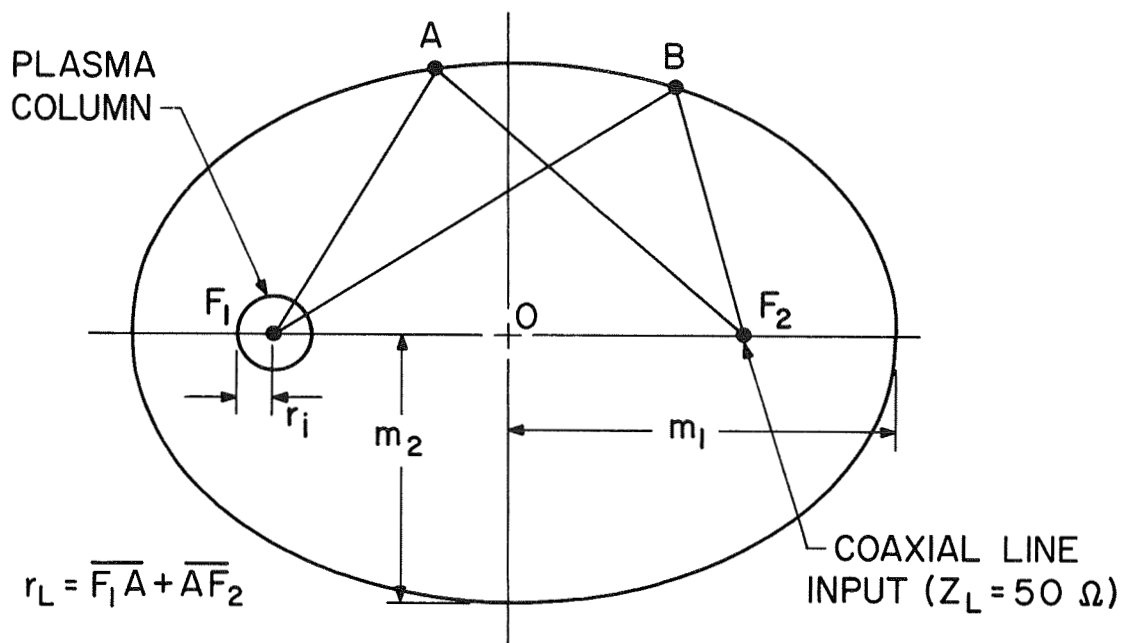


FIG. 7.3 CONCEPT OF AN ELLIPTIC CAVITY COUPLER.

the plasma column, as is desired for a beam-plasma interaction. Phase errors are introduced due to the fact that the path lengths are not all exactly equal since the plasma column and the coaxial line transition have finite dimensions. This problem may in part be compensated for in an actual cavity by making trial and error adjustments in the matching antenna between the coaxial line and the cavity.

To be suitable with the experimental device described in Chapter VI the cavity dimensions were taken as shown in Table 7.1.

Table 7.1

Cavity Dimensions

Major Axis of Ellipse	6.25 cm
Minor Axis of Ellipse	5.70 cm
Eccentricity of Ellipse	0.407
Cavity Height	1.06 cm
Design Center Frequency	2.5 GHz
$r_i$	0.793 cm
$k_o r_i$	0.416
$k_o r_L$ (from Fig. 7.2)	6.545

This choice of dimensions for the cavity places the operating point of 2.5 GHz near the center of one of the broad valleys in the resistive component of the input impedance shown in Fig. 7.2. The reactive component is near zero for those conditions. Thus operation should be possible over a band of frequencies around 2.5 GHz. Note that the input impedance is in the range of 20 to 100  $\Omega$ , requiring a plasma column corresponding to Fig. 2.12 rather than Figs. 2.8 through 2.11.

This implies that the plasma column is required to fill the tube, necessitating a hot-cathode discharge or possibly a beam-generated plasma operating in the total glow mode. A beam-generated plasma in the beam confined mode, as available in the present experimental device, could not be expected to be matched to the cavity. These points will be discussed more fully in the next section.

A cross section through an elliptic cavity coupler is shown in Fig. 7.4. A standard type-N RF connector modified for this purpose was used at the input.

For a coaxial line the characteristic impedance is given by

$$Z_c = \frac{\zeta}{2\pi\sqrt{\epsilon/\epsilon_0}} \ln\left(\frac{r_2}{r_1}\right), \quad (7.14)$$

where  $\zeta = 377 \Omega$  and  $\epsilon$  is the dielectric constant of the material (with permeability  $\mu = \mu_0$ ) filling the coaxial line. The radius of the inner conductor is  $r_1$  and the inside radius of the outer conductor is  $r_2$ . In the transducer between the coaxial line and the cavity the spacing between the inner and outer conductors of the line was tapered to maintain a  $50 \Omega$  impedance, as shown in Fig. 7.4. The inner conductor thus forms a conical antenna at the input to the cavity. The exact shape of the cone, particularly at its base, was determined by trial and error so that a good match to the cavity impedance was achieved. A photograph of a disassembled cavity is shown in Fig. 7.5. The tapered steps around the hole through which the plasma tube passes were used to reduce the impedance of the cavity by trial and error. This was done in order to obtain a better impedance match for the hot-cathode discharge plasma.

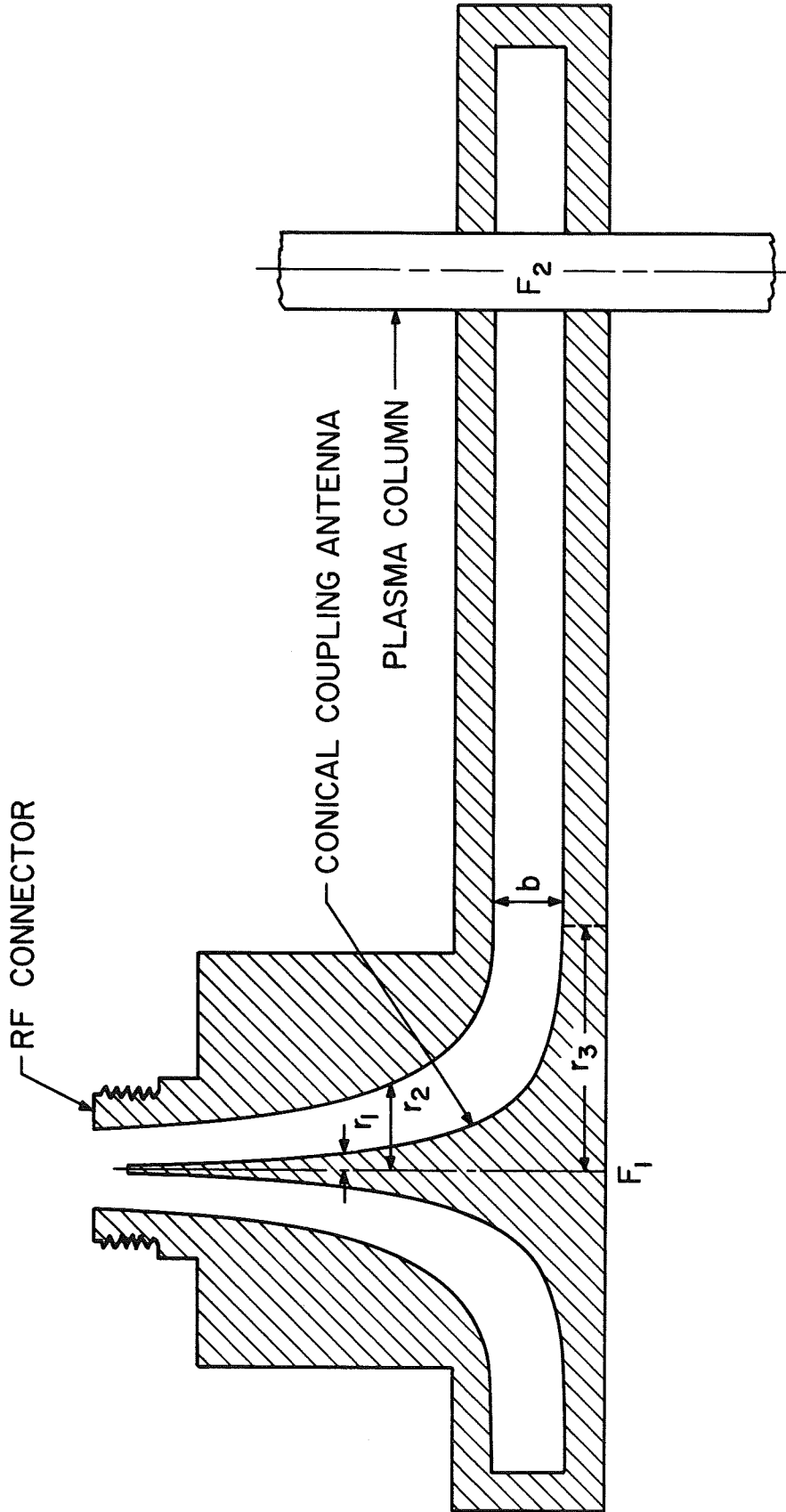


FIG. 7.4 CROSS SECTION THROUGH AN ELLIPTIC CAVITY COUPLER.

PLASMA COLUMN  
IMPEDANCE TRANSFORMER

ELLIPTIC  
CAVITY WALL

CONICAL COUPLING  
ANTENNA

TOP  
PLATES  
OF  
CAVITY

FIG. 7.5 PHOTOGRAPH SHOWING THE INSIDE OF AN ELLIPTIC CAVITY COUPLER.

### 7.3 Test Results Using Elliptic Cavity Couplers

It already has been pointed out that the elliptic cavity couplers can be expected to couple best to the hot-cathode discharge plasma column which required a gas pressure of approximately  $1 \cdot 10^{-2}$  Torr for stable operation. The results of a coupling experiment are shown in Fig. 7.6. The cold loss through two cavities and the plasma tube with no plasma present was in the 60-80 dB range from 1.3 to 2.6 GHz. When a plasma was present the cold loss dropped markedly over this range, particularly for a discharge current of 400 mA per cathode. In the upper L-band the insertion loss varied from 30 to 40 dB while in the lower S-band it was in the vicinity of 25 to 30 dB. Just below the design frequency of 2.5 GHz the insertion loss was only 21 dB. Since the RF losses in the cavities and the plasma column may be expected to be small compared to the coupling loss, most of the 21 dB may be attributed to the coupling. Thus a loss of 10 to 15 dB per coupler was observed over a fairly wide range of frequencies. Since the beam-plasma interaction yielded a gain of more than 30 dB in the device tested, net gain should be possible with this method of coupling.

Unfortunately the electron beam emission could not be maintained at pressures in the  $10^{-2}$  Torr range due to ion bombardment of the cathode. When the pressure was lowered sufficiently so that an electron beam with rated current could be obtained, the hot-cathode discharge became unstable due to an anomalous diffusion and extinguished due to sputter pumping in the discharge region. These problems were discussed in Chapter VI.



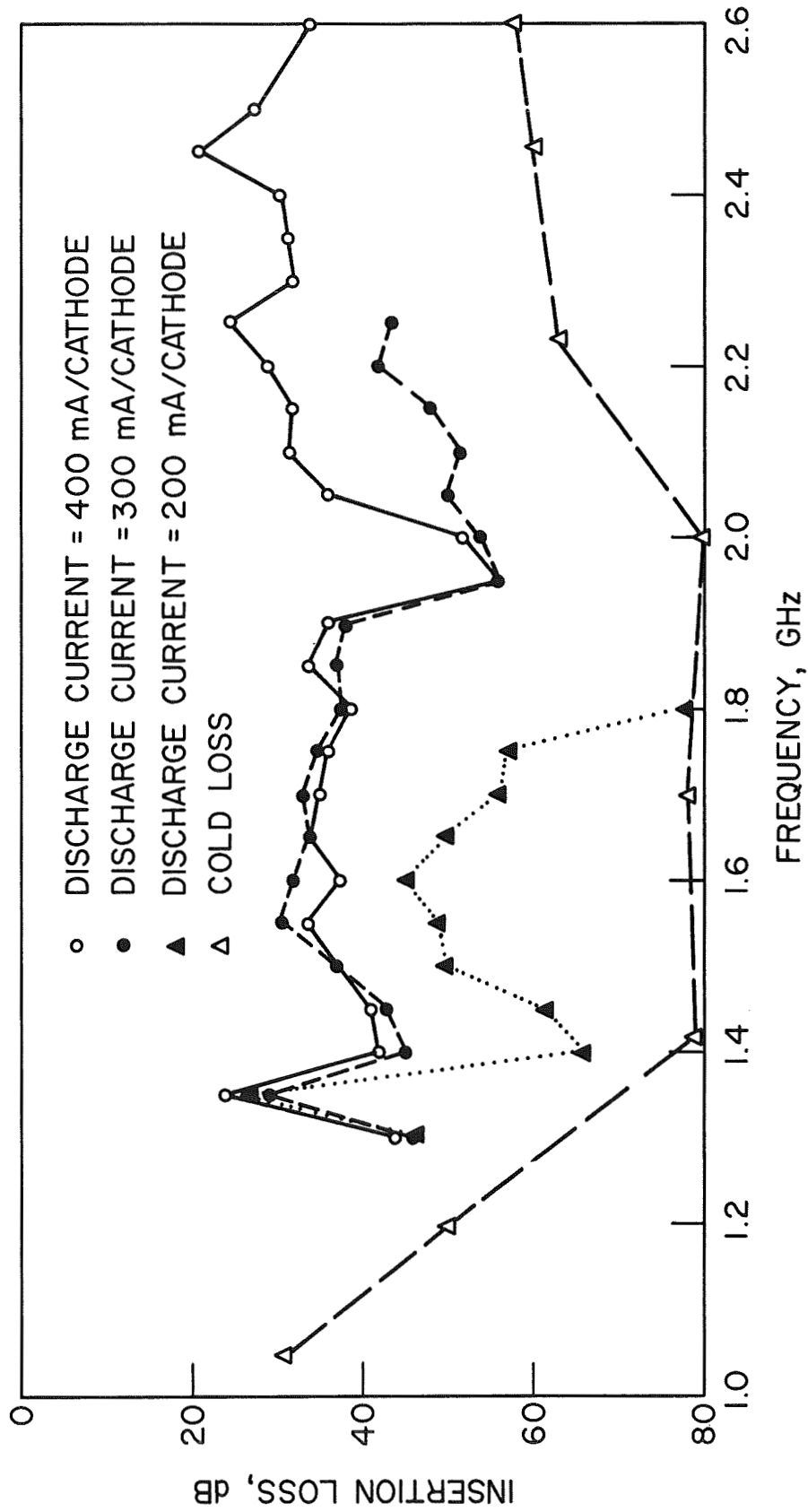


FIG. 7.6 INSERTION LOSS THROUGH TWO ELLIPTIC CAVITY COUPLERS AND A 2.36 cm LONG PLASMA COLUMN CREATED BY A DUAL HOT-CATHODE DISCHARGE FOR VARIOUS VALUES OF DISCHARGE CURRENT. ( $P = 3 \cdot 10^{-2}$  TORR,  $B_0 = 332$  G,

$f_c = 934$  MHz)

The plasma that could be maintained at lower pressures was the beam-generated plasma. The beam confined mode, which existed at pressures below  $2 \cdot 10^{-3}$  Torr and for which the best experimental gain was obtained with the coupled-helix couplers, had a characteristic impedance of several hundred ohms, as shown in Figs. 2.8 through 2.11. Thus it was not possible to match the cavity impedance to the plasma column over a sufficiently wide frequency region. Even the total glow mode of the beam-generated plasma yielded negative results in a coupling experiment with the elliptic cavities. Apparently the plasma density was still too low to yield a sufficiently low impedance to be matched to the cavities.

These results are in general agreement with the work at Microwave Associates,<sup>60</sup> where it was found that the best plasma density for coupling does not ordinarily correspond to the plasma density for optimum gain. To overcome this difficulty it may be necessary to taper the density and possibly the magnetic field<sup>84</sup> in order to obtain better radial propagation and hence tighter coupling to the system.

## CHAPTER VIII. CONCLUSIONS AND RECOMMENDATIONS FOR FURTHER STUDY

### 8.1 Summary and Conclusions

The equivalent circuit representation of a plasma column was found to be an effective and convenient method of modeling the plasma in a beam-plasma interaction. The characteristic impedance found in this way included a loss term due to plasma collisions. Collisions due to the beam electrons with the plasma were also accounted for by an additional term in the beam force equation.

One of the chief stipulations in the development of the equivalent circuit concept for a plasma column was that the plasma remain linear under all conditions. It was shown that under ordinary circumstances this requirement is easily satisfied. In other applications such as plasma heating or plasma containment in high fields this may not be the case and would have to be investigated before plasma linearity may be assumed.

Even though the one-dimensional interaction model resulted in a good qualitative understanding of the interaction process, it was generally optimistic in predicting the output levels from the device. In particular, the interaction distance required for saturation to occur was consistently too low. The two-dimensional model, which took radial variations into account, corrected these shortcomings, so that fairly good agreement could be obtained with the experimental measurements.

The beam-plasma device was found to be considerably more dispersive than a conventional helix-type traveling-wave amplifier, for example. For this reason the appropriate dispersion equation had to be solved in order to find the  $\omega$ - $\beta$  characteristics before the characteristic impedance could be calculated. Even though the phase velocity along the plasma column was appropriate for beam-plasma interaction over a bandwidth of approximately 20 percent, the characteristic impedance remained at a substantial level over a frequency band of several octaves. This suggests that a beam-plasma device might be rich in harmonics, provided they can be coupled out. This was in fact found to be the case. Experimental results indicated that in some cases the second harmonic was as little as 3 to 6 dB below the fundamental. In other cases, when the second harmonic was 12 to 15 dB below the fundamental, the third harmonic was actually several dB larger than the second.

Nonuniformities in the plasma density were not taken into account in the theoretical development, but they did play a major role in the experimental device. For one thing, they resulted in a considerable broadening of the frequency region over which gain could be observed. Second, the interaction length required for saturation to take place was increased by nonuniformities. Most significantly, however, it appears that nonuniformities permitted some of the higher harmonics to be generated that otherwise would not have existed. Since the density varied across the plasma column, the plasma frequency varied also. The higher harmonics appearing in these experiments were ordinarily generated by an inductive wall interaction, which may take place between the hybrid frequency and  $\omega_p$  when  $\omega \gtrsim \omega_c$  and  $\omega_p$  is several times  $\omega_c$ .

Thus the increase in plasma density toward the center of the column broadened this interaction region and resulted in the production of additional harmonics.

Two methods of coupling into and out of the experimental device were employed. One made use of coupled-helix couplers and short sections of helical slow-wave structure at both ends of the plasma region. This method worked quite well and was used almost exclusively in the gain and harmonic generation tests. The main shortcoming of this method of coupling is that a slow-wave structure is required, just as in a conventional microwave tube. As the operating frequency becomes high this slow-wave circuit becomes very small, is difficult to fabricate and is not able to handle large amounts of RF power.

For that reason elliptic cavity couplers were built and placed directly around the plasma column. Being a quasi-optical method of coupling, it did not suffer from size limitations, as the coupled helices did. A coupling loss of 10 to 15 dB per cavity could be obtained over a substantial frequency region. Since high RF gain per unit length is possible in a beam-plasma interaction, this method of coupling holds great promise to yield net gain in a device similar to the one used for the experimental work of this study. Some ways of overcoming the problems encountered with the elliptic cavities in the device used for this study will be mentioned in the next section.

## 8.2 Recommendations for Further Study

The experimental work demonstrated that plasma nonuniformities are quite important in altering the theoretically calculated values of interaction length, the harmonic current magnitudes and the gain.

For that reason they should be included in the theoretical analyses. Conceptually the approach to this problem appears to be straightforward. One merely has to make allowance for axial and radial plasma density variations by letting the equivalent dielectric constant of the plasma column and hence the characteristic impedance be a function of axial and radial distance. This could be done in a continuous manner, but with a stepwise approximation for use in the digital computer programs. From a programming standpoint and in view of the much longer computing time needed in such a case, the problems that would be encountered are immediately apparent. Nevertheless, in some cases it could be worthwhile to make such an analysis.

The requirement of linearity for the plasma is believed to be readily met in beam-plasma interactions of the type considered in this study. In any case, the equivalent circuit approach does not appear to lend itself easily to the inclusion of nonlinearities. If nonlinearities should become important in this or related applications, it would be necessary to treat the plasma on a particle basis, as is done for the electron beam. The double-stream interaction approach is a step in that direction. A completely nonlinear analysis would be interesting in that it would point out exactly how negligible plasma nonlinearities really are. Particularly if thermal effects in the plasma and the beam played an important role, this type of analysis would be very useful.

In the experimental work it would have been desirable to have a method of measuring the radial density distribution of the beam-generated plasma by means of cavities and/or probes. The effects of

sheaths should be investigated. Also, the instabilities in the plasma column along with the effects of anomalous diffusion, when a focusing magnetic field is present, should be studied.

Far more important than these considerations is the experimental solution to the coupling problem. By improving the stability of the plasma column it should be possible to operate the hot-cathode discharge at a lower pressure, so that a dense plasma suitable for coupling to the cavities can be obtained without poisoning the beam cathode. A lower pressure is desirable also from the standpoint of achieving a lower collision frequency and hence obtaining more gain. Ion trapping might be employed to cut down cathode bombardment and sputtering. Positioning the gun off the axis would also help in this matter because the positive ions in following the magnetic field lines would not strike the cathode.

Instead of lowering the characteristic impedance of the plasma column, an attempt should be made to raise the cavity impedance, particularly if cavity coupling to a plasma column operating in the beam confined mode is desired. It is not likely that these adjustments can be made by impedance matching outside of the cavity, but a reduction in the hole diameter through which the plasma enters the cavity should yield the desired results. To this end it may be necessary to make the cavity an integral part of the plasma tube in order to bring the coupling gap into the immediate vicinity of the beam-generated plasma column.

APPENDIX A. DISPERSION RELATION FOR A GENERAL BEAM-PLASMA SYSTEM

In Fig. A.1 the geometry is shown for which the dispersion equation is to be obtained. Region I contains an electron beam and the plasma, while Region II contains only the plasma. Region III is a dielectric cylinder with relative dielectric constant  $\kappa_e$ . At radius  $a$  there is a metallic boundary. The plasma is assumed to be cold, uniform, stationary and neutral. The velocity,  $u_0$ , of the monoenergetic beam electrons and the dc magnetic field coincide along the z-direction. Nonrelativistic mechanics is assumed to apply so that the ac magnetic field is negligible. The equations of motion applicable to the various regions yield expressions for the specific inductive capacity and hence the dielectric tensor. These quantities are derived in Appendix B for Region II, which contains a stationary plasma only. In Region I, where the beam is present in addition to the plasma, the specific inductive capacity components have a term just as for Region II plus a term where  $\omega$  is everywhere replaced by  $\omega - ku_0$ . Thus in Region I

$$\kappa_{\perp} = 1 - \frac{\left(\frac{\omega_p}{\omega}\right)^2 \left(1 - j \frac{v}{\omega}\right)}{\left(1 - j \frac{v}{\omega}\right)^2 - \left(\frac{\omega_c}{\omega}\right)^2} - \frac{\left(\frac{\omega_b}{\omega - ku_0}\right)^2 \left(1 - j \frac{v}{\omega - ku_0}\right)}{\left(1 - j \frac{v}{\omega - ku_0}\right)^2 \left(\frac{\omega_c}{\omega - ku_0}\right)}, \quad (A.1)$$



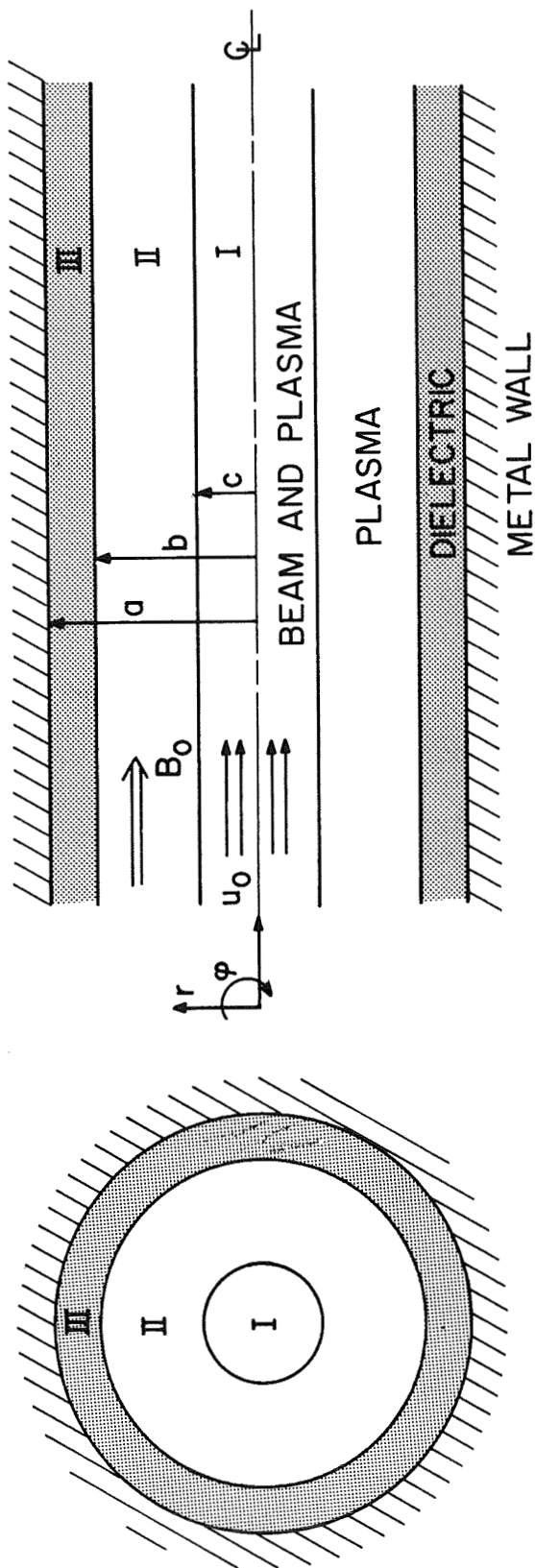


FIG. A.1.1 GENERAL BEAM-PLASMA GEOMETRY.

$$\kappa_x = - \left[ \frac{\left(\frac{\omega_p}{\omega}\right)^2 \left(\frac{\omega_c}{\omega}\right)}{\left(1 - j \frac{v}{\omega}\right)^2 - \left(\frac{\omega_c}{\omega}\right)^2} + \frac{\left(\frac{\omega_b}{\omega - ku_0}\right)^2 \left(\frac{\omega_c}{\omega - ku_0}\right)}{\left(1 - j \frac{v}{\omega - ku_0}\right)^2 - \left(\frac{\omega_c}{\omega - ku_0}\right)^2} \right] \quad (\text{A.2})$$

and

$$\kappa_{||} = 1 - \frac{\left(\frac{\omega_p}{\omega}\right)^2}{1 - j \frac{v}{\omega}} - \frac{\left(\frac{\omega_b}{\omega - ku_0}\right)^2}{1 - j \frac{v}{\omega - ku_0}}, \quad (\text{A.3})$$

where  $\omega_p$  and  $\omega_b$  are the plasma frequencies in the plasma and the beam regions, respectively.

In order to obtain a dispersion relation for the beam-plasma system, Maxwell's equations must be combined to obtain the wave equations. These must be solved along with the appropriate boundary conditions. The Maxwell equations in terms of ac quantities are

$$\nabla \times \vec{E}_1 = -\mu_0 \frac{\partial \vec{H}_1}{\partial t}, \quad (\text{A.4})$$

$$\nabla \times \vec{H}_1 = \vec{J}_1 + \epsilon_0 \frac{\partial \vec{E}_1}{\partial t}, \quad (\text{A.5})$$

$$\nabla \cdot \vec{E}_1 = \frac{\rho_1}{\epsilon_0} \quad (\text{A.6})$$

and

$$\nabla \cdot \vec{H}_1 = 0. \quad (\text{A.7})$$

Assuming all field quantities to vary as  $\exp[j(\omega t - n\phi - kz)]$ , considering the geometry of Fig. A.1 as regions of current-free noncharged dielectrics, and making use of

$$\nabla \cdot \vec{D}_1 = \nabla \cdot (\epsilon_0 \vec{\kappa} \vec{E}_1) = 0, \quad (\text{A.8})$$

one may expand Maxwell's curl equations in cylindrical coordinates to yield

$$\frac{n}{r} E_z - k E_\varphi = \omega \mu_0 H_r, \quad (\text{A.9})$$

$$jk E_r + \frac{\partial E_z}{\partial r} = j \omega \mu_0 H_\varphi, \quad (\text{A.10})$$

$$\frac{1}{r} \frac{\partial(r E_r)}{\partial r} + j \frac{n}{r} E_r = -j \omega \mu_0 H_z, \quad (\text{A.11})$$

$$-j \frac{n}{r} H_z + j k H_\varphi = j \epsilon_0 E_r A_1 - \epsilon_0 E_\varphi A_x, \quad (\text{A.12})$$

$$-j k H_r - \frac{\partial H_z}{\partial r} = \epsilon_0 E_r A_x + j \epsilon_0 E_\varphi A_1 \quad (\text{A.13})$$

and

$$\begin{aligned} \frac{1}{r} \frac{\partial}{\partial r} (r H_\varphi) + j \frac{n}{r} H_r &= j \epsilon_0 E_z \kappa_{II} \left( \omega - k u_0 + k u_0 \frac{\kappa_{III}}{\kappa_{II}} \right) \\ &+ \mu_0 \epsilon_0 \omega H_z \kappa_{III} \left( \frac{\kappa_{XII}}{\kappa_{III}} - \frac{\kappa_{XI}}{\kappa_{II}} \right). \end{aligned} \quad (\text{A.14})$$

In the above,

$$A_1 \triangleq \omega \kappa_{II} - k u_0 \kappa_{II} - k u_0 \kappa_{III}$$

and

$$A_x \triangleq \omega \kappa_{XI} - k u_0 \kappa_{XI} + k u_0 \kappa_{XII}.$$

The  $\kappa$ 's with subscripts I and II apply to Regions I and II, respectively.

In the following the quasistatic assumption will be made, which reduces the full set of Maxwell's equations to the equations of electrostatics. Thus

$$\nabla \times \vec{E}_1 \cong 0 . \quad (\text{A.15})$$

This approximation is valid in systems where the space-charge waves, or slow waves, travel at a small fraction of the speed of light.

In view of Eq. A.15, it is possible to obtain

$$E_r = - \frac{1}{jk} \frac{\partial E_z}{\partial r} \quad (\text{A.16})$$

and

$$E_\phi = \frac{n}{kr} E_z \quad (\text{A.17})$$

from Eqs. A.9 and A.10. Substituting these into Eq. A.8, the following wave equation for Region I is obtained:

$$\frac{1}{r} \frac{\partial}{\partial r} \left( r \frac{\partial E_{zI}}{\partial r} \right) - \frac{n^2}{r^2} E_{zI} - k^2 \frac{\kappa_{||I}}{\kappa_{\perp I}} E_{zI} = 0 .$$

Let

$$T_b^2 \triangleq -k^2 \frac{\kappa_{||I}}{\kappa_{\perp I}} , \quad (\text{A.18})$$

so that

$$\frac{1}{r} \frac{\partial}{\partial r} \left( r \frac{\partial E_{zI}}{\partial r} \right) + \left( T_b^2 - \frac{n^2}{r^2} \right) E_{zI} = 0 . \quad (\text{A.19})$$

The solution to Eq. A.19 is

$$E_{zI}(r) = A_n J_n(T_b r) , \quad (\text{A.20})$$

where the  $A_n$  are arbitrary constants and where the Bessel functions of the first kind only appear, because  $E_{zI}$  is required to be bounded as  $r \rightarrow 0$ . In Region II, by a similar procedure,

$$E_{zII}(r) = B_n J_n(T_p r) + C_n N_n(T_p r) \quad , \quad (A.21)$$

where  $B_n$  and  $C_n$  are arbitrary constants and where

$$T_p^2 = -k^2 \frac{\kappa_{II}}{\kappa_{III}} \quad . \quad (A.22)$$

In Region III,

$$E_{zIII}(r) = D_n I_n(kr) + F_n K_n(kr) \quad , \quad (A.23)$$

where  $D_n$  and  $F_n$  are arbitrary constants and where the modified Bessel functions have been used. The boundary conditions are

$$E_{zIII}(a) = 0 \quad ,$$

$$E_{zII}(b) = E_{zIII}(b) \quad ,$$

$$\kappa_{III} \left. \frac{\partial E_{zII}(r)}{\partial r} \right|_{r=b} = \kappa_e \left. \frac{\partial E_{zIII}(r)}{\partial r} \right|_{r=b} \quad ,$$

$$E_{zI}(c) = E_{zII}(c)$$

and

$$\kappa_{II} \left. \frac{\partial E_{zI}(r)}{\partial r} \right|_{r=c} = \kappa_{III} \left. \frac{\partial E_{zII}(r)}{\partial r} \right|_{r=c} \quad .$$

Combining these boundary conditions with the expressions for  $E_z$  given in Eqs. A.20, A.21 and A.23 yields the following dispersion equation, in which only the mode without  $\phi$ -variations ( $n = 0$ ) is considered:

$$\frac{\kappa_{II} T_b J_1(T_b c)}{\kappa_{III} T_p J_0(T_b c)}$$

$$= \frac{\left[ \begin{aligned} & [J_1(T_p c)N_1(T_p b) - N_1(T_p c)J_1(T_p b)][I_0(ka)K_0(kb) - K_0(ka)I_0(kb)] \\ & - \frac{\kappa_e k}{\kappa_{III} T_p} [J_1(T_p c)N_0(T_p b) - N_1(T_p c)J_0(T_p b)][I_0(ka)K_1(kb) + K_0(ka)I_1(kb)] \end{aligned} \right]}{\left[ \begin{aligned} & [J_0(T_p c)N_1(T_p b) - N_0(T_p c)J_1(T_p b)][I_0(ka)K_0(kb) - K_0(ka)I_0(kb)] \\ & - \frac{\kappa_e k}{\kappa_{III} T_p} [J_0(T_p c)N_0(T_p b) - N_0(T_p c)J_0(T_p b)][I_0(ka)K_1(kb) + K_0(ka)I_1(kb)] \end{aligned} \right]}$$

(A.24)

Equation A.24 is the desired dispersion equation. It must be solved by means of a digital computer. It yields the phase constant and the small-signal growth or attenuation constant of the beam-plasma system as a function of frequency. The fact that the arguments of the Bessel functions are complex complicates the solution greatly. Even if the collision frequency can be neglected the solution is not appreciably simplified.

Simpson<sup>39</sup> has obtained solutions to Eq. A.24 for the case of a beam and plasma completely or partially filling a metallic pipe so that Regions I and II of Fig. A.1 coincide and Region III is not present. This model is appropriate to a beam-generated plasma. Solutions to a case closely approximating the experimental conditions of Chapter VI are shown in Fig. A.2. The imaginary parts of  $k$  are seen to be negative and thus represent the small-signal gain due to the beam-plasma interaction.

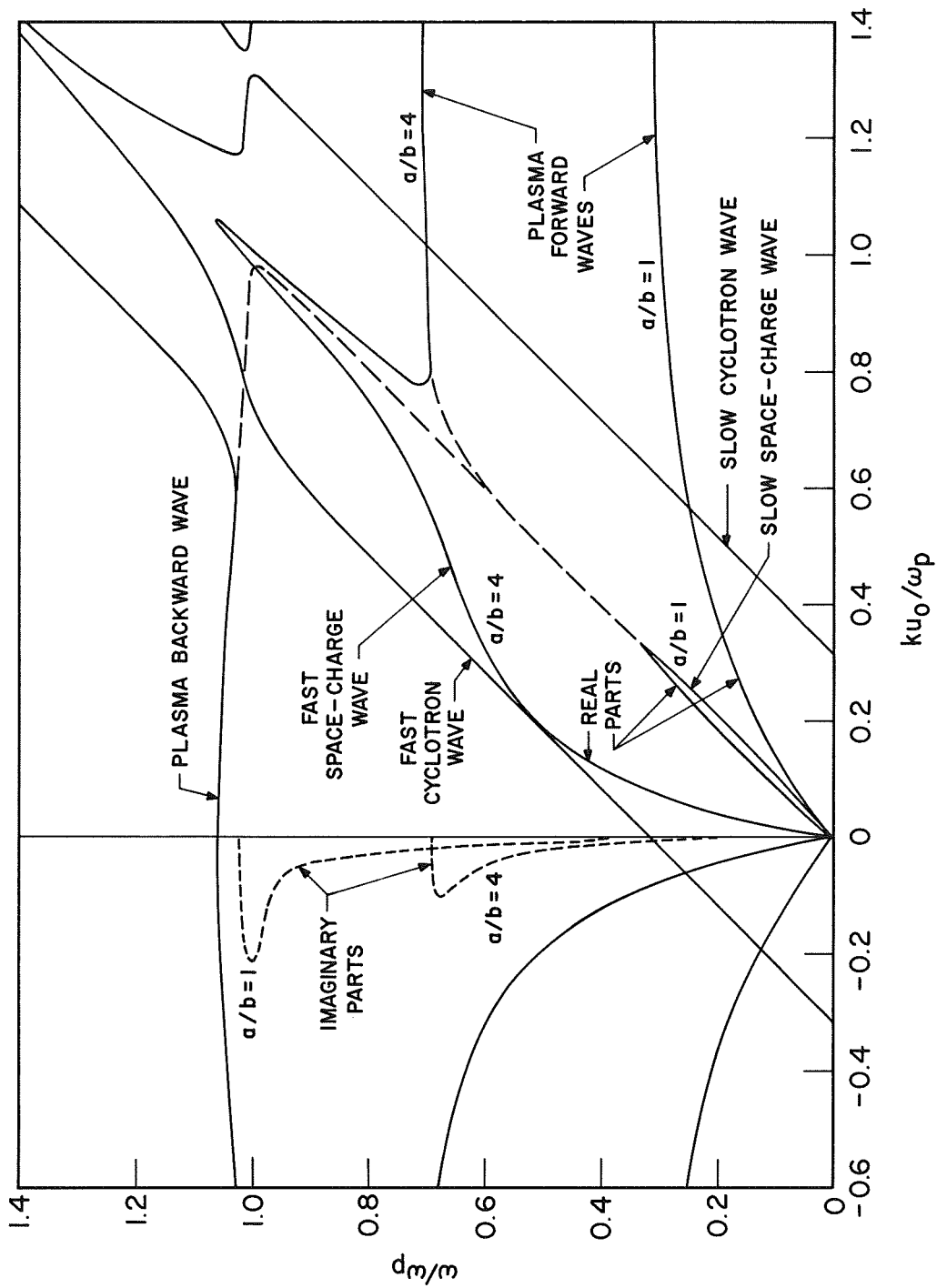


FIG. A.2 SOLUTION OF THE DISPERSION EQUATION FOR A BEAM-PLASMA SYSTEM. ( $\omega_c/\omega_p = 0.316$ ,  $\rho_p/\rho_b = 10^3$ , BEAM MICROPERVEANCE = 1.0) (SIMPSON<sup>99</sup>)

APPENDIX B. DERIVATION OF THE DIELECTRIC TENSOR FOR A PLASMA

Consider a stationary, homogeneous, neutral and cold plasma column. The ions are assumed to form an immobile background. A static magnetic field  $\vec{B} = B_z \hat{z}$  is applied along the z-direction, which coincides with the column axis. Nonrelativistic mechanics is assumed to apply so that the ac magnetic field may be neglected. The electron equation of motion, including a viscous damping term, is given by

$$m \frac{d\vec{v}}{dt} = -m\nu\vec{v} - e(\vec{E} + \vec{v} \times \vec{B}) \quad , \quad (\text{B.1})$$

where the parameter  $\nu$  is the collision frequency for momentum transfer. The quantity  $-m\nu\vec{v}$  represents the time rate of change of momentum, and hence, the statistical average force exerted on an electron by the massive ion-neutral component of the plasma. This form of damping term is strictly correct only when the collision frequency is independent of electron velocity. Equation B.1 is now written as

$$\frac{\partial\vec{v}}{\partial t} + (\vec{v} \cdot \nabla)\vec{v} + \nu\vec{v} = -\eta(\vec{E} + \vec{v} \times \vec{B}) \quad . \quad (\text{B.2})$$

Taking the ac components of Eq. B.2 and assuming an  $\exp[j(\omega t - kz)]$  variation of the ac quantities one obtains

$$j\omega\vec{v}_1 + 0 + \nu\vec{v}_1 = -\eta(\vec{E}_1 + \vec{v}_1 \times \vec{B}_0) \quad .$$

Expanding the right-hand side, the following component equations are obtained in cylindrical coordinates:



$$(j\omega + \nu)v_r = -\eta E_r - \eta v_\phi B_z, \quad (\text{B.3})$$

$$(j\omega + \nu)v_\phi = -\eta E_\phi + \eta v_r B_z \quad (\text{B.4})$$

and

$$(j\omega + \nu)v_z = -\eta E_z. \quad (\text{B.5})$$

From these equations the following expressions for the velocity components are obtained:

$$v_z = -\frac{\eta E_z}{j\omega + \nu}, \quad (\text{B.6})$$

$$v_\phi = -\eta \frac{(j\omega + \nu)E_\phi + \omega_c E_r}{(j\omega + \nu)^2 + \omega_c^2} \quad (\text{B.7})$$

and

$$v_r = -\eta \frac{(j\omega + \nu)E_r - \omega_c E_\phi}{(j\omega + \nu)^2 + \omega_c^2}. \quad (\text{B.8})$$

The equation of continuity is given by

$$\nabla \cdot \vec{J} + \frac{\partial \rho}{\partial t} = 0. \quad (\text{B.9})$$

But

$$\vec{J} = \rho \vec{v} = (\rho_0 + \rho_1)(\vec{u}_0 + \vec{v}_1).$$

Since there is no dc drift velocity and neglecting second-order terms, the continuity equation may now be written as

$$\nabla \cdot (\rho_0 \vec{v}_1) + j\omega \rho_1 = 0$$

or

$$\rho_1 = -\nabla \cdot \frac{\rho_o \vec{v}_1}{j\omega} .$$

But

$$-\nabla \cdot \vec{P}_1 = \rho_1 , \quad (\text{B.10})$$

where  $\vec{P}_1$  is the ac volume polarization and  $\rho_1$  is the volume charge density. Thus

$$\vec{P}_1 = \frac{\rho_o \vec{v}_1}{j\omega} . \quad (\text{B.11})$$

Equation B.11 may now be expanded in terms of Eqs. B.6 through B.8. Thus

$$\vec{P}_1 = -\frac{\eta\rho_o}{j\omega} \left( \frac{(j\omega + \nu)E_r - \omega_c E_\phi}{(j\omega + \nu)^2 + \omega_c^2} \hat{r} + \frac{(j\omega + \nu)E_\phi + \omega_c E_r}{(j\omega + \nu)^2 + \omega_c^2} \hat{\phi} + \frac{E_z}{j\omega + \nu} \hat{z} \right) .$$

Since

$$\omega_p^2 = -\frac{e\rho_o}{m\epsilon_o} ,$$

it follows that

$$\vec{P}_1 = -\epsilon_o \left( \frac{\omega_p}{\omega} \right)^2 \left[ \frac{\left( 1 - j \frac{\nu}{\omega} \right) E_r + j \left( \frac{\omega_c}{\omega} \right) E_\phi}{\left( 1 - j \frac{\nu}{\omega} \right)^2 - \left( \frac{\omega_c}{\omega} \right)^2} \hat{r} + \frac{\left( 1 - j \frac{\nu}{\omega} \right) E_\phi - j \left( \frac{\omega_c}{\omega} \right) E_r}{\left( 1 - j \frac{\nu}{\omega} \right)^2 - \left( \frac{\omega_c}{\omega} \right)^2} \hat{\phi} - \frac{E_z}{1 - j \frac{\nu}{\omega}} \hat{z} \right] . \quad (\text{B.12})$$

Recall that the electric displacement vector,  $\vec{D}$ , is given by<sup>85</sup>

$$\vec{D} = \epsilon_0 \vec{E} + \vec{P} . \quad (\text{B.13})$$

Note that  $\vec{D}$  represents only a partial field due to the true charges in the plasma.<sup>85</sup> The flux arising from the polarization charges gives rise to the polarization field  $\vec{P}$ . The polarization is proportional to the field, but the medium under consideration here does not polarize isotropically. Hence the proportionality "constant" between  $\vec{P}$  and  $\vec{E}$ , known as the electric susceptibility,  $\vec{\chi}$ , is a tensor. Thus

$$\vec{P} = \epsilon_0 \vec{\chi} \vec{E} . \quad (\text{B.14})$$

Then

$$\vec{D} = \epsilon_0 (1 + \vec{\chi}) \vec{E}$$

and so

$$\vec{D} = \epsilon_0 \vec{\kappa} \vec{E} = \vec{\epsilon} \vec{E} , \quad (\text{B.15})$$

where  $\vec{\kappa}$  is the specific inductive capacity tensor and  $\vec{\epsilon}$  is the dielectric tensor. A common definition of  $\vec{\kappa}$  in this connection is the following:<sup>86</sup>

$$\vec{\kappa} = \begin{bmatrix} \kappa_{\perp} & j\kappa_x & 0 \\ -j\kappa_x & \kappa_{\perp} & 0 \\ 0 & 0 & \kappa_{\parallel} \end{bmatrix} . \quad (\text{B.16})$$

Since

$$\vec{P} = \epsilon_0 (\vec{\kappa} - 1) \vec{E} ,$$

it follows that the ac polarization may be written as

$$\vec{P}_1 = \epsilon_0 \left\{ \left[ \kappa_{\perp} E_r + j\kappa_x E_{\phi} - 1 \right] \hat{r} + \left[ \kappa_{\perp} E_{\phi} - j\kappa_x E_r - 1 \right] \hat{\phi} + \left[ \kappa_{\parallel} E_z - 1 \right] \hat{z} \right\}. \quad (\text{B.17})$$

Comparing Eqs. B.12 and B.17 it is apparent that the specific inductive capacity tensor components are given by

$$\kappa_{\perp} = 1 - \frac{\left(\frac{\omega_p}{\omega}\right)^2 \left(1 - j\frac{\nu}{\omega}\right)}{\left(1 - j\frac{\nu}{\omega}\right)^2 - \left(\frac{\omega_c}{\omega}\right)^2}, \quad (\text{B.18a})$$

$$\kappa_x = - \frac{\left(\frac{\omega_p}{\omega}\right)^2 \left(\frac{\omega_c}{\omega}\right)}{\left(1 - j\frac{\nu}{\omega}\right)^2 - \left(\frac{\omega_c}{\omega}\right)^2} \quad (\text{B.18b})$$

and

$$\kappa_{\parallel} = 1 - \frac{\left(\frac{\omega_p}{\omega}\right)^2}{1 - j\frac{\nu}{\omega}}. \quad (\text{B.18c})$$

If the collision frequency is low enough to be negligible, which is the case for many plasmas to be encountered, Eqs. B.18 reduce to

$$\kappa_{\perp} = 1 - \frac{\omega_p^2}{\omega^2 - \omega_c^2}, \quad (\text{B.19a})$$

$$\kappa_x = - \frac{\left(\frac{\omega_c}{\omega}\right) \omega_p^2}{\omega^2 - \omega_c^2} \quad (\text{B.19b})$$

and

$$\kappa_{\parallel} = 1 - \left(\frac{\omega_p}{\omega}\right)^2. \quad (\text{B.19c})$$

## APPENDIX C. DERIVATION OF THE SPACE-CHARGE FIELD EXPRESSIONS

In a Lagrangian analysis it is necessary to calculate the Coulomb forces between electrons or charge groups. The more elegant approach of deriving expressions for the potential and the fields from a continuous charge distribution does not lend itself very well to this type of analysis. The general approach here is to solve Poisson's equation for the electron stream by the Green's function method or by expanding the beam space-charge density in a Fourier series (harmonic method). One- and two-dimensional formulations will be carried out along the lines developed by Rowe.<sup>46</sup> In both analyses it will be assumed that relativistic effects are negligible due to the fact that the electron velocities are much less than the speed of light. Hence the formulas of electrostatics can be used. It is also assumed that a sufficient quantity of positive ions is present to neutralize the average space charge.

Consider the one-dimensional case first. The electron stream space-charge density is expanded in a Fourier time series with a particular spatial distribution assumed.

$$\rho(z,t) = \sum_{n=1}^{\infty} \rho_n(z,t) e^{-jn\omega t} . \quad (C.1)$$

For this reason the method is called the harmonic method of calculating the space-charge field. Assume that the RF wave impressed on the beam-plasma system bunches the electron stream such that the space-charge

density is constant in amplitude and varies sinusoidally with distance. If the plasma is replaced with a drift tube, as shown in Fig. C.1, the steady-state space-charge potential for this distribution may be calculated. The space-charge density is assumed to have the form

$$\rho(z) = \rho_0 e^{-j\beta z} \quad . \quad (C.2)$$

The harmonics of the charge distribution are given by

$$\rho_n(z, z') = \rho_0 e^{-j\beta_n(z-z')} \quad ,$$

from which the axial electric field due to each harmonic may be determined. The  $\beta_n$  is the propagation constant for the nth harmonic propagating along the plasma column in the absence of the electron stream.

For the model under consideration Maxwell's equations reduce to the electrostatic equations

$$\nabla \times \vec{E} = 0 \quad , \quad (C.3)$$

$$\vec{E} = -\nabla V \quad . \quad (C.4)$$

Thus in the beam region Poisson's equation,

$$\nabla^2 V_{nsc}(r, z) = -\frac{\rho_n(z)}{\pi \epsilon b'^2} = -A \rho_0 e^{-j\beta_n z} \quad , \quad (C.5)$$

applies, while in the region outside of the beam Laplace's equation applies. The solution to Eq. C.5 is given by

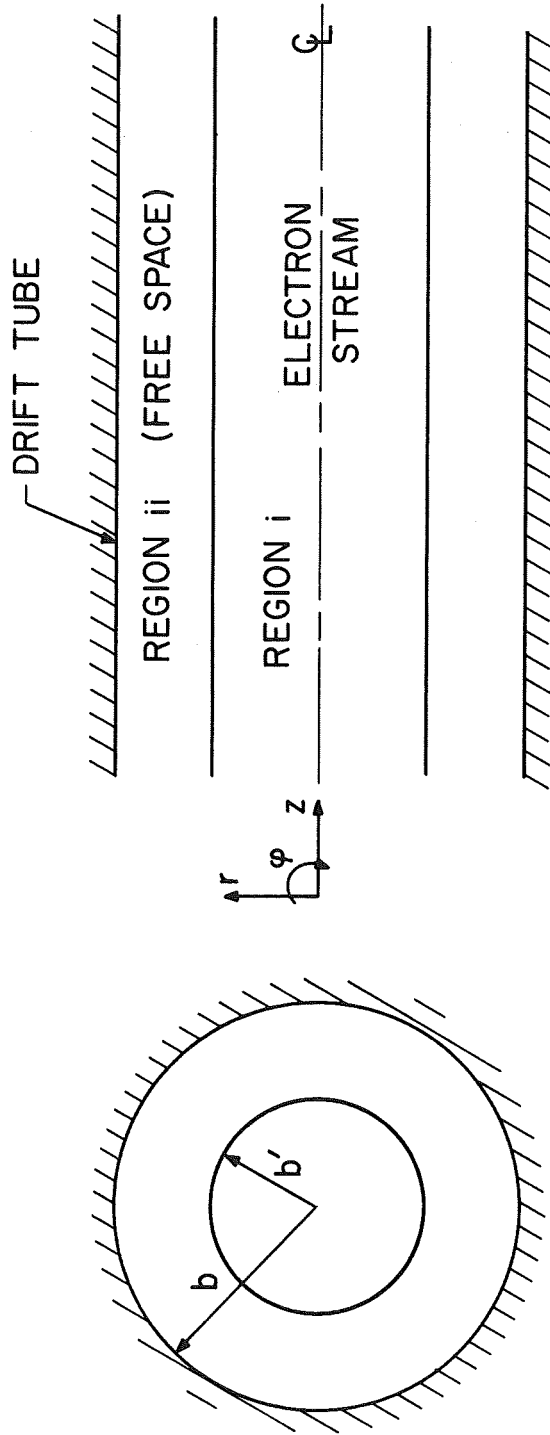


FIG. C.1.1 MODEL FOR THE DERIVATION OF THE SPACE-CHARGE FIELDS.

$$V_{\text{nsc}}(r) e^{-j\beta_n z} = \left( \frac{A\rho_o}{\beta_n^2} + BI_o(\beta_n r) \right) e^{-j\beta_n z}, \quad (\text{C.6})$$

where  $I_o(\beta_n r)$  is the zero-order modified Bessel function of the first kind. The function of the second kind does not appear so that the solution is bounded at  $r = 0$ . By differentiation of Eq. C.6 the electric field may be found as follows:

$$E_{\text{nsc-z}}(r, z) = j\beta_n \left( \frac{A\rho_o}{\beta_n^2} + BI_o(\beta_n r) \right) e^{-j\beta_n z}. \quad (\text{C.7})$$

At the beam boundary ( $r = b'$ ) the following boundary conditions apply:

$$E_r^i(b') = E_r^{ii}(b')$$

and

$$E_z^i(b') = E_z^{ii}(b'),$$

while at the drift tube wall,  $r = b$ ,

$$E_z^{ii}(b) = 0.$$

The solution to the eigenvalue problem defined by the field expressions for Regions i and ii and by the above boundary conditions yields a solution of the form

$$E_{\text{nsc-z}}(r, z) = \frac{j\rho_o A}{\beta_n} \left[ 1 - \beta_n b' \frac{I_o(\beta_n r)}{I_o(\beta_n b)} \left( I_1(\beta_n b') K_o(\beta_n b) + I_o(\beta_n b) K_1(\beta_n b') \right) \right] e^{-j\beta_n z}. \quad (\text{C.8})$$



Along the axis of Fig. C.1, Eq. C.8 may be written as

$$E_{nsc-z} = \frac{j\rho_o A}{\beta_n} R_n^2 e^{-j\beta_n z}, \quad (C.9)$$

where the plasma frequency reduction factor,  $R_n$ , is defined by

$$R_n^2 \triangleq 1 - \frac{\beta_n b'}{I_o(\beta_n b)} \left( I_1(\beta_n b') K_0(\beta_n b) + I_0(\beta_n b) K_1(\beta_n b') \right). \quad (C.10)$$

Note that  $R_n$  is a purely geometric factor and has been calculated for various geometries.<sup>73</sup> The radian plasma frequency for the electron beam is given by

$$\omega_b^2 = -\frac{\eta\rho_o}{\epsilon_o} \triangleq \frac{\eta I_o}{\pi b'^2 u_o \epsilon_o}, \quad (C.11)$$

where  $I_o$  is the beam current and  $u_o$  is the dc electron velocity. In view of Eqs. C.5 and C.11 it is possible to write Eq. C.9 as

$$E_{nsc-z} = \frac{j}{\beta_n} \frac{\rho_n(z)}{\pi b'^2 \epsilon} R_n^2$$

or

$$E_{nsc-z} = \frac{j}{\beta_n} \rho_n(z) \frac{u_o \omega_b^2}{\eta I_o} R_n^2.$$

If the effective radian plasma frequency,  $\omega_{qn}$ , is defined by

$$\omega_{qn}^2 \triangleq \omega_b^2 R_n^2, \quad (C.12)$$

one obtains

$$E_{nsc-z} = \frac{j}{\beta_n} \rho_n(z) \frac{u_o \omega_{qn}^2}{\eta I_o}. \quad (C.13)$$

Under small-signal conditions,

$$\beta_n = \frac{n\omega}{v_{on}} , \quad (C.14)$$

where  $v_{on}$  is the unperturbed phase velocity for the  $n$ th harmonic. It is assumed that Eq. C.14 is approximately correct even for large-signal operation. Thus Eq. C.13 may be written as

$$E_{nsc-z} = j\rho(z) \left( \frac{\omega_{qn}}{\omega} \right)^2 \frac{\omega u_o v_{on}}{nI_o \eta} e^{-j\Phi_n} ,$$

where  $\Phi_n$  is the instantaneous phase of the  $n$ th harmonic of the RF wave causing the bunching, as defined in Eq. 3.22. Thus the space-charge field at the  $n$ th harmonic may be written as

$$E_{nsc-z} = -\rho(z) e^{-j[\Phi_n + (\pi/2)]} \left( \frac{\omega_{qn}}{\omega} \right)^2 \left( \frac{\omega u_o v_{on}}{nI_o \eta} \right) . \quad (C.15)$$

If the space-charge density is expanded in a Fourier series in  $\Phi_n$  as in Chapter III, Eq. C.15 becomes

$$E_{nsc-z} = -\frac{I_o}{u_o} \left( \frac{\omega u_o v_{on}}{I_o \eta} \right) \sum_{n=1}^{\infty} \frac{1}{n} \left( \frac{\omega_b}{\omega} \right)^2 R_n^2 e^{-j[\Phi_n + (\pi/2)]} \cdot \left( \frac{1}{\pi L} \int_0^{2\pi L} \frac{e^{j\Phi_n(y_1, \Phi'_{o1})}}{1 + 2C_1 u(y_1, \Phi'_{o1})} d\Phi'_{o1} \right) . \quad (C.16)$$

This expansion in a Fourier series in space is valid provided there is little change in amplitude of the waves over the few adjacent RF cycles and provided the influence of the space charge extends no more than a few cycles in either direction.

Since the integrand in Eq. C.16 is uniformly convergent, the order of integration and summation may be reversed. Thus

$$E_{\text{nsc-z}} = -\frac{2\omega v_{on}}{\eta} \left(\frac{\omega_b}{\omega}\right)^2 \int_0^{2\pi L} \sum_{n=1}^{\infty} \frac{R_n^2}{2\pi n L} e^{-j[\Phi_n - \Phi'_n + (\pi/2)]} \cdot \frac{d\Phi'_{o1}}{1 + 2C_1 u(y_1, \Phi'_{o1})} .$$

Since a sinusoidal variation of the space-charge density was postulated, the real part of the right-hand side is taken. This yields

$$E_{\text{nsc-z}} = -\frac{2\omega v_{on}}{L\eta} \left(\frac{\omega_b}{\omega}\right)^2 \int_0^{2\pi L} \sum_{n=1}^{\infty} \frac{R_n^2}{2\pi n} \sin(\Phi_n - \Phi'_n) \frac{d\Phi'_{o1}}{1 + 2C_1 u(y_1, \Phi'_{o1})} .$$

Defining the one-dimensional space-charge weighting function by

$$F_{1-z}(\Phi_n - \Phi'_n) \triangleq \sum_{n=1}^{\infty} \frac{\sin(\Phi_n - \Phi'_n) R_n^2}{2\pi n} , \quad (\text{C.17})$$

the space-charge field term for the nth harmonic becomes

$$E_{\text{nsc-z}} = -\frac{2\omega v_{on}}{L\eta} \left(\frac{\omega_b}{\omega}\right)^2 \int_0^{2\pi L} \frac{F_{1-z}(\Phi_n - \Phi'_n) d\Phi'_{o1}}{1 + 2C_1 u(y_1, \Phi'_{o1})} . \quad (\text{C.18})$$

For the two-dimensional analysis of Chapter IV it is necessary to find the two-dimensional space-charge field weighting functions. It is assumed that angular spreading of the electron stream can be neglected. For the cylindrical symmetry shown in Fig. C.2 the Green's function for a delta-function ring of charge in an infinite-conductivity

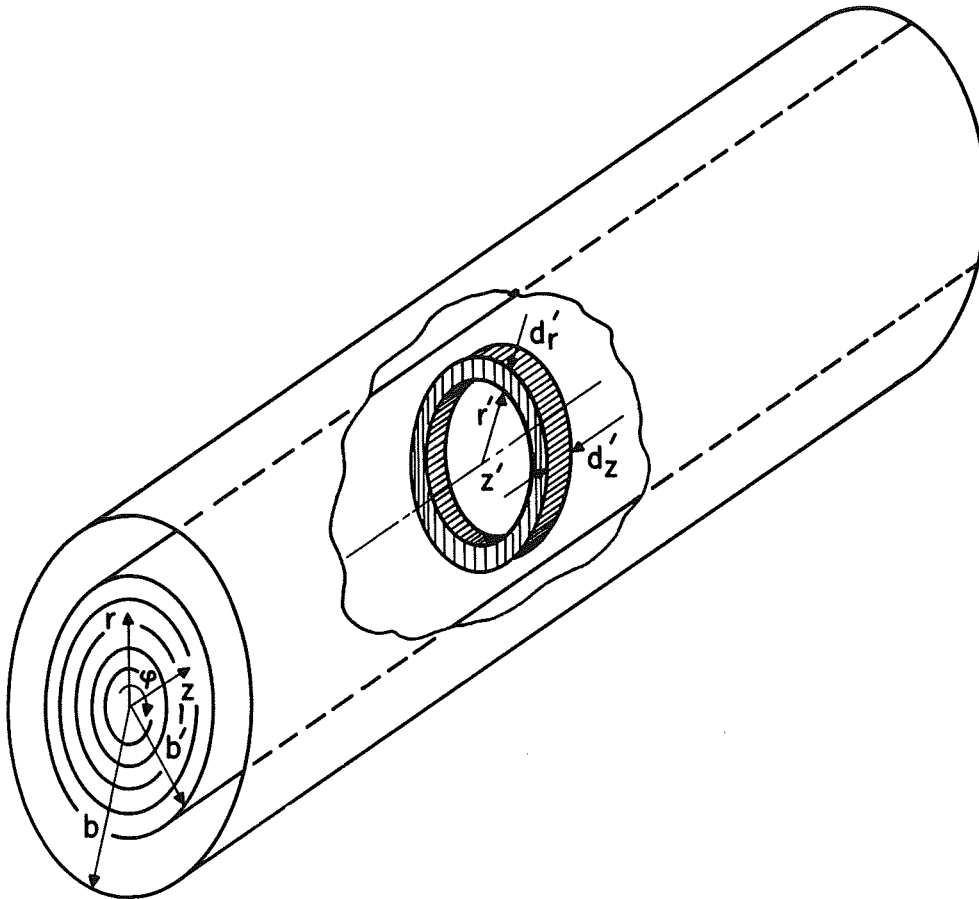


FIG. C.2 RINGS OF CHARGE IN AN ELECTRON STREAM FLOWING THROUGH A DRIFT TUBE.

drift tube of radius  $b$  may therefore be used. If the stream of radius  $b'$  is divided into a number of concentric annular rings of charge, two-dimensional space-charge effects resulting in radial motion can be studied.

Let  $G$  be the potential due to a charged ring located at  $r'$  and  $z'$  with the thickness  $dr'$  and  $dz'$ . Except at an actual charge point of the ring,  $G$  satisfies the Laplace equation

$$\nabla^2 G = \frac{\partial^2 G}{\partial z^2} + \frac{1}{r} \frac{\partial}{\partial r} \left( r \frac{\partial G}{\partial r} \right) = 0 . \quad (\text{C.19})$$

The boundary conditions are that the potential due to the ring of charge be zero at the drift tube and go to zero at  $z$  far from  $z'$ .

Thus

$$G(b) = 0$$

and

$$G(|z| \rightarrow \infty) = 0 .$$

Solution of Eq. C.19 gives the Green's function<sup>87</sup>

$$G(r, z) = \sum_{\ell=1}^{\infty} A_{\ell} e^{-\mu_{\ell} |z-z'|} J_0(\mu_{\ell} r) , \quad (\text{C.20})$$

where  $\mu_{\ell}$  is chosen so that

$$J_0(\mu_{\ell} b) = 0 . \quad (\text{C.21})$$

The surface charge density of the ring is

$$\rho_s = 2\pi r' \rho' dr' dz' \delta(r - r') , \quad (\text{C.22})$$

where  $\delta(r - r')$  is the Dirac delta function defined by

$$2\pi \int_0^b \delta(r - r') r \, dr = 1 \quad . \quad (C.23)$$

At the plane  $z = z'$ , where the charge ring is located, the discontinuity of  $\partial G/\partial z$  is equal to  $-1/\epsilon_0$  multiplied by the surface charge density of the ring. Thus

$$\left( \frac{\partial G}{\partial z} \right)_{z=z'} = -\frac{\rho_s}{\epsilon_0} = -\frac{2\pi r' \rho'}{\epsilon_0} \, dr' \, dz' \, \delta(r - r') \quad , \quad (C.24)$$

and from Eq. C.20,

$$\sum_{\ell=1}^{\infty} A_{\ell} \mu_{\ell} J_0(\mu_{\ell} r) = \frac{2\pi r' \rho'}{\epsilon_0} \, dr' \, dz' \, \delta(r - r') \quad . \quad (C.25)$$

Due to the orthogonality properties of Bessel functions,  $A_{\ell}$  may be determined by multiplying the left-hand side of Eq. C.25 by  $r J_0(\mu_s r)$  and integrating between  $r = 0$  and  $r = b$ . All terms vanish except  $A_s \mu_s \int_0^b r [J_0(\mu_s r)]^2 \, dr$ . Note that

$$\int_0^b r [J_0(\mu_s r)]^2 \, dr = \frac{b^2}{2} [J_1(\mu_s b)]^2 \quad . \quad (C.26)$$

Thus

$$A_s = \sum_{\ell=1}^{\infty} \frac{2}{\mu_s [b J_1(\mu_s b)]^2} \int_0^b A_{\ell} \mu_{\ell} J_0(\mu_{\ell} r) J_0(\mu_s r) r \, dr \quad .$$

In view of Gauss' theorem and from Eq. C.25 this becomes

$$A_s = \frac{2}{\mu_s [bJ_1(\mu_s b)]^2} \int_0^b J_0(\mu_s r') r dr \left( \frac{1}{2} \right) \frac{2\pi r' \rho'}{\epsilon_0} dr' dz' \delta(r - r')$$

or

$$A_s = \frac{1}{\mu_s [bJ_1(\mu_s b)]^2} J_0(\mu_s r') \frac{r' \rho'}{\epsilon_0} dr' dz' .$$

It then follows that

$$A_l = \frac{1}{\mu_l [bJ_1(\mu_l b)]^2} J_0(\mu_l r') \frac{r' \rho'}{\epsilon_0} dr' dz' . \quad (C.27)$$

Substituting Eq. C.27 into Eq. C.20 yields

$$G = \sum_{n=1}^{\infty} \frac{\rho' r' J_0(\mu_l r') J_0(\mu_l r)}{\epsilon_0 \mu_l b^2 [J_1(\mu_l b)]^2} e^{-\mu_l |z-z'|} . \quad (C.28)$$

The space-charge potential may thus be written as

$$V_{sc} = \iint \frac{\rho' r' dr' dz'}{\epsilon_0 b^2} \sum_{l=1}^{\infty} \frac{J_0(\mu_l r') J_0(\mu_l r)}{\mu_l [J_1(\mu_l b)]^2} e^{-\mu_l |z-z'|} .$$

Since by conservation of charge

$$\rho' r' dr' dz' = \rho'_0 r'_0 dr'_0 dz'_0 ,$$

where the zero subscripts denote quantities at the entrance to the interaction region and

$$\rho_0 = - \frac{I_0}{\pi b^2 u_0} ,$$

where  $I_0$  is the dc beam current and  $u_0$  is the dc velocity of the beam electrons, the space-charge potential may be written as

$$V_{sc} = - \iint \frac{I_0 r' dr' dz'}{u_0 \pi b^2 \epsilon_0} \sum_{\ell=1}^{\infty} \frac{J_0(\mu_\ell r') J_0(\mu_\ell r)}{\mu_\ell [J_1(\mu_\ell b)]^2} e^{-\mu_\ell |z-z'|} . \quad (C.29)$$

The space-charge field expressions are found by appropriate differentiation of Eq. C.29. Making use of the normalized variables, one obtains

$$E_{nsc-y} = - \frac{\partial V_{sc}}{\partial z} = - \int_0^{x_b'} \int_0^{2\pi L} \frac{C^2 \omega I_0 d\phi_0'}{u_0^2 \pi L \epsilon_0 x_b'^2 x_b'^2} \sum_{\ell=1}^{\infty} e^{-v_\ell |y_1 - y_1'|} \operatorname{sgn}(y_1 - y_1') \cdot \frac{J_0(v_\ell x') J_0(v_\ell x)}{[J_1(v_\ell x_b)]^2} x_0' dx_0' \quad (C.30)$$

and

$$E_{nsc-x} = - \frac{\partial V_{sc}}{\partial r} = - \int_0^{x_b'} \int_0^{2\pi L} \frac{C^2 \omega I_0 d\phi_0'}{u_0^2 \pi L \epsilon_0 x_b'^2 x_b'^2} \sum_{\ell=1}^{\infty} e^{-v_\ell |y_1 - y_1'|} \cdot \frac{J_0(v_\ell x') J_1(v_\ell x)}{[J_1(v_\ell x_b)]^2} x_0' dx_0' , \quad (C.31)$$

where

$$v_\ell = \frac{\mu_\ell u_0}{C \omega} .$$



## BIBLIOGRAPHY

1. Tonks, L. and Langmuir, I., "Oscillations in Ionized Gases," Phys. Rev., vol. 33, No. 2, pp. 195-210; February, 1929.
2. Bohm, D. and Gross, E. P., "Theory of Plasma Oscillations. A. Origin of Medium-Like Behavior," Phys. Rev., vol. 75, No. 12, pp. 1851-1864; June 15, 1949.
3. Bohm, D. and Gross, E. P., "Theory of Plasma Oscillations. B. Excitation and Damping of Oscillations," Phys. Rev., vol. 75, No. 12, pp. 1864-1876; June 15, 1949.
4. Bohm, D. and Gross, E. P., "Effects of Plasma Boundaries in Plasma Oscillations," Phys. Rev., vol. 79, No. 6, pp. 992-1001; September 15, 1950.
5. Merrill, J. H. and Webb, H. W., "Electron Scattering and Plasma Oscillations," Phys. Rev., vol. 55, No. 12, pp. 1191-1198; June 15, 1939.
6. Looney, D. H. and Brown, S. C., "The Excitation of Plasma Oscillations," Phys. Rev., vol. 93, No. 5, pp. 965-969; March 1, 1954.
7. Sturrock, P. A., "Excitation of Plasma Oscillations," Phys. Rev., vol. 117, No. 6, pp. 1426-1429; March 15, 1960.
8. Dawson, J., "On Landau Damping," Phys. Fluids, vol. 4, No. 7, pp. 869-874; July, 1961.
9. Trivelpiece, A. W. and Gould, R. W., "Space Charge Waves in Cylindrical Plasma Columns," Jour. Appl. Phys., vol. 30, No. 11, pp. 1784-1793; November, 1959.
10. Bevc, V. and Everhart, T. E., "Fast-Wave Propagation in Plasma-Filled Waveguides," Jour. Electron. Control, vol. XIII, No. 3, pp. 185-212; September, 1962.
11. Bevc, V., "Power Flow in Plasma-Filled Waveguides," Jour. Appl. Phys., vol. 37, No. 8, pp. 3128-3137; July, 1966.
12. Kislov, V. J. and Bogdanov, E. V., "Interaction Between Slow Plasma Waves and an Electron Stream," Electromagnetics and Fluid Dynamics of Gaseous Plasma, Microwave Research Institute Symposia Series, vol. XI, Polytechnic Press of the Polytechnic Institute of Brooklyn, New York, pp. 249-268; 1962.

13. Crepeau, P. J. and Keegan, T., "A Beam Plasma Surface Wave Interaction," IEEE Trans. on Microwave Theory and Techniques, vol. MTT-10, No. 5, pp. 391-392; September, 1962.
14. Allis, W. P. et al., Waves in Anisotropic Plasmas, The M.I.T. Press, Cambridge, Mass.; 1963.
15. Margenau, H. and Hartman, L. M., "Theory of High Frequency Gas Discharges. II. Harmonic Components of the Distribution Function," Phys. Rev., vol. 73, No. 4, pp. 309-315; February 15, 1948.
16. Inada, K. et al., "On the Harmonics Radiating from Microwave Discharge in Air," Ionization Phenomena in Gases, vol. II, North Holland Publishing Co., Amsterdam, pp. 768-773; 1959.
17. Krenz, J. H., "Harmonic Generation in a Plasma Due to a Velocity Dependent Collision Frequency," Phys. Fluids, vol. 8, No. 10, pp. 1871-1875; October, 1965.
18. Desloge, E. A. and Coleman, D. J., "Harmonic Generation in an Ionized Gas," Phys. Fluids, vol. 9, No. 7, pp. 1389-1393; July, 1966.
19. Sturrock, P. A., "Amplifying and Evanescent Waves, Convective and Nonconvective Instabilities," Plasma Physics, Drummond, J. E. (Ed.), McGraw-Hill Book Co., Inc., New York, Chap. 4, pp. 124-142; 1961.
20. Buneman, O., "How to Distinguish Between Attenuating and Amplifying Waves," Plasma Physics, Drummond, J. E. (Ed.), McGraw-Hill Book Co., Inc., New York, Chap. 5, pp. 143-164; 1961.
21. Briggs, R. J., Electron-Stream Interaction with Plasmas, Research Monograph No. 29, The M.I.T. Press, Cambridge, Mass.; 1964.
22. Sudan, R. N., "Classification of Instabilities from Their Dispersion Relation," Phys. Fluids, vol. 8, No. 10, pp. 1899-1904; October, 1965.
23. Getty, W. D. and Smullin, J. D., "Beam-Plasma Discharge: Buildup of Oscillations," Jour. Appl. Phys., vol. 34, No. 12, pp. 3421-3429; December, 1963.
24. Targ, R. and Levine, L. P., "Backward-Wave Microwave Oscillations in a System Composed of an Electron Beam and a Hydrogen Gas Plasma," Jour. Appl. Phys., vol. 32, No. 4, pp. 731-737; April, 1961.
25. Hedvall, P., "Properties of a Plasma Created by an Electron Beam," Jour. Appl. Phys., vol. 33, No. 8, pp. 2426-2429; August, 1962.

26. Allen, M. A. et al., "High Power Beam Plasma Amplifier," Final Report, 15 December 1962 to 15 March 1965, Microwave Associates, Inc., Burlington, Mass.; 1965.
27. Ferrari, R. L., "An Electron Beam-Plasma Amplifier at Microwave Frequencies," Jour. Electron. Control, vol. XVII, No. 1, pp. 49-65; July, 1964.
28. Chorney, P. and Madore, R. J., "Millimeter Wave Component Development (Beam-Plasma Amplifier)," Tech. Report No. RADC-TR-65-53; Techniques Branch, Rome Air Development Center, Griffiss Air Force Base, New York; April, 1965.
29. Boyd, G. D. et al., "Interactions Between an Electron Stream and an Arc Discharge Plasma," Electronic Waveguides, Microwave Research Institute Symposia Series, vol. VIII, Polytechnic Press of the Polytechnic Institute of Brooklyn, New York, pp. 367-377; 1958.
30. Bogdanov, E. V. et al., "Interaction Between an Electron Stream and Plasma," Millimeter Waves, Microwave Research Symposia Series, vol. IX, Polytechnic Press of the Polytechnic Institute of Brooklyn, New York, pp. 57-67; 1960.
31. Berezin, A. K. et al., "The Interaction of Strong Electron Beams with a Plasma," Jour. Nucl. Energy: Part C., vol. 4, No. 4, pp. 291-295; 1962.
32. Berezin, A. K. et al., "The Interaction of Pulsed High-Current Beams with a Plasma in a Magnetic Field," Jour. Nucl. Energy: Part C., vol. 6, No. 2, pp. 173-180; 1964.
33. Vlaardingerbroek, M. T. et al., "On Wave Propagation in Beam-Plasma Systems," Philips Res. Reports, vol. 17, No. 4, pp. 344-362; August, 1962.
34. Vlaardingerbroek, M. T. and Weimer, K. R. U., "On Wave Propagation in Beam-Plasma Systems in a Finite Magnetic Field," Philips Res. Reports, vol. 18, No. 2, pp. 95-108; April, 1963.
35. Groendijk, H. et al., "Waves in Cylindrical Beam-Plasma Systems Immersed in a Longitudinal Magnetic Field," Philips Res. Reports, vol. 20, No. 5, pp. 485-504; October, 1965.
36. Weimer, K. R. U. et al., "Interaction of an Electron Beam-Plasma System with Slow-Wave Structures," Microwave Tubes, Proc. of the 5th Int. Congress, Paris, 1964; Academic Press, Inc., New York, pp. 465-468; 1965.
37. Crawford, F. W., "Beam-Plasma Interaction in a Warm Plasma," Int. Jour. Electron., vol. XIX, No. 3, pp. 217-232; September, 1965.

38. Hahn, W. C., "Small Signal Theory of Velocity-Modulated Electron Beams," Gen. Elec. Rev., vol. 42, No. 6, pp. 258-270; June, 1939.
39. Simpson, J. E., "An Instability of a Beam-Generated Plasma in a Uniform Magnetic Field," Tech. Report No. AFAL-TR-66-3, Report SUIPR No. 38, Plasma Physics Laboratory, Stanford Electronics Laboratories, Stanford University, Stanford, Calif.; November, 1965.
40. Karplyuk, K. S. and Levitskii, S. M., "Dispersion Equation of the Electron Stream in Plasma in the Presence of a Magnetic Field," Soviet Phys.—Tech. Phys., vol. 9, No. 8, pp. 1063-1066; February, 1965.
41. Golant, V. E. et al., "Electromagnetic Radiation from a Magnetized Plasma Traversed by an Electron Beam," Soviet Phys.—Tech. Phys., vol. 10, No. 11, pp. 1559-1565; May, 1966.
42. Stover, H. L., "Microwave and Electron Beam Interactions with a Finite Plasma," Tech. Doc. Report No. RADC-TDR-64-117, Techniques Branch, Rome Air Development Center, Griffiss Air Force Base, New York; April, 1964.
43. Berezin, A. K. et al., "High-Frequency Oscillations Excited by the Interaction of an Electron Beam with a Plasma," Jour. Nucl. Energy: Part C., vol. 7, No. 6, pp. 593-604; 1965.
44. Gorbatenko, M. F., "Interaction of an Electron Beam with a Plasma," Soviet Phys.—Tech. Phys., vol. 8, No. 2, pp. 124-125; August, 1963.
45. Rowe, J. E., "Harmonic Currents in Nonlinear Beam-Plasma Interactions," Microwave Tubes, Proc. 5th Int. Congress, Paris, 1964; Academic Press, Inc., New York, pp. 427-431; 1965.
46. Rowe, J. E., Nonlinear Electron-Wave Interaction Phenomena, Academic Press, Inc., New York; 1965.
47. Rowe, J. E., "Nonlinear Beam-Plasma Interactions," Tech. Report No. 69, Contract No. AF33(657)-8050, Electron Physics Laboratory, Department of Electrical Engineering, The University of Michigan, Ann Arbor; March, 1964
48. Gould, R. W. and Allen, M. A., "Large Signal Theory of Beam-Plasma Amplifiers," Microwave Tubes, Proc. 5th Int. Congress, Paris, 1964; Academic Press, Inc., New York, pp. 445-449; 1965.
49. Geidne, B., "Nonlinear Analysis of a Microwave Beam-Plasma Amplifier," Research Report No. 52, Research Laboratory of Electronics, Chalmers University of Technology, Gothenburg, Sweden; 1965.

50. Berezin, A. K. et al., "The Interaction of Modulated High-Current Pulsed Electron Beams with Plasmas in a Longitudinal Magnetic Field," Jour. Nucl. Energy: Part C., vol. 8, No. 3, pp. 289-300; 1966.
51. Allison, J. and Kino, G. S., "A Directly Radiating Beam-Plasma Oscillator," Microwave Tubes, Proc. 5th Int. Congress, Paris, 1964; Academic Press, Inc., New York, pp. 378-382; 1965.
52. Dattner, A., "A Study of Plasma Resonance," Proc. 5th Int. Conf. on Ionization Phenomena in Gases, Munich, 1961; North Holland Publishing Co., Amsterdam, pp. 1477-1483; 1962.
53. Nickel, J. C. et al., "Resonance Oscillations in a Hot Nonuniform Plasma Column," Phys. Rev. Letters, vol. 11, No. 5, pp. 183-185; September 1, 1963.
54. Kronlund, S., "Measurements on a Beam-Plasma Microwave Amplifier," Research Report No. 68, Research Laboratory of Electronics, Chalmers University of Technology, Gothenburg, Sweden; 1966.
55. Chow, K. K., "Applied Research on Methods of Coupling to Electromagnetic Waves in Plasma Amplifiers," Tech. Doc. Report No. AL-TDR-64-150; Air Force Avionics Laboratory, Wright-Patterson Air Force Base, Ohio; October, 1964.
56. Feinstein, J., "The Conversion of Space-Charge Wave Energy into Electromagnetic Radiation," Electronic Waveguides, Microwave Research Institute Symposia Series, vol. VIII, Polytechnic Press of the Polytechnic Institute of Brooklyn, New York, pp. 345-352; 1958.
57. Neufeld, J. and Doyle, P. H., "Electromagnetic Interaction of a Beam of Charged Particles with Plasma," Phys. Rev., vol. 121, No. 3, pp. 654-658; February 1, 1961.
58. Allen, M. A. et al., "Electron Beam-Plasma Interaction," Microwaves, Proc. 4th Int. Congress on Microwave Tubes, Scheveningen, 1963; Centrex Publishing Co., Eindhoven, The Netherlands, pp. 327-333; 1963.
59. Stover, H. L. and Kino, G. S., "A Field Theory for Propagation Along a Non-Uniform Plasma," Microwave Tubes, Proc. 5th Int. Congress, Paris, 1964; Academic Press, Inc., New York, pp. 374-378; 1965.
60. Allen, M. A. et al., "RF Coupling to an Electron Beam Through a Plasma," Appl. Phys. Letters, vol. 4, No. 6, pp. 107-108; March 15, 1964.
61. Pashitskii, E. A., "Interaction of an Electron Beam with a Plasma in a Magnetic Field. I. Longitudinal Oscillations," Soviet Phys. —Tech. Phys., vol. 8, No. 1, pp. 34-38; July, 1963.

62. Pashitskii, E. A., "Interaction of an Electron Beam with a Plasma in a Magnetic Field. II. Transverse Oscillations," Soviet Phys.—Tech. Phys., vol. 8, No. 1, pp. 39-42; July, 1963.
63. Gorbatenko, M. F., "Interaction of an Electron Beam with a Plasma Existing in a Magnetic Field," Soviet Phys.—Tech. Phys., vol. 8, No. 9, pp. 798-804; March, 1964.
64. Gould, R. W. and Trivelpiece, A. W., "A New Mode of Wave Propagation on Electron Beams," Electronic Waveguides, Microwave Research Institute Symposia Series, vol. VIII, Polytechnic Press of the Polytechnic Institute of Brooklyn, New York, pp. 215-229; 1958.
65. Guest, G., "The Effect of Convective Instabilities on the Longitudinal RF Impedance of a One-Dimensional Beam-Plasma System," Int. Jour. Electron., vol. XVIII, No. 2, pp. 147-157; 1965.
66. Christy, E. H., "Plasma Impedance Measuring Technique," Rev. Sci. Instr. vol. 36, No. 11, pp. 1659-1660; November, 1965.
67. Kislov, V. Ya. and Bogdanov, E. V., "The Interaction of Slow Plasma Waves with an Electron Flux," Radio Eng. Electron., vol. 5, No. 12, pp. 145-162; 1960.
68. Beck, A. H. W., Space-Charge Waves, Pergamon Press, New York; 1958.
69. Chodorow, M. and Susskind, C., Fundamentals of Microwave Electronics, McGraw-Hill Book Co., Inc., New York; 1964.
70. von Engel, A., Ionized Gases, Second Edition, Oxford University Press, London; 1965.
71. Brewer, G. R. and Birdsall, C. K., "Normalized Propagation Constants for a Traveling Wave Tube for Finite Values of C," Tech. Memo. No. 331, Electron Tube Laboratory, Hughes Aircraft Company, Culver City, Calif.; October, 1953.
72. El-Shandwily, M. E., "Analysis of Multi-Signal Traveling-Wave Amplifier Operation," Tech. Report No. 85, Contract No. NObsr-89274, Electron Physics Laboratory, Department of Electrical Engineering, The University of Michigan, Ann Arbor; June, 1965.
73. Branch, G. M. and Mihran, T. G., "Plasma Frequency Reduction Factors in Electron Beams," IRE Trans. on Electron Devices, vol. ED-2, No. 2, pp. 3-11; April, 1955.
74. Cook, J. S. et al., "Coupled Helices," Bell System Tech. Jour., vol. 35, No. 1, pp. 127-178; January, 1956.

75. Chorney, P. and Madore, R. J., "Millimeter Wave Component Development," Final Tech. Note, Contract No. AF30(602)-2948, Microwave Associates, Inc., Burlington, Mass.; February, 1965.
76. Trivelpiece, A. W., Slow-Wave Propagation in Plasma Waveguides, San Francisco Press, Inc., San Francisco, Calif.; 1967.
77. Hoh, F. C. and Lehnert, B., "Diffusion Processes in a Plasma Column in a Longitudinal Magnetic Field," Phys. Fluids, vol. 3, No. 4, pp. 600-607; July-August, 1960.
78. Allis, W. P., "Motions of Ions and Electrons," Handbuch der Physik, S. Flügge (Ed.), vol. 21, Springer Verlag, Berlin; 1957.
79. Dunn, D. A. et al., "Oscillations and Noise Generation in a Beam-Generated Plasma," Jour. Appl. Phys., vol. 36, No. 10, pp. 3273-3275; October, 1965.
80. Levitskii, S. M. and Shashurin, I. P., "Diffusion Theory of a Beam-Generated Plasma," Soviet Phys.—Tech. Phys., vol. 10, No. 7, pp. 915-919; January, 1966.
81. Frey, J., "Interacting Components in Beam-Generated Beam-Plasma Systems," Jour. Appl. Phys., vol. 39, No. 3, pp. 1887-1889; 15 February, 1968.
82. Marcuvitz, N., Waveguide Handbook, M.I.T. Radiation Laboratory Series, vol. 10, McGraw-Hill Book Co., Inc., New York; 1951.
83. Ramo, S. and Whinnery, J. R., Fields and Waves in Modern Radio, Second Edition, John Wiley and Sons, Inc., New York; 1953.
84. Sasiela, R., "Exploratory Development on Coupling Schemes for Plasma Amplifiers," Microwave Associates, Inc., Tech. Report AFAL-TR-68-109, Air Force Avionics Laboratory, Air Force Systems Command, Wright-Patterson Air Force Base, Ohio; April, 1968.
85. Panofsky, W. K. H. and Phillips, M., Classical Electricity and Magnetism, Addison-Wesley Publishing Company, Inc., Reading, Mass.; 1955.
86. Heald, M. A. and Wharton, C. B., Plasma Diagnostics with Microwaves, John Wiley and Sons, Inc., New York; 1965.
87. Smythe, W. R., Static and Dynamic Electricity, Second Edition, McGraw-Hill Book Co., Inc., New York; 1950.

## LIST OF SYMBOLS

$\vec{A}$	Vector potential.
$A_n$	Normalized circuit voltage amplitude of the nth harmonic.
$A_{no}$	Normalized input signal level relative to $C_1 I_0 V_0$ .
$a$	Inner radius of the metallic drift tube surrounding beam and plasma.
$B$	Space-charge force range parameter.
$\vec{B}$	Magnetic field strength.
$B'$	Ratio of Bessel functions, defined by Eq. 2.55.
$B_0$	Static axial magnetic field.
$B_{Br}$	Brillouin magnetic field, defined by Eq. 5.1.
$B_c$	Axial magnetic field at the electron beam cathode.
$b$	Inner radius of the dielectric tube containing the plasma column.
$b'$	Radius of electron beam.
$b_1$	Injection velocity parameter of the fundamental signal.
$b_n$	Injection velocity parameter, $(u_0 - v_{on})/c v_{on}$ .
$C_{on}$	Complex capacitance of the equivalent transmission line for the nth harmonic.
$C'_{on}$	Capacitance of the equivalent transmission line for the collisionless case.
$C_1$	Beam-circuit coupling parameter, or gain parameter, defined by Eq. 3.7.
$C_n$	Gain parameter for the nth harmonic.
$c$	Radius of the region containing a beam and plasma, used in Appendix A.



$\vec{D}$	Electric displacement vector.
$\vec{D}_1$	Ac component of the electric displacement vector.
$d_n$	Loss parameter for the nth harmonic.
$\vec{E}$	Electric field strength.
$E_{nsc-z}$	Longitudinal space-charge field for the nth harmonic.
$e$	Absolute value of the charge of an electron.
$F_{1-z}$	One-dimensional space-charge weighting function.
$F_{2-r}$	Two-dimensional radial space-charge weighting function.
$F_{2-z}$	Two-dimensional longitudinal space-charge weighting function.
$f$	Signal frequency in Hz.
$f_a$	Lower frequency signal in two-signal operation.
$f_b$	Upper frequency signal in two-signal operation.
$f_b$	Beam plasma frequency.
$f_n, (n=2,3,\dots)$	Harmonic signal generated in the beam-plasma system.
$f_p$	Plasma-plasma frequency.
$f_s$	Signal frequency.
$G$	Green's function.
$G_n$	Combination of nth-order Bessel functions.
$\vec{H}$	Magnetic field intensity.
$I$	Dc beam current, a positive quantity.
$I_o$	Injected dc beam current, a positive quantity.
$I_D$	Electron beam current density.
$I_n$	Modified Bessel function of the first kind and nth order.

$I_{zc}$	Convection current in the plasma column.
$I_{zd}$	Displacement current in the plasma column.
$i_n$	RF current of the nth harmonic.
$i_z$	Convection current in the electron beam, a positive quantity.
$\vec{J}$	Current density.
$J_n$	Bessel function of the first kind and nth order.
$J_{zc}$	Convection current density in the plasma column.
$j$	Charge group label.
$K$	Magnetic field factor, defined by Eq. 4.61.
$K_n$	Modified Bessel function of the second kind and nth order.
$k$	Boltzmann constant, $1.380 \cdot 10^{-23}$ J/°K.
$k$	Complex propagation constant.
$k_0$	Propagation constant of free space.
$k_n$	Complex propagation constant for the nth harmonic.
$L$	Distance.
$L$	Integer used in the Fourier series coefficient integrals.
$L_{on}$	Complex inductance of the equivalent transmission line for the nth harmonic.
$L'_{on}$	Inductance of the equivalent transmission line for the collisionless case.
$m$	Mass of a particle.
$m_1$	Major axis of an ellipse.
$m_2$	Minor axis of an ellipse.
$N_D$	Number of particles in a Debye sphere.

$N_n$	Bessel function of the second kind and nth order.
$N_s$	Number of stream wavelengths of the fundamental signal.
$n$	Particle density.
$n$	Angular mode number of the field quantities in the plasma.
$n$	Harmonic number.
$n_e$	Electron density in the plasma column.
$P$	Pressure in Torr.
$\vec{P}$	Volume polarization.
$\vec{P}_1$	Ac volume polarization.
$q$	Electric charge of a particle.
$q_z$	Charge giving rise to the convection current $i_z$ .
$R_n$	Plasma frequency reduction factor for the nth harmonic.
$r$	Radial coordinate.
$r_L$	Load radius of a radial transmission line.
$r_i$	Input radius of a radial transmission line.
$T$	Temperature.
$T$	Period over which the circuit equations are integrated.
$T_b$	Radial propagation constant in the region containing a beam and plasma.
$T_e$	Electron temperature.
$T_{pn}$	Radial propagation constant in a plasma column for the nth harmonic.
$t$	Time
$u(y_1, \phi_{01})$	Normalized velocity variable.

$u_0$	Dc beam velocity.
$u_z$	Longitudinal velocity.
$V$	"Circuit" voltage at the plasma edge.
$V'$	Scalar potential.
$V_0$	Beam voltage.
$V_n$	Circuit voltage for the nth harmonic.
$V_{sc}$	Space-charge potential.
$\vec{v}$	Velocity.
$\bar{v}$	Average electron velocity in the plasma.
$v_{on}$	Phase velocity of the nth harmonic along the "circuit."
$\vec{v}_1$	RF velocity.
$x$	Normalized radial position variable, defined by Eq. 4.2.
$y_1$	Normalized axial distance variable, defined by Eq. 3.6.
$Z$	Characteristic impedance of a radial waveguide.
$Z_{on}$	Complex characteristic impedance of the equivalent transmission line, defined by Eq. 3.18.
$Z_{oni}$	Imaginary part of the complex interaction impedance.
$Z_{onr}$	Real part of the complex interaction impedance.
$Z_L$	Load impedance of a radial waveguide.
$Z_c$	Characteristic impedance of a coaxial line.
$Z_i$	Input impedance of a radial waveguide.
$z$	Longitudinal coordinate.
$\alpha$	Attenuation constant.
$\alpha$	Radial charge density variation parameter in a plasma column.

$\alpha_n$	Attenuation constant in a plasma for the nth harmonic.
$\alpha_n$	Bunch injection phase angle for the nth harmonic.
$\beta$	Phase constant.
$\beta_e$	Stream phase constant.
$\beta_n$	Phase constant in a plasma for the nth harmonic.
$\gamma$	Radial propagation constant.
$\delta$	Dirac delta function.
$\vec{\epsilon}$	Permittivity of a plasma, a tensor.
$\epsilon_0$	Permittivity of free space, $8.854 \cdot 10^{-12}$ F/m.
$\epsilon_{rr}$	Radial component of the tensor permittivity in a plasma.
$\epsilon_{zz}$	Longitudinal component of the tensor permittivity in a plasma.
$\zeta$	Characteristic impedance of free space, $(\mu_0/\epsilon_0)^{1/2} = 377 \Omega$ .
$\zeta_{ni}$	Imaginary part of the normalized interaction impedance for the nth harmonic.
$\zeta_{nr}$	Real part of the normalized interaction impedance for the nth harmonic.
$\eta$	Absolute value of the charge-to-mass ratio of an electron.
$\theta$	Phase angle for a radial transmission line, defined by Eq. 7.9.
$\theta_n$	Phase shift of the actual nth harmonic signal traveling along the "circuit" with respect to a hypothetical wave traveling at the beam velocity.
$\theta_{xn}$	Radial phase shift variable.
$\vec{\kappa}$	Specific inductive capacity tensor.
$\kappa_e$	Specific inductive capacity of the cylinder surrounding the plasma column.

$\kappa_{  }, \kappa_{\perp}, \kappa_x$	Components of the specific inductive capacity tensor, defined in Eq. B.16.
$\lambda$	Mean-free-path of gas particles.
$\lambda_D$	Debye length.
$\lambda_e$	Mean-free-path of the plasma electrons.
$\lambda_s$	Stream wavelength.
$\mu_0$	Permeability of free space, $4\pi/10^7$ H/m.
$\mu_l, \mu_s$	Arguments that define zeros of Bessel functions.
$\nu$	Plasma collision frequency in rad/s.
$\nu_c$	Collision frequency between beam electrons and plasma particles in rad/s.
$\nu_l$	Normalized Bessel function argument.
$\rho$	Charge density.
$\rho_0$	Dc charge density.
$\rho_1$	Ac charge density.
$\rho_z$	Charge density due to $q_z$ .
$\sigma$	Linear charge density.
$\Phi_{01}$	Entry phase of the fundamental RF component, defined by Eq. 3.8.
$\Phi_n$	Phase of the nth harmonic component relative to the phase at the entrance to the interaction region.
$\Phi'_n$	Phase position of a charge group that influences the charge group at $\Phi_n$ , used in the space-charge field weighting functions.
$\varphi$	Azimuthal coordinate.
$\vec{\chi}$	Electric susceptibility tensor.
$\psi$	Phase angle for a radial transmission line, defined by Eq. 7.10.
$\psi_n(x)$	Weighting function proportional to the radial variation of the longitudinal electric field across the plasma column.

$\omega$	Signal frequency in rad/s.
$\omega_b$	Beam plasma frequency.
$\omega_c, \omega_{ce}$	Electron cyclotron frequency.
$\omega_{ci}$	Ion cyclotron frequency.
$\omega_p$	Plasma-plasma frequency.
$\omega_{pe}$	Plasma frequency at the plasma column edge.
$\omega_{pm}$	Maximum plasma frequency in the plasma column.
$\omega_{qn}$	Reduced plasma frequency of the beam electrons for the nth harmonic.
$\omega_s$	Signal frequency.
$\omega_\infty$	Frequency in the forward-wave branch of the $\omega$ - $\beta$ diagram where $\beta \rightarrow \infty$ .

**DOCUMENT CONTROL DATA - R & D**

*(Security classification of title, body of abstract and indexing annotation must be entered when the overall report is classified)*

<b>1. ORIGINATING ACTIVITY (Corporate author)</b> The University of Michigan Electron Physics Laboratory Ann Arbor, Michigan 48104		<b>2a. REPORT SECURITY CLASSIFICATION</b> Unclassified	
		<b>2b. GROUP</b>	
<b>3. REPORT TITLE</b> Harmonic Generation in Nonlinear Beam-Plasma Systems			
<b>4. DESCRIPTIVE NOTES (Type of report and inclusive dates)</b> Technical Report No. 112			
<b>5. AUTHOR(S) (First name, middle initial, last name)</b> G. T. Konrad			
<b>6. REPORT DATE</b> January, 1969		<b>7a. TOTAL NO. OF PAGES</b> 272	<b>7b. NO. OF REFS</b>
<b>8a. CONTRACT OR GRANT NO.</b> NGL 23-005-183		<b>9a. ORIGINATOR'S REPORT NUMBER(S)</b> Technical Report No. 112	
<b>b. PROJECT NO.</b>		<b>9b. OTHER REPORT NO(S) (Any other numbers that may be assigned this report)</b>	
<b>c.</b>			
<b>d.</b>			
<b>10. DISTRIBUTION STATEMENT</b> N/A			
<b>11. SUPPLEMENTARY NOTES</b>		<b>12. SPONSORING MILITARY ACTIVITY</b> Office of Space Science and Applications National Aeronautics and Space Administration, Washington, D. C.	
<b>13. ABSTRACT</b> <p>Nonlinear operation and the saturation characteristics of beam-plasma devices are investigated both theoretically and experimentally. The gain, power output, efficiency and the magnitude of the higher harmonic components that pertain to such devices are of particular interest. The geometry analyzed in this study consists of a cylindrical plasma column, treated in a linear fashion, which serves as a slow-wave circuit along which electromagnetic energy can propagate. A cylindrical electron stream, treated in a nonlinear fashion, is assumed to be concentric with the plasma column. RF amplification takes place when a fraction of the kinetic energy of the stream electrons is converted into RF wave energy. One- as well as two-dimensional stream models are used to calculate the RF currents and circuit voltages of the fundamental signal and its harmonics by use of a digital computer.</p> <p>An experimental test vehicle is used to correlate the theoretically calculated results with those obtained from an actual beam-plasma interaction. A xenon plasma column 10.5 cm long yields electronic gain as high as 35 dB in the vicinity of 2 GHz. Harmonic components through the fifth are observed with the second harmonic being only 5 dB below the fundamental under certain conditions. Two methods of coupling RF energy to the device are employed. The quasi-optical technique making use of elliptic cavity couplers reduces the coupling losses significantly compared to previously used coupling schemes.</p>			



14. KEY WORDS	LINK A		LINK B		LINK C	
	ROLE	WT	ROLE	WT	ROLE	WT
Beam-Plasma Amplification Nonlinearities Harmonics RF Coupling						